The 2010 Interim Report of the Long-Baseline Neutrino Experiment Collaboration Physics Working Groups

Collaboration, TLBNE; Akiri, T; Allspach, D; Andrews, M; Arisaka, K; Arrieta-Diaz, E; Artuso, M; Bai, X; Balantekin, B; Baller, B; Barletta, W; Barr, G; Bass, M; Beck, A; Becker, B; Bellini, V; Benhar, O; Berger, B; Bergevin, M; Berman, E; Berns, H; Bernstein, A; Beroz, F; Bhatnagar, V; Bhuyan, B; Bionta, R; Bishai, M; Blake, A; Blaufuss, E; Bleakley, B; Blucher, E; Blusk, S; Boehnlein, D; Bolton, T; Brack, J; Bradford, R; Breedon, R; Bromberg, C; Brown, R; Buchanan, N; Camilleri, L; Campbell, M; Carr, R; Carminati, G; Chen, A; Chen, H; Cherdack, D; Chi, C; Childress, S; Choudhary, B; Church, E; Cline, D; Coleman, S; Corey, R; D'Agostino, M; Davies, G; Dazeley, S; Jong, JD; DeMaat, B; Demuth, D; Dighe, A; Djurcic, Z; Dolph, J; Drake, G; Drozhdin, A; Duan, H; Duyang, H; Dye, S; Dykhuis, T; Edmunds, D; Elliott, S; Enomoto, S; Escobar, C; Felde, J; Feyzi, F; Fleming, B; Fowler, J; Fox, W; Friedland, A; Fujikawa, B; Gallagher, H; Garilli, G; Garvey, G; Gehman, V; Geronimo, G; Gill, R; Goodman, M; Goon, J; Gorbunov, D; Gran, R; Guarino, V; Guarnaccia, E; Guenette, R; Gupta, P; Habig, A; Hackenberg, R; Hahn, A; Hahn, R; Haines, T; Hans, S; Harton, J; Hays, S; Hazen, E; He, Q; Heavey, A; Heeger, K; Hellauer, R; Himmel, A; Horton-Smith, G; Howell, J; Huber, P; Hurh, P; Huston, J; Hylen, J; Insler, J; Jaffe, D; James, C; Johnson, C; Johnson, M; Johnson, R; Johnson, W; Johnston, W; Johnstone, J; Jones, B; Jostlein, H; Junk, T; Junnarkar, S; Kadel, R; Kafka, T; Kaminski, D; Karagiorgi, G; Karle, A; Kaspar, J; Katori, T; Kayser, B; Kearns, E; Kettell, S; Khanam, F; Klein, J; Kneller, J; Koizumi, G; Kopp, J; Kopp, S; Kropp, W; Kudryavtsev, V; Kumar, A; Kumar, J; Kutter, T; Lackowski, T; Lande, K; Lane, C; Lang, K; Lanni, F; Lanza, R; Latorre, T; Learned, J; Lee, D; Lee, K; Li, Y; Linden, S; Ling, J; Link, J; Littenberg, L; Loiacono, L; Liu, T; Losecco, J; Louis, W; Lucas, P; Lunardini, C; Lundberg, B; Lundin, T; Makowiecki, D; Malys, S; Mandal, S; Mann, A; Mann, A; Mantsch, P; Marciano, W; Mariani, C; Maricic, J; Marino, A; Marshak, M; Maruyama, R; Mathews, J; Matsuno, S; Mauger, C; McCluskey, E; McDonald, K; McFarland, K; McKeown, R; McTaggart, R; Mehdiyev, R; Melnitchouk, W; Meng, Y; Mercurio, B; Messier, M; Metcalf, W; Milincic, R; Miller, W; Mills, G; Mishra, S; MoedSher, S; Mohapatra, D; Mokhov, N; Moore, C; Morfin, J; Morse, W; Moss, A; Mufson, S; Musser, J; Naples, D; Napolitano, J; Newcomer, M; Norris, B; Ouedraogo, S; Page, B; Pakvasa, S; Paley, J; Paolone, V; Papadimitriou, V; Parsa, Z; Partyka, K; Pavlovic, Z; Pearson, C; Perasso, S; Petti, R; Plunkett, R; Polly, C; Pordes, S; Potenza, R; Prakash, A; Prokofiev, O; Qian, X; Raaf, J; Radeka, V; Raghavan, R; Rameika, R; Rebel, B; Rescia, S; Reitzner, D; Richardson, M; Riesselman, K; Robinson, M; Rosen, M; Rosenfeld, C; Rucinski, R; Russo, T; Sahijpal, S; Salon, S; Samios, N; Sanchez, M; Schmitt, R; Schmitz, D; Schneps, J; Scholberg, K; Seibert, S; Sergiampietri, F; Shaevitz, M; Shanahan, P; Shaposhnikov, M; Sharma, R; Simos, N; Singh, V; Sinnis, G; Sippach, W; Skwarnicki, T; Smy, M; Sobel, H; Soderberg, M; Sondericker, J; Sondheim, W; Spitz, J; Spooner, N; Stancari, M; Stancu, I; Stewart, J; Stoler, P; Stone, J; Stone, S; Strait, J;

Straszheim, T; Striganov, S; Sullivan, G; Svoboda, R; Szczerbinska, B; Szelc, A; Talaga, R; Tanaka, H; Tayloe, R; Taylor, D; Thomas, J; Thompson, L; Thomson, M; Thorn, C; Tian, X; Toki, W; Tolich, N; Tripathi, M; Trovato, M; Tseung, H; Tzanov, M; Urheim, J; Usman, S; Vagins, M; Berg, RV; Water, RVD; Varner, G; Vaziri, K; Velev, G; Viren, B; Wachala, T; Walter, C; Wang, H; Wang, Z; Warner, D; Webber, D; Weber, A; Wendell, R; Wendt, C; Wetstein, M; White, H; White, S; Whitehead, L; Willis, W; Wilson, RJ; Winslow, L; Ye, J; Yeh, M; Yu, B; Zeller, G; Zhang, C; Zimmerman, E; Zwaska, R

The 2010 Interim Report of the Long-Baseline Neutrino Experiment Collaboration Physics Working Groups

T. Akiri,[19] D. Allspach,[20] M. Andrews,[20] K. Arisaka,[9] E. Arrieta-Diaz,[38] M. Artuso,[60] X. Bai,[57] B. Balantekin,[68] B. Baller,[20] W. Barletta,[42] G. Barr,[48] M. Bass,[14] B. Becker,[45] V. Bellini,[12] B. Berger,[14] M. Bergevin,[6] E. Berman,[20] H. Berns,[65] A. Bernstein,[33] V. Bhatnagar,[26] B. Bhuyan,[25] R. Bionta,[33] M. Bishai,[5] A. Blake,[11] E. Blaufuss,[37] B. Bleakley,[58] E. Blucher,[13] S. Blusk,[60] D. Boehnlein,[20] T. Bolton,[30] J. Brack,[14] R. Breedon,[6] C. Bromberg,[38] R. Brown,[5] N. Buchanan,[14] L. Camilleri,[16] M. Campbell,[20] R. Carr,[16] G. Carminati,[7] A. Chen,[20] H. Chen,[5] D. Cherdack,[14] C. Chi,[16] S. Childress,[20] B. Choudhary,[24] E. Church,[69] D. Cline,[9] S. Coleman,[15] J. Conrad,[42] R. Corey,[57] M. DAgostino,[2] G. Davies,[29] S. Dazeley,[33] J. De Jong,[48] B. DeMaat,[20] C. Escobar,[20] D. Demuth,[40] M. Diwan,[5] Z. Djurcic,[2] J. Dolph,[5] G. Drake,[2] A. Drozhdin,[20] H. Duyang,[56] S. Dye,[21] T. Dykhuis,[20] D. Edmunds,[38] S. Elliott,[35] S. Enomoto,[65] J. Felde,[6] F. Feyzi,[68] B. Fleming,[69] J. Fowler,[19] W. Fox,[27] A. Friedland,[35] B. Fujikawa,[32] H. Gallagher,[63] G. Garilli,[12] G. Garvey,[35] V. Gehman,[35] G. Geronimo,[5] R. Gill,[5] M. Goodman,[2] J. Goon,[1] R. Gran,[41] V. Guarino,[2] E. Guarnaccia,[64] R. Guenette,[69] P. Gupta,[6] A. Habig,[41] R. Hackenberg,[5] A. Hahn,[20] R. Hahn,[5] T. Haines,[35] S. Hans,[5] J. Harton,[14] S. Hays,[20] E. Hazen,[4] Q. He,[51] A. Heavey,[20] K. Heeger,[68] R. Hellauer,[37] A. Himmel,[19] G. Horton-Smith,[30] J. Howell,[20] P. Hurh,[20] J. Huston,[38] J. Hylen,[20] J. Insler,[36] D. Jaffe,[5] C. James,[20] C. Johnson,[27] M. Johnson,[20] R. Johnson,[15] W. Johnston,[14] J. Johnstone,[20] B. Jones,[42] H. Jostlein,[20] T. Junk,[20] S. Junnarkar,[5] R. Kadel,[32] T. Kafka,[63] D. Kaminski,[52] G. Karagiorgi,[16] A. Karle,[68] J. Kaspar,[65] T. Katori,[42] B. Kayser,[20] E. Kearns,[4] S. Kettell,[5] F. Khanam,[14] J. Klein,[49] G. Koizumi,[20] S. Kopp,[62] W. Kropp,[7] V. Kudryavtsev,[55] A. Kumar,[26] J. Kumar,[21] T. Kutter,[36] T. Lackowski,[20] K. Lande,[49] C. Lane,[18] K. Lang,[62] F. Lanni,[5] R. Lanza,[42] T. Latorre,[49] J. Learned,[21] D. Lee,[35] K. Lee,[9] Y. Li,[5] S. Linden,[4] J. Ling,[5] J. Link,[64] L. Littenberg,[5] L. Loiacono,[53] T. Liu,[59] J. Losecco,[46] W. Louis,[35] P. Lucas,[20] B. Lundberg,[20] T. Lundin,[20] D. Makowiecki,[5] S. Malys,[44] S. Mandal,[24] A. Mann,[49] A. Mann,[63] P. Mantsch,[20] W. Marciano,[5] C. Mariani,[16] J. Maricic,[18] A. Marino,[15] M. Marshak,[39] R. Maruyama,[68] J. Mathews,[45] S. Matsuno,[21] C. Mauger,[35] E. McCluskey,[20] K. McDonald,[51] K. McFarland,[53] R. McKeown,[10] R. McTaggart,[58] R. Mehdiyev,[62] Y. Meng,[9] B. Mercurio,[56] M. Messier,[27] W. Metcalf,[36] R. Milincic,[18] W. Miller,[39] G. Mills,[35] S. Mishra,[56] S. Moed Sher,[20] D. Mohapatra,[64] N. Mokhov,[20] C. Moore,[20] J. Morfin,[20] W. Morse,[5] S. Mufson,[27] J. Musser,[27] D. Naples,[50] J. Napolitano,[52] M. Newcomer,[49] B. Norris,[20] S. Ouedraogo,[33] B. Page,[38] S. Pakvasa,[21] J. Paley,[2] V. Paolone,[50] V. Papadimitriou,[20] Z. Parsa,[5] K. Partyka,[69] Z. Pavlovic,[35] C. Pearson,[5] S. Perasso,[18] R. Petti,[56] R. Plunkett,[20] C. Polly,[20] S. Pordes,[20] R. Potenza,[12] A. Prakash,[42] O. Prokofiev,[20] X. Qian,[10] J. Raaf,[20] V. Radeka,[5] R. Raghavan,[64] R. Rameika,[20] B. Rebel,[20] S. Rescia,[5] D. Reitzner,[20] M. Richardson,[55] K. Riesselman,[20] M. Robinson,[55] M. Rosen,[21] C. Rosenfeld,[56] R. Rucinski,[20] T. Russo,[5] S. Sahijpal,[26] S. Salon,[52] N. Samios,[5] M. Sanchez,[29] R. Schmitt,[20] D. Schmitz,[20] J. Schneps,[63] K. Scholberg,[19] S. Seibert,[49] F. Sergiampietri,[9] M. Shaevitz,[16] P. Shanahan,[20] R. Sharma,[5] N. Simos,[5] V. Singh,[23] G. Sinnis,[35] W. Sippach,[16] T. Skwarnicki,[60] M. Smy,[7] H. Sobel,[7] M. Soderberg,[60] J. Sondericker,[5] W. Sondheim,[35] J. Spitz,[69] N. Spooner,[55] M. Stancari,[20] I. Stancu,[1] J. Stewart,[5] P. Stoler,[52] J. Stone,[4] S. Stone,[60] J. Strait,[20] T. Straszheim,[37] S. Striganov,[20] G. Sullivan,[37] R. Svoboda,[6] B. Szczerbinska,[17] A. Szelc,[69] R. Talaga,[2] H. Tanaka,[5] R. Tayloe,[27] D. Taylor,[32] J. Thomas,[34] L. Thompson,[55] M. Thomson,[11] C. Thorn,[5] X. Tian,[56] W. Toki,[14] N. Tolich,[65] M. Tripathi,[6] M. Trovato,[12] H. Tseung,[65] M. Tzanov,[36] J. Urheim,[27] S. Usman,[44] M. Vagins,[28] R. Van Berg,[49] R. Van de Water,[35] G. Varner,[21] K. Vaziri,[20] G. Velev,[20] B. Viren,[5] T. Wachala,[14] C. Walter,[19] H. Wang,[9] Z. Wang,[5] D. Warner,[14] D. Webber,[68] A. Weber,[48] R. Wendell,[19] C. Wendt,[68] M. Wetstein,[2] H. White,[35] S. White,[5] L. Whitehead,[22] W. Willis,[16] R.J. Wilson,[14, *] L. Winslow,[42] J. Ye,[59] M. Yeh,[5] B. Yu,[5] G. Zeller,[20] C. Zhang,[10] E. Zimmerman,[15] and R. Zwaska[20]

(The Long-Baseline Neutrino Experiment Science Collaboration (LBNE))

A. Beck,[19] O. Benhar,[54] F. Beroz,[19] A. Dighe,[61] H. Duan,[45] D. Gorbunov,[43] P. Huber,[64] J. Kneller,[47] J. Kopp,[20] C. Lunardini,[3] W. Melnitchouk,[8] A. Moss,[19] and M. Shaposhnikov[31]

(Additional Contributors)

[1] *Univ. of Alabama, Tuscaloosa, AL 35487-0324, USA*
[2] *Argonne National Laboratory, Argonne, IL 60437, USA*
[3] *Arizona State University, Tempe, AZ 85287-1504*
[4] *Boston Univ., Boston, MA 02215, USA*
[5] *Brookhaven National Laboratory, Upton, NY 11973-5000, USA*
[6] *Univ. of California at Davis, Davis, CA 95616, USA*
[7] *Univ. of California at Irvine, Irvine, CA 92697-4575, USA*

[8] *Jefferson Lab, Newport News, Virginia 23606, USA*
[9] *Univ. of California at Los Angeles, Los Angeles, CA 90095-1547, USA*
[10] *California Inst. of Tech., Pasadena, CA 91109, USA*
[11] *Univ. of Cambridge, Madingley Road, Cambridge CB3 0HE, United Kingdom*
[12] *Univ. of Catania and INFN, I-95129 Catania, Italy*
[13] *Univ. of Chicago, Chicago, IL 60637-1434, USA*
[14] *Colorado State Univ., Fort Collins, CO 80521, USA*
[15] *Univ. of Colorado, Boulder, CO 80309 USA*
[16] *Columbia Univ., New York, NY 10027 USA*
[17] *Dakota State University, Brookings, SD 57007, USA*
[18] *Drexel Univ., Philadelphia, PA 19104, USA*
[19] *Duke Univ., Durham, NC 27708, USA*
[20] *Fermilab, Batavia, IL 60510-500, USA*
[21] *Univ. of Hawai'i, Honolulu, HI 96822-2216, USA*
[22] *Univ. of Houston, Houston, Texas, USA*
[23] *Banaras Hindu Univ., Varanasi UP 221005, India*
[24] *Univ. of Delhi, Delhi 110007, India*
[25] *Indian Institute of Technology, North Guwahata, Guwahata 781039, Assam, India*
[26] *Panjab Univ., Chandigarh 160014, U.T., India*
[27] *Indiana Univ., Bloomington, Indiana 47405, USA*
[28] *Institute for the Physics and Mathematics of the Universe University of Tokyo, Chiba 277-8568, Japan*
[29] *Iowa State Univ., Ames, IA 50011, USA*
[30] *Kansas State Univ., Manhattan, KS 66506, USA*
[31] *Ecole Polytechnique Fédérale de Lausanne, CH-1015 Lausanne, Switzerland*
[32] *Lawrence Berkeley National Lab., Berkeley, CA 94720-8153, USA*
[33] *Lawrence Livermore National Lab., Livermore, CA 94551, USA*
[34] *University College London, London, WIC1E 6BT, England, UK*
[35] *Los Alamos National Lab., Los Alamos, NM 87545, USA*
[36] *Louisiana State Univ., Baton Rouge, LA 70803-4001, USA*
[37] *Univ. of Maryland, College Park, MD 20742-4111, USA*
[38] *Michigan State Univ., East Lansing, MI 48824, USA*
[39] *Univ. of Minnesota, Minneapolis, MN 55455, USA*
[40] *Univ. of Minnesota, Crookston, Crookston, MN 56716-5001, USA*
[41] *Univ. of Minnesota, Duluth, Dululth, MN 55812, USA*
[42] *MIT Massachusetts Inst. of Technology, Cambridge, MA 02139- 4307, USA*
[43] *Institute for Nuclear Research of the Russian Academy of Sciences, Moscow 117312, Russia*
[44] *National Geospatial-Intelligence Agency, Reston, VA 20191, USA*
[45] *New Mexico State Univ., Albuquerque, NM 87131, USA*
[46] *Univ. of Notre Dame, Notre Dame, IN 46556-5670, USA*
[47] *North Carolina State University, Raleigh, North Carolina 27695, USA*
[48] *Univ. of Oxford, Oxford OX1 3RH England, UK*
[49] *Univ. of Pennsylvania, Philadelphia, PA 19104- 6396, USA*
[50] *University of Pittsburgh, Pittsburgh, PA 15260, USA*
[51] *Princeton University, Princeton, NJ 08544-0708, USA*
[52] *Rensselaer Polytechnic Inst., Troy, NY 12180- 3590, USA*
[53] *Univ. of Rochester, Rochester, NY 14627-0171, USA*
[54] *"Sapienza" Università di Roma, I-00185 Roma, Italy*
[55] *Univ. of Sheffield, Sheffield, S3 7RH, England, UK*
[56] *Univ. of South Carolina, Orangeburg, SC 29117, USA*
[57] *South Dakota School of Mines and Technology, Rapid City, SD 57701, USA*
[58] *South Dakota State Univ., Brookings, SD 57007, USA*
[59] *Southern Methodist Univ., Dallas, TX 75275, USA*
[60] *Syracuse Univ., Syracuse, NY 13244-1130, USA*
[61] *Tata Institute of Fundamental Research, Homi Bhabha Road, Colaba, Mumbai 400005, India*
[62] *Univ. of Texas, Austin, Texas 78712, USA*
[63] *Tuffs Univ., Medford, Massachusetts 02155, USA*
[64] *Virginia Tech., Blacksburg, VA 24061-0435, USA*
[65] *Univ. of Washington, Seattle, WA 98195-1560, USA*
[66] *Institute for Nuclear Theory, University of Washington, Seattle, WA 98195, USA*
[67] *University of Western Ontario, London, Canada*
[68] *Univ. of Wisconsin, Madison, WI 53706, USA*
[69] *Yale Univ., New Haven, CT 06520, USA*

(Dated: October 31, 2011)

Abstract

In early 2010, the Long-Baseline Neutrino Experiment (LBNE) science collaboration initiated a study to investigate the physics potential of the experiment with a broad set of different beam, near- and far-detector configurations. Nine initial topics were identified as scientific areas that motivate construction of a long-baseline neutrino experiment with a very large far detector. We summarize the scientific justification for each topic and the estimated performance for a set of far detector reference configurations. We report also on a study of optimized beam parameters and the physics capability of proposed Near Detector configurations. This document was presented to the collaboration in fall 2010 and updated with minor modifications in early 2011.

* Corresponding author: bob.wilson@colostate.edu

CONTENTS

I. INTRODUCTION

This report is the first of an anticipated series of documents from the Long-Baseline Neutrino Experiment (LBNE) Science Collaboration Physics Working Group (PWG) that are intended to assist the collaboration and LBNE Project [1] with establishing the best possible science case. This first document in the series focuses on the relative performance of a set of Far Detector configurations with large water Cerenkov and liquid argon detectors.

Nine initial topics (Table I) were identified as scientific areas that motivate construction of a long-baseline neutrino experiment with a very large far detector. In each section of this report we summarize the scientific justification for each topic, the expected state of knowledge in each area from current and planned experiments, and the estimated performance in these areas for each of a set of reference configurations described in Section II. In each section the performance parameters most relevant to that topic are presented–it must be emphasized that these parameters are in various stages of development and will evolve as the detector groups develop more sophisticated simulations.

Although the primary focus of this report is on the Far Detector configurations, we have included a substantial chapter on the physics requirements for the Near Detector complex. Though the emphasis is on topics that most impact the long-baseline mixing parameter measurements, we summarize also some of the broad range of additional neutrino interaction studies that would be enabled with an enhanced complex and higher neutrino flux than assumed for the long-baseline studies.

Long-Baseline Physics:	Proton decay
(a) Mass Hierarchy and CP violation	UHE neutrinos
(b) Theta13 measurement	Atmospheric neutrinos
(c) Oscillation parameters precision measurement	Solar neutrinos
(d) New Phenomena	Geo- & Reactor neutrinos
Supernova Burst Neutrinos	Supernova Relic Neutrinos

TABLE I. List of topics investigated.

II. FAR DETECTOR REFERENCE CONFIGURATIONS

In order to explore the sensitivity of LBNE in the physics topic areas, a set of "reference" detectors are defined. A reference detector is not a specific detector design, and likely not an optimal one, but rather is a set of performance parameters based on preliminary designs for LBNE, simulations in some cases and from previous experience (Super-Kamiokande water Cerenkov and ICARUS liquid argon detectors, for example). These parameterized detectors can be used to study the physics case for various configurations, where a configuration is defined as a set of reference detectors at specified locations at the near and far sites. The depth requirements for a massive detector at Homestake are discussed in detail in Ref. [2].

Previous studies have indicated that the expected sensitivity to neutrino oscillation parameter measurements for a 17-kt fiducial mass liquid argon detector is roughly equivalent to a 100-kt water Cerenkov detector. For the purposes of this comparative study, we have considered the fourteen far detector configurations, listed below, that total 300-kt Water Cerenkov Equivalent (WCE) fiducial mass. Although the enumerated configurations are 300-kt WCE, most sections first calculate the performance for 100-kt WCE modules and these results are combined for larger configurations; this means that the relative performance of many other combinations of lower and higher mass can be deduced relatively straightforwardly. In Section III, Long-Baseline Physics, the focus is on a 200-kt WCE configuration to match the LBNE Project reference designs. Table II shows the configuration list in a more compact form that will be referred to throughout the document.

1. Three 100-kt fiducial water Cherenkov detectors at a depth of 4850 feet at DUSEL. Photosensitive area coverage is 15% of total surface area with 10 inch High-QE PMT's.

   1a. Same as 1, but with 30% coverage.

   1b. Same as 1a, but with gadolinium loading also.

2. Three 17-kt fiducial liquid argon detectors at a depth of 4850 feet at DUSEL. Assume a scintillation photon trigger is available for proton decay and supernova neutrinos.

   2a. Same as 2, but with depth 300 feet and no photon trigger.

2b. Same as 2, but with depth 800 feet and no photon trigger.

3. Two 100-kt fiducial water Cherenkov detectors at 4850 foot depth as specified in 1, plus one 17-kt fiducial liquid argon detector at 300 foot depth as specified in 2a.

   3a. Same as 3, but with the water Cherenkov modules as in 1a.

   3b. Same as 3, but with one water Cherenkov modules as in 1b.

4. Two 100-kt fiducial water Cherenkov detectors at 4850 foot depth as specified in 1, plus one 17-kt fiducial liquid argon detector at 800 foot depth as specified in 2b.

   4a. Same as 4, but with the water Cherenkov modules as in 1a.

   4b. Same as 4, but with one water Cherenkov modules as in 1b.

5. One 100-kt fiducial gadolinium loaded water Cherenkov detector at 4850 depth as specified in 1b. Two 17-kt liquid argon modules at 300 feet as specified as in 2a.

6. One 100-kt fiducial gadolinium loaded water Cherenkov detector at 4850 depth as specified in 1b. Two 17-kt liquid argon modules at 800 feet as specified as in 2b.

Config. Number	Detector Configuration Description
1	Three 100 kt WC, 15%
1a	Three 100 kt WC, 30%
1b	Three 100 kt WC, 30% with Gd
2	Three 17 kt LAr, 4850 ft, γ trig
2a	Three 17 kt LAr, 300 ft, no γ trig
2b	Three 17 kt, LAr, 800 ft, γ trig
3	Two 100 kt WC, 15% + One 17 kt LAr, 300 ft, no γ trig
3a	Two 100 kt WC, 30% + One 17 kt LAr, 300 ft, no γ trig
3b	One 100 kt WC, 15% + One 100 kt WC, 30% & Gd + One 17 kt LAr, 300 ft, no γ trig
4	Two 100 kt WC, 15% + One 17 kt LAr, 800 ft, γ trig
4a	Two 100 kt WC, 30% + One 17 kt LAr, 800 ft, γ trig
4b	One 100 kt WC, 15% + One 100 kt WC, 30% & Gd + One 17 kt LAr, 800 ft, γ trig
5	One 100 kt WC, 30% & Gd + Two 17 kt LAr, 300 ft, no γ trig
6	One 100 kt WC, 30% & Gd + Two 17 kt LAr, 800 ft, γ trig

TABLE II. Summary of the far detector reference configurations.

III. LONG-BASELINE PHYSICS

A. Motivation and Scientific Impact

Long-baseline neutrino oscillation physics is the primary focus for the Long-Baseline Neutrino Experiment (LBNE); the motivation and scientific impact has been well-discussed in numerous documents [3] so it will not be repeated here. In each of the following sections, we summarize the motivation for the specific measurement and discuss the precision expected from current and planned experiments worldwide.

B. Optimization of the LBNE Beam Design

The neutrino beamline is the central component of the Long-Baseline Neutrino Experiment. For several years, beamline designs have been investigated in an effort to optimize the physics reach of the experiment. In this section, we report on the most recent work showing the direct impact of different beam design on the sensitivity to neutrino oscillation parameters.

The LBNE beamline will be a new neutrino beamline that uses the Main Injector (MI) 120 GeV proton accelerator. The longest baseline neutrino oscillation experiment currently in operation is the Main Injector Neutrino Oscillation Search (MINOS) experiment based at Fermilab. It uses the NuMI (Neutrinos at the Main Injector) [4] beamline from the MI. The NuMI beamline has been operational since Jan 21, 2005 and delivered in excess of 1×10^{21} protons-on-target (POT) to the MINOS experiment through 2010 [5]. The GEANT [6] based simulation of the NuMI beamline has been validated using data from the MINOS experiment. The NuMI simulation software has proven to be a remarkable success at predicting the measured neutrino charged-current (CC) interaction rates observed in the MINOS near detector with the level of agreement between the data and simulation CC interaction rates within 10% in the region of interest to the MINOS experiment. The current LBNE beamline design is based on the NuMI design and uses the same simulation framework.
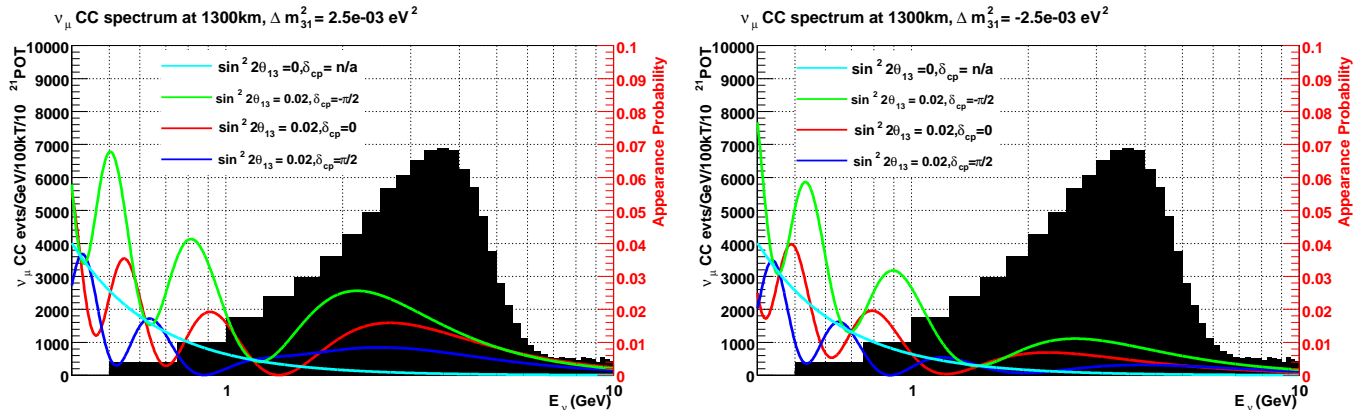
FIG. 1. The $\nu_\mu \to \nu_e$ oscillation probability for the LBNE to DUSEL baseline of 1300 km for different mixing parameter with normal hierarchy (left) and inverted hierarchy (right), is shown as colored curves. The unoscillated CC ν_μ spectrum from an LBNE candidate beam is shown as the solid black histogram.

The design specifications of the LBNE neutrino beamline is driven by the physics of $\nu_\mu \to \nu_\mu$, and $\nu_\mu \to \nu_e/\nu_\tau$ oscillations. In Fig. 1, the $\nu_\mu \to \nu_e$ oscillation probability for the LBNE to DUSEL baseline of 1300 km for different mixing parameters is shown as colored curves. The total CC ν_μ spectrum from an LBNE candidate beam is shown as the black solid histogram. In principle, the ideal LBNE neutrino beam would be one that has a wide energy band that covers the energy region from low energies to the energy of the first ($\pi/2$) oscillation maximum and minimal flux beyond the region of interest. Low flux at high neutrino energies is desired to eliminate neutral-current backgrounds from high energy neutrinos that are not sensitive to oscillations but still produce significant background at low observed energies in the neutrino detectors.

In 2008/2009 we specified the following broad requirements for the LBNE beam based on examination of the oscillation nodes in Fig. 1:

1. We require the highest possible neutrino fluxes to encompass at least the 1st and 2nd oscillation nodes, the maxima of which occur at 2.4 and 0.8 GeV respectively.

2. Since neutrino cross sections scale with energy, larger fluxes at lower energies are desirable to achieve the physics sensitivities using effects at the 2nd oscillation node and beyond.

3. To detect $\nu_\mu \rightarrow \nu_e$ events at the far detector, it is critical to minimize the neutral-current contamination at lower energy, therefore it is highly desirable to minimize the flux of neutrinos with energies greater than 5 GeV where there is little sensitivity to the oscillation parameters (including the CP phase and the mass hierarchy).

4. The irreducible background to $\nu_\mu \rightarrow \nu_e$ appearance signal comes from beam generated ν_e events, therefore, a high purity ν_μ beam (lowest possible ν_e contamination) is required.

We studied the physics performance of several conventional horn focused neutrino beam designs in 2008-2010. We considered different decay pipe geometries and different aluminum horn designs (AGS, NuMI, T2K) and different beam tunes (horn/target placement and horn currents). A solid cylindrical water cooled graphite target, two nuclear-interaction-lengths long was chosen as the initial target material and geometry for use with the 700 kW LBNE proton beam pending the result of radiation damage studies with different target materials. An optimization of the target material and geometry is underway.

We found that a two horn focusing design using parabolic horns similar to the NuMI horns gave the best performance of the conventional horn focused beams. We chose the radius of the decay pipe to be 2 m to maximize the yield of low energy neutrinos in the oscillation region (< 5 GeV). Ideally the length of the decay pipe should be chosen such that the pions generating neutrinos in the oscillation energy range to decay will decay. The 1st oscillation maxima at 2.5 GeV is generated by 6 GeV pions, for which the decay length is 333 m. The length of the decay pipe was chosen to be only 250 m to reduce the excavation volume required. The LBNE decay pipe in the "March 2010" design was chosen to be air cooled to mitigate the risks associated with a water cooled decay pipe - such as NuMI's. However, the air in the decay pipe absorbs some of the pions in the beam before they decay so for this study we used an evacuated or helium-filled decay pipe. A technical design for a helium-filled decay pipe is currently being assessed.

The current (2010) best candidate LBNE beam spectrum obtained using a 120 GeV proton beam is shown as the solid black histogram in Fig. 1. As shown in the figure, the rate of ν_μ CC events in the region of the 2nd oscillation maxima (< 1.5 GeV) is much lower than at the 1st oscillation maxima. Currently, we do not have a conventional horn focused beamline design that can provide sufficient neutrino flux at the 2nd maxima (< 1.5 GeV) or below where the impact of the CP violating phase is maximal. Therefore for this study, we have focused on optimizing the neutrino flux coverage in the oscillation region of the 1st maximum (1.5–6 GeV).

The unoscillated ν_μ CC spectra optimized for $\nu_\mu \rightarrow \nu_e$ appearance obtained using variations of the conventional two horn LBNE beamline design are shown in Fig. 2. The beam spectrum used for the ν_e appearance studies and ν_μ disappearance studies reported in this document is shown in red.

As a first step, we studied the impact of possible beam design variations on the *resolution* of the value of $\sin^2 2\theta_{13}$ and δ_{CP}. For this initial study, a simultaneous χ^2 fit to the binned neutrino and anti-neutrino appearance spectrum (Fig. 3) was performed for each candidate beam - including the irreducible ν_e background from the beam. In the fit, the parameters $\sin^2 2\theta_{13}$ and δ_{CP} were allowed to vary, while the mass hierarchy and the other oscillation parameters were fixed to their correct values. A 2% systematic uncertainty on the ν_e background was included. All other uncertainties included statistical errors only. The 1σ δ_{CP} uncertainty returned from the fit was then examined for different beam configurations. We considered the impact of horn currents and the graphite target position w.r.t to horn 1 on the resolution of δ_{CP} as shown in Figs. 4 and 5, respectively. The δ_{CP} measurement is discussed in more detail in Section III C 4. From this, we see that the "March 2010" design and the 2008/2009 reference design (shown in Fig. 2) have similar resolution for δ_{CP} and $\sin^2 2\theta_{13}$ in the absence of NC backgrounds and detector effects. These same studies indicate that the "August 2010" reference beam design with either a 350 kA current and embedded target OR a 250 kA with the target approximately -0.5 m from the face of horn 1 produces significantly improved resolution for δ_{CP} and $\sin^2 2\theta_{13}$ as compared to the "March 2010" or 2008/2009 reference designs.

To further pursue these apparent gains, full oscillation sensitivity fits were performed using a GLoBES-based [7] LBNE analysis, which includes detector effects and background sources as described in Appendix A. Fig. 6 shows the resultant comparison of LBNE oscillation sensitivities in WC for the 2008/2009 reference design beam and the newer "August 2010" beam. Fig. 7 shows the same for LAr. For both WC and LAr detectors, the sensitivities are very similar for the two beam designs. Adding detector effects and NC backgrounds may have lessened the gains we expected to see based on the resolution studies (Figs. 4 and 5); however, the fact that the sensitivities are also so similar for LAr suggests that the apparent gains were more likely lost once parameter degeneracies were taken into account in the full oscillation fits. Recall that in the resolution studies, only a single oscillation parameter was studied at a time. This highlights the importance of performing full oscillation fits before making final conclusions about a given beam design.
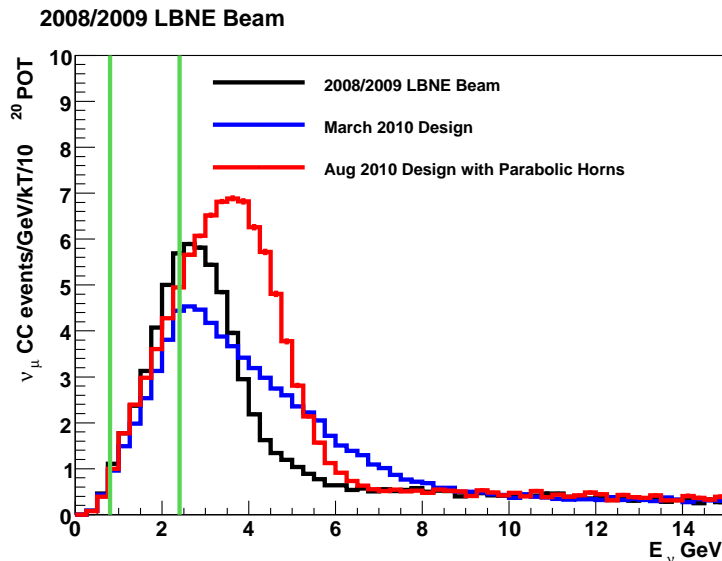
FIG. 2. Various ν_μ CC spectra obtained using variations of the two horn LBNE design. In black is the 2008/2009 LBNE design using an embedded high density carbon target 0.6 cm in radius and 80 cm in length and the two NuMI horns with an evacuated decay pipe 2 m in radius and 280 m in length. In blue is an LBNE design from "March 2010", which has an embedded graphite target with 0.77 cm radius and 96 cm in length, a modified NuMI horn 1 with a cylindrical front end and NuMI horn 2 operating at 300 kA. The decay pipe in the "March 2010" design is air filled, 2 m in radius and 250 m in length. In red is the "August 2010" LBNE candidate beam design, which has two parabolic NuMI horns operating at 250 kA with the target pulled back 30 cm from the face of horn 1.
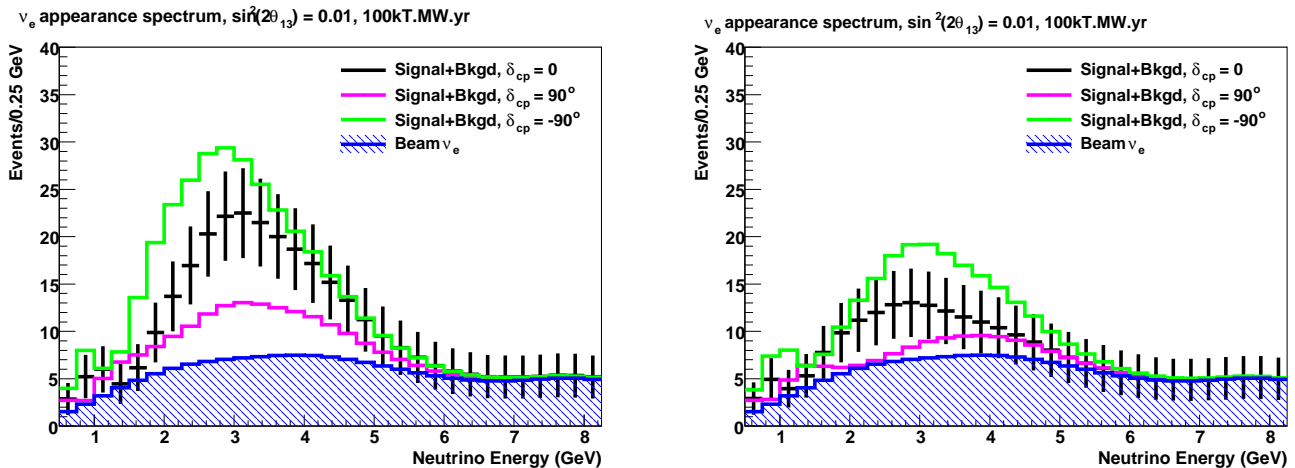
FIG. 3. The ν_e appearance spectrum from the 2008/2009 reference beam for an exposure of 100 kT.MW.yr, $\sin^2(2\theta_{13}) = 0.01$, normal hierarchy (left), and inverted hierarchy (right). No detector effects are included.

1. Conclusion

Despite the fact that the "August 2010" beam design has about a 30% higher flux, it appears to yield similar sensitivity to $\sin^2 2\theta_{13} \neq 0$, CP violation, and the mass hierarchy as the original 2008/2009 reference beam. This holds for both WC and LAr detectors. This suggests that LBNE's long-baseline oscillation sensitivity may not be very sensitive to the exact shape of the flux between 3 and 6 GeV.

For the physics studies reported here, we have chosen the "August 2010" beam design with two NuMI parabolic horns ∼6 m apart, 250 kA current and with the target upstream end -30 cm from the upstream face of horn 1 (red spectrum in Fig. 2). [The decay pipe is assumed to be evacuated or helium filled to allow the maximum number of pions to decay.] The advantage of this beam is that it may be technically easier to build and maintain the target/focusing
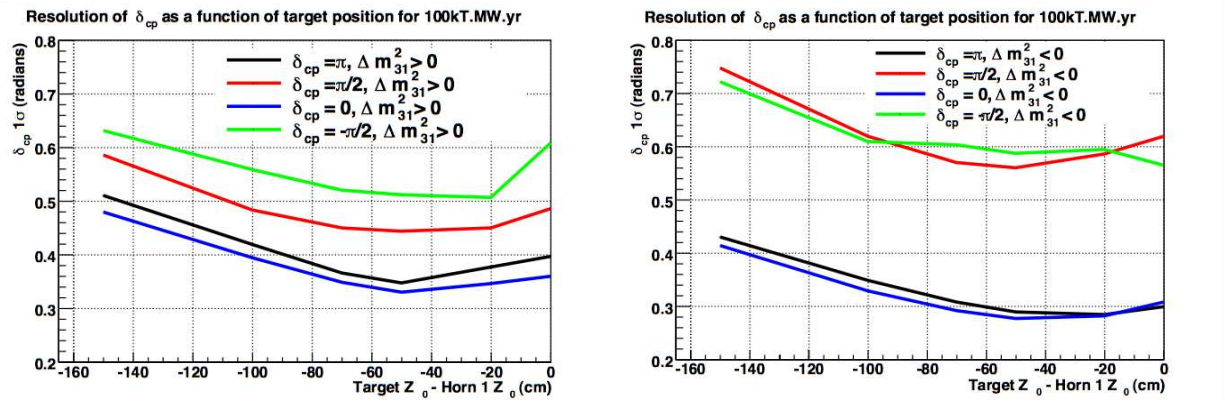
FIG. 4. The 1σ resolution of δ_{CP} as the target position is changed in the 2008/2009 LBNE beam design. Normal hierarchy (left) and inverted hierarchy (right). An exposure of 100 kt.MW.yr is assumed with $\nu : \bar{\nu}$ running in the ratio 1:1. No detector effects included.
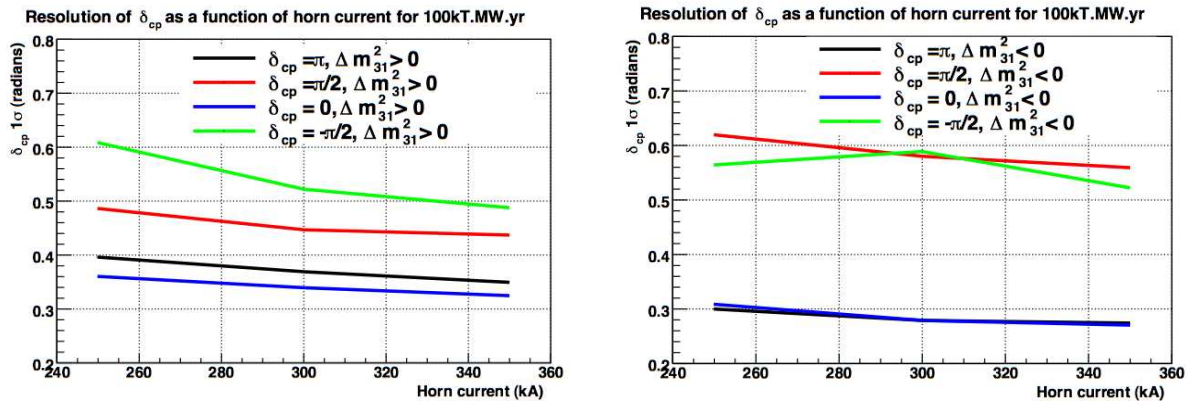
FIG. 5. The 1σ resolution of δ_{CP} as the horn current is changed in the 2008/2009 LBNE beam design. Normal hierarchy (left) and inverted hierarchy (right). An exposure of 100 kt.MW.yr is assumed with $\nu : \bar{\nu}$ running in the ratio 1:1. No detector effects included.

system.

We note that none of the beams studied so far have sufficient flux at the second maxima to impact the measurement of δ_{CP} and $\sin^2 2\theta_{13}$. Preliminary estimates indicate that we would require at least 5X more flux at the 2nd maxima to significantly improve the measurement of δ_{CP} and $\sin^2 2\theta_{13}$ [8].

C. ν_e Appearance

Motivated by an exciting history of discoveries in neutrino oscillations over the course of the past decade, a major experimental effort is underway to probe the last unknown mixing angle, θ_{13}. To date, only an upper limit on θ_{13} exists (Table III). Information from reactor (Daya Bay, Double CHOOZ, RENO) and accelerator-based (NOvA, T2K) experiments will be able to test whether $\sin^2 2\theta_{13}$ is non-zero down to the ~ 0.01 level in the coming years. The next generation of experiments will need to be able to provide:

- a more precise measurement of θ_{13} (or extension of the limit in the case of non-observation);

- a determination of the neutrino mass hierarchy, assuming non-zero θ_{13} (i.e. to determine whether the mass ordering is normal $\Delta m_{31}^2 > 0$ or inverted $\Delta m_{31}^2 < 0$);

- a measurement of leptonic CP violation (through measurement of the CP violating phase, δ_{CP}, assuming non-zero θ_{13}).

θ₁₃ Sensitivity (3σ)

Mass Hierarchy Sensitivity (3σ)
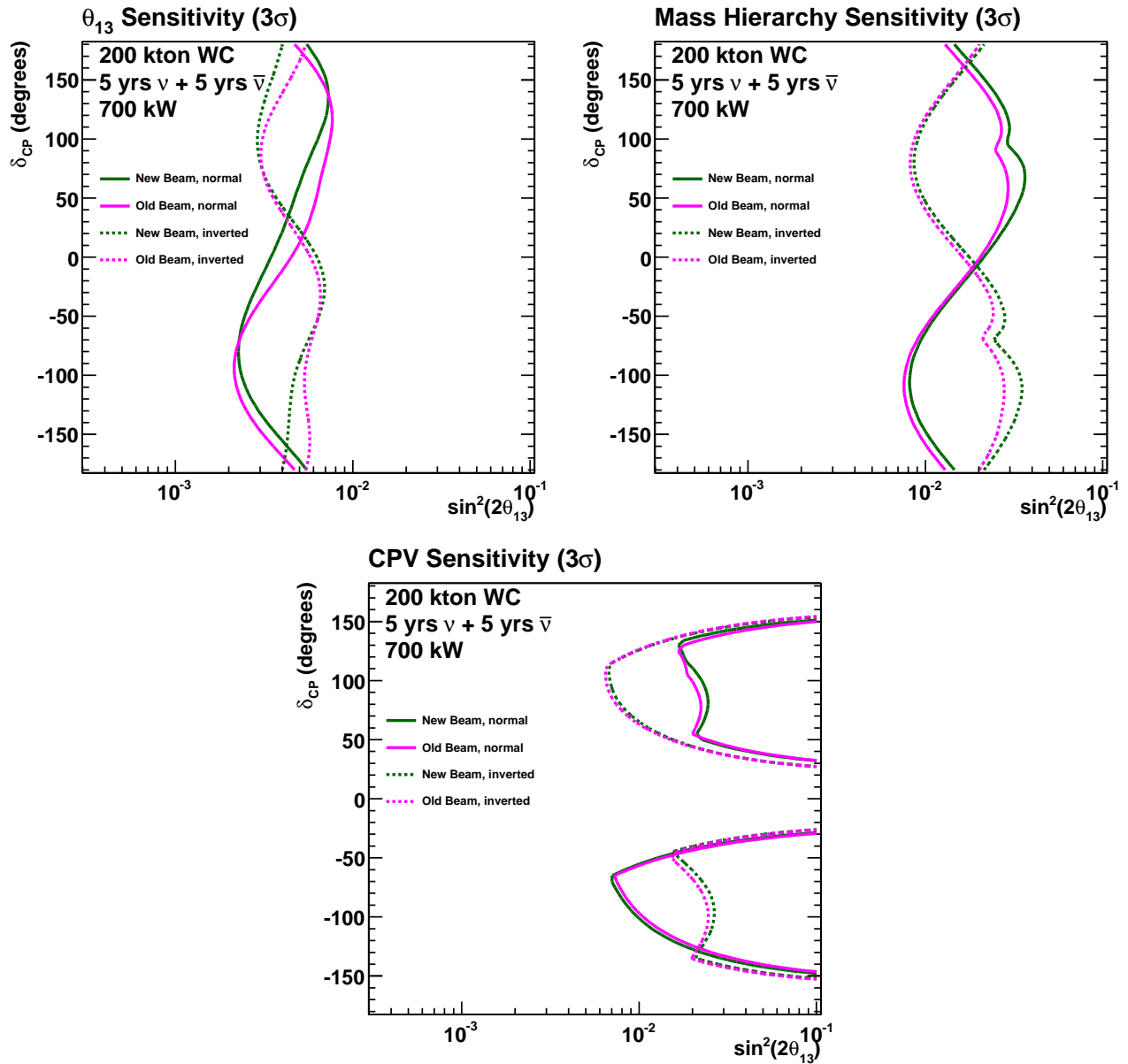
CPV Sensitivity (3σ)

FIG. 6. Comparison of the sensitivity of LBNE to discovering $\sin^2 2\theta_{13} \neq 0$, the mass hierarchy, and CP violation at 3σ for two different LBNE beam designs. Sensitivities are shown for 200 kt WC in 5+5 years of $\nu + \bar{\nu}$ running in a 700 kW beam for both normal (solid) and inverted (dashed) mass hierarchies. The projections include detector effects, all background sources and their uncertainties (see Appendix A). "Old beam" (magenta) refers to the 2008/2009 LBNE reference design and corresponds to the flux plotted in black in Fig. 2. "New beam" (black) refers to the "August 2010" beam and corresponds to the flux plotted in red in Fig. 2.

The following sections detail measurement capabilities of LBNE in each of these three areas for water Cherenkov and liquid argon TPC detector technologies as a function of beam exposure. For context, we discuss the state of knowledge on the target parameters expected by the time LBNE would be operational.

1. Current and Planned Experiments θ_{13} Reach

Before discussing the θ_{13} reach of LBNE, we provide an overview of the precisions that might be achieved by current and planned experiments. A valuable resource for this is the 2009 EURONU annual report [9], which included their updated projections. The EURONU calculations were based, to the extent possible, on official statements from the

θ₁₃ Sensitivity (3σ)

θ₁₃ Sensitivity (3σ)

34 kton LAr
5 yrs ν + 5 yrs ν̄
700 kW

- New Beam, normal
- Old Beam, normal
- New Beam, inverted
- Old Beam, inverted

Mass Hierarchy Sensitivity (3σ)

Mass Hierarchy Sensitivity (3σ)

34 kton LAr
5 yrs ν + 5 yrs ν̄
700 kW

- New Beam, normal
- Old Beam, normal
- New Beam, inverted
- Old Beam, inverted

CPV Sensitivity (3σ)

CPV Sensitivity (3σ)

34 kton LAr
5 yrs ν + 5 yrs ν̄
700 kW

- New Beam, normal
- Old Beam, normal
- New Beam, inverted
- Old Beam, inverted

FIG. 7. Comparison of the sensitivity of LBNE to discovering $\sin^2 2\theta_{13} \neq 0$, the mass hierarchy, and CP violation at 3σ for two different LBNE beam designs. Sensitivities are shown for 34 kt LAr in 5+5 years of $\nu + \bar{\nu}$ running in a 700 kW beam for both normal (solid) and inverted (dashed) mass hierarchies. The projections include detector effects, all background sources and their uncertainties (see Appendix A). Same labelling convention as Fig. 6.

collaborations and assume that the data are continuously analyzed and the results made available immediately.

Fig. 8(left) shows the evolution of the θ_{13} sensitivity limit (90% CL) as a function time from upcoming reactor and accelerator-based experiments (we note that at Neutrino 2010 [10], the schedule for most of the experiments had slipped by about one year). As can be seen from the figure, the global sensitivity will be dominated by the reactor experiments, with Daya Bay possibly reaching $\sin^2 2\theta_{13}$ sensitivity down to ~ 0.006 (at 90% CL) before LBNE operation.

Fig. 8(right) shows the projected discovery potential from these same experiments, also plotted as a function of time. For the accelerator-based experiments, there is some ambiguity resulting from the mass hierarchy and δ_{CP}, so in their case, a normal mass hierarchy is assumed and the dependence on δ_{CP} is indicated by colored bands. Note that, for some values of δ_{CP}, the discovery reach of T2K and NOvA can approach that of Daya Bay. From these projections, upcoming experiments should be able to distinguish θ_{13} from zero at the 3σ level for $\sin^2 2\theta_{13}$ values

Parameter	Value
$\sin^2 2\theta_{12}$	0.87 ± 0.03
$\sin^2 2\theta_{23}$	> 0.91 (at 90% CL)
$\sin^2 2\theta_{13}$	< 0.15 (at 90% CL)
Δm_{21}^2	$(7.59 \pm 0.20) \times 10^{-5}$ eV^2
Δm_{32}^2	$(2.35^{+0.11}_{-0.08}) \times 10^{-3}$ eV^2
δ_{CP}	no measurement

TABLE III. Current knowledge of neutrino oscillation parameters. Values are from the Particle Data Group [11]. $\sin^2 \theta_{23}$ and Δm_{32}^2 have been updated to reflect the new measurements from MINOS [12].
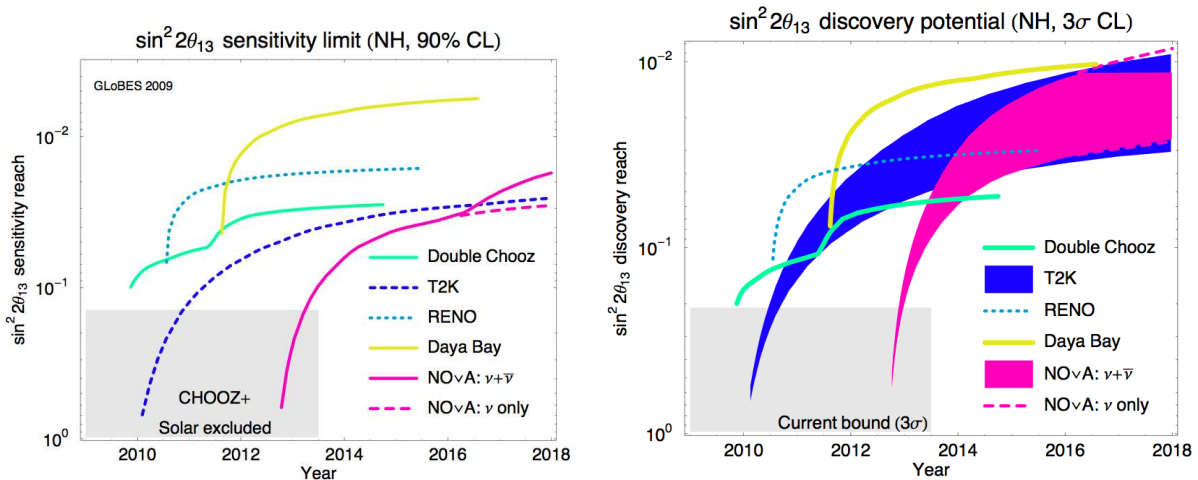
FIG. 8. Projected θ_{13} sensitivity (left) and discovery potential (right) as a function of time for experiments that will run before LBNE. Sensitivity is defined as the 90% CL limit that will be obtained if the true θ_{13} is zero. Discovery potential is defined as the smallest value of θ_{13} that can be distinguished from zero at 3σ. A normal mass hierarchy is assumed and the bands reflect the variation for different values of δ_{CP} for the accelerator-based experiments. Plots are reproduced from the 2009 EURONU annual report [9]; experiment schedules shown at Neutrino 2010 [10] imply the horizontal axis should be delayed by about one year from those shown for most of the experiments.

down to 0.01 by the year 2016-2018.

2. LBNE θ_{13} Reach

The LBNE detectors will have excellent sensitivity to θ_{13}, further extending the reach of upcoming reactor and accelerator-based experiments by roughly an order of magnitude. Observation of $\nu_\mu \to \nu_e$ oscillations in LBNE will be the key to measuring θ_{13} at this level. Figs. 9 and 10 show the expected event rates for ν_e appearance measurements in LBNE in both a WC and LAr far detector for normal and inverted mass hierarchies, respectively. Figs. 11 and 12 show the same for antineutrino running. As expected, the rates are higher for the normal mass hierarchy in the case of neutrinos and for the inverted hierarchy in the case of antineutrinos. We also see that the effect of positive and negative δ_{CP} phase is opposite for neutrinos that has more events for negative phase (both normal and inverted hierarchy), compared to antineutrinos that has more events for positive phase. The detector performance parameters (such as background levels and efficiency) used to produce these plots are detailed in Appendix A.

Fig. 13 shows the sensitivity of LBNE to $\theta_{13} \neq 0$ as a function of δ_{CP} for each of the mass orderings. Here, the discovery reach for $\sin^2 2\theta_{13}$ is defined as the minimum value of $\sin^2 2\theta_{13}$ for which LBNE can rule out $\sin^2 2\theta_{13} = 0$ at the 3σ and 5σ levels. The results are dependent on the value of δ_{CP} and the mass hierarchy. As can be seen, the sensitivity is better if the mass hierarchy is normal rather than inverted unless $\delta_{CP} = 45 - 180^o$, in which case the reverse is true.

Of course, the sensitivity to determining a non-zero value of θ_{13} increases with exposure. Figs. 14 and 15 show the sensitivity as a function of exposure at 90% and 3σ CL, respectively. Both detectors can probe $\sin^2 2\theta_{13}$ down to the 10^{-3} level with reasonable exposures. A WC detector is sensitive to $\sin^2 2\theta_{13} \neq 0$ at 3σ down to a $\sin^2 2\theta_{13}$ value of

FIG. 9. The expected ν_e appearance spectrum for a 200 kt WC (left) and 34 kt LAr (right) detector for $\sin^2 2\theta_{13} = 0.04$ and 5 years of neutrino running in a 700 kW beam assuming a *normal* mass hierarchy. The black points assume $\delta_{CP} = 0$ while the green and pink lines are for $\delta_{CP} = \pm 90^0$. The different background contributions are indicated by the hatched histograms.
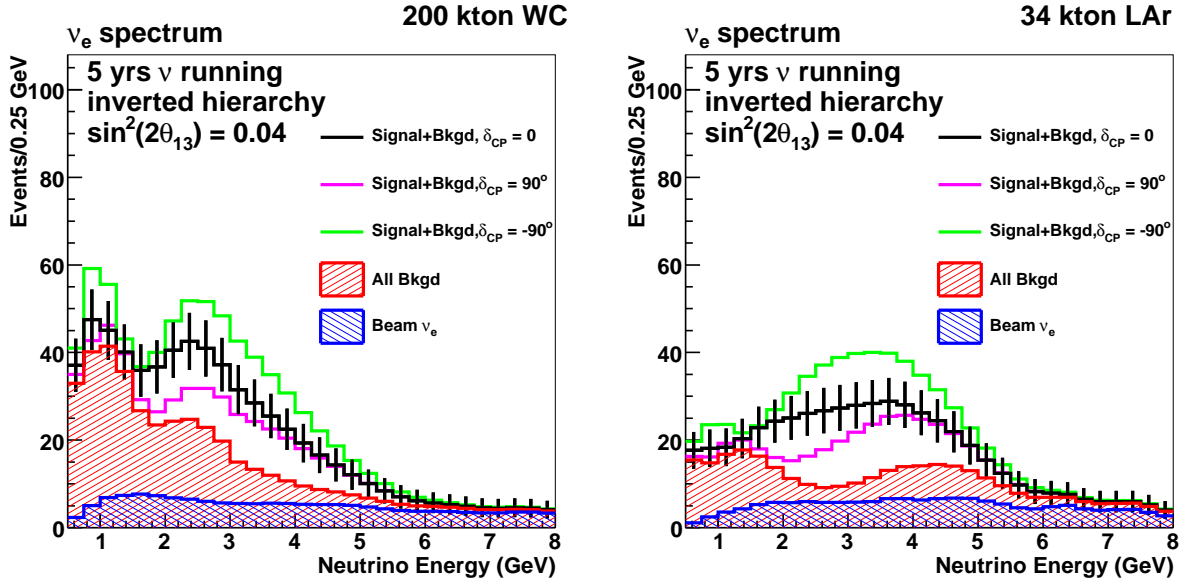
FIG. 10. The ν_e appearance spectrum as described for Fig. 9 except for an *inverted* mass hierarchy.

0.008 for 100% of all possible δ_{CP} values assuming an exposure of 2000 kt-yrs. The same is true for LAr assuming an exposure of 340 kt-yrs. Hence, LAr appears to have similar θ_{13} reach as WC with about 1/6 the exposure. [The main parameter that determines this factor is the ratio of the detector signal efficiencies near the 1st maximum.]
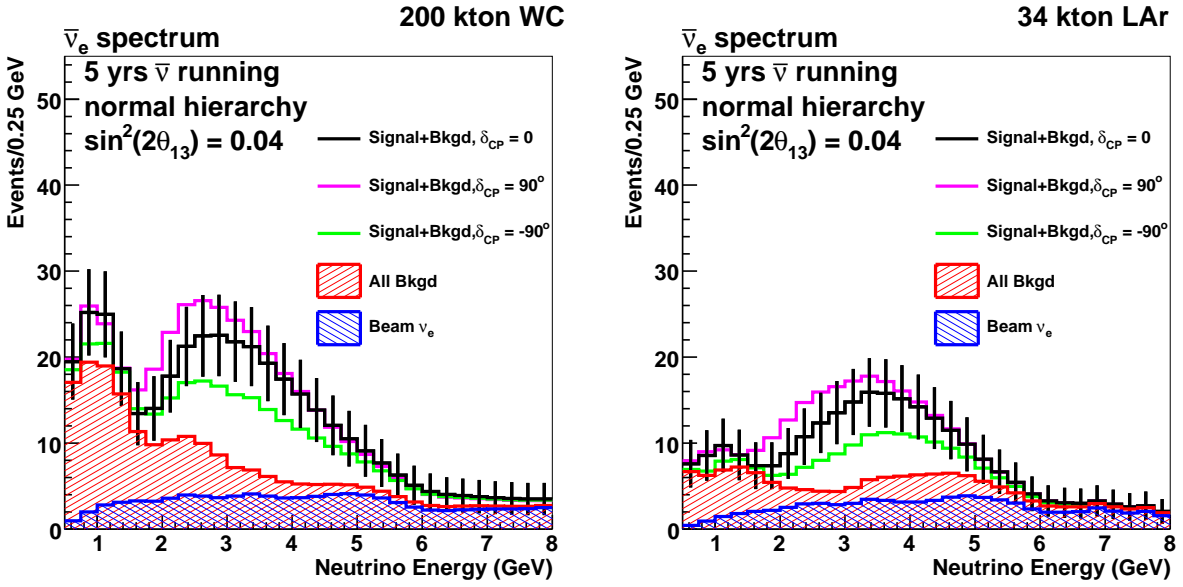
FIG. 11. The expected $\bar{\nu}_e$ appearance spectrum for a 200 kt WC (left) and 34 kt LAr (right) detector for $\sin^2 2\theta_{13} = 0.04$ and 5 years of antineutrino running in a 700 kW beam assuming a *normal* mass hierarchy. The black points assume $\delta_{CP} = 0$ while the green and pink lines are for $\delta_{CP} = \pm 90^0$. The different background contributions are indicated by the hatched histograms. [Note the vertical axis scale change compared to neutrino running.]
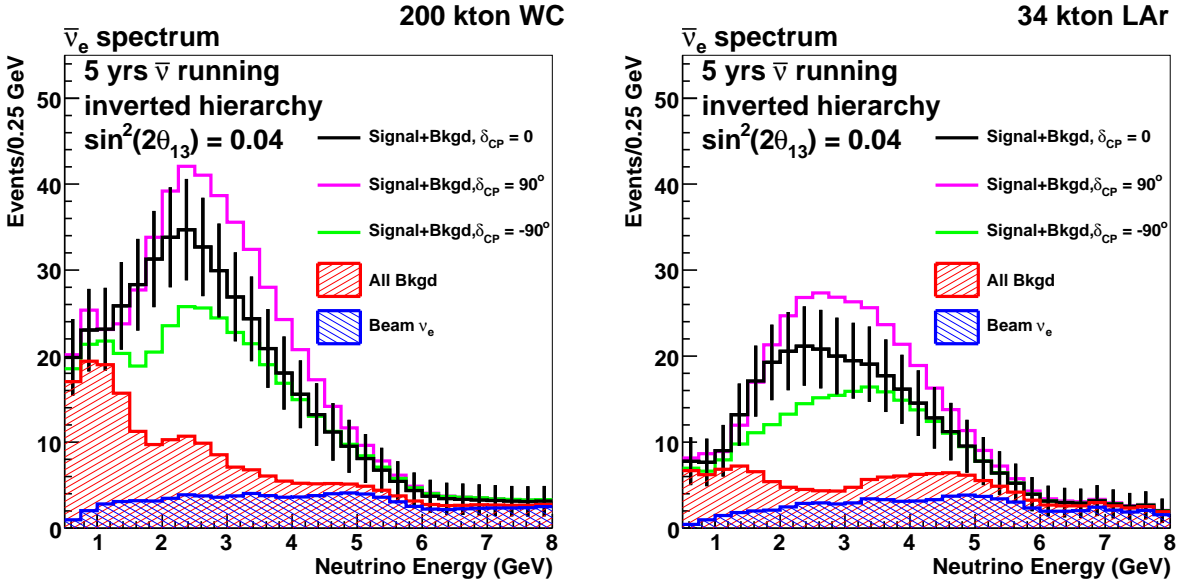
FIG. 12. The $\bar{\nu}_e$ appearance spectrum as described for Fig. 11 except for an *inverted* mass hierarchy.
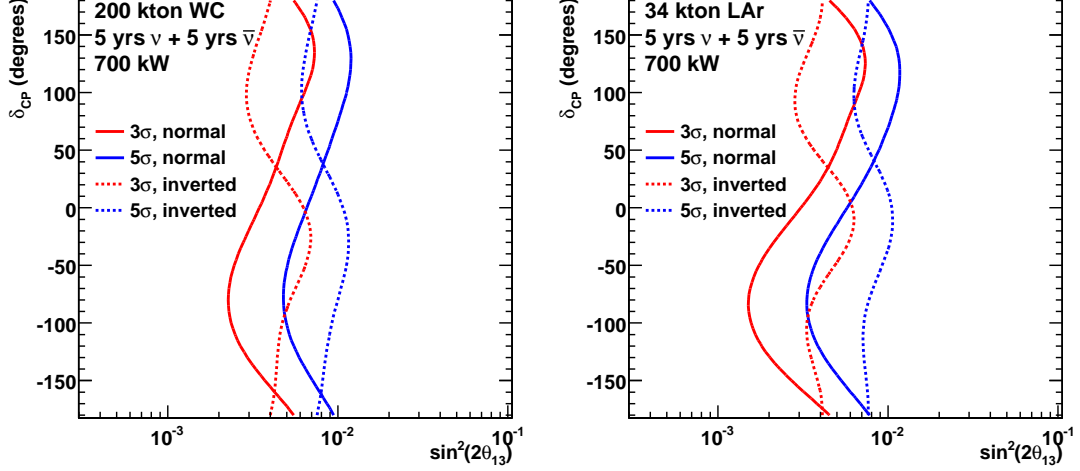
FIG. 13. 3σ (red) and 5σ (blue) sensitivity of LBNE to $\sin\theta_{13} \neq 0$ as a function of δ_{CP} for 200 kt of WC (top) and 34 kt of LAr (bottom). This assumes 5+5 years of ν and $\bar{\nu}$ running in a 700 kW beam. Curves are shown for both normal (solid) and inverted (dashed) mass hierarchies.
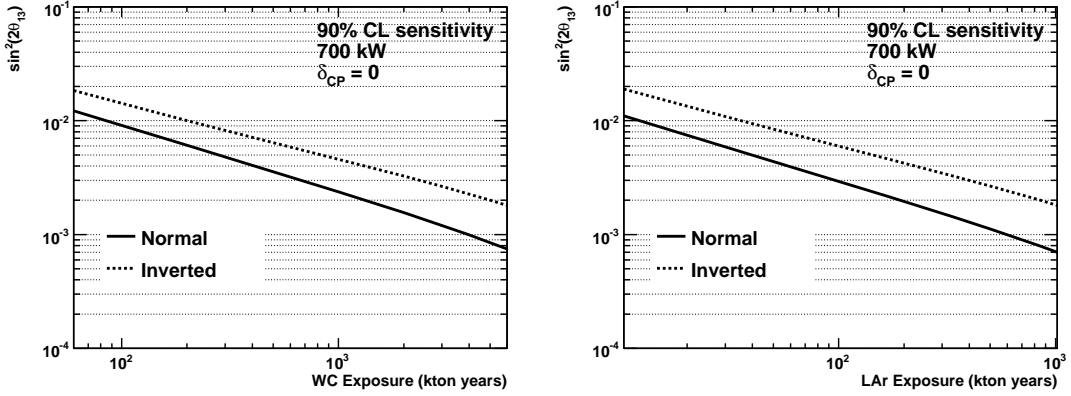
FIG. 14. Sensitivity of LBNE to determining non-zero θ_{13} at the 90% CL as a function of exposure for both WC (left) and LAr (right). The plots show the projections for $\delta_{CP} = 0$ for normal (solid) and inverted (dashed) mass hierarchies.
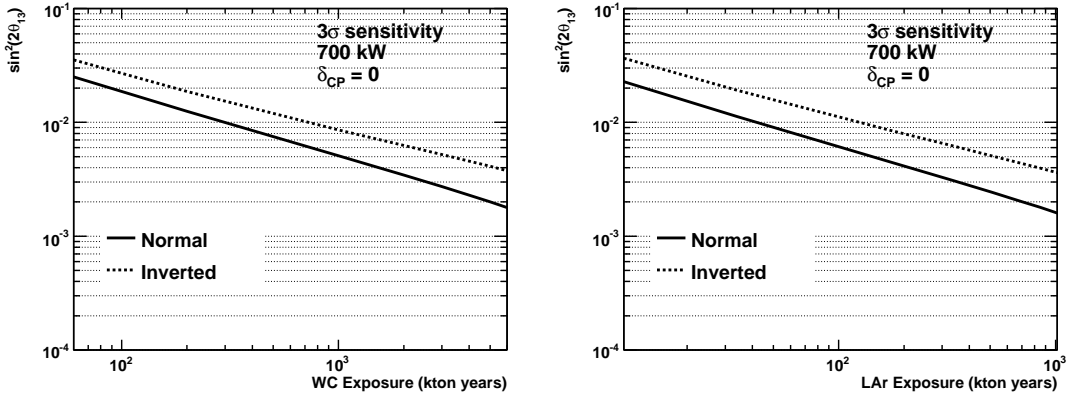
FIG. 15. Sensitivity of LBNE to determining non-zero θ_{13} at 3σ as a function of exposure for both WC (left) and LAr (right). The plots show the projections for $\delta_{CP} = 0$ for normal (solid) and inverted (dashed) mass hierarchies.

3. Neutrino Mass Hierarchy

While the primary goal of upcoming neutrino oscillation experiments is the discovery of the yet unknown mixing angle, θ_{13}, they may also provide information on the mass hierarchy and CP violation if θ_{13} is relatively large. In the 2009 EURONU report [9], referred to in the previous section, "modest upgrades" to the T2K and NOvA experiments were considered; specifically, increase of the T2K beam power from 0.75 MW to 1.66 MW starting in 2015 and a linear beam power increase for NOvA from 0.7 MW to 2.3 MW (Project X) starting in 2018. Fig. 16 illustrates that the projected 3σ discovery regions for mass hierarchy and CP violation for upgraded T2K+NOvA are quite limited, despite the assumption of rather aggressive beam power start times, a global optimization of neutrino and antineutrino running in both beams, and combined limits with information from reactor data. The EURONU report does indicate that these experiments might see hints of the mass hierarchy and CP violation at 90% CL for $\sin^2 2\theta_{13} > 0.05$ and most values of δ_{CP} but concludes: "Although 'minor upgrades' of existing facilities may provide a non-negligible sensitivity to the mass hierarchy and CP violation, there is high risk associated with this strategy, since for $\sim 75\%$ of all possible values of δ_{CP}, no discovery would be possible at the 3σ level. Therefore, we conclude that the upcoming generation of oscillation experiments may lead to interesting indications for the mass hierarchy and CP violation, but it is very likely that an experiment beyond the upcoming superbeams (including reasonable upgrades) will be required to confirm these hints."
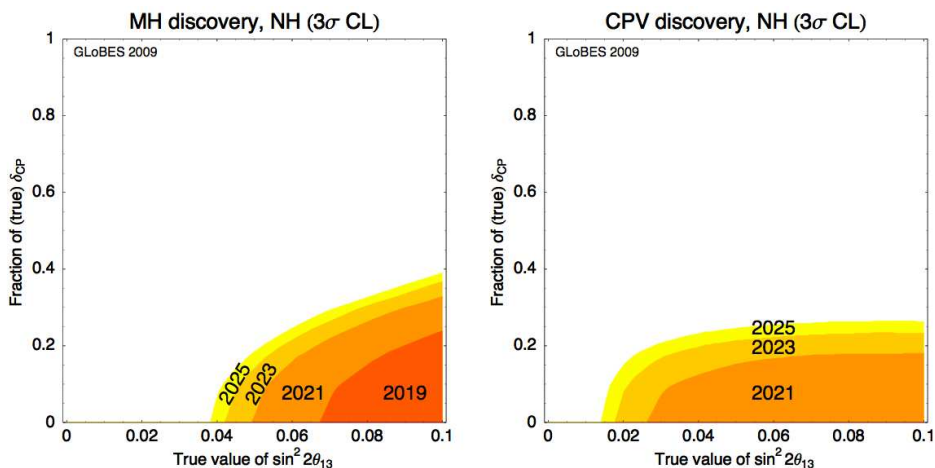
FIG. 16. Mass hierarchy (left) and CP violation (right) discovery potentials at 3σ as a function of true $\sin^2 2\theta_{13}$ for T2K+NOvA+reactor including major beam upgrades to both T2K and NOvA with a global $\nu/\bar{\nu}$ running optimization (plot reproduced from [9]). Different colors correspond to different projections in time after the upgrades.

With poor coverage of the mass hierarchy and CP violation even with factors of 2-3 increase in the beam power delivered to experiments like T2K and NOvA, it is clear that an experiment like LBNE is needed to take the next step in physics reach. Fig. 17 shows LBNE's projected sensitivity to the mass ordering as a function of θ_{13} and the CP-violating phase for both WC and LAr. Here, the mass hierarchy discovery reach is defined as the minimum value of $\sin^2 2\theta_{13}$ for which the wrong hierarchy can be excluded for a given value of δ_{CP}.

Fig. 18 shows the sensitivity of LBNE for resolving the mass hierarchy at 3σ as a function of exposure so one can see how the reach improves with time and/or detector size. In this case, WC can resolve the mass hierarchy at 3σ for 100% of all δ_{CP} values for a $\sin^2 2\theta_{13}$ value down to 0.04 in an exposure of 2000 kt-yrs. The same can be achieved in LAr for $\sin^2 2\theta_{13}$ down to 0.05 in an exposure of 340 kt-yrs.
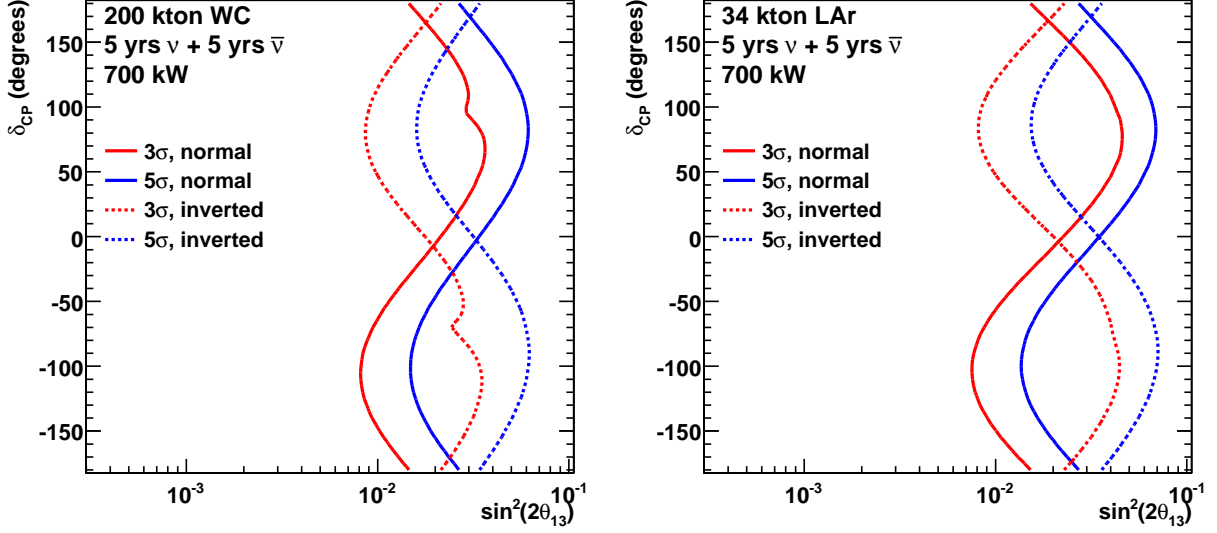
FIG. 17. Resolution of the mass hierarchy for 200 kt of WC (top) and 34 kt of LAr (bottom). This assumes 5+5 years of ν and $\bar{\nu}$ running in a 700 kW beam. To the right of the curves, the normal (solid) or inverted (dashed) mass hierarchy can be excluded at the 3σ (red) or 5σ (blue) level for the indicated values of true $\sin^2 2\theta_{13}$ and δ_{CP}.
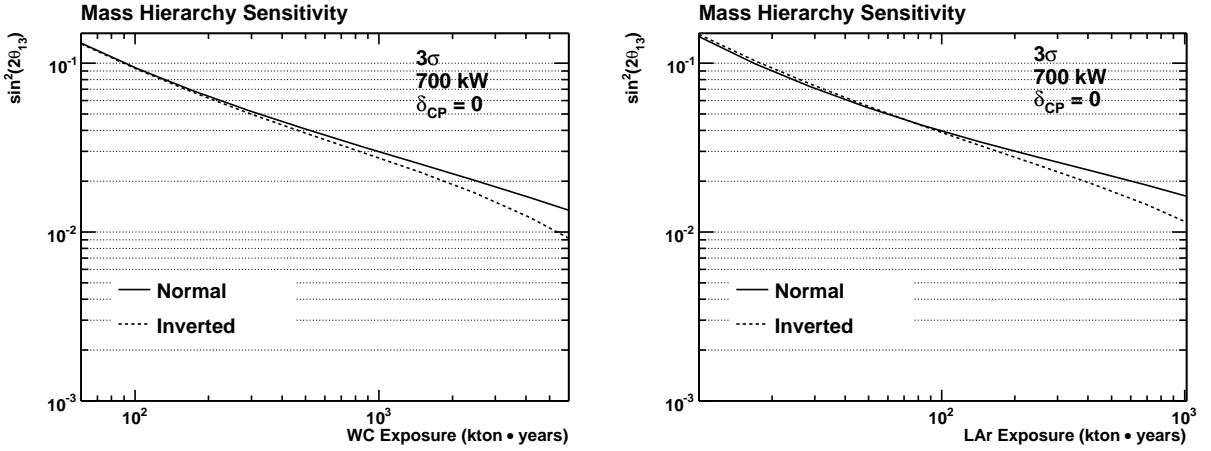
FIG. 18. Sensitivity of LBNE to resolving the mass hierarchy at 3σ as a function of exposure for both WC (left) and LAr (right). The plots show the projections for $\delta_{CP} = 0$ for normal (solid) and inverted (dashed) and inverted (dashed) mass hierarchies.

4. CP Violation

Section III C 3 summarizes the CP violation discovery potential of upcoming oscillation experiments, T2K+NOvA. Fig. 19 shows the CP violation reach. Here, we define CP violation discovery potential as the range of δ_{CP} values as a function of $\sin^2 2\theta_{13}$ for which one can exclude the CP conserving solutions for $\delta_{CP} = 0^o$ and $\delta_{CP} = 180^o$. In the case of LBNE, a WC detector can make a 3σ discovery of CP violation for 50% of all δ_{CP} values for $\sin^2 2\theta_{13}$ values down to 0.03 assuming an exposure of 2000 kt-yrs. The same holds for LAr assuming a 340 kt-yr exposure.
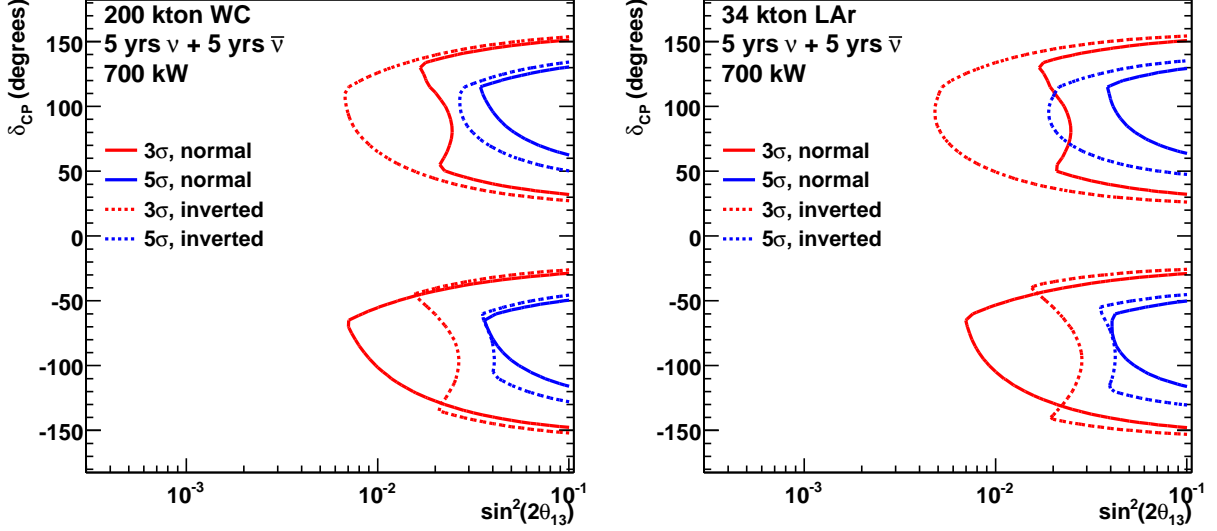
FIG. 19. 3σ (red) and 5σ (blue) sensitivity of LBNE to CP violation for 200 kt of WC (top) and 34 kt of LAr (bottom). This assumes 5+5 years of ν and $\bar{\nu}$ running in a 700 kW beam. Curves are shown for both normal (solid) and inverted (dashed) mass hierarchies.

Fig. 20 shows the resolution on LBNE's ability to measure δ_{CP} as a function of exposure for both WC and LAr. Assuming a normal mass hierarchy, $\sin^2 2\theta_{13} = 0.01$, and $\delta_{CP} = 0$, a WC detector can measure δ_{CP} to within $\pm 19°$ (at 1σ) assuming a 2000 kt-yr exposure. Similarly, LAr can measure δ_{CP} to the same precision with about 1/6 the exposure of WC.
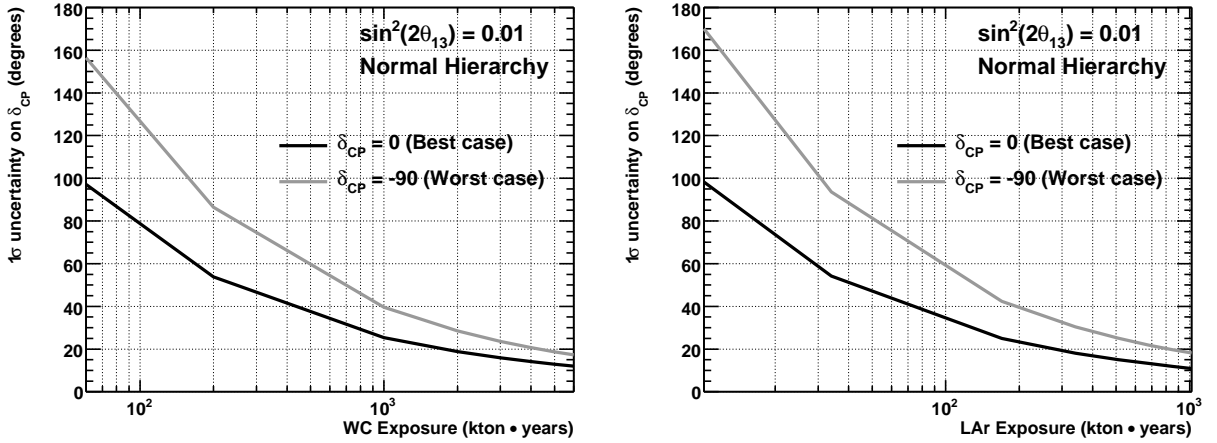
FIG. 20. 1σ resolution on the measurement of δ_{CP} in LBNE for both WC (left) and LAr (right) assuming $\sin^2 2\theta_{13} = 0.01$ and normal mass hierarchy. Projections for both $\delta_{CP} = 0$ (black) and $\delta_{CP} = -90^0$ (gray) are separately shown.

Combining these, Fig. 21 summarizes the overall discovery reach of LBNE to determine $\theta_{13} \neq 0$, the mass hierarchy,

and CP violation as a fraction of δ_{CP} coverage. This side-by-side comparison shows what can be achieved with 200 kt of WC and 34 kt of LAr under the same set of beam exposure assumptions. Similar sensitivities can be achieved in the two cases.
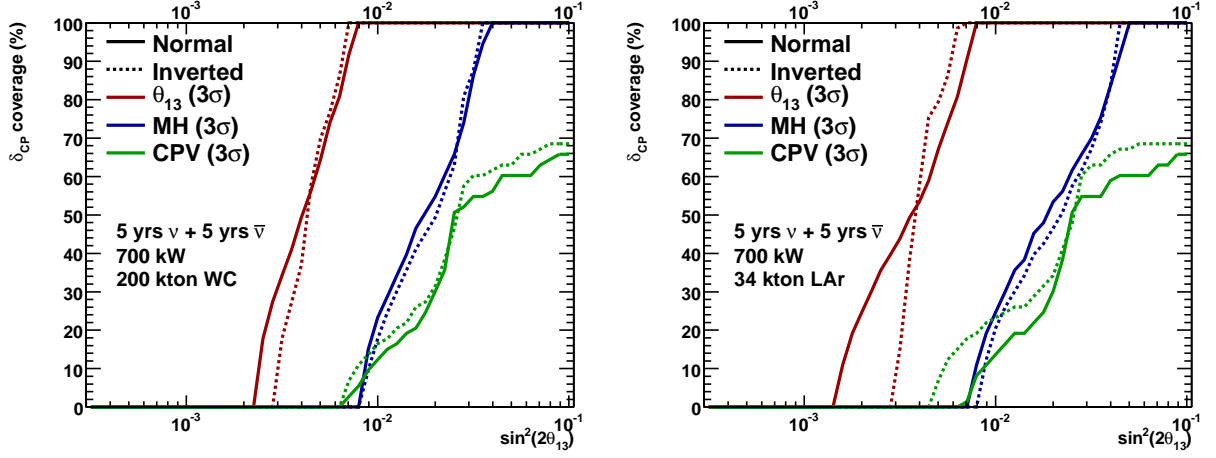
FIG. 21. 3σ discovery potential of LBNE for determining $\sin^2 2\theta_{13} \neq 0$ (red), the mass hierarchy (blue), and CP violation (green) as function of $\sin^2 2\theta_{13}$ and the fraction of δ_{CP} coverage. Here the fraction of δ_{CP} reflects the fraction of all true values of δ_{CP} for which the corresponding quantity can be measured. Sensitivities are shown for both the normal (solid) and inverted (dashed) mass hierarchies for 5+5 years of $\nu+\bar{\nu}$ running in a 700 kW beam. Results for both 200 kt of WC (top) and 34 kt LAr (bottom) are displayed.

D. ν_μ Disappearance

In addition to the ν_e appearance measurements, LBNE will also be able to provide precise measurements of the atmospheric oscillation parameters through measurement of both ν_μ and $\bar{\nu}_\mu$ disappearance. The most precise constraints on the atmospheric oscillation parameters are currently set by the MINOS experiment operating at a baseline distance of 735 km. Figure 22 shows the present constraints on $\sin^2 2\theta_{23}$ and Δm^2_{32} from MINOS as shown at Neutrino 2010 [12]. Currently, a 5% measurement of Δm^2_{32} has been obtained and the results suggest a value of θ_{23} that is very close to maximal. The MINOS ν_μ disappearance results constrain the oscillation parameters to be: $\Delta m^2_{32} = (2.35^{+0.11}_{-0.08}) \times 10^{-3}$ eV^2, $\sin^2 2\theta_{23} = 1.0$ (68% CL) and $\sin^2 2\theta_{23} > 0.91$ at 90% CL. They have also performed fits to $\bar{\nu}_\mu$ disappearance. The results in this case are less precise and are currently $\sim 2\sigma$ from the parameters obtained in neutrino mode: $\overline{\Delta m^2_{32}} = (3.36^{+0.45}_{-0.40} \text{ (stat)} \pm 0.06 \text{ (syst)}) \times 10^{-3}$ eV^2 (68% CL) and $\sin^2 2\overline{\theta_{23}} = 0.86 \pm 0.11$ (stat)± 0.01 (syst) (68% CL).

In the coming years, next generation experiments, such as T2K and NOvA, will be able to push beyond the current values and obtain even more precise measurements of these parameters. For example, with an exposure of 3.75 MW $\times 10^7$ sec, T2K hopes to make a 1% measurement of $\sin^2 2\theta_{23}$ and a measurement of Δm^2_{32} with an error $< 4\%$ [13]. NOvA also aims for more precise measurement of these parameters. Figure 23 shows the projected sensitivity contours for 6 years of NOvA running in the 700 kW NuMI beam. For maximal mixing and after 6 years of $\nu + \bar{\nu}$ running, NOvA plans to measure $\sin^2 2\theta_{23}$ to $\sim 0.3\%$ and Δm^2_{32} to $\sim 1\%$ [16].
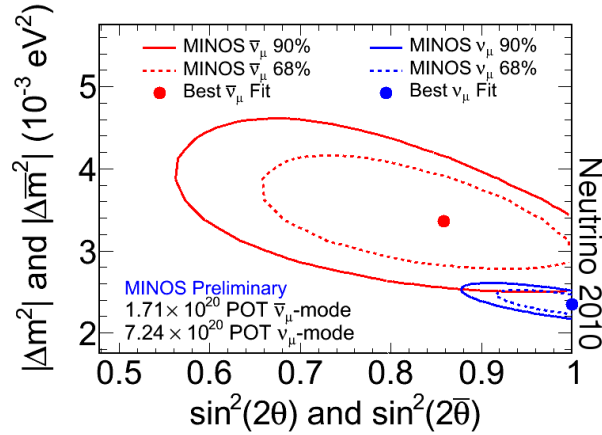
FIG. 22. Confidence interval contours from fits to the MINOS far detector neutrino (blue) and antineutrino (red) data to a two-flavor neutrino oscillation hypothesis (Neutrino 2010). The solid (dashed) curve gives the 90% (68%) contours.
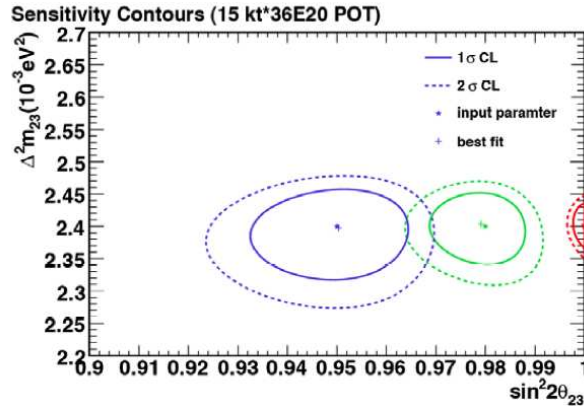
FIG. 23. 1σ and 2σ contours for a simultaneous measurement of Δm^2_{32} and $\sin^2 2\theta_{23}$ in NOvA for a 6-year run at 700 kW equally divided between neutrinos and antineutrinos. Plot is from [16].

LBNE will provide an even more sensitive test of the atmospheric oscillation parameters through its measurement of ν_μ and $\bar{\nu}_\mu$ disappearance. One advantage of the long-baseline in LBNE is that the multiple oscillation pattern in the spectrum will be clearly detectable. This should offer some advantage when it comes to systematics. As such, LBNE should clearly show the bi-modal structure in Δm_{32}^2 (note that KamLAND has already observed this for Δm_{21}^2). Figures 24 and 25 show the expected ν_μ and $\bar{\nu}_\mu$ event distributions at the LBNE far detector site for both WC and LAr detectors. In both cases, the statistics and the size of the expected signal (i.e. distortion in the spectrum) are large.
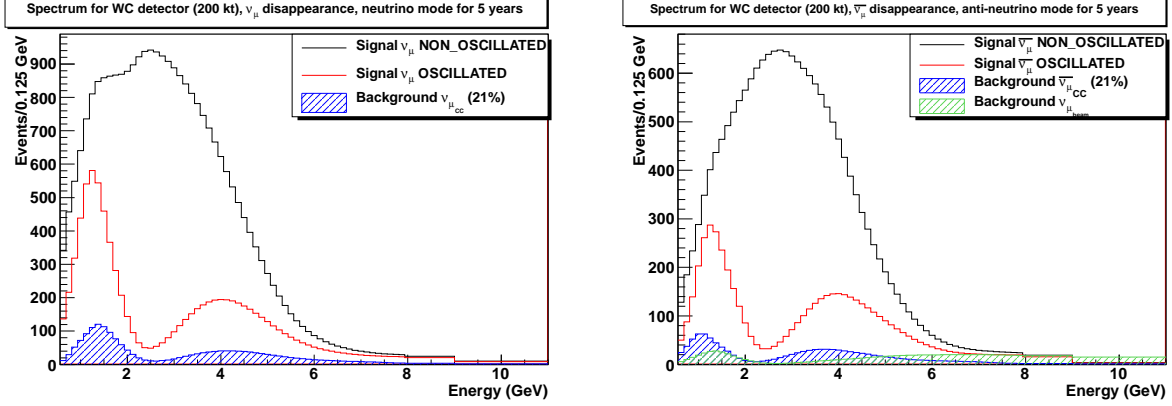
FIG. 24. Number of events expected with (red) and without (black) oscillations as observed by a 200 kt water Cerenkov detector in 5 years of neutrino (left) or 5 years of antineutrino (right) running in a 120 GeV 700 kW beam. In the current set of assumptions, a ν_μ QE sample is used for the signal channel. The backgrounds, are assumed to come from CC π^+ events, are shown in blue. In the case of antineutrino running, there is also an additional background contribution from ν_μ events shown in green.
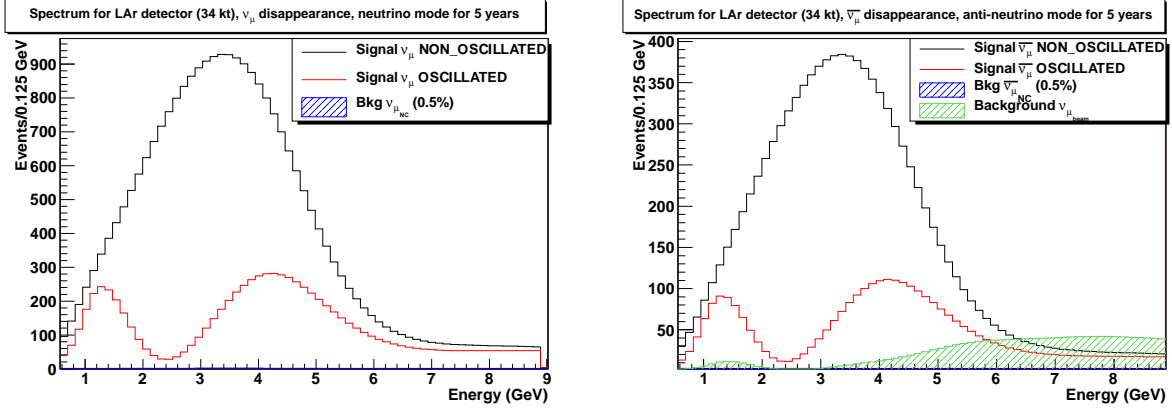
FIG. 25. The same plots and beam conditions as in Fig. 24 except for a 34 kt liquid argon detector (but note the different energy axis scales). In the current set of assumptions, a ν_μ CC sample is used for the signal channel. The assumed NC backgrounds are also plotted but are too small to be visible. In the case of antineutrino running, there is an additional contribution from ν_μ events which is taken into account and shown in green.

The bimodal structure is slightly different for WC and LAr due to the assumed signal selection. For WC, the signal is chosen to be a ν_μ quasi-elastic (QE) sample. This channel is selected because it provides a determination of the incoming neutrino energy based solely on the reconstructed muon kinematics. Background events are then predominately CC non-QE interactions where additional particles are produced but not detected. These are assumed to be largely CC π^+ interactions. They account for 21% of the ν_μ QE sample (based on estimates of background contamination in K2K[14] and MiniBooNE[15]). For WC, a 97% ν_μ QE signal efficiency is assumed.

The signal is assigned a 5% normalization error and a 3% energy scale uncertainty. The CC π^+ backgrounds are assigned a 10% normalization error (based on the current accuracy of existing CC π^+/QE measurements) and a 3% energy scale uncertainty. For LAr, inclusive ν_μ CC events are selected as the signal sample. An 85% signal efficiency is currently assumed with a 5% normalization error and a 2% energy scale uncertainty. In this case, the backgrounds

are NC events, 0.5% of which are assumed to be misidentified as CC events and assigned a 10% (2%) normalization (energy scale) uncertainty. In the case of antineutrino running, these same assumptions are applied with the addition of an extra level of ν_μ contamination. The actual parameter assumptions and GLoBES inputs used for the LBNE ν_μ and $\bar{\nu}_\mu$ disappearance projections are provided for both detectors in Appendix A.

Under these assumptions, the sensitivity of LBNE to $\sin^2 2\theta_{23}$ and Δm_{32}^2 in both neutrino and antineutrino modes is shown in Figures 26 and 27 for both WC and LAr, respectively. As one might expect, the sensitivity improves for large values of $\sin^2 2\theta_{23}$.
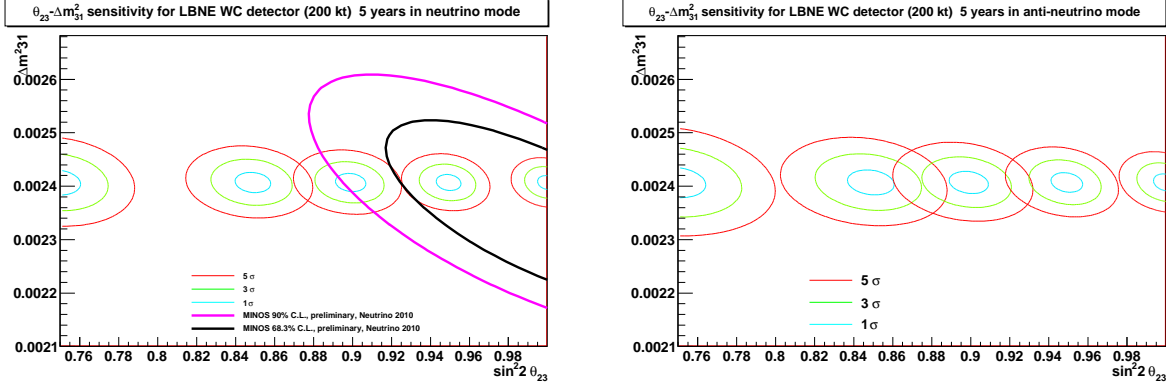
FIG. 26. Sensitivity of LBNE to $\sin^2 2\theta_{23}$ and Δm_{32}^2 for select values of $\sin^2 2\theta_{23}$ for 200 kt of WC. This assumes 5 years of neutrino (left) or 5 years of antineutrino (right) running in a 120 GeV 700 kW beam. Recent results from MINOS are also overlaid in the neutrino case [17].
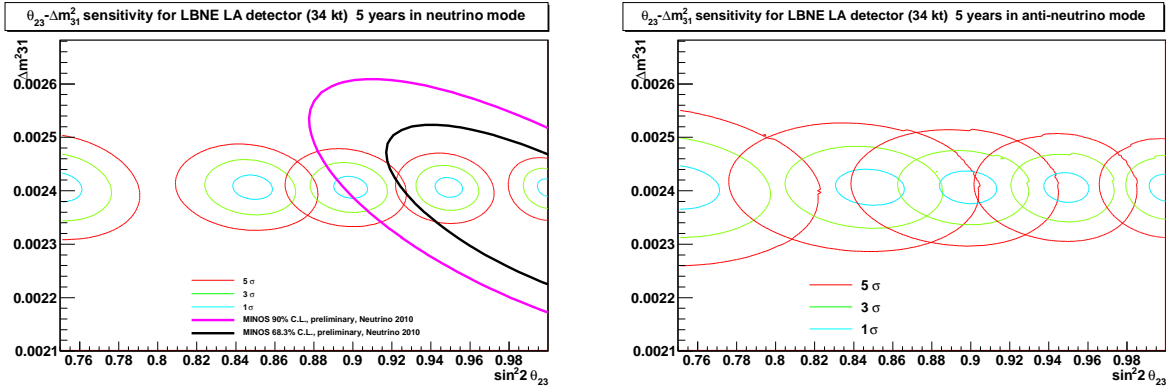
FIG. 27. Same plots as Fig. 26 except for 34 kt of LAr.

To further illustrate how these projections might scale with exposure, Figures 28 and 29 plot the resolutions on $\sin^2 2\theta_{23}$ and Δm_{32}^2 achievable in LBNE as a function of kt-years. Here, the 1σ contours have been used for the resolution calculation. In 5 years of neutrino running only and for maximal mixing, $< 1\%$ measurements of Δm_{32}^2 and $\sin^2 2\theta_{23}$ are possible (at 1σ) with either a 200 kt WC or 34 kt LAr detector. Measurements of these parameters in the antineutrino disappearance channel are possible at the 1% level assuming a similar exposure.
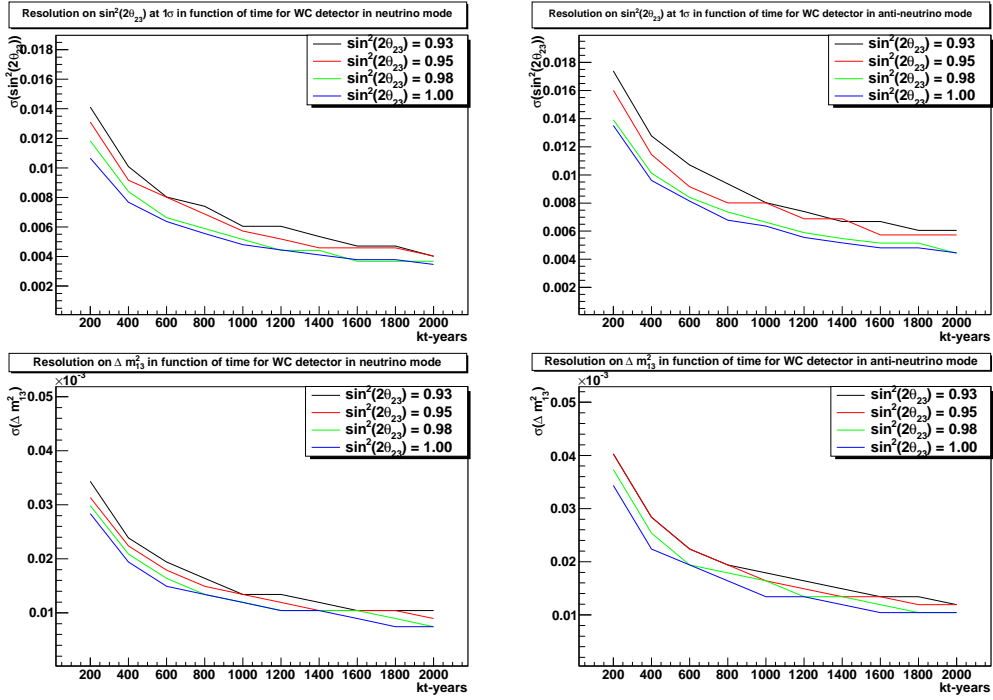
FIG. 28. Resolution on $\sin^2\theta_{23}$ (top) and Δm^2_{32} (bottom) as a function of kt-years that could be achieved in LBNE at the 1σ level for a WC detector running in neutrino (left) and antineutrino (right) mode assuming 700 kW beams.
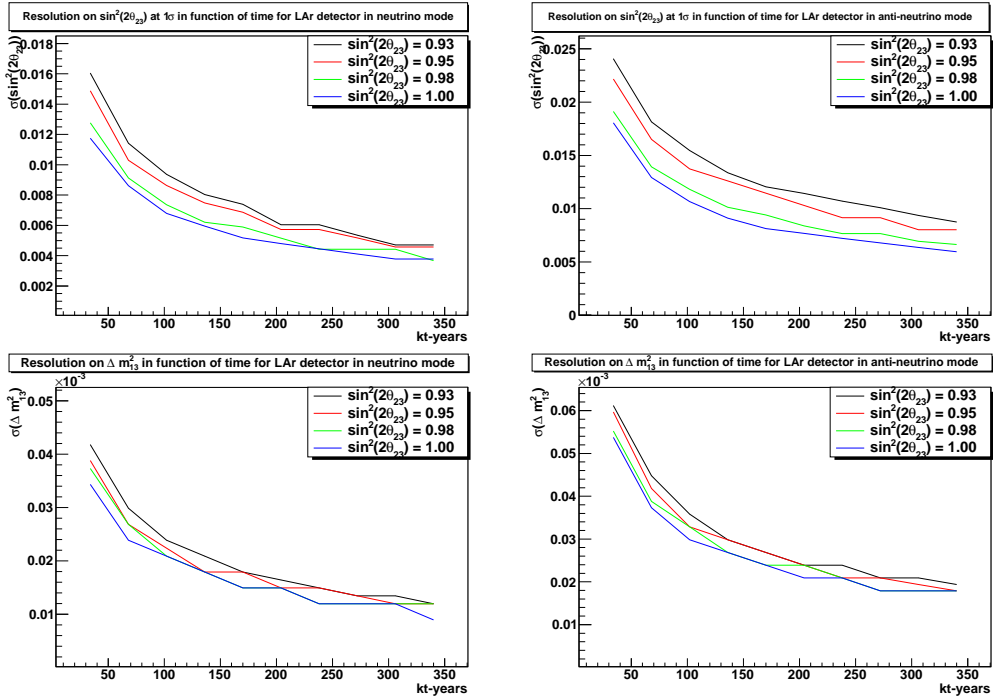
FIG. 29. Resolution on $\sin^2\theta_{23}$ (top) and Δm^2_{32} (bottom) as a function of kt-years that could be achieved in LBNE at the 1σ level for a LAr detector running in neutrino (left) and antineutrino (right) mode assuming 700 kW beams.

E. θ_{23} Octant Degeneracy

Current experimental results tell us that $\sin^2 2\theta_{23}$ is near maximal ($\sin^2 \theta_{23} > 0.91$ at 90% CL [12]), however there exist two solutions of θ_{23} for a given set of measured oscillation parameters, known as the θ_{23} octant ambiguity. If the oscillation associated with ν_μ disappearance is not maximal, then it will be important to determine whether θ_{23} is greater than or less than $\pi/4$. This in turn will help tell us whether the third neutrino mass eigenstate couples more strongly to ν_μ or ν_τ. Fig. 30 displays the capability of LBNE to resolve the θ_{23} octant for both WC and LAr. Running in a 700 kW beam, LBNE is able to resolve the θ_{23} octant degeneracy for θ_{23} values less than 40° at 90\$ CL and 90% of δ_{CP} values if $\sin^2 2\theta_{13}$ is greater than 0.070 for 200 kt WC and greater than 0.075 for 34 kt LAr.
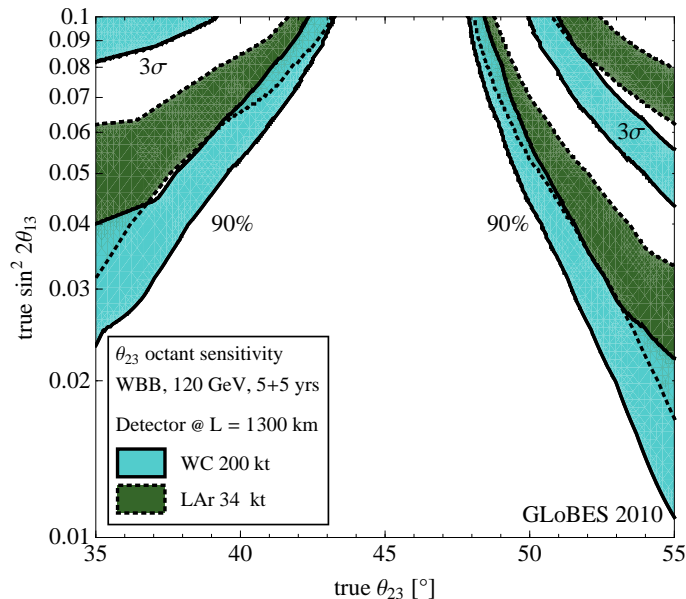
FIG. 30. Sensitivity of LBNE to resolve the θ_{23} octant degeneracy for 5+5 years of $\nu+\bar{\nu}$ running at 700 kW assuming the "August 2010" beam design (red curve in Fig. 2) and normal mass hierarchy. The blue band shows the results for 200 kt WC and the green for 34 kt LAr. The width of the bands corresponds to the impact of different true values for δ_{CP}, ranging from a 10% to 90% fraction of δ_{CP}. In the region above the bands, the determination of the θ_{23} octant is possible at 90% CL (lower bands) and 3σ (upper bands). Resolution of the octant degenerary is determined by using $\pi/2 - \theta_{23}$ as a starting value and the user-defined priors in GLoBES to force the minimizer to remain in the wrong octant (i.e., this includes marginalization over θ_{23}).

F. ν_τ Appearance

The LBNE baseline at 1300 km will be longer than any long baseline experiment currently in operation. As a result, the oscillation probability occurs at higher energy and in particular the energy range is favorable to $\nu_\mu \to \nu_\tau$ appearance since there is a large appearance probability above the τ CC production threshold of 3.2 GeV. In this respect LBNE has a unique ability compared to current long baseline experiments, since oscillation between all three flavors of neutrinos can be observed in a single experiment. To increase the ν_τ CC appearance signal, we are considering several high energy beam tunes produced by moving the target further upstream of horn 1. An example of a high energy beam spectrum produced by pulling the target back by 1.5 m is shown in Fig. 31.

In Table IV, the ν_e and ν_τ CC appearance rates for several LBNE beam tunes are shown. The first two rows in Table IV correspond to the 2009 and "August 2010" reference beams. The last two rows correspond to two proposed high energy beam tunes produced by pulling the target back by 1.5 m and 2.5 m from horn 1. For LBNE, we will label these tunes as HE1 (-1.5 m) and HE2 (-2.5 m); these tunes are very similar to the NuMI/MINOS medium energy (ME) and high energy (HE) beam tunes respectively.

The spectrum of all ν_τ and ν_e CC events appearing at the LBNE far detector as a function of neutrino energy for the 2009, HE1 and HE2 beams are shown in Fig. 32. No detector effects are included. The spectrum of NC events containing a single π^0 obtained from a Nuance [159] simulation as a function of π^0 energy is also shown. In addition,
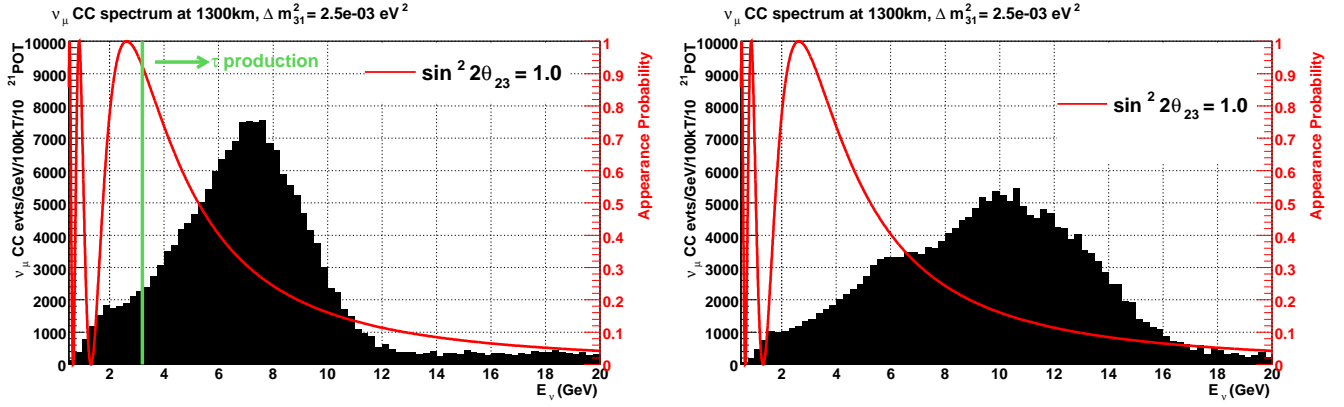
FIG. 31. The unoscillated ν_μ CC spectra at DUSEL obtained by moving the target 1.5 m upstream of horn 1 - HE1 beam (left) and moving the target 2.5 m upstream of horn 2 (right) is shown as the solid black histogram. The $\nu_\mu \to \nu_\tau$ oscillation probability is overlaid as the red curve.
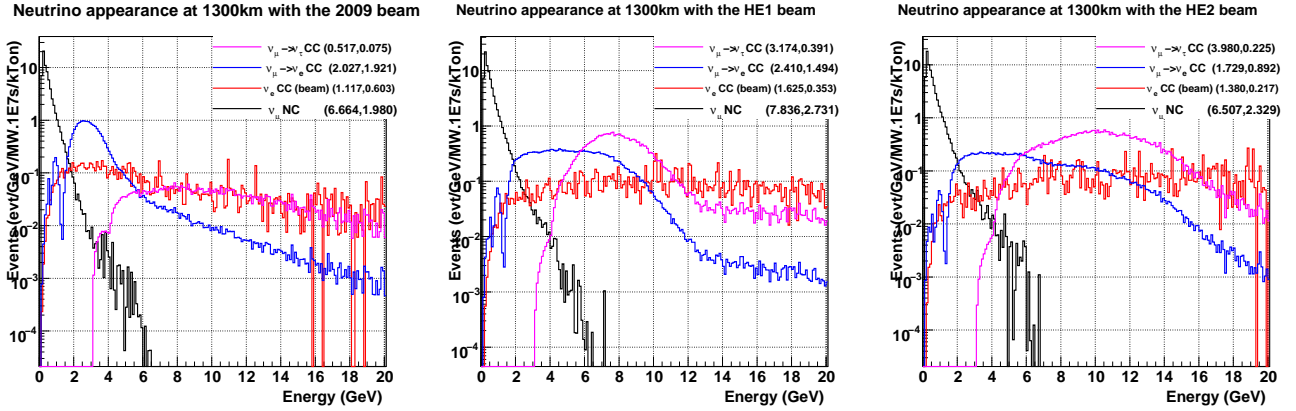
FIG. 32. Total ν_e and ν_τ CC appearance rates at 1300 km with normal hierarchy, $\Delta m_{31}^2 = 2.5 \times 10^{-3}$eV^2, $\delta_{cp} = 0$ and $\sin^2 2\theta_{13} = 0.04$ with the LBNE 2009 beam with the target inserted fully into the 1st horn (left), the HE1 beam tune with the target -1.5 m from 1st horn (center) and the HE2 beam tune with the target -2.5 m from 1st horn (right).

the spectrum of ν_e CC events from the beam contamination is overlaid. The NC single π^0 integrated rate as well as the beam ν_e CC and QE rates are shown in Table IV.

Target Position	ν_μ CC	ν_μ CC osc	ν_e CC beam	ν_e QE beam	NC-$1\pi^0$	$\nu_\mu \to \nu_e$ CC	$\nu_\mu \to \nu_\tau$ CC
0 (2009 tune)	206	78	2.2	0.26	4.0	4.0	1.0
-0.3 m (Aug 2010 tune)	290	108	2.6	0.28	5.2	5.6	1.4
-1.5 m (HE1 tune)	444	282	3.2	0.22	5.4	4.8	6.4
-2.5 m (HE2 tune)	466	350	2.8	0.16	4.6	3.4	8.0

TABLE IV. ν_μ, ν_τ, ν_e appearance rates per kT.MW.yr at the far detector in LBNE for different beam tunes obtained by moving the target w.r.t. horn 1. Normal hierarchy, $\sin^2 2\theta_{13} = 0.04$. The rates are integrated in the region 0-20 GeV. The NC single π^0 rates are given for visible energies >0.5 GeV.

The ν_τ signal in both water Cerenkov and LAr can be observed as an excess of e-like events from leptonic decays of the τ in ν_τ CC events where $\tau \to e\bar\nu_e\nu_\tau(\gamma)$ with a total branching fraction of 19.6% [11], the dominant background will be ν_e CC events from $\nu_\mu \to \nu_e$ oscillations if $\sin^2 2\theta_{13}$ is large, the beam contamination and NC π^0 events. From Fig. 32 and Table IV, we can see that the total appearance rate of ν_τ CC events for both the HE1 and HE2 beams is substantially larger than the irreducible beam ν_e CC background. For the HE2 beam, the appearance signal is well separated from the $\nu_\mu \to \nu_e$ CC signal as a function of true neutrino energy. In addition, there is still a substantial ν_e appearance signal in the HE1 beam, with a total CC appearance rate larger than the 2009 reference beam. The actual signal and spectrum of ν_τ CC events in both detector technologies is yet to evaluated and compared, but with a higher energy beam tune the study outlined in this section demonstrates that it is possible to obtain a large ν_τ

appearance signal rate, while also maintaining a significant portion of the ν_e appearance signal.

G. New Physics Searches in LBNE

In addition to precision measurements of the standard three-flavor neutrino oscillation parameters, LBNE is also well-suited for new physics searches in the neutrino sector. For example, the experiment is sensitive to non-standard neutrino interactions and active-sterile neutrino mixing, provided that these effects are not too weak. To illustrate the potential of new physics searches, we will here focus on non-standard interactions (NSI).

Theories beyond the Standard Model can induce Lagrangian operators that couple neutrinos to normal matter in non-standard ways. In the low-energy effective theory relevant to neutrino oscillation experiments, these non-standard interactions manifest themselves as 4-fermion operators, either of the charged-current (CC) type (e.g. $[\bar\nu_\alpha \gamma^\rho \ell_\beta]\,[\bar q \gamma_\rho q]$, where ℓ_β is a charged lepton) or of the NC type (e.g. $[\nu_\alpha \gamma^\rho \nu_\beta]\,[\bar q q]$). Most (but not all) CC NSI are most easily seen in a near detector, while NC NSI can be understood as non-standard matter effects that are visible only in a far detector at a sufficiently long baseline. This is where LBNE has a unique advantage compared to other long-baseline experiments (except atmospheric neutrino experiments, which are, however, limited by systematic effects). Therefore, and because there is no near detector definition for LBNE yet, we will here focus on NC NSI. They can be parameterized as new contributions to the MSW matrix in the neutrino propagation Hamiltonian:

$$ H = U \begin{pmatrix} 0 & & \\ & \Delta m_{21}^2/2E & \\ & & \Delta m_{31}^2/2E \end{pmatrix} U^\dagger + \tilde{V}_{\mathrm{MSW}}\,, \tag{1} $$

with

$$ \tilde{V}_{\mathrm{MSW}} = \sqrt{2} G_F N_e \begin{pmatrix} 1 + \varepsilon_{ee}^m & \varepsilon_{e\mu}^m & \varepsilon_{e\tau}^m \\ \varepsilon_{e\mu}^{m*} & \varepsilon_{\mu\mu}^m & \varepsilon_{\mu\tau}^m \\ \varepsilon_{e\tau}^{m*} & \varepsilon_{\mu\tau}^{m*} & \varepsilon_{\tau\tau}^m \end{pmatrix}\,. \tag{2} $$

Here, U is the leptonic mixing matrix, and the ε-parameters give the magnitude of the NSI relative to standard weak interactions. For new physics scales of few $\times\,100$ GeV, we expect $|\varepsilon| \lesssim 0.01$. Model-independent bounds on NSI are typically of order 0.01–1 [18–20]. However, in many concrete models, neutrino NSI are related to non-standard effects in the charged lepton sector, which are much more strongly constrained [21, 22]. Thus, one could take the point of view that NSI large enough to be experimentally accessible in the foreseeable future are disfavored by theoretical arguments. On the other hand, since theoretical prejudices about the properties of neutrinos have been wrong in the past, once can also adopt the standpoint that our inability to construct a simple model featuring large NSI does not necessarily mean they cannot exist. Also, NSI provide one explanation [23–25] for the interesting recent observations by the MINOS [12] and MiniBooNE [26] collaborations that could point to a new source of CP violation, but are not significant enough yet to draw any firm conclusions.

To assess the sensitivity of LBNE to NC NSI, we define the NSI discovery reach in the following way: We simulate the expected event spectra, assuming given "true" values for the NSI parameters, and then attempt a fit assuming no NSI. If the fit is incompatible with the simulated data at a given confidence level, we say that the chosen "true" values of the NSI parameters are within the experimental discovery reach. In Fig. 33, we show the NSI discovery reach of LBNE for the case where only one of the $\varepsilon_{\alpha\beta}^m$ parameters is non-negligible at a time.

We conclude from the figure that LBNE will be able to improve model-independent bounds on NSI in the e–μ sector by a factor of two, and in the e–τ sectors by an order of magnitude. Bounds on non-standard effects in the μ–τ sector are already quite strong because of the sensitivity of atmospheric neutrino experiments, but LBNE may be able to improve also some of the bounds in this sector, and in any case, LBNE bounds will be more robust than the ones derived from atmospheric neutrino oscillations. In particular, it has been shown in [27] that atmospheric neutrino bounds can become significantly weaker if the possibility of several NSI being non-zero is taken into account. Since LBNE provides a precise measurement of both the ν_e appearance and ν_μ disappearance channels and can be operated in neutrino and antineutrino mode, we expect it to be more robust with respect to these correlations.

The sensitivity of LBNE to non-unitarity effects in the leptonic mixing matrix (which can be recast into a special case of non-standard interactions) (see e.g. [21]) is not expected to be competitive with existing limits, which are already of order 10^{-3}. Searches for short-baseline oscillations into sterile neutrinos, on the other hand, would certainly be a worthwhile effort at a near detector. While near detector searches for oscillations between ν_e and ν_μ will be limited by systematic uncertainties in our knowledge of the beam spectrum and flavor composition, oscillations into ν_τ would provide a very clean signature. However, this would require the construction of a dedicated near detector that is able to identify ν_τ. It remains to be seen by how much such a detector could improve existing bounds from the NOMAD experiment [28].
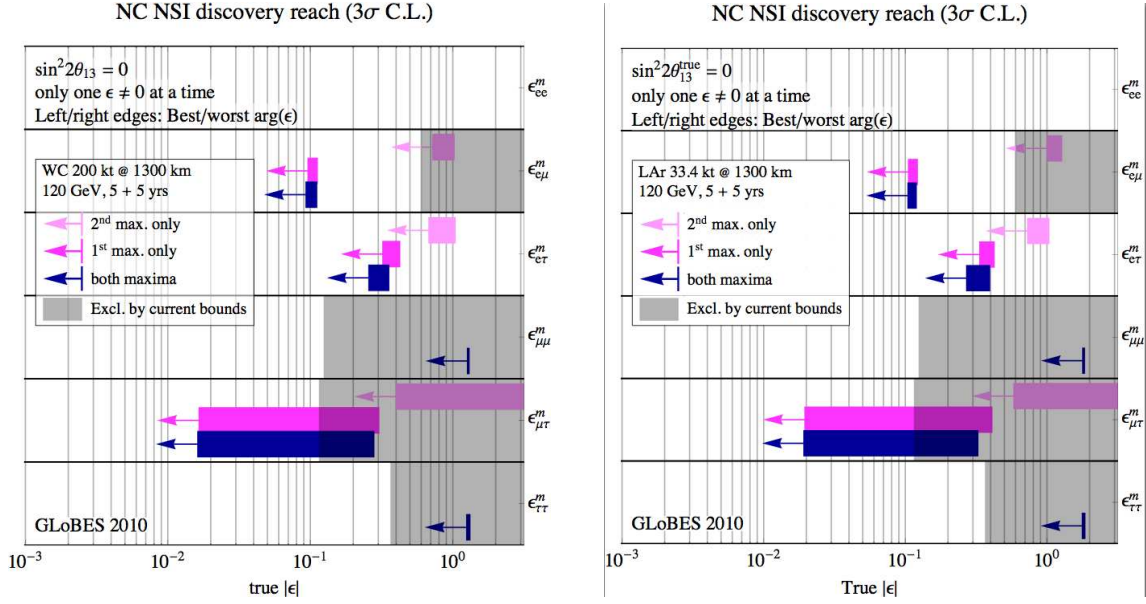
FIG. 33. NSI discovery reach in a WC detector (left) and a LAr detector (right). The left and right edges of the error bars correspond to the most favorable and the most unfavorable values for the complex phase of the respective NSI parameters. The gray shaded regions indicate the current model-independent limits on the different parameters at $3\,\sigma$ [18–20]. For some of them, limits are extremely weak. Note that model-dependent limits can be several orders of magnitude stronger. In this plot, we have assumed only one NSI parameter to be non-negligible at a time. Comparing the dark and light pink bars, we see that the NSI sensitivity comes mainly from the data in the first oscillation maximum; the second one is too polluted by backgrounds to contribute appreciably. The performance of the WC and LAr detectors is very similar.

H.   Next Steps

While there has been much progress in the past year, we list here some of the known issues requiring further study.

- For the ν_e appearance estimates:
  - What is the impact of improved WC reconstruction (similar to what has been accomplished for T2K and MiniBooNE) on our assumed selection efficiencies when applied at LBNE energies?
  - What is the impact of improved LAr reconstruction on our assumed selection efficiencies when applied at LBNE energies? In particular, we need to evaulate energy dependent signal efficiencies and background rejection levels along with improved estimates of energy resolutions in LAr.
  - We need to modify GLoBES to include a more realistic estimate of background uncertainties that are both process and energy dependent.
- For the ν_μ disappearance estimates:
  - We need to improve the energy smearing for CC π^+ background events for WC (the current smearing seems too symmetrical).
  - We need to examine whether a 97% ν_μ QE signal efficiency is the correct number for WC. Our guess is that this number should be lower.
  - We need to assess a more realistic estimate of the neutrino energy resolution for ν_μ CC events in LAr. We are presently using an estimate from ICARUS evaluated for neutrino energies < 1.25 GeV.
  - We need to study whether using a QE or CC sample optimally gives better sensitivity to $\sin^2 2\theta_{23}$ and Δm_{32}^2 for each detector type, WC and LAr.
- Can additional gains be made on our long-baseline oscillation sensitivities if we are able to separate ν from $\bar\nu$ events in a LAr far detector? For now, we have not accounted for potential $\nu/\bar\nu$ separation capabilities in LAr.
- What is the impact of photocathode coverage on our long-baseline oscillation sensitivities in the case of WC? For this, we would need revised efficiencies and energy resolutions for different PMT coverages.
- What is the impact of different likelihood cut placements? Is there a more optimized selection possible for the LBNE beam configuration?

I. Conclusions

The LBNE project, as currently defined, comprises two 100 kt water Cerenkov-equivalent detectors. Since the $\nu_\mu \to \nu_e$ signal is dominated by statistical uncertainties, we chose the mass of the LAr detector to give equivalent signal statistics in both. As described in Appendix A, the energy dependent WC ν_e signal efficiency used in this study is based on Super-K analysis and for LAr we have used a constant signal efficiency of 85%. Based on these assumptions, a fiducial mass of ~ 17 kt LAr TPC produces similar sensitivity for oscillation parameter measurements as a 100 kt WC fiducial mass. The mass ratio of 1/6 is largely a reflection of the ratio of the WC and LAr signal efficiencies (15% and 85%, respectively) at the energy of the first ν_μ oscillation maxima for a 1300 km baseline and $\Delta m_{31}^2 = 2.5 \times 10^{-3} \mathrm{eV}^2$ ($\sim$2.4 GeV).

Published studies for the T2KK long baseline experiment [29], carried out using Super-K simulation and data, indicate that a factor of two increase in the WC ν_e signal efficiency may be possible, albeit with a significant increase in NC backgrounds. For both the LBNE and T2KK studies, the WC detector ν_e reconstruction efficiencies are based on searching for signal events with a single electron like ring. The LBNE ν_e appearance signal is at neutrino energies with significant contributions from deep inelastic interactions with multiple particles in the final state. So future increases in the WC ν_e signal efficiency may be possible when multi-ring signal events with pions are included. The net effect of increased efficiency and backgrounds on oscillation parameter sensitivities is being investigated will be presented in a future document.

We conclude this section with a series of tables to summarize the results of the chapter. Table V shows the LBNE sensitivity to non-zero $\sin^2 2\theta_{13}$ for different exposures, including a 10 year operation of the reference configuration (three '100-kt equivalent' LBNE modules), the CDR '200 kt,' and a single '100 kt' module. We see that the reference configurations reach a sensitivity almost a factor of two higher than a single module; higher beam power would reduce the elapsed time to reach the same sensitivity. Table VI provides examples of the 1σ resolution on the CP phase for these configurations; in Fig. 20 we see that higher mass (or beam power) provides a rapid improvement in resolution in the early years of running.

Tables VII, VIII, IX and X summarize the sensitivity of the 200 kT WC and 34 kT LAr detectors to $\sin^2 2\theta_{13} \neq 0$, the mass hierarchy, CP violation, resolution of $\sin^2 2\theta_{23}$ (ν and $\bar\nu$), resolution of Δm_{32}^2 (ν and $\bar\nu$), and the resolution of the θ_{23} octant. We assumed a running time of 5 years in ν mode and 5 years in $\bar\nu$ mode at 700 kW. We find that given the current assumptions on detector performance, both the water Cerenkov and liquid argon TPC technologies have similar physics sensitivities to the ν_μ oscillation parameters. In the case of mixed technology Far Detector configurations, we assume that the results from each of the detector modules can be combined with no loss of precision compared to single technology configurations.

WC	$\sin^2 2\theta_{13} \neq 0$	LAr	$\sin^2 2\theta_{13} \neq 0$
1000 kt-yrs	0.0050	170 kt-yrs	0.0044
2000 kt-yrs	0.0033	340 kt-yrs	0.0030
3000 kt-yrs	0.0026	510 kt-yrs	0.0023

TABLE V. Sensitivity of LBNE to non-zero $\sin^2 2\theta_{13}$ to 3σ significance after 5+5 years $\nu + \bar{\nu}$ running at 700 kW for one, two, three "100-kt equivalent" LBNE modules if $\delta_{CP} = 0$ and normal mass hierarchy (see Fig. 15).

WC	δ_{CP}	LAr	δ_{CP}
1000 kt-yrs	25°	170 kt-yrs	25°
2000 kt-yrs	19°	340 kt-yrs	18°
3000 kt-yrs	16°	510 kt-yrs	15°

TABLE VI. 1σ resolution on the measurement of δ_{CP} for one, two, three "100-kt equivalent" LBNE modules assuming $\sin^2 2\theta_{13} = 0.01$, $\delta_{CP} = 0$ and normal mass hierarchy (see Fig. 20).

	$\sin^2 2\theta_{13} \neq 0$	Mass Hierarchy	CP violation
2000 kt-yrs WC	0.008	0.04	0.03
340 kt-yrs LAr	0.008	0.05	0.03

TABLE VII. Sensitivity comparisons for an exposure of 2000 kt-yrs of WC (e.g., 200 kt WC, 5+5 years $\nu + \bar{\nu}$ running at 700 kW) and 340 kt-yrs of LAr (e.g., 34 kt LAr, 5+5 years $\nu + \bar{\nu}$ running at 700 kW). These numbers represent the value of $\sin^2 2\theta_{13}$ where a 3σ determination of $\sin^2 2\theta_{13} \neq 0$, the sign of Δm_{31}^2, and CP violation can be made for 100% of the possible values of δ_{CP}. For CP violation, the value is quoted for 50% of possible δ_{CP} values. These numbers were calculated assuming a normal mass hierarchy.

	$\sin^2 2\theta_{13}$	δ_{CP}
2000 kt-yrs WC	0.002	19°
340 kt-yrs LAr	0.002	18°

TABLE VIII. 1σ resolution on the measurement of ν_e appearance parameters in LBNE assuming an exposure of 2000 kt-yrs for WC (e.g., 200 kt WC, 5+5 years $\nu + \bar{\nu}$ running at 700 kW) and 340 kt-yrs for LAr (e.g., 34 kt LAr, 5+5 years $\nu + \bar{\nu}$ running at 700 kW). Values are quoted assuming a normal mass hierarchy, $\sin^2 2\theta_{13} = 0.01$, and $\delta_{CP} = 0$.

	$\delta(\sin^2 2\theta_{23})$ (ν)	$\delta(\Delta m_{32}^2)$ (ν)	$\delta(\sin^2 2\theta_{23})$ ($\bar{\nu}$)	$\delta(\Delta m_{32}^2)$ ($\bar{\nu}$)
1000 kt-yrs WC	0.007	0.015	0.008	0.020
170 kt-yrs LAr	0.007	0.017	0.011	0.025

TABLE IX. 1σ resolution on the measurement of ν_μ (and $\bar{\nu}_\mu$) disappearance parameters in LBNE assuming an exposure of 1000 kt-yrs for WC (e.g., 200 kt WC, 5 years ν (or $\bar{\nu}$) running at 700 kW) and 170 kt-yrs for LAr (e.g., 34 kt LAr, 5 years ν (or $\bar{\nu}$) running at 700 kW). Values are quoted for $\sin^2 2\theta_{23} = 1.0$.

	θ_{23}	$\sin^2 2\theta_{13}$
2000 kt-yrs WC	< 40°	> 0.070
340 kt-yrs LAr	< 40°	> 0.075

TABLE X. LBNE can resolve the θ_{23} octant at 90% CL for values of $\theta_{23} < 40°$ given $\sin^2 2\theta_{13}$ greater than the indicated values assuming an exposure of 2000 kt-yrs for WC (e.g., 200 kt WC, 5+5 years $\nu + \bar{\nu}$ running at 700 kW) and 340 kt-yrs for LAr (e.g., 34 kt LAr, 5+5 years $\nu + \bar{\nu}$ running at 700 kW). Numbers are quoted for a normal mass hierarchy and 90% of δ_{CP} values.

IV. PROTON DECAY

Proton decay, bound neutron decay, and similar processes such as dinucleon decay and neutron-antineutron oscillation test the apparent but unexplained conservation law of baryon number. These decays are already known to be rare based on decades of prior searches, all of which have been negative. If measurable event rates or even single candidate events are found, one immediately concludes that they must have proceeded via unknown virtual processes based on physics beyond the standard model. The impact of demonstrating the existence of a baryon number violating process would be profound.

The class of theories known as Grand Unified Theories (GUTs) make predictions about baryon number violation and the life of the proton that may be within reach of the LBNE detectors. Early GUTs were the original motivation for putting kiloton-scale detectors underground. The 22.5 kiloton Super-Kamiokande experiment extended the search for proton decay by more than an order of magnitude. Although there has been no sign of proton decay, the strict limits from these experiments constrain the construction of contemporary GUTs and indeed, a tension between experiment and theory is now commonly discussed. It is very natural to continue the search with 100-kiloton-scale detectors.

A. Motivation and Scientific Impact of Future Measurements

The grand unified theoretical motivation for the study of proton decay has a long and distinguished history [30–32], and has been reviewed many times [33–35]. Contemporary reviews [36–38] discuss the strict limits already set by Super-Kamiokande and the context of proposed multi-100-kiloton scale experiments such as Hyper-Kamiokande and LBNE. Here are some of the key points related to scientific impact:

- Conservation of baryon number is unexplained, corresponding to no known long-range force.

- Baryon number non-conservation has cosmological consequences, such as a role in inflation and the baryon asymmetry of the universe.

- Proton decay is predicted by a wide range of GUTs.

- Grand unified theories are also often able to accommodate massive neutrinos with characteristics as discovered over the last decade.

- GUTs incorporate other unexplained features of the standard model such as the relationship of quark and lepton electric charges.

- The unification scale is suggested experimentally and theoretically by the apparent convergence of the running coupling constants of the Standard Model. It is in excess of 10^{15} GeV.

- The unification scale is not accessible by any accelerator experiment, and can only be probed by virtual processes such a proton decay.

- GUTs usually predict the relative branching fractions of different nucleon decay modes, requiring of course a sizeable sample of proton decay events to test.

- The dominant proton decay mode is often sufficient to roughly identify the likely characteristics of the GUT, such as gauge mediation or the involvement of supersymmetry.

In summary, the observation of even a single unambiguous proton decay event would signal that the ideas of grand unification are correct and would give guidance as to which models most likely describe the universe. One or two events would also give guidance to what even larger size detector would be needed to explore the physics in more detail.

From the body of literature, two decay modes emerge that dominate our experimental design. First, there is the decay mode of $p \to e^+\pi^0$ that arises from gauge mediation. This is the most famous proton decay mode, often predicted to have the highest branching fraction, and also demonstrably the most straightforward experimental signature for a water Cherenkov detector. The total mass of the proton is converted into the electromagnetic shower energy of the positron and the two photons from π^0 decay, with a net momentum vector near zero.

The second key mode is $p \to K^+\nu$. This mode is dominant in most supersymmetric-GUTs, which also often favor several other modes involving kaons in the final state. The decay mode with a charged kaon is notable because it presents the unique opportunity for a liquid argon TPC to detect it with extremely high efficiency. This is because
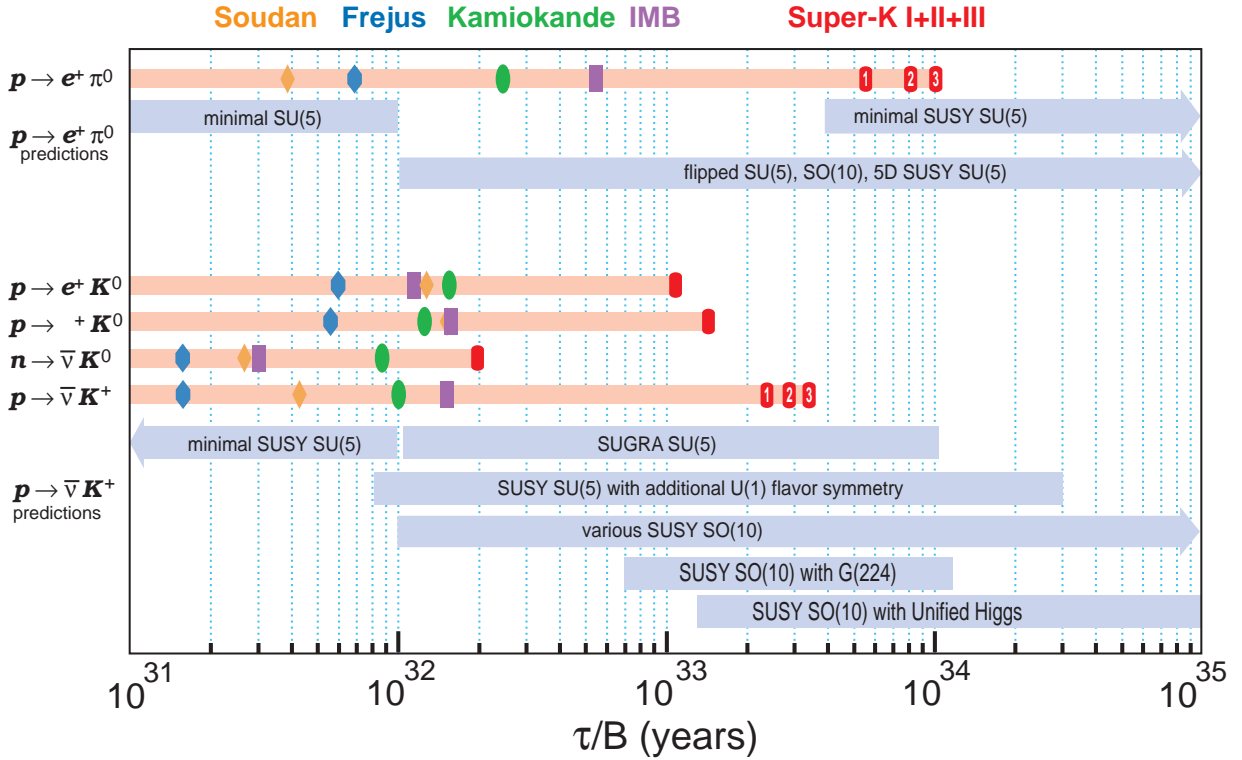
FIG. 34. Proton decay lifetime limits compared to lifetime ranges predicted by Grand Unified Theories. The upper section is for $p \to e^+\pi^0$, most commonly caused by gauge mediation. The lower section is for SUSY motivated models, which commonly predict decay modes with kaons in the final state. The marker symbols indicate published limits by experiments, as indicated by the sequence and colors on top of the figure.

the momentum of the kaon will result in high ionization density which can be compared to the range of the kaon, not to mention the unique final states of K^+ decay that should be fully reconstructed.

There are a number of other proton decay channels to consider, but they will not influence the design of a next-generation experiment beyond the above decay modes. There are 27 allowed modes of proton or bound neutron into anti-lepton plus meson (conserving $B - L$). The most stringent limits besides $p \to e^+\pi^0$ include $p \to \mu^+\pi^0$ and $p \to e^+\eta$, both of which must have partial lifetimes greater than 4×10^{33} years. Any experiment that will do well for $e^+\pi^0$ will do well for these decay modes. The decay $p \to \nu\pi^+$ or $n \to \nu\pi^0$ may have large theoretically predicted branching fractions but are experimentally difficult due to sizeable backgrounds from atmospheric neutrino interactions. The decay $p \to \mu^+K^0$ is detected relatively efficiently by either water Cherenkov or LAr TPC detectors. There are a number of other possibilities such as modes that conserve $B + L$, or violate only baryon number, or that decay into only leptons. These possibilities are less well-motivated theoretically, as they do not appear as frequently in the literature. In any case, they can be accommodated with equal ease or difficulty by the large detectors considered here.

Fig. 34 shows experimental limits, dominated by recent results from Super-Kamiokande, compared to the ranges of lifetimes predicted by an assortment of GUTs. At this time, the theory literature does not attempt to precisely predict lifetimes, concentrating instead on suggesting the dominant decay modes and relative branching fractions. The uncertainty in the lifetime predictions come from details of the theory, such as unknown heavy particles masses and coupling constants, as well as poorly known details of matrix elements for quarks within the nucleon.

It is apparent from this figure that a continued search for proton decay is by no means assured of success. In addition to the lifetime ranges shown, there are models that predict essentially no proton decay or lifetimes out of reach of likely experiments. With that caveat, an experiment with sensitivity between 10^{33} and 10^{35} years is searching in the right territory over a wide range of GUTs and even if no proton decay is detected, the stringent lifetime limits will restrict efforts to build such theories. Minimal SU(5) was ruled out by the early work of IMB and Kamiokande; minimal SUSY SU(5) is considered to be ruled out by Super-Kamiokande. In most cases, another order of magnitude in limit will not rule out specific theories, but will constrain their allowed parameters, perhaps leading to the conclusion that some are fine-tuned.

B. Sensitivity of Reference Configurations

The experimental requirements of the search for proton decay can be found in the basic formula for the partial lifetime τ for branching fraction B:

$$\frac{\tau}{B} = \frac{N_0 \, \Delta t \, \epsilon}{n_{obs} - n_{bg}}, \tag{3}$$

where N_0 is the number of nucleons exposed, Δt is the exposure time, ϵ is the detection efficiency, n_{obs} is the observed number of events, and n_{bg} is the estimated number of background events. To measure τ/B, one would like the numerator to be as large as possible, which calls for the largest possible exposure of nucleons as well as the highest possible efficiency.

The sensitivity for a detector configuration is determined by the detector mass, efficiency, expected background, and running time, following Eq. 3. For the purpose of generating sensitivity curves, we calculate the 90% C.L. lifetime limit one would publish after a given exposure under the assumption that the number of detected events exactly equals the number of background events, and the background is subtracted. The efficiency and background estimates are drawn from Table XI.

The lifetime limit is calculated for the 90% confidence level based on the *Poisson processes with background* method from the 1996 Review of Particle Properties [40]. This method does not take into account systematic uncertainty; doing so typically weakens these limits by 20%.

Mode	Water Cherenkov		Liquid Argon	
	Efficiency	Background Rate (evts/100 kt-y)	Efficiency	Background Rate (evts/100 kt-y)
$p \to e^+\pi^0$	45% ± 19%	0.2(±40%)	45%	0.1
$p \to \nu K^+$	13.4% ± 22%	0.67(±30%) (SK1)	97%	0.1
$p \to \nu K^+$	10.6% ± 22%	0.83(±30%) (SK2)		

TABLE XI. Efficiency and background numbers used for sensitivity calculations. The water Cherenkov numbers are based on published or preliminary Super-Kamiokande studies. The systematic uncertainties are included for reference but play no role in the sensitivity calculation. The liquid argon numbers come from the paper by Bueno *et al.* [39].

1. Proton decay to $e^+\pi^0$

In the decay $p \to e^+\pi^0$, the total mass of the proton is converted into the electromagnetic shower energy of the positron and the two photons from π^0 decay, with a net momentum vector near zero. For the decay of a free proton, the momentum should be zero within the limits of detector resolution; for the decay of a bound proton, the momentum is smeared up to the fermi level (225 MeV/c in ^{16}O). No muon-decay electron should be present, a requirement that eliminates a great deal of atmospheric neutrino background. Compared to other possible nucleon decay modes, this is a very clean signature.

For $e^+\pi^0$, the detection efficiency is dominated by nuclear absorption when the proton decays in ^{16}O, with 37% of the pions being absorbed or undergoing charge exchange; in either case the signature is lost. Decay of the free proton is detected efficiently, however, with an experimental efficiency of 87%. Overall, a proton decay to $e^+\pi^0$ in water event will pass the standard set of Super-Kamiokande cuts with an efficiency of 45%.

Figure 35 shows the 90% sensitivity curve for $p \to e^+\pi^0$ plotted as a function of calendar year. The leftmost curve is that for Super-K. The first smooth section reflects the initial running period known as Super-K–I (SK1) that started in May 1996. Then there is a flat period reflecting a planned small shutdown in 2001 that was lengthened due to the PMT chain reaction accident. The subsequent smooth curve is SK2, followed by a brief shutdown, and then SK3 changing smoothly into SK4 in 2008. The Super-K official limit for these three running periods (SK1+2+3) is 1×10^{34} years [41, 42]. Future running with SK4 may have slightly higher efficiency or lower backgrounds due to new electronics, but the improvement levels are not finally estimated and assumed to be small.

The curves for LBNE assume a start date for the first 100 kilotons starting in mid-2019 with subsequent detector masses turning on one year and two years later. The efficiencies and background rates were taken to be identical to those for Super-K. Based on the SK2 studies of $p \to e^+\pi^0$ [41], the efficiency and background rates for 20% photocoverage were indistinguishable from 40% photocoverage (SK1 and SK3). Therefore, we take the LBNE curves to represent configurations with either 15%-HQE or 30%-HQE.

Fig. 35 does not include sensitivity curves for LAr for $p \to e^+\pi^0$. This is because the detector mass, even in the optimistic case of 51 kilotons, cannot compete with the long exposure of Super-Kamiokande. Based on Bueno *et al.* [39],

FIG. 35. Proton decay lifetime limit for $p \to e^+ \pi^0$ as a function of time for Super-Kamiokande compared to 300 kt of water Cherenkov detector starting in 2019. The water Cherenkov detector is assumed to commission 100 kt each year for the first three years; the limits from the partial detector masses of 100 kt or 200 kt is indicated with dashed lines. All limits use the same detection efficiency of 45% and background rate of 0.2 events/100 kt-years; systematic uncertainties are not included. The limits are at the 90% C.L., calculated for a poisson process including background assuming the detected events equals the expected background.

an efficiency of 45% with a background rate of 0.1 events per 100 kt-years results in a background subtracted limit at the 90% CL of 2.6×10^{34} years for a 500 kt-year exposure. So a ten year run starting in 2020 of a 51 kt LAr detector does not exceed the projected Super-K limit of 3×10^{34} in 2030. Although there is no reason not to search for this mode if such a detector is built, we do not consider $e^+ \pi^0$ to be a critical physics topic for a 51 kt or smaller liquid argon detector.

Hybrid configurations can be roughly appreciated from the 100, 200, and 300 kt water Cherenkov curves. For example, configurations 5 or 6, 100 kt WC plus 34 kt LAr will lie between the WC100 and WC200 lines in Fig. 35.

After 10 years, a 300 kt water Cherenkov detector would have an expected background of 6 events given our assumed background rate. This has a significant impact on the 90% C.L. limit we would set, or conversely, the ability to identify one or two candidate events in such an exposure. It is possible that atmospheric neutrino backgrounds could be reduced in a detector with gadolinium such that it can detect coincident neutron capture. This assumes that (a) proton decay does not eject neutrons from a ^{16}O nucleus and (b) atmospheric neutrino interactions are frequently accompanied by primary or secondary neutrons. If the background rate could be convincingly reduced by a factor of two, from 0.2 events to 0.1 events per 100 kt-years, then a 10-year exposure would set a limit of 1.0×10^{35} years instead of 0.8×10^{35} years.

2. Proton decay to νK^+

Fig. 36 shows the 90% sensitivity curve for $p \to \nu K^+$ plotted as a function of calendar year. The leftmost curve is that for Super-K as described above. The Super-K analysis is described in several publications [43, 44].

The Super-K analysis uses three methods: (i) gamma tag with $K^+ \to \mu + \nu$, (ii) $K^+ \to \pi^+ \pi^0$, and (iii) a background limited search for a monoenergetic muon. For the purpose of the Super-K and LBNE water Cherenkov curves, only (i) and (ii) are used, because the the background limited search contributes very little for large exposures. The SK1 analysis using methods (i) and (ii) has a relatively high background rate of 0.67 events per 100 kt-year. It is likely that some re-optimization would benefit large exposures, but for the sake of argument, we assume the final sensitivity would not change much, as the most likely alteration would be some loss in proton decay signal efficiency in exchange
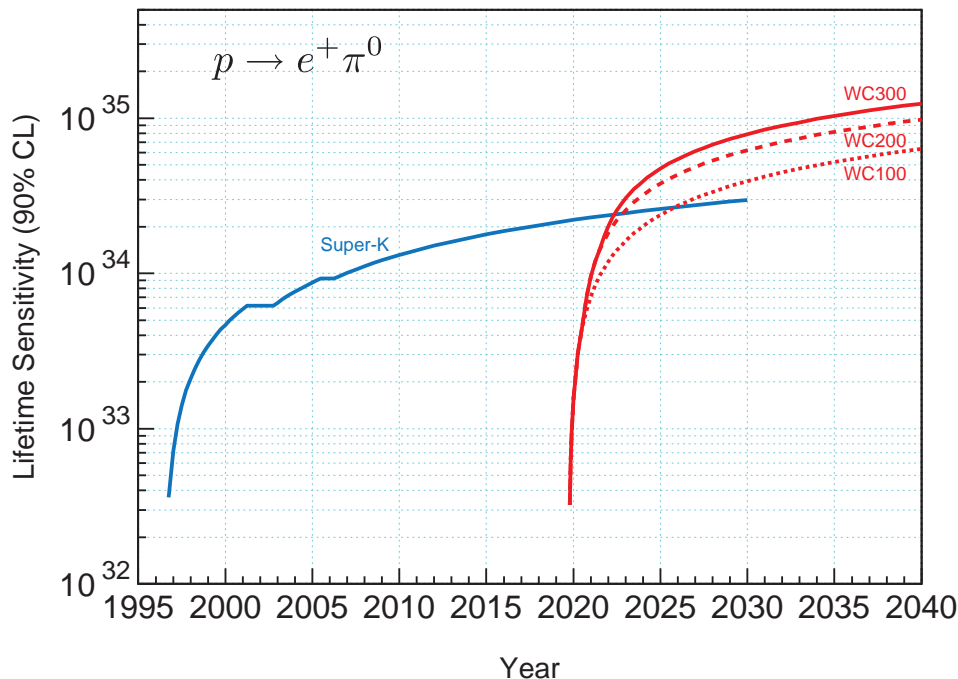
FIG. 36. Proton decay lifetime limit for $p \to \nu K^+$ as a function of time for Super-Kamiokande compared to 300 kt of water Cherenkov detector starting in 2019. The water Cherenkov detector is assumed to commission 100 kt each year for the first three years; the limits from the partial detector masses of 100 kt or 200 kt is indicated with dashed lines. The bold lines use the efficiency and background numbers for the SK1 analysis; the thin lines use the efficiency and background numbers for the SK2 analysis. The limits are at the 90% C.L., calculated for a poisson process including background assuming the detected events equals the expected background.

for lower atmospheric neutrino background. It is also possible that the LBNE detector with smaller PMTs and better timing could result in a sharper set of cuts to find the gamma ray tag. In other words, there is some hope that a well-instrumented LBNE water cherenkov detector would perform slightly better than Super-K for $p \to \nu K^+$, which is not likely to be true for $e^+\pi^0$. But we have no estimates of this yet, so we conservatively use the SK efficiencies and backgrounds as our benchmark.

As seen in Table XI, the performance of the Super-K analysis is markedly worse for SK2 (20% photocoverage) than SK1 (40% photocoverage). The efficiency is lower and the background rate is slightly higher. To study this difference, two sets of LBNE water Cherenkov curves are provided in Fig. 36, one set for each case.

Shown on Fig. 37 is the projected sensitivity for a liquid argon TPC of various masses. The efficiency and background rates are taken from Bueno et $al.$ [39]. The high efficiency for $p \to \nu K^+$ is a classic strong point in favor of liquid argon. Such a proton decay event signature would be highly described by such a detector, with a unique range and ionization level for the charged kaon. The charged kaon will decay at rest to fully reconstructible final states, for example, a subsequent muon with no other particle, indicating $K^+ \to \mu^+\nu$ (predominant, with 65% branching fraction) should have a muon with momentum reconstructed at 236 MeV/c. Therefore a high efficiency in excess of 90%, with very low background, is quite plausible.

The most serious background is cosmogenic neutral kaons undergoing charge exchange in the sensitive volume. These could result in the appearance of a charged kaon, mimicking proton decay if the K^+ had just the right momentum (339 MeV/c). This background process could be effectively studied by measuring the rate of such events in momentum sidebands and close to the detector walls. In any case, a fiducial mass reduction is anticipated to eliminate such events, by cutting out candidates near the side walls. In the Bueno et $al.$ paper [39], several different overburden and active veto scenarios were considered, with fiducial cuts as much as 6 meters from the wall, resulting in fiducial mass reductions ranging from 66% to 90%. For the sensitivity curves plotted in Fig. 37 we will take a generic value of 70%. This corresponds to a 2 meter cut from the sidewalls of the planned LBNE detector, reducing the volume from 14×15×71 meters³ to 14×11×67 meters³. At shallow depths, a key detector element required to allow even this fiducial restriction is some sort of active muon tracking veto that extends wider than the LAr detector itself. This is used to track nearby cosmic ray muons that could produce neutral kaons or neutrons. Whether such a veto could be constructed with ease and reasonable cost at either the 300-ft level or 800-ft level is unknown, and
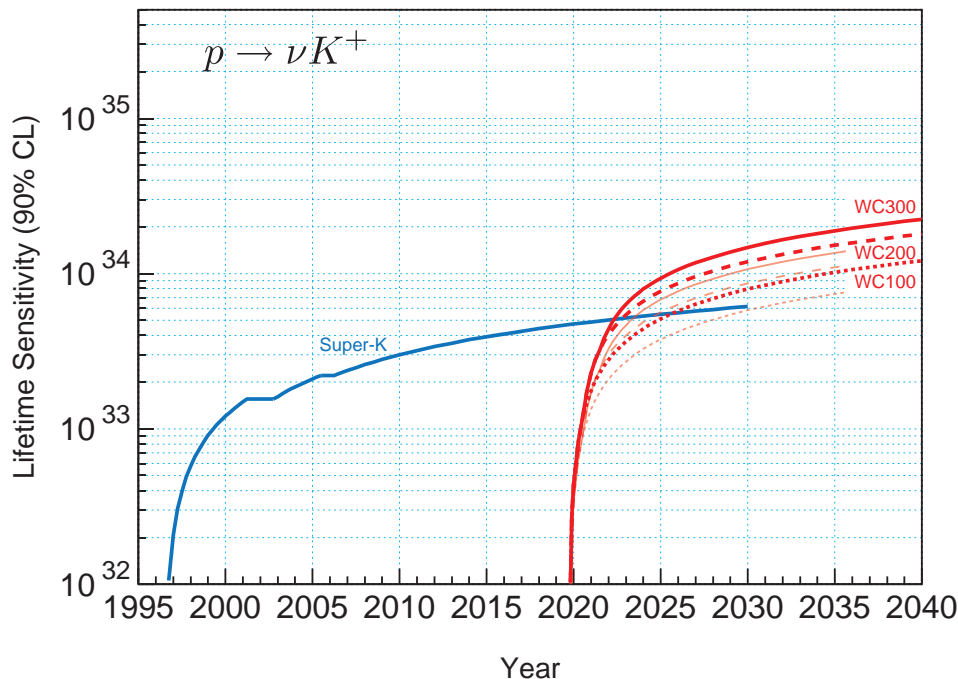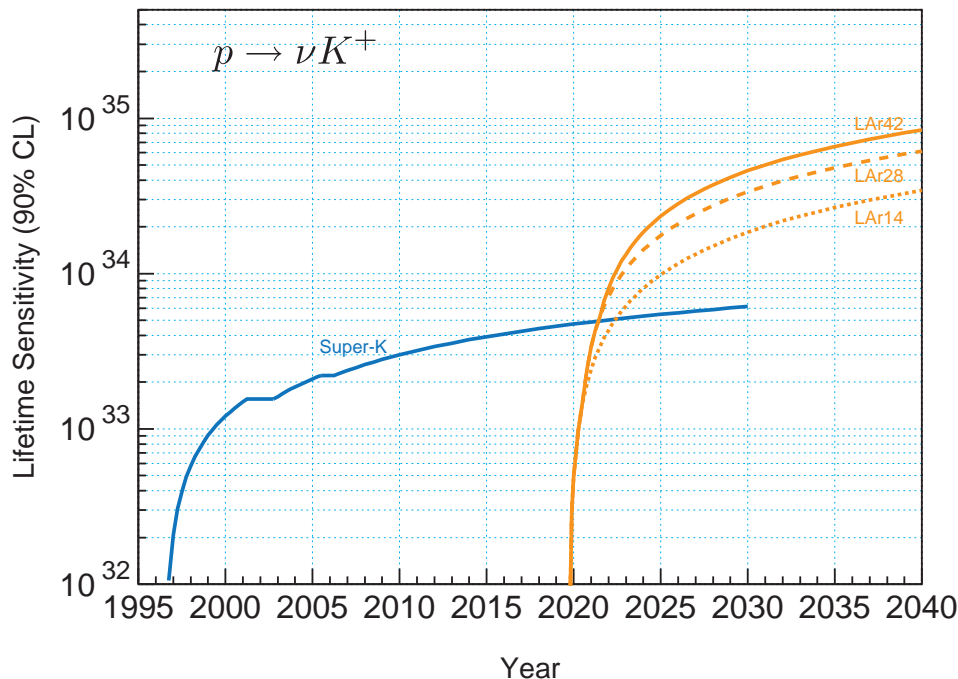
FIG. 37. Proton decay lifetime limit for $p \rightarrow \nu K^+$ as a function of time for Super-Kamiokande compared to 60 kilotons total, 42 kt fiducial, of LAr TPC starting in 2019. The LAr detector modules are assumed to commission 20 kt each year for the first three years; the limits from the partial detector fiducial masses of 14 and 28 kt are indicated with dashed lines. The limits are at the 90% C.L., calculated for a poisson process including background assuming the detected events equals the expected background.

not the topic of this report, although it can be safely assumed that no external tracking veto is needed at the 4850-ft level. Therefore, one 20-kiloton LAr module, assumed to have a 17 kt fiducial mass for long-baseline neutrinos, is taken to have a 14 kt fiducial mass for this proton decay mode if at shallow depth, but the full 17 kt at the 4850-ft level.

C. Conclusions

The case for proton decay rests on either discovering a small number of events or extending existing lifetime limits after an extensive search by Super-Kamiokande. We assume a Super-K limit of 3×10^{34} years for $p \rightarrow e^+ \pi^0$ and a limit of 6×10^{33} years for $p \rightarrow e^+ \pi^0$ in 2030. To characterize the power of a search using LBNE detectors, we look at the improvement factor of a lifetime limit by LBNE in 2020 over these hypothetical Srper-K limits.

Even the most massive configurations being considered, 300 kilotons of water Cherenkov detector, are projected to improve the lifetime limit on $p \rightarrow e^+ \pi^0$ by only a factor of 2.7 after a decade-long run starting around 2020. Such a detector will cross the symbolic milestone of 10^{35} years in 2035, after running for 15 years. Because a 10-year exposure of 300 kilotons would have an expected background of six events, background rejection using neutron tagging via gadolinium is desirable. Assuming a background reduction factor of two, the improvement factor is raised to 3.4.

For $p \rightarrow e^+ \pi^0$, a liquid argon TPC of fiducial mass 42 kilotons makes no improvement over the projected Super-K limit by itself. As supplementary detector mass to water Cherenkov, liquid argon will contribute slightly.

For $p \rightarrow \nu K^+$ and 300 kilotons of water Cherenkov, the improvement on the lifetime limit ranges from 1.8 to 3.3 depending on photocathode coverage and the addition of neutron tagging using gadolinium (again assuming a factor of two reduction in background rate with Gd).

The improvement factor in the lifetime limit is largest for a 50 kt scale liquid argon detector. Assuming that the high performance characteristics projected for a large LAr TPC are realized, such a detector could achieve an improvement factor of 8 to 9 on the lifetime limit for $p \rightarrow K^+ \nu$ after 10 years and could continue to do well with further exposure, having accumulated a modest background estimate of roughly one-half event after that time. However, a LAr TPC would have an impact on fewer decay modes than a water Cherenkov detector of a few times greater mass. The LAr detector is effective chiefly for the SUSY mode of $p \rightarrow K^+ \nu$, due to the high detection efficiency.

The experimental prognosis for a large LAr TPC is less certain than that for a large water Cherenkov detector, particularly if operated at shallow depth. A highly effective cosmic ray veto shield is essential at shallow depths. For the purpose of the tables below, no attempt is made to distinguish the 300-ft and 800-ft depths, although option 2 is given the benefit of a full 51 kilotons at 4850 feet. With respect to the LAr detector configurations, the naive assumption would be that an array of photomultiplier tubes that trigger based on scintillation light in the liquid argon is required for non-accelerator contained events such as proton decay. However, work is underway to develop a pattern recognition trigger that uses the TPC data, dubbed *K-select*, that would efficiently trigger on kaon tracks in the region of interest for proton decay. Since the prospect of such a trigger is hopeful, albeit speculative, no attempt is made to compare relative efficiencies with and without the photon trigger. Tables XII and XIII summarize the results of this section.

Configuration	WC Mass	PMT	Gd	LAr Mass	WC BG evts	LAr BG evts	10-yr Limit ($\times 10^{34}yr$)	Factor
1	300 kt	15%	N		6		8.2	2.7
1a	300 kt	30%	N		6		8.2	2.7
1b	300 kt	30%	Y		3		10.3	3.4
2				51 kt		0.51	2.7	0.9
2a				51 kt		0.51	2.7	0.9
2b				51 kt		0.51	2.7	0.9
3	200 kt	15%	N	14 kt	4	0.14	7.1	2.4
3a	200 kt	30%	N	14 kt	4	0.14	7.1	2.4
3b	200 kt	15%/30%	N/Y	14 kt	3	0.14	9.3	3.1
4	200 kt	15%	N	14 kt	4	0.14	7.1	2.4
4a	200 kt	30%	N	14 kt	4	0.14	7.1	2.4
4b	200 kt	15%/30%	N/Y	14 kt	3	0.14	9.3	3.1
5	100 kt	30%	Y	28 kt	1	0.28	6.2	2.1
6	100 kt	30%	Y	28 kt	1	0.28	6.2	2.1

TABLE XII. Summary of $p \to e^+\pi^0$ proton decay results of the reference configurations (see Table II for more details). The background number of events and 90% C.L. limit is calculated assuming a 10-year exposure of the tabulated mass. Efficiencies and background rates are documented in the narrative. For hybrid configurations, the limits from WC and LAr are combined. The factor is compared to the projected Super-K limit in 2030 of 3×10^{34} years.

Configuration	WC Mass	PMT	Gd	LAr Mass	WC BG evts	LAr BG evts	10-yr Limit ($\times 10^{34}yr$)	Factor
1	300 kt	15%	N		25		1.1	1.8
1a	300 kt	30%	N		20		1.5	2.6
1b	300 kt	30%	Y		10		2.0	3.4
2				51 kt		0.51	5.7	9.5
2a				42 kt		0.42	4.8	8.1
2b				42 kt		0.42	4.8	8.1
3	200 kt	15%	N	14 kt	17	0.14	2.7	4.5
3a	200 kt	30%	N	14 kt	13	0.14	3.0	5.0
3b	200 kt	15%/30%	N/Y	14 kt	12	0.14	3.4	5.6
4	200 kt	15%	N	14 kt	17	0.14	2.7	4.5
4a	200 kt	30%	N	14 kt	13	0.14	3.0	5.0
4b	200 kt	15%/30%	N/Y	14 kt	12	0.14	3.4	5.6
5	100 kt	30%	Y	28 kt	3.4	0.28	4.4	7.3
6	100 kt	30%	Y	28 kt	3.4	0.28	4.4	7.3

TABLE XIII. Summary of $p \to \nu K^+$ proton decay results of the reference configurations (see Table II for more details). The background number of events and 90% C.L. limit is calculated assuming a 10-year exposure of the tabulated mass. Efficiencies and background rates are documented in the narrative. For hybrid configurations, the limits from WC and LAr are combined. The factor is compared to the projected Super-K limit in 2030 of 0.6×10^{34} years.

V. SUPERNOVA BURST PHYSICS

A. Motivation and Scientific Impact of Future Measurements

A nearby core collapse supernova will provide a wealth of information via its neutrino signal (see [45, 46] for reviews). The neutrinos are emitted in a burst of a few tens of seconds duration, with about half in the first second. Energies are in the few tens of MeV range, and luminosity is divided roughly equally between flavors. The baseline model of core collapse was confirmed by the observation of 19 neutrino events in two water Cherenkov detectors for SN1987A in the Large Magellanic Cloud, 55 kpc away [47, 48]. An observed high-statistics core collapse neutrino signal will shed light on a variety of physics and astrophysics topics.

Core collapses are rare events: the expected rate is 2-3 per century in the Milky Way. As for the Homestake and Super-Kamiokande detectors, the large LBNE detector(s), once constructed, may operate for decades. On this time scale, there is a significant likelihood of a supernova exploding in our galaxy. In a 20-year run of an experiment, the probability of observing a collapse event is about 40%. The detection of the neutrino burst from such an event would dramatically expand the science reach of these detectors: from measuring the neutrino mass hierarchy and θ_{13} mixing angle, to observing the development of the explosion in the core of the star, to probing the equation of state of matter at nuclear densities, to constraining physics beyond the Standard Model. Each of these questions represents an important outstanding problem in modern physics, worthy of a separate, dedicated experiment. The possibility to target them all at once is very attractive, especially since it may come only at incremental cost to the project. The expected harvest of physics is rich enough that is essential to prepare to collect as much information as possible when a burst happens.

In contrast to the SN1987A, for which a few dozen neutrinos were observed, the detectors currently on the drawing board would register thousands or tens of thousands of interactions from the burst. The exact type of interactions depends on the detector technology: a water-Cherenkov detector would be primarily sensitive to the electron antineutrinos, while a liquid argon detector has an excellent sensitivity to electron neutrinos. In each case, the high event rates imply that it should be possible to measure not only the time-integrated spectra, but also their second-by-second evolution. This is the key reason behind the impressive physics potential of the planned detectors.

The interest in observationally establishing the supernova explosion mechanism comes from the key role supernova explosions play in the history of the universe. In fact, it would not be an exaggeration to say that the ancient supernovae have in a very large measure shaped our world. For example, modern simulations of galaxy formation cannot reproduce the structure of our galactic disk without taking the supernova feedback into account. Shock waves from ancient supernovae triggered further rounds of star formation. The iron in our blood was once synthesized inside a massive star and ejected in a supernova explosion.

For over half a century, researchers have been grappling to understand the physics of the explosion. The challenge of reconstructing the explosion mechanism from the light curves and the structure of the remnants is akin to reconstructing the cause of a plane crash from a debris field, without a black box. In fact, the supernova neutrinos are just like a black box: they record the information about the physical processes in the center of the explosion during the first several seconds, as it happens.

The explosion mechanism is thought to have three distinct stages: the collapse of the iron core, with the formation of the shock and its breakout through the neutrinosphere; the accretion phase, in which the shock temporarily stalls at the radius of about 200 km, while the material keeps raining in; and the cooling stage, in which the hot proto-neutron star loses its energy and trapped lepton number, while the reenergized shock expands to push out the rest of the star. All these stages are predicted to have distinct signatures in the neutrino signal. Thus, it should be possible to directly observe, for example, how long the shock is stalled. More exotic features of the collapse may be observable in the neutrino flux as well, such as possible transitions to quark matter or to a black hole. (An observation in conjunction with a gravitational wave detection would be especially interesting.)

To correctly interpret the neutrino signal, one needs to take into account neutrino flavor oscillations. Over the last decades, the oscillations have been firmly established in solar neutrinos and a variety of terrestrial sources, which means that including them in the supernova case is no longer optional. As it turns out, however, the physics of the oscillations in the supernova environment is much richer than in any of the cases measured to date. Neutrinos travel through the changing profile of the explosion, with stochastic density fluctuations behind the expanding shock. Their flavor states are also coupled due to their coherent scattering off each other: "collective" neutrino effects may be dramatic. The net result is a problem that requires supercomputers, as well as state-of-the-art analytical models, to understand.

The effort to understand this complicated evolution has its reward: the oscillation patterns come out very differently for the normal and inverted mass hierarchies. There are also several smoking gun signatures one can look for: for example, the expanding shock and turbulence leave a unique imprint in the neutrino signal. The supernova signal also has a very high sensitivity to values of θ_{13}, down to the levels inaccessible in any laboratory experiment. Additional

information on oscillation parameters, free of supernova model-dependence, will be available if Earth matter effects can be observed in detectors at different locations around the Earth [49, 50]. The observation of this potentially copious source of neutrinos will also allow limits on coupling to axions, large extra dimensions, and other exotic physics (*e.g.* [51, 52]).

Two comments need to be made at this point. First, it would be extremely valuable to detect both the neutrinos and antineutrinos with high statistics, as the oscillations occur very different in the two channels. In the neutrino channel the oscillation features are in general more pronounced, since the initial spectra of ν_e and ν_μ (ν_τ) are always significantly different. Second, the problem is truly multidisciplinary and the neutrino physics and astrophysics go hand-in-hand. One needs to model both, and the payout one gets is simultaneous for both fields. For instance, one learns the sign of the neutrino hierarchy, the value of θ_{13}, the speed at which the shock expands, and the density profile of the star, "all in one package". The better one understands the astrophysics, the better the quality of information about neutrino physics, and vice versa. Hence it is essential to gather as much high-quality information as possible, and to optimize ability to disentangle the flavor components of the flux.

As a final note, because the neutrinos emerge promptly after core collapse, in contrast to the electromagnetic radiation which must beat its way out of the stellar envelope, an observed neutrino signal can provide a prompt supernova alert [53, 54]. This will allow astronomers to find the supernova in early light turn-on stages, which may yield information about the progenitor (in turn important for understanding oscillations). The LBNE detector(s) should be designed to allow prompt alert capability.

Several other experiments sensitive to supernova neutrinos will be online over the next few decades [45, 55]. However one should not consider these to be "competition" for a supernova detection by LBNE: more experiments online during a supernova burst will only enhance the science yield from a supernova, and the ability to measure fluxes at different locations around the Earth will make the whole more than the sum of the parts [49].

B. Sensitivity of Reference Configurations

The predicted event rate from a supernova burst may be calculated by folding expected neutrino differential spectra with cross sections for the relevant channels, and with detector response. Although WCsim [56], the LBNE water Cherenkov simulation package, is nearly mature and can be used for some studies, LAr simulation packages are not yet ready for detailed studies of low energy response. Furthermore, neutrino interaction generators which properly handle products from interactions with nuclei in the tens-of-MeV range are currently lacking. For this reason, for this study we have chosen to do the event rate computation by using parameterized detector responses with a software package called SNOwGLoBES [57], written for this purpose, which makes use of GLoBES software [7]. This package employs only the front-end rate engine part of GLoBES, and not the oscillation sensitivity part. SNOwGLoBES takes as input fluxes, cross sections, "smearing matrices" and post-smearing efficiencies. The smearing matrices incorporate both interaction product spectra and detector response.

1. Supernova Neutrino Flux Models

We have examined several flux models. We assume fluxes at 10 kpc, which is just beyond the center of the Galaxy: event rates just scale as $1/D^2$, where D is the distance to the supernova.

We consider here the "Livermore" model [58], and the "GKVM" model [59]. The Livermore model was digitized using Fig. 1 of reference [58], assuming spectra given by Eqn. 10 of that reference. The model is somewhat out of date; however it is one of the few fluxes available for the full burst time interval, and it appears frequently in the literature, so it is considered for comparison purposes. The GKVM flux includes shock and collective effects. We consider also "Duan" fluxes [60, 61] for which different oscillation hypotheses have been applied: see Section V B 4. The Duan flux represents only a single late time slice of the supernova burst and not the full flux.

2. Event Rates in Water

Detector response assumptions for water are described in Appendix B.

The cross sections for relevant interactions in water are shown in Fig. 39. Some of these cross sections– in particular, inverse beta decay $\bar{\nu}_e + p \to e^+ + n$ (IBD) and elastic scattering (ES) of neutrinos on electrons $\nu_{e,x} + e^- \to \nu_{e,x} + e^-$ (both NC and CC) are known to few percent or better level. In contrast, others have relatively large uncertainties, and have never been measured in the few tens-of-MeV energy range.
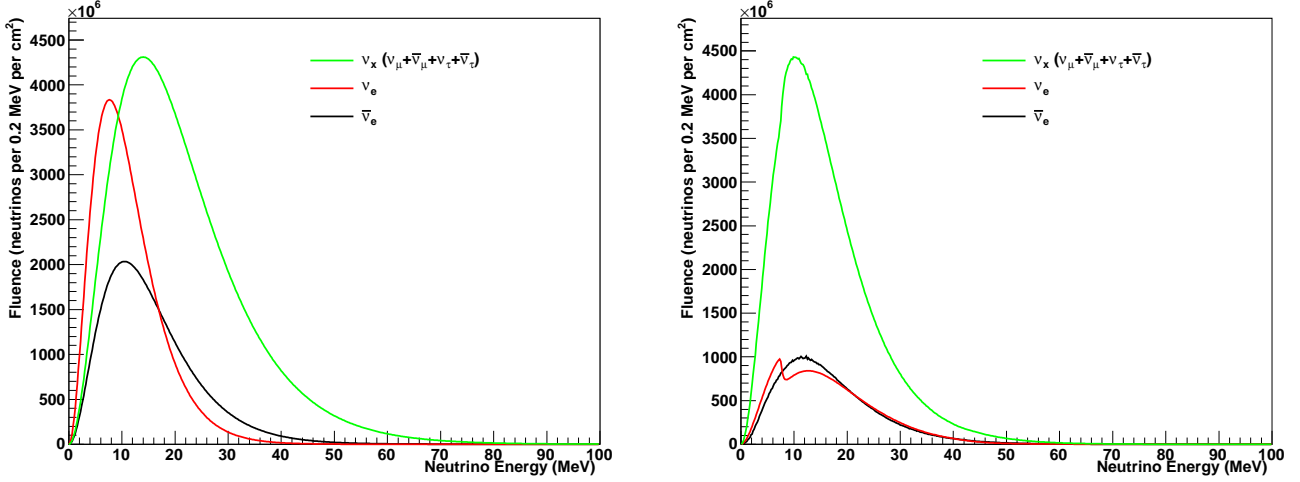
FIG. 38. Flavor components of the fluxes used for this study: red is ν_e, black is $\bar{\nu}_e$ and green is the sum of all other flavors. The left plot shows the Livermore model, integrated from $t = 0$ to $t = 14$ seconds. The right plot shows the GKVM model, integrated over 10 seconds.
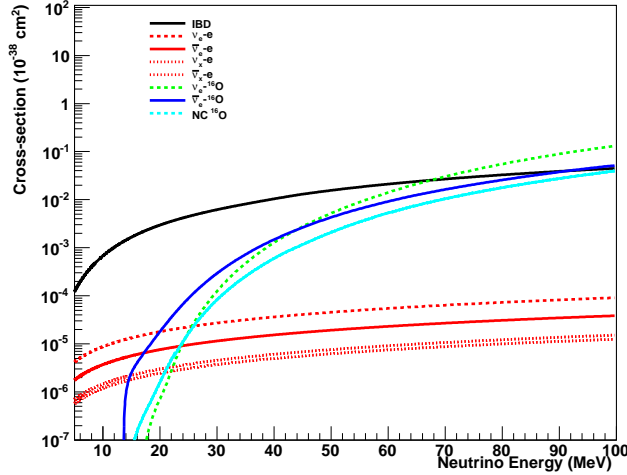
FIG. 39. Cross sections for relevant processes in water.

In particular, interactions on oxygen, $\nu_e +^{16} O \rightarrow e^- +^{16} F$, $\bar{\nu}_e +^{16} O \rightarrow e^+ +^{16} N$, have diverse final states, including ejected nucleons and deexcitation gammas. For this study, we are considering only the lepton in the final state response for the CC interactions, taking into account the energy threshold. For the NC interaction with ^{16}O, $\nu_x +^{16} O \rightarrow \nu_x +^{16} O^*$, we are using a simplified model of the resulting deexcitation gammas by assuming relative final energy levels according to reference [62]. Because this reference does not provide differential final state information, we assume the distribution of these levels is independent of neutrino energy (which is an incorrect assumption, but probably not a terrible approximation). The resulting gamma cascade was simulated using relative probabilities of the transitions for a given excited state; the resulting gamma spectrum was then run through WCsim detector simulation. We found rather poor efficiency for detecting these gammas, in contrast to the results in reference [63], due to the fact that gammas frequently scatter electrons below Compton threshold.

Figure 40 shows the resulting differential energy spectra for the different channels. The plot on the left shows the interaction rates as a function of neutrino energy. The plot on the right shows the distribution of observed

event energies in the detector. Table XIV shows the breakdown of detected event channels, for two different specific supernova models.
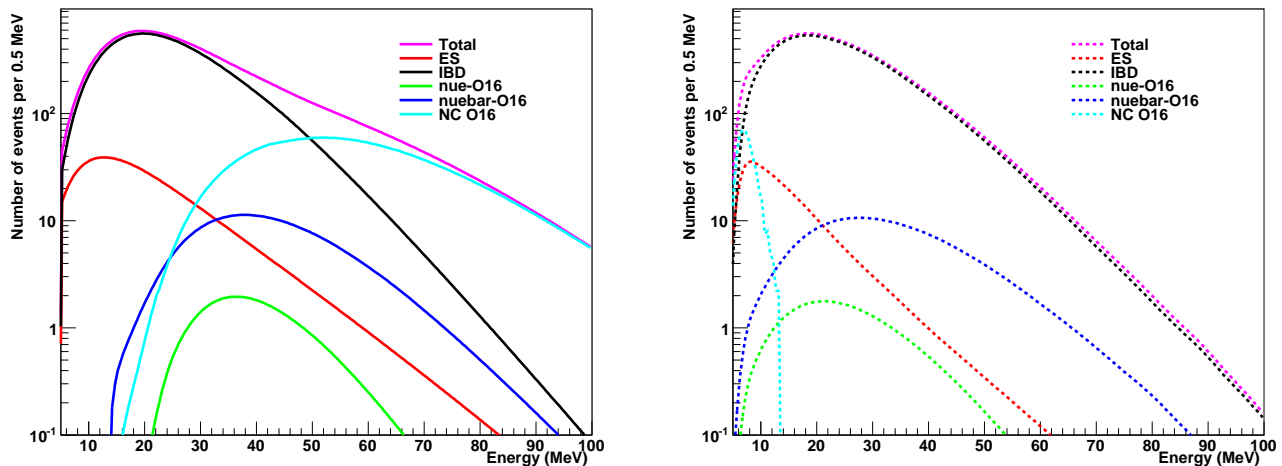
FIG. 40. Event rates in water, for the Livermore model and 30% coverage (events per 0.5 MeV).

Channel	Events, Livermore model	Events, GKVM model
$\bar{\nu}_e + p \to e^+ + n$	27116	16210
$\nu_x + e^- \to \nu_x + e^-$	868	534
$\nu_e + {}^{16}O \to e^- + {}^{16}F$	88	378
$\bar{\nu}_e + {}^{16}O \to e^+ + {}^{16}N$	700	490
$\nu_x + {}^{16}O \to \nu_x + {}^{16}O^*$	513	124
Total	29284	17738

TABLE XIV. Event rates for different models in 100 kt of water, for the 30% coverage reference configuration.

These results show that IBD is overwhelmingly dominant: water Cherenkov is primarily sensitive to the $\bar{\nu}_e$ component of the flux. However there are non-negligible contributions from other channels. IBD positrons are emitted nearly isotropically; however, because ES and CC interactions on oxygen have anisotropic angular distributions, one may be able to use the reconstructed Cherenkov angular information to help disentangle the flavor components (see Section V B 5. (Or, if the direction of the supernova is unknown, which is likely at early times, the angular information can be used to point to it [64, 65].)

We also note that different flux models can give substantially different event rates. In particular, because of the thresholds of the ^{16}O interactions, the rates of the CC interactions on oxygen are quite sensitive to the ν_e and $\bar{\nu}_e$ spectra.

Figure 41 shows the difference in observed event rates between the 15% and 30% PMT coverage reference configurations. For the 15% configuration, one loses about 9% of self-triggered events below ~10 MeV. The loss includes most of the NC excitation events. (We note that clever triggering may mitigate this loss.)

The addition of Gd to a water detector will not substantially change event rates, but will enhance ability to determine the flavor composition of an observed signal by allowing tagging of IBD events: see Section V B 5 (although note that interactions on ^{16}O may produce ejected neutrons as well).

Because all of the supernova burst events arrive in a time window of a few tens of seconds, background is a much less serious issue than for relic supernova neutrino searches. For water detectors, it should be nearly negligible for Galactic bursts. To estimate it, we scale from Super-K [66, 67]: the rate in 22.5 kt with loose selection cuts is about 3×10^{-2} Hz at a 7 MeV threshold. Scaling by mass, this gives only about 4 background events in a 30 second burst. For a distant supernova search [75], background becomes more important and limits the distance sensitivity.
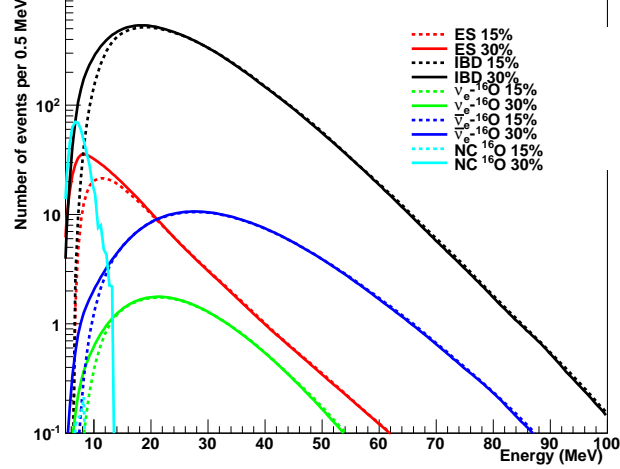
FIG. 41. Comparison of event rates for 15% and 30% PMT coverage configurations in 100 kt of water.

3. Event Rates in Argon

Detector response assumptions for LAr are described in Appendix B.

The cross sections for interactions in argon [68, 69], are shown in Fig. 42. The uncertainties for the recent calculations are at around the 10-20% level. For the CC channels we have included energy deposition of the leading lepton; in the detector response, we also incorporate additional visible energy from deexcitation gammas (these gammas may also possibly help to tag the ν_e or $\bar{\nu}_e$ channels, although we made no assumptions about such tagging). We found no information in the literature about resulting excited levels for the NC interactions, so for the moment this channel is not included in the study, even though event rates may be fairly large.
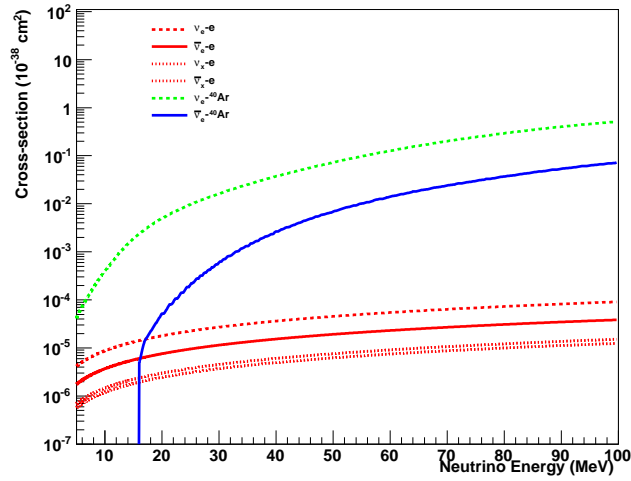
FIG. 42. Cross sections for relevant processes in argon.

Figure 43 shows resulting interaction rates as a function of neutrino energy (left) and distribution of observed energies (right) in argon, for the Livermore model. Table XV gives a table of event rates for two models. Note here that primary sensitivity is to the ν_e component for argon.

For liquid argon, we have little information about backgrounds at the time of this writing, although again we can
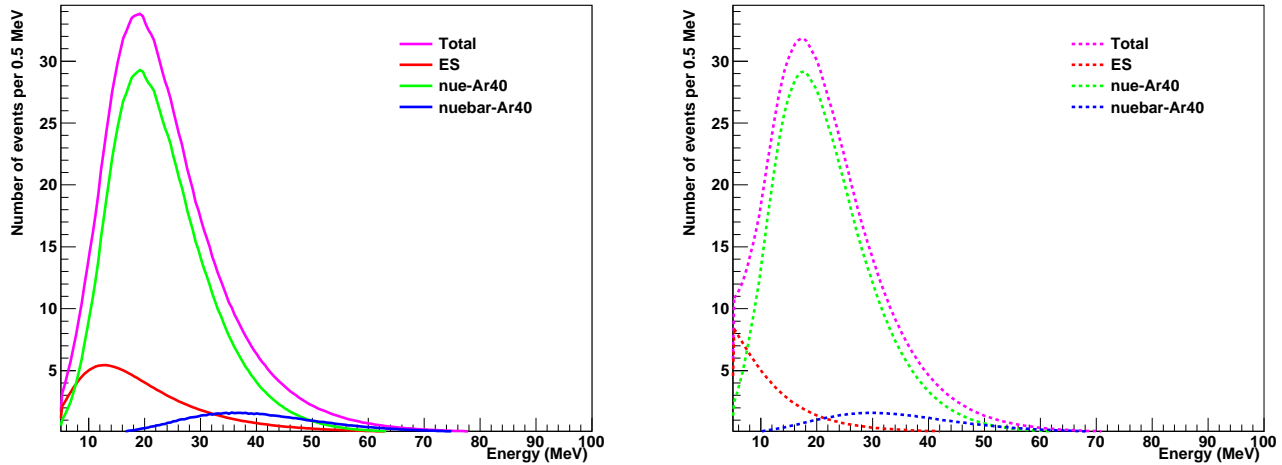
FIG. 43. Event rates in 17 kt of argon (events per 0.5 MeV).

Channel	Events, Livermore model	Events, GKVM model
$\nu_e + {}^{40}\mathrm{Ar} \rightarrow e^- + {}^{40}\mathrm{K}^*$	1154	1424
$\bar{\nu}_e + {}^{40}\mathrm{Ar} \rightarrow e^+ + {}^{40}\mathrm{Cl}^*$	97	67
$\nu_x + e^- \rightarrow \nu_x + e^-$	148	89
Total	1397	1580

TABLE XV. Event rates for different models in 17 kt of LAr.

assume that they will be less of an issue for burst than for relic supernova neutrinos; furthermore backgrounds will be well known and can be statistically subtracted from a burst signal. We can assume that cosmic ray muons will be easily identifiable as long tracks, and Michel electrons can be tagged in association with muons. Backgrounds for supernova neutrinos in the range from 5-100 MeV will include events from radioactive products associated with muon spallation (some of which can be substantially delayed with respect to their parent muon). The distribution of spallation products in argon is currently unknown; however, most radioactive decays will deposit less than about 10 MeV. At the 300 ft level, the muon rate in one 17 kt module will be about 800 Hz; at 800 ft it is about 200 Hz. Assuming that the fraction of muons producing radioisotopes which decay in the supernova neutrino range of interest (and which cannot be vetoed using space and time correlation information) is less than ~ 0.01, we can assume that this background will not be overwhelming during a nearby supernova burst, even at 300 ft.

4. Comparing Oscillation Scenarios

As described in the introduction to this section, there will likely be significant and observable imprints of oscillation parameters on the observed spectrum of burst supernova neutrino events. For oscillation sensitivity, ability to measure and tag the different flavor components of the spectrum is essential.

Figure 44 compares event rates for normal and inverted hierarchy, for a particular spectrum (a late time slice, not the full flux) provided by Huaiyu Duan [60]. While information about the hierarchy is clearly present in the water spectrum, which is mostly $\bar{\nu}_e$, the difference between the hierarchies is most dramatic in the observed mostly-ν_e argon spectrum.

We have attempted a simple quantification of the relative sensitivity of the different single detector configurations to mass hierarchy. Because fluxes with oscillation signatures are at this time only available representing a fraction of the total flux, we cannot evaluate the full statistical sensitivity. However we have done the following: we have determined the minimum statistics for which normal hierarchy is distinguishable from inverted hierarchy, for the Duan multi-angle spectrum [60]. For water Cherenkov (either 15% or 30% coverage), approximately 3500 events are required to distinguish the hierarchy at 3σ; 15% and 30% PMT coverage configurations are equally sensitive, because the differences occur at relatively high energy. For LAr, about 550 events are required.
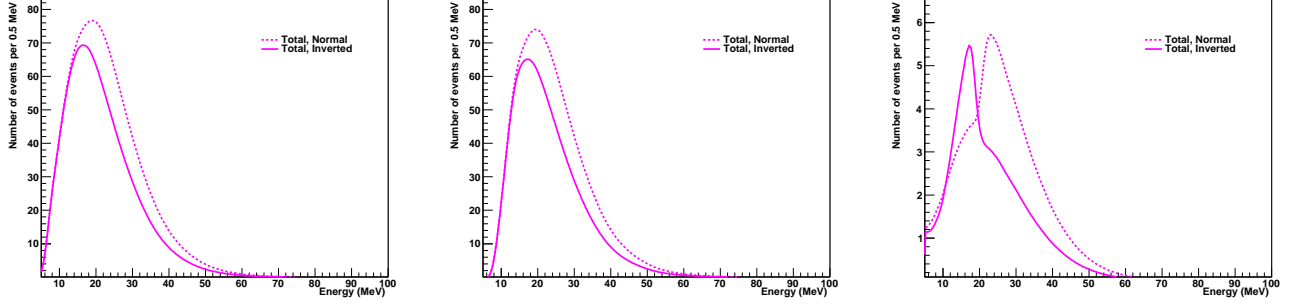
FIG. 44. Comparison of total event rates for normal and inverted hierarchy, for the Duan flux (a late time slice, not the full flux) , for WC 30% (left), WC 15% (center) and 17 kt LAr (right) configurations, in events per 0.5 MeV.
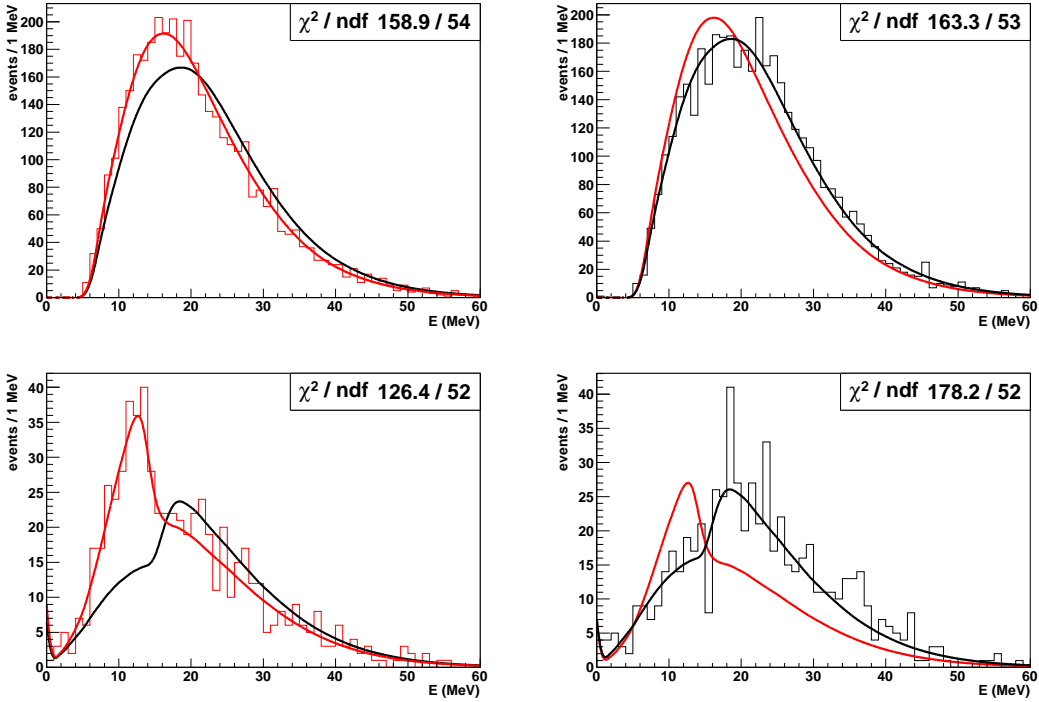
FIG. 45. Example fits to the expected spectral shapes for normal and inverted hierarchies for the Duan model. Top plots: 100 kt water, 30% PMT coverage, assuming 4000 events. Bottom plots: 17 kt argon, assuming 630 events observed. Left plots: true hierarchy is inverted. Right plots: true hierarchy is normal. The χ^2/dof is given for the fit to the "wrong" hierarchy.

Figure 45 shows examples of observed spectra for the different configurations and hierarchies, for statistics near distinguishability. Since number of events scales as inverse square of the distance to the supernova, we convert this to a *relative* figure of merit based on the distance at which hierarchy is distinguishable: assigning a value of 1 to the distance sensitivity of one 17 kt module of LAr, we assign relative distance sensitivity of other single-detector configurations according to $D_{\max}$(detector configuration)$/D_{\max}$(17 kt LAr). The results are reported in the last column of Table XVI.

Although this study was done for one specific model, the relative evaluation of the configurations based on statistical reach can be considered relatively robust.

5. Flavor Tagging

In order to extract interesting physics from a supernova burst signal, it is desirable to be able to determine the flavor content as a function of energy and time. In practice, given a real supernova burst signal, one would perform a fit to energy, angle and time distributions, making use of all available information, in order to determine flavor and interaction channel content. At this point we have not yet developed the tools for such a comprehensive analysis, so we focus on a few possible signatures which could be exploited to help disentangle flavor content of a supernova burst signal in a WC detector. The statistics considered in these studies are for a 100 kt WC detector with 30% PMT coverage.

Neutron Tagging: In a water detector, the bulk of detected events will be IBD, $\bar{\nu}_e + p \rightarrow e^+ + n$. If gadolinium (Gd) is added to a water Cherenkov detector, we expect some fraction of IBD events to be tagged using neutron capture on Gd, which produces about 4.3 MeV of energy in the detector, on a ~ 20 μs timescale [83]. The efficiency of tagging is expected to be about 67% [84]. The tagged sample will represent a highly enriched $\bar{\nu}_e$ sample. Events with no neutron tag will be enriched in flavors other than $\bar{\nu}_e$, and in principle, the IBD contribution can be subtracted from the overall signal using the tagged rates. [Note that with sufficient PMT coverage it may be possible to use 2.2 MeV gammas from neutron capture on protons even in the absence of Gd doping, but the efficiency would be lower.]

To get a general idea of the value of neutron tagging of $\bar{\nu}_e$ we have done a simple study: we looked at flavor composition for tagged and untagged events. We assume that 67% of the true IBD events will be tagged; we also assume that no events without a neutron will be falsely tagged as having a neutron (the false tagging rate should be $\sim 10^{-4}$ according to reference [84]). We also take into account CC and NC reactions of neutrinos on ^{16}O, for which some final states have neutrons. To estimate this contribution we use tables II, III and IV from reference [62] and (in absence of differential final state information) we assume that the relative fractions of final states with neutrons are independent of neutrino energy.

Figure 46 shows the contributions of the different interaction channels for tagged and untagged events, for the GKVM flux. The neutron-tagged event rate is a nearly-pure IBD sample. The untagged event rate has contributions from elastic scattering (ES), and from CC and NC interactions on ^{16}O, but is dominated by untagged IBD.
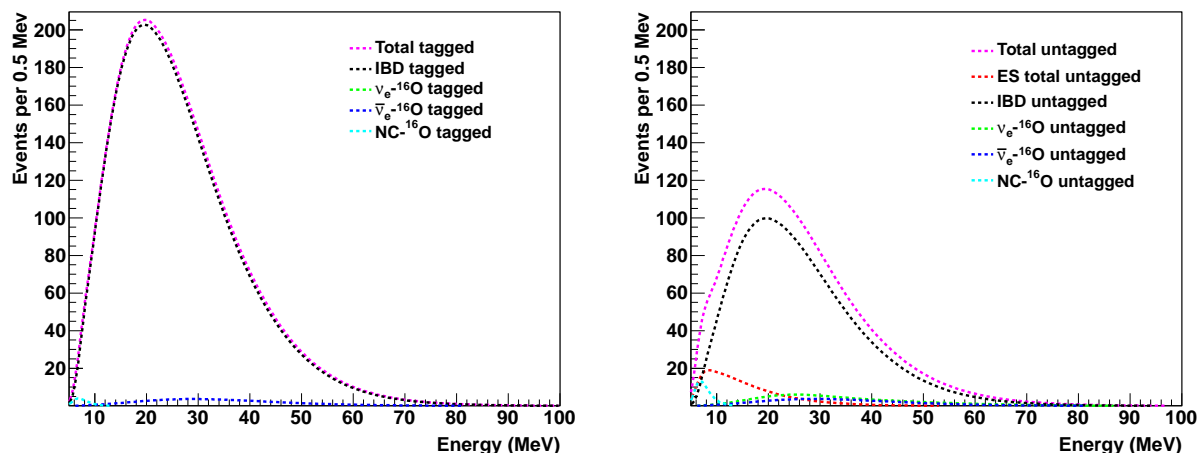
FIG. 46. Total events in WC showing contribution from the different interaction channels, for neutron-tagged (left) and untagged (right) events.

Figure 47 shows the contributions of the different neutrino flavors for tagged and untagged events. The tagged sample is nearly pure $\bar{\nu}_e$. The untagged sample has contributions from other flavors, and large contamination from untagged IBD $\bar{\nu}_e$.

Given a burst neutrino signal, one would estimate flavor composition using the known tagging fraction. The tagged sample represents a $\bar{\nu}_e$-enriched sample (in fact, it is a nearly pure one). To estimate non-$\bar{\nu}_e$ (*i.e.* $\nu_{e,x}$; x refers to any non-electron flavor) content in the untagged sample (which has more ν_e than any other flavor) one can subtract the IBD contribution measured using the tagged rate. Figure 48 shows plots with error bars of estimated $\bar{\nu}_e$ flux and $\nu_{e,x}$ flux.

Tagging here clearly allows selection of a clean $\bar{\nu}_e$ sample; however the $\nu_{e,x}$-enriched sample suffers significant contamination, and quality of determination of non-$\bar{\nu}_e$ component of the flux will be dependent on tagging fraction
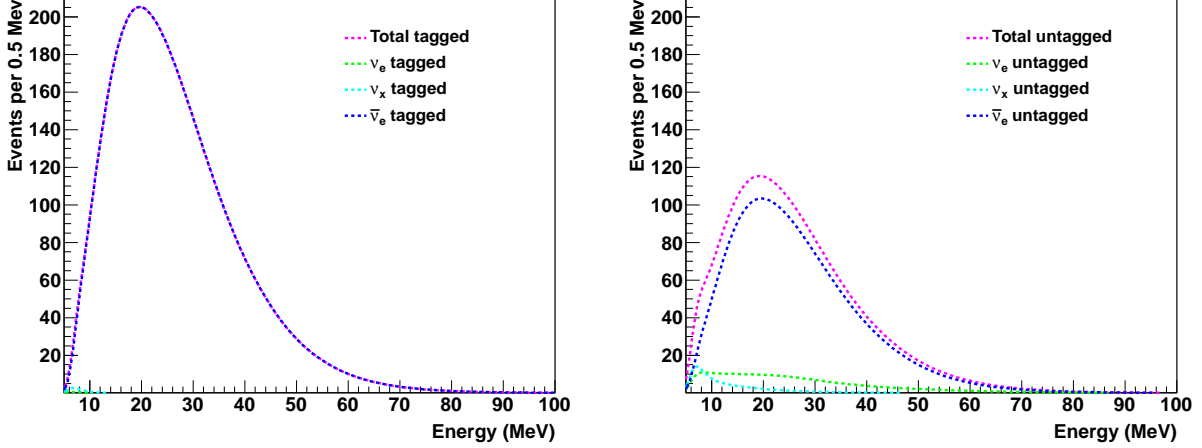
FIG. 47. Total events in WC showing contribution from the different flavors, for neutron-tagged (left) and untagged (right).
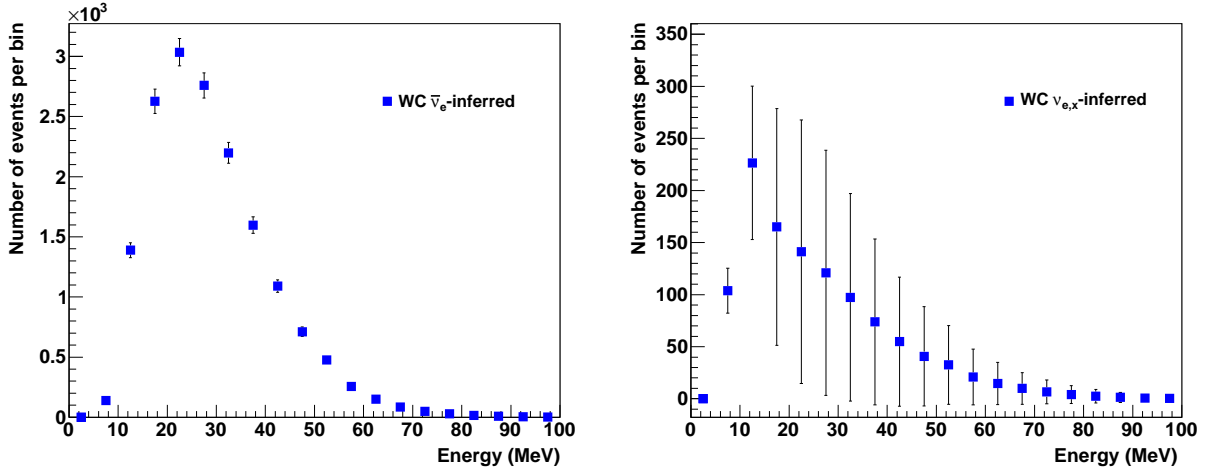
FIG. 48. Inferred $\bar{\nu}_e$ (left) and $\nu_{e,x}$ (right) signals using neutron-tagging information, with uncertainties, for the GKVM flux.

uncertainty (as well as on relative size of that component). The mean number of $\nu_{e,x}$ events must be greater than the uncertainty on the number of untagged $\bar{\nu}_e$ events for the non-$\bar{\nu}_e$ component to be measurable. Figure 48 clearly shows that given our assumptions, it will be possible to determine the size of the $\nu_{e,x}$ component for the GKVM flux at 10 kpc. However the untagged sample represents a mix of flavors, and the spectral information for any given flavor is not cleanly measured.

Selection of Elastic Scattering Events: Another potential method for selecting a flavor-enhanced sample in WC is to use the directionality of the neutrino-electron scattering signal: electrons are scattered away from the supernova. (This anisotropy is likely the best method for pointing to the supernova [64, 65].) The ES sample is enriched in ν_e and ν_x relative to $\bar{\nu}_e$. The relative amounts of the different flavors are sensitive to the neutrino spectrum, and the fractions vary substantially from model to model.

We estimate the quality of a flavor-enriched ES sample by assuming that a fraction $\epsilon_s = 0.66$ of ES events will have $\cos\theta > 0.9$, where θ is the reconstructed angle of the scattered event [64]. Such a cut will reduce isotropic background by 95%. Figure 49 shows the interaction and flavor compositions of the "ES-enriched" sample selected by an angular cut, for the GKVM model. The non-ES background can be determined by counting events outside of the angular cut window (where we assume for the purpose of determining statistical uncertainty on the ES background subtraction that non-ES events have isotropic background, although that is not completely true– IBD events have a weak asymmetry, and interactions on ^{16}O have a backwards asymmetry). Figure 50 shows the background-subtracted

ES-enriched signal, with statistical error bars, for the GKVM flux.
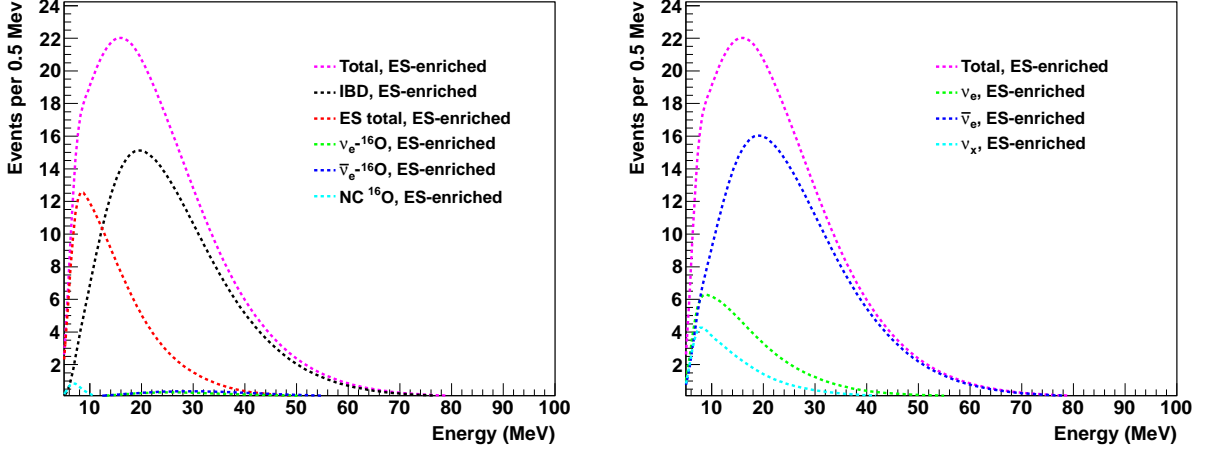
FIG. 49. For the GKVM model, interaction (left) and flavor (right) composition of the ES-enriched sample.
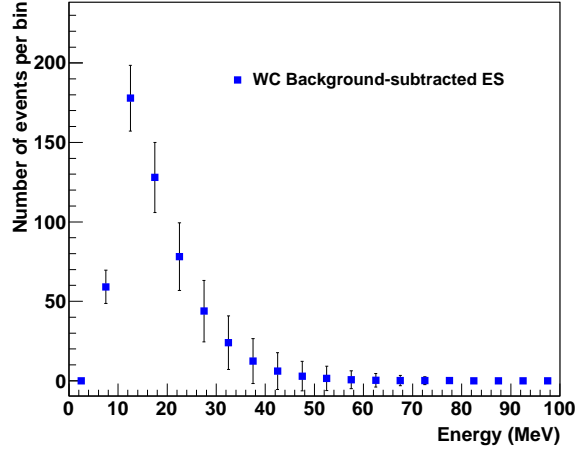
FIG. 50. Background-subtracted ES signal in 5 MeV bins, for the GKVM flux. Error bars are statistical.

Combining Neutron Tagging and Angular Information: It should also be possible to combine angular selection with neutron-tagging to further enhance flavor information in the ES signal. First, because ES events do not have neutrons, the isotropic background in this sample can be reduced by selecting only untagged events.

Second, one can use the tagged sample to determine the $\bar{\nu}_e$ flux, and then subtract the $\bar{\nu}_e$ component from the ES sample to determine the $\nu_{e,x}$ content. Going one step farther: if there were an independent measurement of the ν_e flux from LAr (or some other detector), one could in principle determine the ν_x flux, of considerable interest in itself. Figure 51 summarizes the total ES, $\nu_{e,xES}$, and ν_{xES} scattering rates for the GKVM flux, assuming neutron-tagging and angular selection.

C. Next Steps

We have made preliminary estimates of event rates and simple "anecdotal" evidence of observability of oscillation features for a supernova burst signal, as well as simple studies of information available from flavor tagging. There are several improvements and further studies in progress.
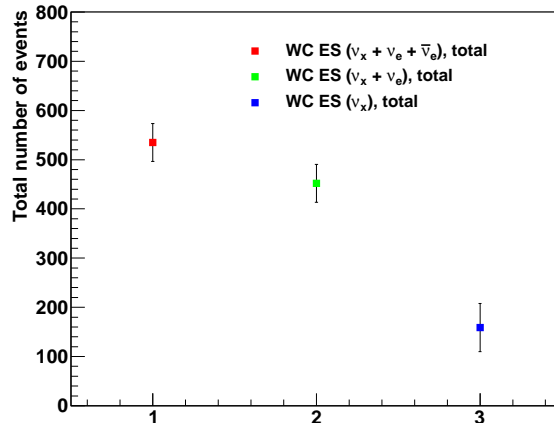
FIG. 51. Inferred flavor components of a WC ES signal, assuming neutron-tagging, angular selection, and a ν_e measurement from LAr. 1: total ES signal from all flavors; 2: non-$\bar{\nu}_e$ flavors; 3: ν_x flavor.

- We will refine the detector response parametrization as simulations improve.

- The information on products (especially deexcitation gammas and ejected nucleons) of interactions on ^{16}O and ^{40}Ar is quite sparse in the literature. We will work on improving our modeling of these interactions. Other isotopes of oxygen and argon, although making a small contribution to the total signal, should also be considered. We will also study the effect of systematic uncertainties (*e.g.* on the cross sections) on the physics sensitivity.

- Angular distributions of products will provide valuable information. ES and CC interactions on oxygen have pronounced anisotropy (IBD is weakly anisotropic). These anisotropies can be exploited for pointing to the core collapse [64, 65] (for an early alert, or to aid in finding the remnant in the case of weak supernova signal), for disentangling flavor components, and for making more precise measurements of the neutrino energy spectrum. We will evaluate the angular distribution of the expected signal.

- In practice, given a burst signal, one would perform a multiparameter fit to all available energy, angle and flavor information in order to extract supernova and oscillation physics. We will develop such an analysis and explore the physics sensitivity given different models.

- Sensitivity to numerous other physics features will be explored. For example, matter oscillations in the Earth may provide additional information about neutrino oscillation parameters. We will explore the potential to observe physics signatures, possibly in conjunction with other experiments likely to be running over the next decades. Other examples include: observability of the breakout peak, the accretion-to-cooling transition, and transition to a black hole.

- At the moment we have very little information on the nature of spallation background in argon, on the potential quality of signal tagging in LAr using gammas, and on background reduction in an LAr detector. These issues are critical for evaluation of relic supernova neutrino sensitivity, and they may also be relevant for burst supernova neutrinos, especially for low-statistics bursts for core collapses beyond 10 kpc. We will continue to investigate these issues.

D. Conclusions

Table XVI shows overall evaluation of the different reference configurations.

Sensitivity to physics in a supernova burst is good for any of the configurations; it improves with larger active mass. The 15% coverage gives somewhat degraded performance with respect to the 30% coverage: about 10% of the total number of events are lost. All of the loss is below 10 MeV and includes a very large fraction of NC ^{16}O excitation events. The addition of Gd will improve flavor tagging. A combination of different detector types offers the best physics sensitivity, because of ability to distinguish different flavor components of the supernova burst flux.

Configuration Number	Events in water at 10 kpc	Events in argon at 10 kpc	Relative hierarchy sensitivity
1	60,000	N/A	2.6
1a	66,000	N/A	2.6
1b	66,000; enhanced flavor ID	N/A	2.6+
2	N/A	4500	1.7
2a	N/A	4500	1.7
2b	N/A	4500	1.7
3	40,000	1500	2.1+
3a	44,000	1500	2.1+
3b	44,000; enhanced flavor ID	1500	2.1++
4	40,000	1500	2.1+
4a	44,000	1500	2.1+
4b	44,000; enhanced flavor ID	1500	2.1++
5	22,000; enhanced flavor ID	3000	1.5++
6	22,000; enhanced flavor ID	3000	1.5++

TABLE XVI. Summary of supernova burst capabilities of the reference configurations (see Table II for more details). See text for explanation of the last column, which refers to a specific model. A "+" is included if Gd is present to enhance flavor tagging, and "++" indicates a configuration in which both LAr and WC are running simultaneously.

VI.   SUPERNOVA RELIC NEUTRINOS

All of the neutrinos which have ever been emitted by every supernova since the onset of stellar formation suffuse the universe. These supernova relic neutrinos [SRN], also known as the diffuse supernova neutrino background [DSNB], have not yet been observed but they may be just of reach of the current generation of operating detectors. In this section we will see that with the appropriate technology the relic neutrinos can play a unique and powerful role in the physics output that can be expected from LBNE.

A.   Motivation and Scientific Impact of Future Measurements

1.   Motivation for the Measurement

Supernova neutrinos carry unique information about one of the most dramatic processes in the stellar life-cycle, a process responsible for the production and dispersal of all the heavy elements (i.e., just about everything above helium) in the universe, and therefore a process absolutely essential not only to the look and feel of the universe as we know it, but also to life itself.

As a gauge of the level of interest in these particular particles, it is worth noting that, based upon the world sample of twenty or so neutrinos detected from SN1987A, there has on average been a paper published once every ten days... for the last twenty-three years. After a quarter of a century, this handful of events remain the only recorded neutrinos known to have originated from a more distant source than our own Sun (by an easily-remembered factor of 10^{10}).

Unfortunately, galactic supernovas are relatively rare, occurring somewhere between once and four times a century (Section V). However, while nearby supernovas are rare, supernovas themselves are not – there are thousands of neutrino-producing explosions every hour in the universe as a whole. There is a small but dedicated industry devoted to trying to predict the flux of these relic supernova neutrinos here on Earth; a representative selection of modeled spectra [70–77] are shown in Fig. 52, along with some of the key physics backgrounds one might face.
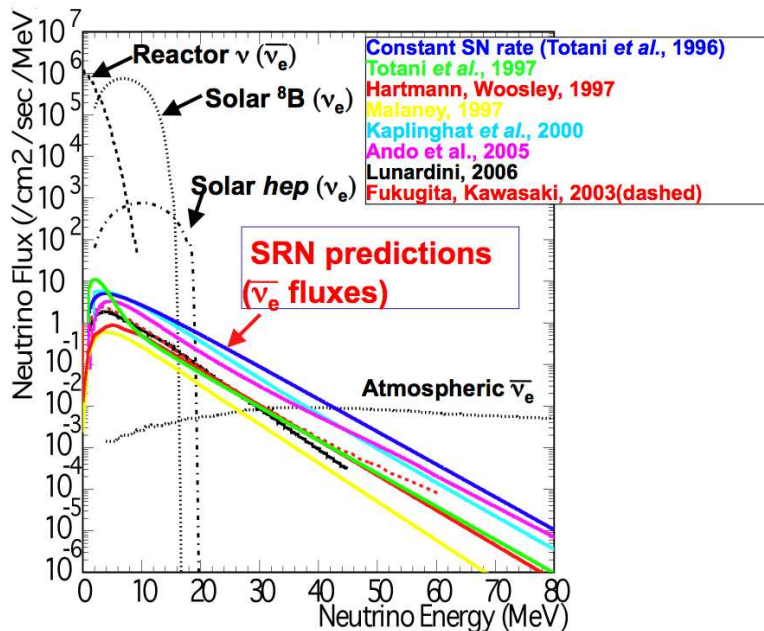
FIG. 52. A variety of predicted SRN spectra and some key neutrino backgrounds.

So, in addition to being the first to measure this new flux of neutrinos, what scientific benefits would such a measurement bring? Aside from any potential surprises, which we have often encountered when peering into a new corner of the neutrino sector, measuring the relics can shed light on the following topics:

- Understanding supernovas, central to understanding many aspects of the present physical universe, requires the detection of their neutrino emissions. More supernova neutrino data is strongly needed, but galactic supernova explosions are rare; the SRN will provide a continuous stream of input to theoretical and computational models.

- The shape of the SRN spectrum will provide a test of the uniformity of neutrino emissions in core-collapse supernovas, determining both the total and average neutrino energy emitted.

- Was SN1987A a "normal" explosion or not? The sparse, 23-year-old data concerning a single neutrino burst cannot say, but the SRN data can (see Fig. 53).

- How common are optically dark explosions? No one knows. Comparing the SRN rate with optical data of distant supernovas can tell us, and is probably the only way to get this information (see Fig. 54).

Contrary to what is often stated, measuring the SRN flux will not uniquely determine the cosmic core-collapse (and hence star formation) rate, a key factor in cosmology, stellar evolution, and nucleosynthesis. Rather, the SRN measurement will be a new and independent probe of this rate, which will be well constrained by current and near-future astronomical observations [78].
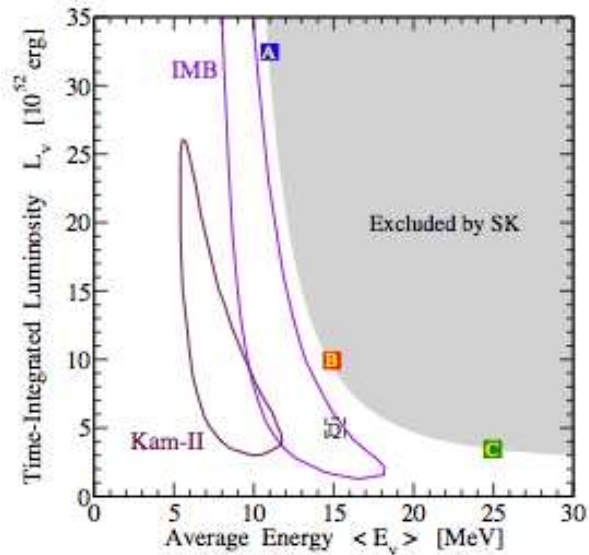
FIG. 53. The parameter space of total supernova neutrino luminosity vs. average energy showing the approximate allowed regions from the SN1987A data, along with the region excluded by the 2003 Super–K SRN limit.

2. Predicting the Relic Flux

Predicting what the flux of neutrinos generated by these distant explosions will look like is a complex and subtle business, and the details of the calculations are well beyond the scope of this brief section. However, there are two extensive reviews of the subject [79, 80] from which many of this SRN section's theoretical plots and event rate predictions are drawn.

That being said, here are the basic components that necessarily must go into any such calculation:

1. The initial supernova collapse model, and its neutrino emission. Computational models have famously resisted producing robust, realistic explosions, so there is no one "standard" explosion model as of yet. These models encode both the total and average neutrino energies, and are responsible for much of the variation seen in predicted relic rates.

2. The oscillations and self-interactions of the neutrinos as they exit the dying star. This determines the flavor mix which will eventually reach Earth, a key component in predicting various detectors' responses. There is still considerable uncertainty in the precise blend of flavors which will arrive at Earth, which is also reflected in the width of the predicted rates for each detector configuration.

3. The stellar core collapse rate, which is expected to be proportional to the star formation rate. This is now determined from astronomical observations to $\pm 40\%$, and the next generation of synoptic sky surveys are expected to narrow this uncertainty to the 5% level within the next few years. This contributes an overall (though steadily shrinking) normalization uncertainty to the predictions.
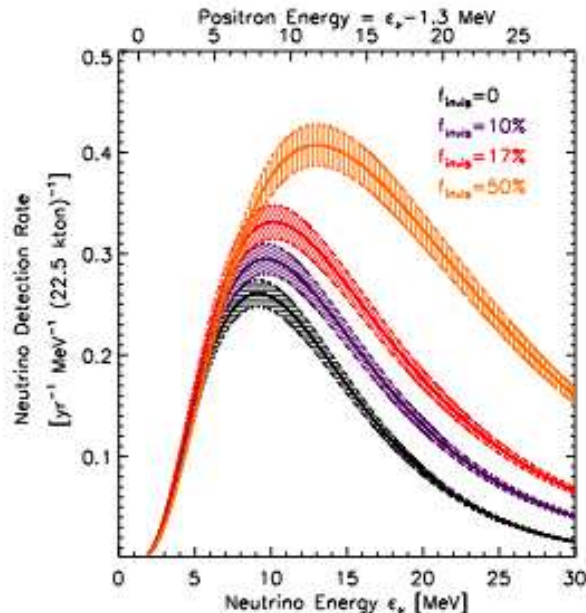
FIG. 54. Expected SRN spectra in 22.5 kt of water Cherenkov volume per year as a function of different invisible supernova fractions within the range currently allowed. The width of the bands represents the expected state of knowledge (from upcoming supernova survey missions) of the stellar core collapse rate by the time LBNE turns on, about a 5% uncertainty.

Once the relic flux and spectrum at the Earth is predicted, then the rate of neutrino interactions in each detector must be calculated using the best available knowledge of the relevant cross sections. Finally, performance characteristics of the individual detectors and their locations on Earth must be taken into account, such that backgrounds can be estimated and appropriate energy windows for relic detection defined.

What all this boils down to is an uncertainty on the predicted relic rates of about a factor of 12 for a conventional (SK-style) water Cherenkov detector, and about a factor of six for a gadolinium-loaded water Cherenkov detector (described in more detail later) due to its widened energy window covering more of the competing models' spectral ranges.

While its energy window is quite similar to that of a regular water Cherenkov detector, a liquid argon detector has an uncertainty in the predicted relic rate of only about a factor of seven. This is due to more solid predictions for the survival probability at Earth of the ν_e seen in argon as opposed to the $\overline{\nu}_e$ seen in water.

3. Current and Future Experimental Status

The only significant competition for relic neutrino discovery comes from the Super–Kamiokande experiment [generally referred to as Super–K or just SK], which is located at a depth of 3300 feet in an old zinc mine near Kamioka, Japan. As a 50 kiloton (22.5 kt fiducial) water Cherenkov detector, Super–K's sensitivity to the SRN is strictly through the inverse beta reaction, $\overline{\nu}_e + p \rightarrow e^+ + n$. The outgoing positron makes Cherenkov light which can be detected (note that WC detectors generally cannot differentiate between matter and antimatter), while the neutron is eventually invisibly absorbed by a hydrogen nucleus, forming a deuteron.

In 2003, Super–Kamiokande published the results of a search for the supernova relic neutrinos [81]. However, as seen in Fig. 55 this study was strongly background limited, especially by Michel decay electrons from sub-Cherenkov threshold muons produced by atmospheric neutrino interactions in the detector. The low energy cutoff of the analysis was imposed not due to elastically scattered electrons from solar neutrinos, which SK can identify by their angular correlation with the direction back to the Sun, but due to by the many cosmic ray muon-induced spallation events below 19 MeV which unfortunately swamped any possible DSNB signal in that most likely energy range. This plot is the result of 1496 days of data, or about 92 kt-years. It took just over five years of continuous data-taking (April 1996 through July 2001) to collect 4.1 years of usable data for the relic analysis, a rather typical real-world duty cycle of 80%.
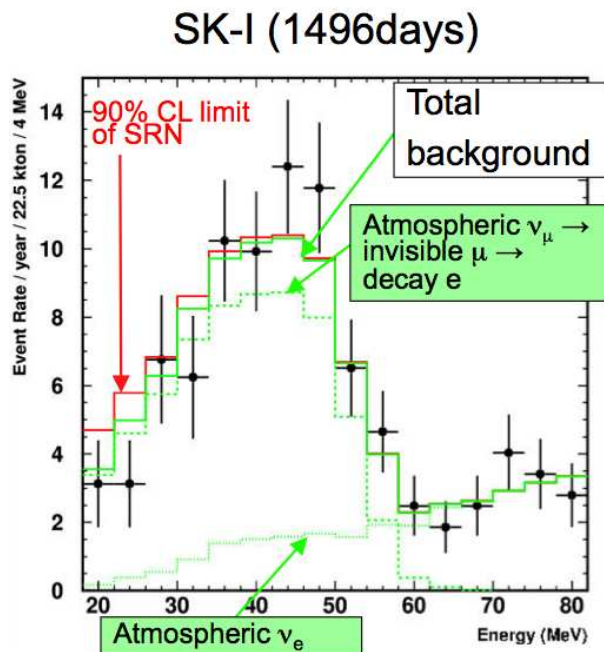
FIG. 55. The data (points) from the 2003 Super–Kamiokande relic search. The dashed histogram peak centered around 42 MeV is that expected from decays of sub-Cherenkov muons into electrons, while the dotted line slanting down from right to left is that expected to be produced by atmospheric electron neutrinos and antineutrinos. The (green) lower solid line is the sum of these two backgrounds, while the (red) upper solid line represents the 90% upper limit on potential excess caused by the relic neutrinos.

Consequently, this Super–K study could see no statistically significant excess of events and therefore was only able to set the world's most stringent upper limits on the relic flux: < 1.2 $\bar{\nu}_e$ cm^{-2} s^{-1} for $E_\nu > 19.3$ MeV. Fig. 56 indicates how close this Super–K limit is to some of the predictions including their theoretical uncertainties, while Fig. 57 compares the range of predicted spectra to several experimental limits. Note in both of these figures how tantalizingly close to theory the experimental limits from Super–K are getting: perhaps we are on the brink of discovery.

However, after seven more years of Super–K data-taking and intensive efforts to improve the relic analysis, it now appears unlikely that any existing, unmodified detector will be able to make this discovery.

Fifteen years from now, Super–K will have only roughly doubled its present (as yet largely unpublished) statistics. In the useful energy range shown in Fig. 55 one expects between 0.25 and 2.8 signal events per year depending on the model [75, 76, 79, 82], as compared to a measured 14 background events. Therefore, in the best possible case – which means the flux lies just below the current published SK limit – fifteen years hence, Super–K would have recorded 54 relic events and 269 background events in the energy window between 19 and 30 MeV. This would be a 3.3-σ effect, and they could have beaten LBNE to the discovery. However, if the relic flux is lower, say 1.4 events a year (which is still the *maximum* value for Lunardini's predicted range in Super–K), then after 29 years of operations Super–Kamiokande would have just 27 events and a mere 1.6-σ effect; certainly no discovery. These numbers are based on 80% typical detector livetime over 24 years, with the five year period between mid-2001 and mid-2006 having been removed from consideration for reasons apparent in Fig. 58.

B. Sensitivity of Reference Configurations

In this section we consider the performance and sensitivity of the various reference configurations in R&D Document 643v2 (Table XVII provides a summary). In the case of the relics this largely equates to discovery potential.

Reference Configuration 1: Three 100 kt fiducial water Cherenkov detectors. Depth 4850 foot level of DUSEL. Coverage 15% 10 inch high QE PMT's.

Since 15% coverage with high quantum efficiency photomultiplier tubes is nearly equivalent to 19% coverage with normal efficiency tubes, it is instructive to examine the case of Super–Kamiokande–II.

After the Super–K accident in 2001, the detector was initially rebuilt with about half (∼19%) of the original photocathode coverage of 40%. This phase of operation, known as Super–K–II, yielded 49 kt-years of data before
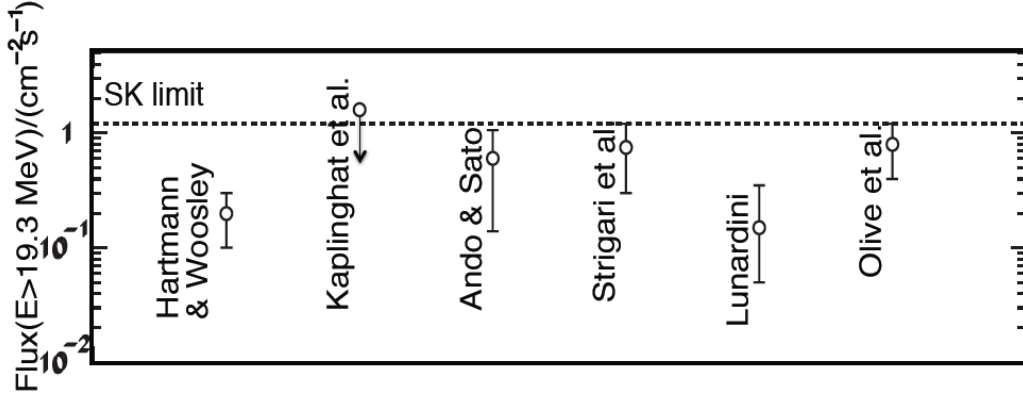
FIG. 56. Super–K relic flux limit from 2003 compared with some theoretically predicted ranges.
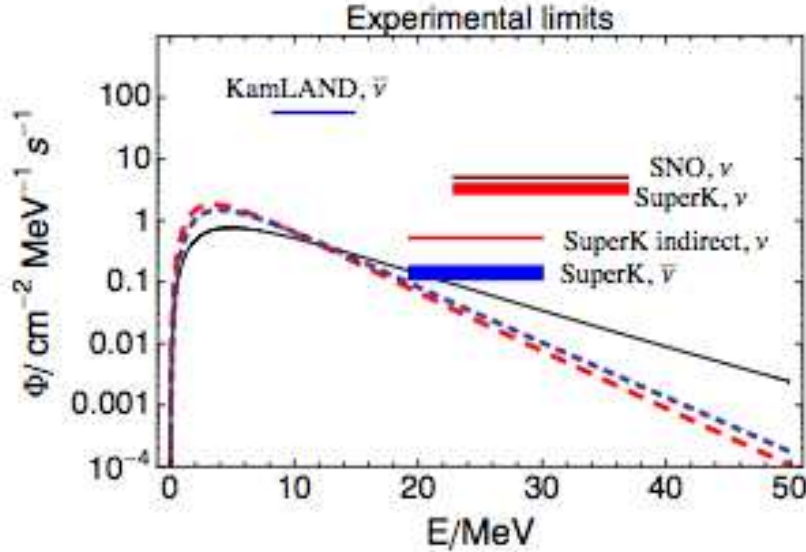
FIG. 57. Experimental SRN limits are approaching theoretical curves. The Super–K ν_e lines have been theoretically extracted based on the measured $\overline{\nu}_e$ results.

the full density of phototubes could be recovered in 2006. Fig. 58 graphically demonstrates how much lower quality this data set was for the SK–II phase relic search as compared to the SK–I data shown in Fig. 55. Due to impaired energy resolution, spallation events with true energies below 19 MeV can be seen leaking into the signal region. This was reflected in this period's much degraded upper limit on the SRN flux: $< 3.7 \ \overline{\nu}_e \ cm^{-2} \ s^{-1}$ for $E_\nu > 19.3$ MeV.

Increasing the overburden from that at Kamioka to Homestake means there will be about a factor of 15 less spallation (see the DUSEL depth document), but a factor of 1.5 more atmospheric neutrinos (see Wurm et al.). This will serve to make reference configuration 1's performance very similar to Super–Kamiokande–I's. The spallation leakage in Fig. 58 will be nearly eliminated, but the backgrounds per unit volume seen in Fig. 55 are increased by 50%.

Therefore, expect 280 background events per year in 300 kilotons, and somewhere between 3 and 38 relic events per year. This range in the relic flux reflects the range of the various models' predictions, with the upper bound somewhat below the current SK limit. It is evident that this configuration will probably not be much of a discovery machine in terms of relic detection. In the best possible case, reaching 3.0-σ would take a minimum of 2.2 years of operation. If the true relic rate is half of the maximum prediction (but still six times the minimum!) then getting to 3.0-σ would take a painful but possible 9 years. However, if the true relic rate falls at the low end of the predicted range, then this particular reference configuration would take 350 years to reach 3.0-σ.
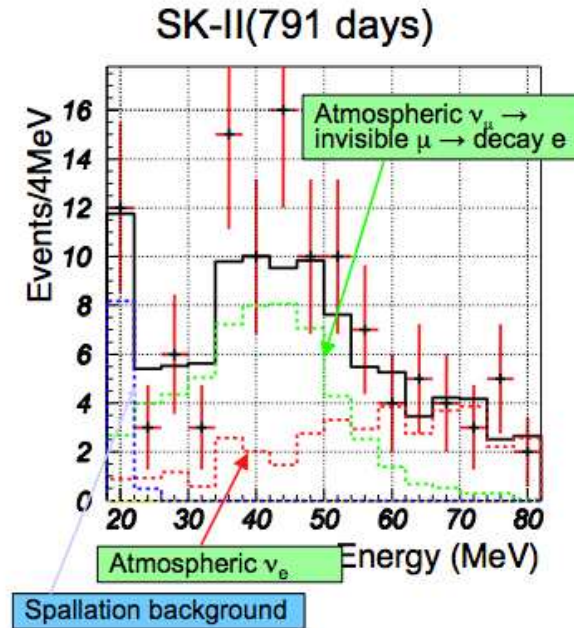
FIG. 58. The Super–Kamiokande–II relic search. The reduced photocathode coverage of SK–II (19% vs. SK–I's 40%) and shorter running time makes this a much less useful data set than that seen in Figure 55.

Reference Configuration 1a: Three 100 kt fiducial water Cherenkov detectors. Depth 4850 foot level of DUSEL. Coverage 30% 10 inch high QE PMT's.

Since 30% coverage with high quantum efficiency photomultiplier tubes is nearly equivalent to 40% coverage with normal efficiency tubes, it is instructive to examine the case of Super–Kamiokande–I.

The lowered spallation rates mean that the energy window can be extended 2.5 MeV below that used in SK–I and shown in Fig. 55 , but the higher atmospheric backgrounds are again troublesome. The enlarged energy window means that we should expect 320 background events per year in 300 kt, while at the same time increasing the expected relic flux by a factor of 1.4, making the predicted range of relic events per year fall between 5 and 52.

Therefore, repeating the same calculations as above, in the best case the 3.0-σ level would take just 1.3 years of running at 80% livetime. If the true relic rate is half of the maximum prediction (but still five times the minimum) then getting to 3.0-σ would take a tolerable 5.3 years. Unfortunately, at the bottom of the predicted SRN range, getting to 3.0-σ would take 144 years.

If the relic signal turns out to lie not far from the current experimental limits, giving us a strong hint after just a few years, this detector configuration could – in principle – be improved by adding gadolinium in order to quickly achieve a conclusive discovery. Which brings us naturally to...

Reference Configuration 1b: Three 100 kt fiducial water Cherenkov detectors. Depth 4850 foot level of DUSEL. Coverage 30% 10 inch high QE PMTs. Gadolinium dissolved in water.

Inspired by the 2003 Super–K SRN limit, adding 0.2% by mass of a soluble gadolinium compound like $GdCl_3$ or $Gd_2(SO_4)_3$ to water Cherenkov detectors has been suggested [83]. The neutrons produced by inverse beta reactions would thermalize in the water and then be captured on gadolinium, emitting an 8 MeV gamma cascade in the process. In coincidence with the prompt position signal, this delayed neutron capture signal would serve to dramatically lower backgrounds from spallation and atmospheric neutrinos, at the same time allowing an enlarged energy window for detection of the relic neutrinos. Fig. 59 shows the expected signals in a gadolinium-loaded Super–K. Such a 22.5 kt detector would expect to see between 1 and 5.6 relic events a year, with about 4 background events.

While this proposal has drawn both considerable interest and funding support, after more than half a decade of study [84, 85] it has not yet received approval from the Super–K leadership to move beyond the R&D stage. Consequently, its immediate future in Japan is uncertain, especially with regards to potentially perturbing the newly operational T2K experiment by attempting to modify Super–K in the early stages of the long-baseline experimental program. For this reason and others (such as a desire to first fix a slow leak in the detector's main tank) it *is* relatively certain that no gadolinium will be added to Super–K during the next five years. Beyond that it is unknown what

will happen, but if Super–K does add gadolinium in 2016 it will be able to extract meaningful spectral information before LBNE comes on-line only if the true relic flux is in the upper half of the currently allowed range. Regardless what decisions are made by the Super–K Collaboration in the coming years, higher statistics SRN data, which only a next-generation detector can provide, will be urgently desired by the middle of the next decade.
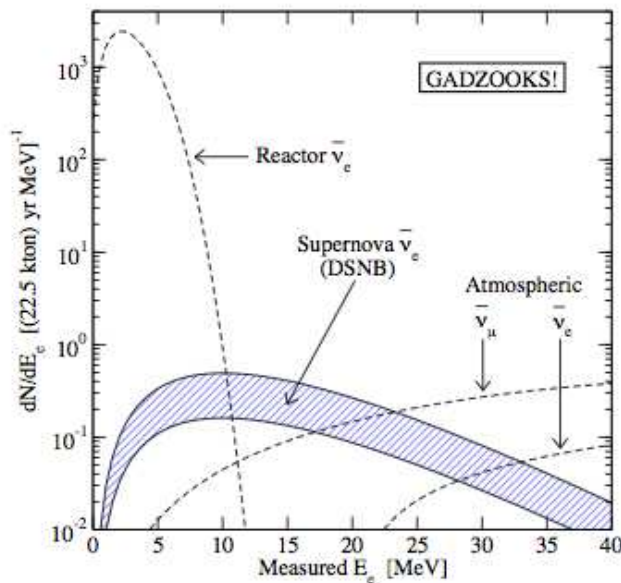
FIG. 59. Expected spectrum of positrons seen in coincidence with neutron capture signals in a gadolinium-loaded Super–Kamiokande detector. The band shows the theoretical range of predictions for the diffuse supernova neutrino background (relic) flux. GADZOOKS! stands for Gadolinium Antineutrino Detector Zealously Outperforming Old Kamiokande, Super!.

Transferring these results to LBNE, the coincident detection made possible by gadolinium greatly reduces spallation, which is rarely accompanied by a neutron within the expected timing window [86]. This allows the SRN window to be opened all the way down to the irreducible wall formed by the antineutrinos from nuclear power reactors around the United States. Note that, primarily due to the remoteness of its South Dakota location, this reactor flux is a factor of 24 times lower in Homestake than it is in Kamioka [87]. However, a 300 kt detector has a fiducial volume 13.3 times bigger than Super–K, so LBNE would observe about half the reactor rate that Super–K does. As one can see from Fig. 59, a factor of two reduction in the reactor curve has very little effect on the available energy window for relic supernova neutrinos, perhaps gaining us another MeV or so. At any rate, opening up the energy window down to 11.3 MeV means that we would expect between 13 and 74 SRN events per year in 300 kilotons of Gd-loaded detector. The coincident technique reduces the atmospheric neutrino background by about a factor of five, and so by comparison with configuration 1a we would expect 64 background events a year across the entire energy spectrum, with 87% of this background in the bins above 19 MeV.

Repeating the same calculations as above over the entire energy window, in the best case the 3.0-σ would take only 0.13 years (48 days) of running at 80% livetime. If the true relic rate is half of the maximum prediction (and in this case just three times bigger than the minimum due to the more complete spectral range of the models contained in the window) then getting to 3.0-σ would take an entirely painless 0.53 years. Even in the most pessimistic case it would still only take us 4.3 years to reach the 3.0-σ level.

The signal to noise ratio improves as one goes down in energy, however, so considering the entire spectral window is really a worst case analysis in terms of time to discovery. As an example, if one restricts the range to between 11.3 MeV and 19.3 MeV, we would expect between 10 and 36 relic events per year in 300 kilotons, and 8 background events. This means we would reach the 3.0-σ level in less than one year, even for the worst case.

Clearly this is an SRN discovery configuration. What's more, it will be able to extract spectral information in addition to a simple flux measurement. The spectrum is a necessary input for the supernova modelers as it encodes the total neutrino energy and the average neutrino energy of bursts. In concert with astronomical observations it also provides a way to determine the rate of invisible explosions (see Fig. 54 [78]).

Conversely, and perhaps even more interesting, if this configuration sees *no* relic signal after a year's time, then we would have a smoking gun for new physics, strongly implying the existence of neutrino decay, new particles, or something similar. This "Diffuse Supernova Neutrino Problem" would arise from a non-detection because we know

from SN1987A that supernovas do emit neutrinos, and we know from the sky surveys about how many explosions there are, what types, and at what distances. But thus far we have never seen neutrinos older than those from 170,000 light-years away. The relic neutrinos have had to travel four orders of magnitude further, and are therefore a more sensitive probe of unusual processes.

Reference Configuration 2: Three 17 kt fiducial liquid argon detectors. Depth 4850 foot level of DUSEL. Assume a scintillation photon trigger for proton decay and supernova neutrinos.

There are different issues to consider in the case of liquid argon, which detects relic supernova neutrinos primarily via the charged-current process $\nu_e + {}^{40}\text{Ar} \rightarrow {}^{40}\text{K}^* + e^-$. The electron track should be accompanied by evidence – shorter tracks sharing a common vertex – of ionization from the de-excitation of the potassium; this is expected to be helpful in reducing backgrounds. Unlike inverse beta decay, whose cross section is known to the several-percent level in the energy range of interest [88, 89], the cross section for neutrino interactions on argon is uncertain at the 20% level [69, 90, 91]. Another wrinkle is that the solar *hep* neutrinos, which have an endpoint at 18.8 MeV, will determine the lower bound of the SRN search window. The upper bound is determined by the atmospheric ν_e flux.

In the case of liquid argon no multi-kiloton detectors have yet been built. In addition to having to rely on estimates of efficiencies and downtime in a huge new detector, this necessarily forces us to rely heavily on some important assumptions concerning potential background processes which might fall inside the 18 to 30 MeV window defined by the solar *hep* and atmospheric ν_e fluxes.

For our analysis, we will adopt the following strong assumptions [92]. They have been listed from least speculative (most certain) most speculative (least certain):

- No nuclear recoils from fast neutrons will be able to produce a signal-like event in the energy range of interest.

- Unlike in water Cherenkov detectors, liquid argon detectors do not suffer from sub-Cherenkov muons decaying into electrons and faking the SRN signal, as no muons (or evidence of their decays) should escape detection in the detector.

- No spallation products will be produced that generate electrons in the energy range of interest without clear evidence of their parent muon allowing the event to be removed from consideration. (The full family of spallation daughters of argon does not seem to be known, but it must include all possible oxygen spallation products.)

- No radioactive background or impurity, electronic effect in the detector, track-finding inefficiency, particle misidentification, or failed event reconstruction will ever be able to lead to a signal in the energy range of interest.

Before the first long-term, high-statistics, real-world neutrino data in liquid argon becomes available, this last requirement in particular might strike some as a rather optimistic. Also it is worth noting that, contrary to what some references have stated [92], there *are* spallation decays in this energy range, i.e. ^{11}Li, which has a Q value of 20.6 MeV and is a beta emitter [93], so efficient identification of the parent muon is vital.

Based on these potentially "best case" assumptions we reach the following performance estimates. In Fig. 60 we see the expected relic supernova ν_e spectrum for a 5 year exposure of a 3 kiloton liquid argon detector in Gran Sasso, along with the limiting backgrounds of solar and atmospheric neutrinos. For the relic flux, normal hierarchy and a large value for $\sin^2\theta_{13}$ ($\geq 10^{-3}$) has been assumed; inverted hierarchy or very small $\sin^2\theta_{13}$ ($\leq 10^{-6}$) would result in a relic flux some 25% lower. For this 15 kt-year exposure, 1.7 ± 1.6 relic events are expected in the energy window between 16 MeV and 40 MeV.

Transferring this to to LBNE, and using a more beneficial (in terms of signal to background) energy window of 18 to 30 MeV, we would expect between 0.5 and 3.3 relic events per year in 51 kilotons of liquid argon, and 0.3 background events from atmospheric neutrinos. These numbers are sufficiently small that quoting expectations in terms of sigma has little meaning; they are solidly in the Poissonian domain. Suffice it to say that any events in the signal region would have to be taken very seriously, since in all cases the signal is expected to exceed the background rate, a very attractive feature.

On the other hand, this serves to underline just how vital the assumptions listed above regarding backgrounds are for liquid argon, since even a single unexpected false event a year combined with the expected background could easily equal or exceed the true signal's rate in all but the more optimistic cases. This equates to an event-purity requirement of less than one false event per kiloton per century. Until kiloton-centuries of LAr data have been taken and are shown to be background-free, this uncertainty is the biggest risk inherent in configuration 2.

Given these caveats, this configuration has discovery potential for a non-zero SRN flux. Unfortunately, in even the most optimistic high-rate cases useful spectral information would only become available after a decade of running due to both the low number of events observed and the flatness of the predicted spectrum in the sensitive region.
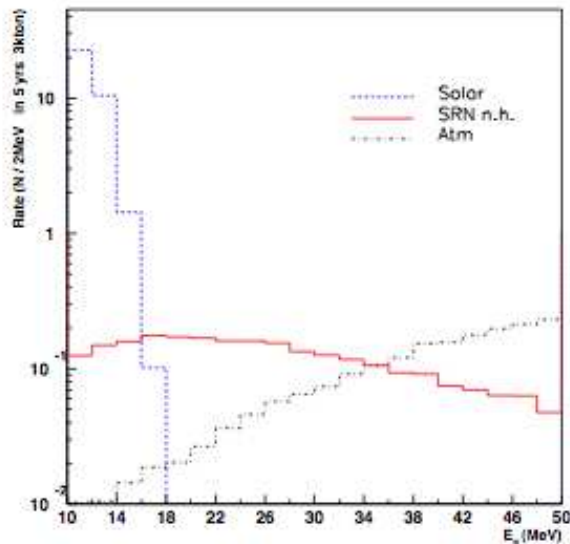
FIG. 60. Expected relic supernova ν_e spectrum for a 5 year exposure of a 3 kiloton liquid argon detector in Gran Sasso, along with the limiting backgrounds of solar and atmospheric neutrinos.

Reference Configuration 2a: Three 17 kt fiducial liquid argon detectors. Depth 300 foot level of DUSEL. No photon trigger.

For the previous configuration we considered the best-case scenario for 51 kilotons of LAr at the 4850 level of DUSEL. All assumptions about zero background are predicated on control of the environment and understanding of the detector. As that configuration assumed both a photon trigger and a high degree of depth shielding from cosmic ray muons, it is clearly the most favorable design to meet the stringent requirements of no more than one false event per kiloton per century.

However, at 300 feet the cosmic ray muon rate will be 32,600 times the rate at the 4850 level (see the official DUSEL Depth Document). As a result, a detector at this depth will suffer an effective loss of fiducial volume due to the intense muon flux. For a liquid argon detector, it has been estimated [94] that at 300 feet approximately 20% of the effective volume will be lost due to cutting out a 10 centimeter slice in each 2D view around all muon tracks. This will serve to reduce the numbers in the previous section (both the relic flux and the atmospheric background) by 20%: between 0.4 and 2.6 relic events and 0.2 background events per year.

Additionally and more critically, because the drift time in a large liquid argon detector is on the order of a few milliseconds, the several kilohertz of through-going cosmic ray muon tracks at this depth means that there will always be several lines of charge drifting through the fiducial volume of the detector at any given moment. Multiple muons from a single cosmic ray interaction will likely be especially troublesome. Without a photon trigger to establish the exact t_0 of each track, it may not be possible to guarantee that there will be no failed track reconstructions, very low energy muons misidentified as electrons, or untagged spallation debris capable of mimicking a relic signal in this configuration, at the extremely stringent levels required. In fact, since the expected relic signal will be reduced by 20% due to spallation cuts, protecting against background signals is that much more vital for this configuration.

The uncertainty from lack of high-exposure operation and exquisite sensitivity to this issue makes it difficult to consider this configuration capable of making a convincing SRN discovery at this time.

Reference Configuration 2b: Three 17 kt fiducial liquid argon detectors. Depth 800 foot level of DUSEL. Assume a scintillation photon trigger for proton decay and supernova neutrinos.

At 800 feet the cosmic ray muon flux is reduced by a factor of about four as compared to the 300 foot level. The good news is that there is almost no loss of fiducial volume required due to cutting around muon tracks [94], so the 20% of events lost in configuration 2a is recovered here. We would therefore once again expect between 0.5 and 3.3 relic events per year, and 0.3 background events from atmospheric neutrinos. Also good is that in this configuration the photon trigger is restored, which should help considerably with low energy triggering.

Though significantly lower than at 300 feet, the muon flux at 800 feet is still some 8000 times more intense than at the 4850 foot level. Even with the benefit of photon triggering, it is challenging to guarantee that there will be

no false events at the level of less than one a year arising from failed track reconstructions, very low energy muons misidentified as electrons, or spallation debris capable of mimicking a relic signal in this configuration. In terms of cosmic ray-related background rejection (but, sadly, not signal collection), every successful year at 800 feet is equivalent to false-background-free exposure of 408 Mt-years on the 4850 level.

Again here, some high-exposure proof-of-principle data, in this case with a photon trigger, is needed to properly assess the viability and hence the potential of this configuration for SRN discovery.

Reference Configuration 3: Two 100 kt fiducial water Cherenkov detectors at 4850 feet as specified in configuration 1, plus one 17 kt fiducial liquid argon detector at 300 feet with no photon trigger as specified in configuration 2a.

This begins a long series of combinatoric configurations where the various detectors and depths of the the previous configurations are mixed and matched. In all cases one or two components are dominant in terms of SRN discovery potential. The expected rates and known backgrounds will be listed; details can be found in the discussions of configurations 1, 1a, 1b, 2, 2a, and 2b.

By referring to configuration 1, the two 100 kt WC modules of this design would expect to record between 2 and 26 relic events a year with 187 background events. By comparison with configuration 2a, a single liquid argon detector at 300 feet would be expected to see between 0.1 and 0.9 relic events a year, adding little to the configuration even if detector-related backgrounds could be well controlled.

WC: SRN signal = 2 – 26 events/year, background = 187 events/year

LAr: SRN signal = 0.1 – 0.9 events/year, atmospheric ν_e background = 0.1 events/year

Reference Configuration 3a: Two 100 kt fiducial water Cherenkov detectors at 4850 feet as specified in configuration 1a, plus one 17 kt fiducial liquid argon detector at 300 feet with no photon trigger as specified in configuration 2a.

WC: SRN signal = 3 – 34 events/year, background = 214 events/year

LAr: SRN signal = 0.1 – 0.9 events/year, atmospheric ν_e background = 0.1 events/year

Reference Configuration 3b: One 100 kt fiducial water Cherenkov detector at 4850 feet as specified in configuration 1, plus one 100 kt fiducial water Cherenkov detector at 4850 feet with gadolinium as specified in configuration 1b, plus one 17 kt fiducial liquid argon detector at 300 feet with no photon trigger as specified in configuration 2a.

WC: SRN signal = 1 – 13 events/year, background = 93 events/year

WC+Gd: SRN signal = 4 – 25 events/year, background = 21 events/year

LAr: SRN signal = 0.1 – 0.9 events/year, atmospheric ν_e background = 0.1 events/year

Reference Configuration 4: Two 100 kt fiducial water Cherenkov detectors at 4850 feet as specified in configuration 1, plus one 17 kt fiducial liquid argon detector at 800 feet with a photon trigger as specified in configuration 2b.

WC: SRN signal = 2 – 26 events/year, background = 187 events/year

LAr: SRN signal = 0.2 – 1.1 events/year, atmospheric ν_e background = 0.1 events/year

Reference Configuration 4a: Two 100 kt fiducial water Cherenkov detectors at 4850 feet as specified in configuration 1a, plus one 17 kt fiducial liquid argon detector at 800 feet with a photon trigger as specified in configuration 2b.

WC: SRN signal = 3 – 34 events/year, background = 214 events/year

LAr: SRN signal = 0.2 – 1.1 events/year, atmospheric ν_e background = 0.1 events/year

Reference Configuration 4b: One 100 kt fiducial water Cherenkov detector at 4850 feet as specified in configuration 1, plus one 100 kt fiducial water Cherenkov detector at 4850 feet with gadolinium as specified in configuration 1b, plus one 17 kt fiducial liquid argon detector at 800 feet with a photon trigger as specified in configuration 2b.

WC: SRN signal = 1 – 13 events/year, background = 93 events/year

WC+Gd: SRN signal = 4 – 25 events/year, background = 21 events/year

LAr: SRN signal = 0.2 – 1.1 events/year, atmospheric ν_e background = 0.1 events/year

Reference Configuration 5: One 100 kt fiducial water Cherenkov detector at 4850 feet with gadolinium as specified in configuration 1b, plus two 17 kt fiducial liquid argon detectors at 300 feet with no photon trigger as specified in configuration 2a.

WC+Gd: SRN signal = 4 – 25 events/year, background = 21 events/year

LAr: SRN signal = 0.2 – 1.8 events/year, atmospheric ν_e background = 0.2 events/year

Reference Configuration 6: One 100 kt fiducial water Cherenkov detector at 4850 feet with gadolinium as specified in configuration 1b, plus two 17 kt fiducial liquid argon detectors at 800 feet with photon trigger as specified in configuration 2b.

WC+Gd: SRN signal = 4 – 25 events/year, background = 21 events/year

Reference Configuration Number	Expected Annual SRN Signal (events/year)	Expected Annual Background (events/year)	Years of LBNE Data Needed for a 3.0-σ Signal Assuming Maximum SRN Flux	Years of LBNE Data Needed for a 3.0-σ Signal Assuming Minimum SRN Flux
1	$3 - 38$	280	2.2	350
1a	$5 - 52$	320	1.3	144
1b	$13 - 74$	64	0.13	0.9
2	$0.5 - 3.3$	0.3	~ 1	unknown
2a	$0.4 - 2.6$	0.2	~ 2	unknown
2b	$0.5 - 3.3$	0.3	~ 1	unknown
3	$2 - 27$	187	2.9	526
3a	$3 - 35$	214	2.0	268
3b	$5 - 39$	114	0.35	3
4	$2 - 27$	187	2.9	526
4a	$3 - 35$	214	2.0	268
4b	$5 - 39$	114	0.35	3
5	$4 - 27$	21	0.32	3
6	$4 - 27$	21	0.32	3

TABLE XVII. Summary of the reference configurations' sensitivity to detecting the supernova relic neutrino flux.

LAr: SRN signal = 0.3 – 2.2 events/year, atmospheric ν_e background = 0.2 events/year

C. Conclusions

To observe the supernova relic neutrinos we will clearly need large detector mass, low irreducible backgrounds, and well understood detector systematics.

From Table XVII one can see that if the actual relic flux in the universe is at the high end of predictions and the detectors function with possibly optimistic assumptions, we could observe the relic flux with almost any configuration. However, it should be noted that if the flux is very high then a long-running Super–K could make the discovery before LBNE is fully operational.

The best option for timely supernova relic neutrino flux discovery requires one of the configurations containing at least one 100 kt gadolinium-loaded water Cherenkov detector (i.e., configurations 1b, 3b, 4b, 5, and 6 in R&D Document 643v2). No matter where in the range of model predictions the true SRN flux lies, these configurations would need no more than three years, and in some cases much less, to make a 3.0-σ discovery. Furthermore, these configurations will allow us to extract useful physics data in the form of spectral information; in the worst cases this could require ten years or so of running, but it should be possible nevertheless.

VII. ATMOSPHERIC NEUTRINOS

In this section we summarize the potential contributions that atmospheric neutrinos studies could contribute to the overall LBNE physics program.

A. Motivation and Scientific Impact

Atmospheric neutrinos have played a crucial role in the discovery of neutrino oscillations and the measurement of neutrino masses and mixing parameters. Atmospheric neutrinos are sensitive, at least in principle, to all of the physics remaining to be discovered in the PMNS matrix; the flux consists of neutrinos and anti-neutrinos of all flavors, and passes through significant densities of material, introducing modifications due to matter effects. The size of the earth is nearly optimal for the study of the large neutrino mass splitting, with large oscillation probabilities in the dominant channel. Three-flavor matter-enhanced atmospheric neutrino mixing is described by a rich phenomenology [95–101] and offers significant opportunities for discovery. In addition to the precision measurements of the dominant oscillation parameters [102, 103], the super-Kamiokande experiment has already carried out studies searching for tau appearance [104], mixing at the solar mass scale [105], three flavor oscillations [106] , as well as more exotic scenarios [107–109]. Magnetized underground detectors have the ability to distinguish neutrinos from anti-neutrinos with high accuracy, which provides additional strength for resolution of the mass hierarchy and possible measurement of non-zero θ_{13} [110, 111].

Similar studies can also be carried out with the high-statistics data sample of the LBNE detector, and may provide an important complementary measurement of the oscillation parameters as determined using neutrinos from the accelerator beam.

Atmospheric neutrinos are unique among sources used to study oscillations: the oscillated flux contains neutrinos and antineutrinos of all flavors, matter effects may play a significant role, and the oscillation phenomenology plays out over several decades in energy and path length. These characteristics of the atmospheric flux make it an ideal source for studying a wide range of oscillation and mixing effects.

1. Confirmatory Role

Atmospheric neutrinos have the potential to play a vital role in the context of a comprehensive program to study the lepton sector because all of the physics that one might hope to examine with beam neutrinos can also be explored (albeit with reduced precision) using atmospheric neutrinos. This includes oscillations at the large Δm^2, tau appearance, $\nu_\mu \to \nu_e$ mixing in the presence of a non-zero θ_{13}, the CP-violating phase, and the study of the mass hierarchy. Because these phenomena play out over a wide range of energy and path lengths, atmospheric neutrinos are very sensitive to alternative explanations or subdominant new physics effects that predict something other than the characteristic (L/E) dependence predicted by oscillations in the presence of matter. This power has already been exploited by the Super-Kamiokande in fits that compare their data binned in terms of energy and zenith angle to a host of new physics including CPT violation [112, 113], Lorentz invariance violation [114, 115], non-standard interactions [116], Mass Varying Neutrinos (MaVaNs) [117], and sterile neutrinos [107–109]. In numerous cases the best limits on exotic scenarios come from atmospheric neutrino analyses.

The breadth of physics that one can study with atmospheric neutrinos, the ability to study oscillation phenomena in a complementary way to beam studies, and the sensitivity to small admixtures of 'new physics' make atmospheric neutrinos an important part of the overall physics mission of the LBNE experiment. One concrete example is the study of ν_τ appearance in the atmospheric neutrino flux. While a large fraction of the muon neutrinos are thought to oscillate to tau neutrinos, the overall rate of tau interactions is small due to the energy threshold for tau production. Tau events are expected at a rate of around 1 event per kiloton-year in the oscillated atmospheric flux. These events can be identified on a statistical basis in water Cerenkov detectors [104], and can be selected in liquid argon detectors focussing on hadronic modes and in particular for up-down asymmetries. A recent paper estimates that with a set of simple cuts on visible energy, reconstructed zenith angle, and energy of the highest energy pion in events lacking a charged lepton, a 4.3 σ excess over background can be identified in a 100 kt-yr exposure [118]. Confirmation of the appearance of tau neutrinos at the expected level in the atmospheric flux will be an important consistency check on our overall oscillation picture.

2. PMNS Matrix Measurements

The key observable for atmospheric neutrinos will be the data binned in (energy,zenith angle) for events separated by flavor, and ideally by neutrino/anti-neutrino. For upgoing neutrinos ($\cos(\theta) < 0$), oscillations at the atmospheric mass splitting introduce large effects and matter effects introduce significant distortions of the spectrum, particularly for neutrinos which pass through the Earth's core. Mixing involving electron neutrinos is enhanced for non-zero θ_{13} for neutrinos (anti-neutrinos) due to matter effects if the hierarchy is normal (inverted).

The two key measurements, and the data samples that would be used to study them, are:

- Octant of θ_{23}: Upward-going, sub-GeV electron neutrinos are affected by sub-dominant oscillations at the solar mass scale. This may allow the ability to determine whether θ_{23} is less than or greater than 45 degrees, even if θ_{13} is zero. Recent work suggests that the effects for $\sim$ sub-GeV (E<100 MeV) neutrinos may be as large as 10-15% [95].

- Mass hierarchy and θ_{13}: A non-zero θ_{13}, combined with matter effects, leads to a complicated structure of oscillation peaks for upgoing, roughly 1-10 GeV electron and muon neutrinos. Matter effects lead to an enhancement for electron neutrinos if the hierarchy is normal, and anti-neutrinos if the hierarchy is inverted.

Many of the possible signatures in the atmospheric neutrino flux appear in the few hundred MeV to few GeV energy range. Key performance characteristics for the detector include being able to distinguish ν_μ CC, ν_e CC, and NC events at these energies, as well as being able to accurately determine the energy and direction of the incoming neutrino.

Atmospheric neutrinos, when combined with beam neutrinos in a global analysis, may help to resolve some degeneracies. In particular if θ_{23} is not $45°$, and θ_{13} is small, the analysis of atmospheric neutrinos may contribute significantly to resolving degeneracies present in the analysis of beam data alone [119].

B. Evaluation of Physics Sensitivities

In this section we will evaluate atmospheric neutrino physics sensitivities for water Cerenkov and liquid argon detectors. We will begin by describing the key detector performance characteristics, describe the tools developed for carrying out these studies, and present results on two key measurements: the octant of θ_{23} and resolution of the mass hierarchy.

1. Water Cerenkov / Liquid Argon Differences

Due to the success of the Super-Kamiokande experiment, the performance of water Cerenkov detectors for measurements of atmospheric neutrinos, and the ways in which the data are to be analyzed, are well understood. The smaller size of liquid argon detectors is compensated by several advantages resulting from the higher imaging resolution:

1. Improved energy and angular resolution for the initial neutrino.

2. The ability to image sub-relativistic particles and therefore improve the determine the incoming neutrino direction at sub-GeV neutrino energies. The capability of liquid argon detectors to image sub-relativistic particles significantly improves the pointing resolution for these relatively low energy interactions [120], compared with the capabilities of water Cerenkov detectors which are capable of identifying protons at higher energies [121].

3. Improved flavor separation and NC/CC-like event separation.

4. Somewhat improved ability to tag events as coming from neutrinos/anti-neutrinos.

These differences may have significant ramifications. As stated previously, the key detector performance characteristics are whether the resolution is sufficient to resolve the features in the 'oscillograph' of the earth and distinguish neutrinos from anti-neutrinos. If the angular resolution, energy resolution, and neutrino/anti-neutrino identification are up to this task, then atmospheric neutrinos hold the potential to make confirmatory discoveries even with limited statistics. For example, Reference [122] calculates that for a detector with excellent imaging characteristics the hierarchy can be identified at 2σ with only around 200 events in the upgoing multi-GeV sample.

2. Method and Tools

For sensitivity studies we have developed a fast, four-vector level simulation tool that performs event classification, measurement, binning, and statistical analysis. This is done with a set of software based on the MINOS atmospheric analysis framework.

The simulation proceeds in several steps:

Event Generation: Four-vector level events are generated using the GENIE neutrino event generator [123]. For this purpose new flux drivers were developed which implement both the Bartol [124] and FLUKA 3-d [125] flux calculations at the Soudan, MN site, which is a reasonable approximation for the geomagnetic latitude of DUSEL. Figure 61 shows the two inputs to the event rate calculation and event generation, the Bartol flux and the GENIE cross sections. The event rate on water varies over the solar cycle, from a minimum of 288 (275) events/kt-yr to a maximum of 331 (303) events/kt-yr as calculated using the Bartol (FLUKA) flux. Predicted event rates in liquid argon differ from these values by less than 2%.
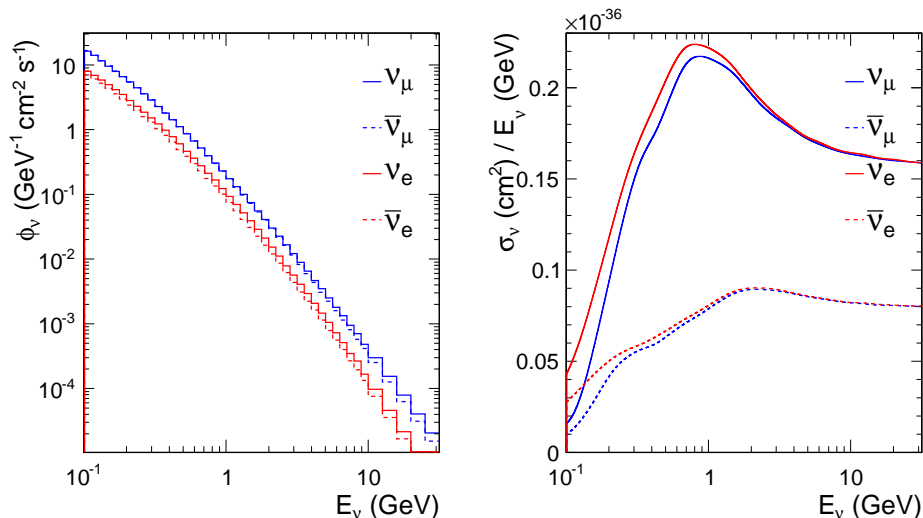
FIG. 61. The Bartol 3d atmospheric flux (left) and the GENIE neutrino-water cross sections (right).

GENIE is then used to generate large samples of interactions on argon or water. These simulations include all known scattering mechanisms of relevance in this energy range as well as a simulation of nuclear effects including fermi motion, Pauli blocking, and intranuclear rescattering. The output of these events are a set of 4-vector for particles emerging from the struck nucleus. These can either be input to a detector simulation or to a fast parametrized simulation of detector response. Figure 62 shows such an event input to the WCSim detector simulation.

Pseudo-Reconstruction Events are passed through a fast parameterized 'pseudo-reconstruction'. In atmospheric neutrino analyses events are categorized in a number of ways: containment (fully/partially contained), flavor (e-like/mu-like/NC-like), energy (sub/Multi-GeV), topology (single/multi-ring, QEL/non-QEL), and neutrino/antineutrino tag. The classification is made based on truth level characteristics, accounting for detection thresholds and misidentification via the following steps:

1. Classify containment by simulating vertex and end points for each event using a toy detector geometry. For the 100 kt fiducial mass WC detector the geometry is a cylinder with 26.5 m radius and 60 m height. For the 17 kt fiducial mass LAr detector the geometry is a box with 71 m length, 15 m width, and 14 m height. Vertex points are chosen at random, and energy loss formulas are used to obtain end points of final state particles. A fiducial volume cut is then placed on the vertex (2 m for WC, 1 m for LAr) and track end positions (0.5 m for WC, 0.25 m for LAr) to determine if the event is fully or partially contained.

2. Simulate trigger by selecting those events containing particles above threshold ("visible" particles), here taken to be 50 MeV. In addition, charged particles in WC are required to be above Cerenkov threshold.

3. Assign neutrino flavor to events using true $\rightarrow$ reconstructed classification matrices, giving probabilities for different reconstructed event types. These matrices are adapted from versions in the literature, for WC from
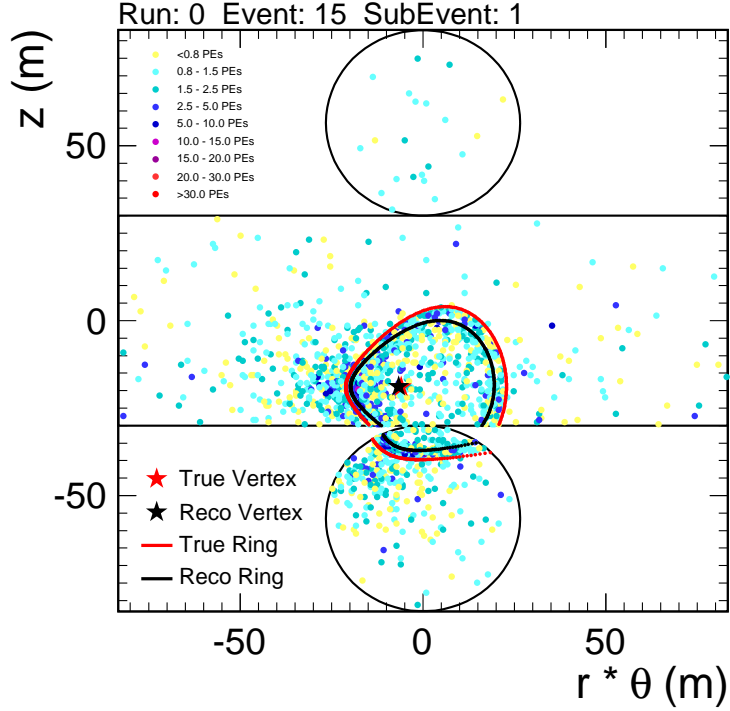
FIG. 62. A simulated 1 GeV ν_μ CC interaction in a water Cerenkov detector. This event was produced using the GENIE atmospheric neutrino flux driver to produce final state four-vectors, which were converted into Nuance tracker format for input into the WCSim detector simulation and reconstruction.

Reference [127], for LAr from Reference [128]. For the WC option the classification categories are e-like and mu-like, for the liquid argon option they are e-like, mu-like, and NC-like.

4. Smear energy and angle of leptons and hadronic final states, using the resolution functions given in Table XVIII.

Resolution	WC	LAr
FC Lepton		
Energy:	$2\% + 2\%/\sqrt{E}$	$2\% + 2\%/\sqrt{E}$
Angle:	$2°$	$2°$
PC Lepton		
Energy:	50%	50%
Angle:	$2°$	$2°$
Hadronic System		
Energy:	$30\% + 30\%/\sqrt{E}$	$30\%/\sqrt{E}$
Angle:	$45° + 15°/\sqrt{E}$	$10°$

TABLE XVIII. Summary of resolution functions. Water Cerenkov resolutions were taken from, or tuned to, SuperKamiokande resolution plots [130], LAr resolutions are from [156] and [129].

5. Apply minimum energy cuts of 100 MeV for selected FC and 300 MeV for PC events. The same minimum energy cuts are used for both detector configurations.

Figures 63 and 64 show the simulated zenith angle distributions for the analysis categories defined above, for five years of data taking in water Cerenkov and liquid argon detectors.

Sensitivity Evaluation: Binned pseudo-reconstructed data are then compared to oscillation hypotheses and relevant statistics are calculated. Three-flavor oscillation probabilities including matter effects [131] incorporating the PREM earth model are calculated using code provided by Mark Messier [132]. Neutrino production heights as

FIG. 63. Simulated zenith angle distributions for 500 kt-yrs of atmospheric neutrino data in a water Cerenkov detector. No oscillations (solid blue), with oscillations (black), NC contribution (dashed blue).

a function of energy and zenith angle are calculated using parametrizations and code developed by the MINOS and Soudan-2 experiments [133].

The effect that oscillations would have on the experimental distributions in a water Cerenkov and liquid argon detector are shown in Figures 65 and 66, respectively. The low energy $(0 < E_\nu < 1$ GeV) sample (left figure in each plot) is sensitive to the octant of θ_{23} in changes in the rate of upward-going electron like events. The high energy $(4 < E_\nu < 12$ GeV) sample is sensitive to the mass hierarchy and non-zero θ_{13} via changes in the rate of upward-going electron-like events. In all of these plots, the default values for oscillation parameters are $\Delta m_{32}^2 = 2.3 \times 10^{-3}$ eV^2, $\sin^2 \theta_{23} = 0.5$, $\Delta m_{12}^2 = 7.5 \times 10^{-5}$ eV^2, $\sin^2 \theta_{12} = 0.31$, $\sin^2 \theta_{13} = 0$, $\delta_{CP} = 0$, and normal hierarchy. The changes from these default values are shown on each plot.

For both detectors, data in each of the analysis categories (FC/PC, e-like/mu-like/NC-like) are binned in energy and zenith angle with $\Delta \log_{10}(E) = 0.2$ and $\Delta \cos \theta = 0.1$. For some input true value of the oscillation parameter, the log-likelihood difference is computed between this 'expected' data and data for any other set of oscillation parameters. For the sensitivities computed here, log-likelihood curves were generated in this way for a single parameter, using statistical errors only for the chosen exposure.

To validate the method as well as the misidentification matrix and resolution functions for WC, a simulation was done of the SuperKamiokande detector geometry for a 7.68 year exposure, in order to compare with published results [134]. Even with perfect parameterizations of detector performance one would not expect complete agreement, in part because we are comparing an expected sensitivity to a result derived from actual data. This comparison does yield results in reasonable agreement, giving us confidence in our ability to accurately calculate WC sensitivities for larger detectors and exposures.

3. Physics Sensitivities

For this report we have calculated sensitivities for a 100 kt fiducial mass WC and 17 kt fiducial mass liquid argon detector with five years of data.

Figure 67 shows the sensitivity to the octant of θ_{23}. In this case the likelihood difference is calculated between the value of θ_{23} in the correct octant to that in the wrong octant. As this plot indicates, the larger mass of the WC detector outweighs the advantages in purity and directional resolution of the liquid argon detector for this measurement.

Figure 68 shows the sensitivity to the resolution of the mass hierarchy, as a function of true θ_{13}. In these plots,
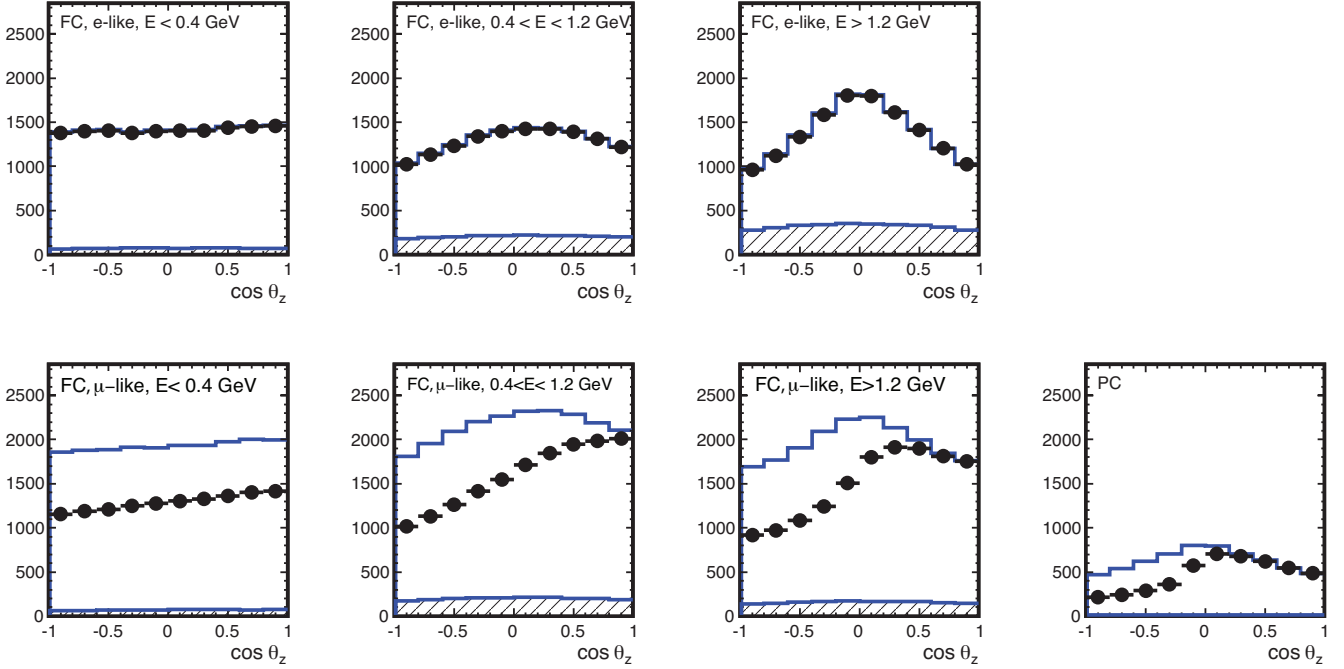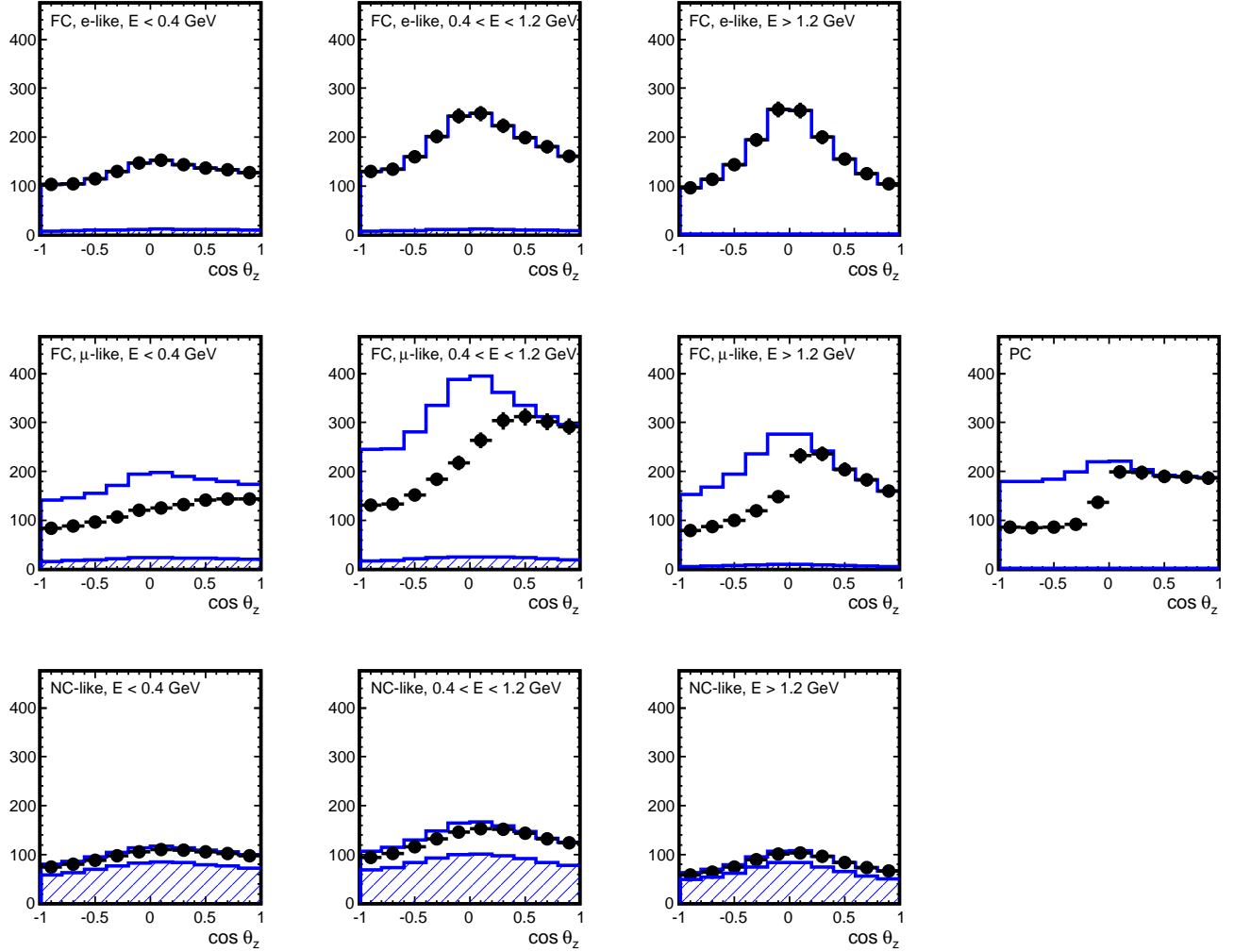
FIG. 64. Simulated zenith angle distributions for 85 kt-yrs of atmospheric neutrino data in a liquid argon detector. No oscillations (solid blue), with oscillations (black), NC contribution (dashed blue).

normal mass hierarchy corresponds to positive values, inverted hierarchy to negative values. One feature to note is that both technologies have a weak sensitivity to the sign of the mass hierarchy even for $\theta_{13} = 0$, resulting from interference between oscillations at the solar and atmospheric mass scales. For either technology it is easier to resolve a normal mass hierarchy, since resonant matter effects occur for neutrinos rather than anti-neutrinos, with larger interaction cross sections. For the resolution of the mass hierarchy, the larger mass of the WC detector is again the dominant factor. In future revisions we will explore in more depth the different capabilities of the detector technologies for distinguishing neutrinos from anti-neutrinos, which may provide an additional compensating factor for liquid argon.

C. Comments on Configuration Options

Configuration options that are designed primarily to improve capabilities for lower energy neutrinos are not expected to have a significant effect on the study of atmospheric neutrinos. These include having gadolinium in a water Cerenkov detector, or including a photon trigger for an atmospheric neutrino detector.

The two options for phototube coverage are also expected to have minimal impact on the atmospheric neutrino analysis. Since the Super-K data sets included periods where the photodetector coverage was lower (Super-K–II), many studies were done on the differences in detection efficiency and measurement resolution for atmospheric neutrinos when comparing the Super-K–I and II detector configurations. These studies [130] indicate that the differences are
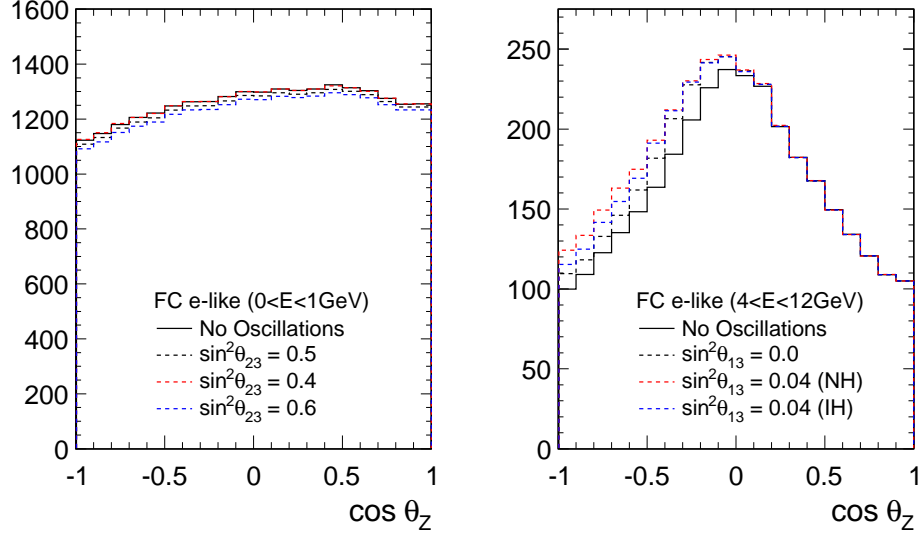
FIG. 65. Zenith angle distributions for a low energy (left) and high energy (right) WC e-like data sample. Oscillation parameter values are given in the text.
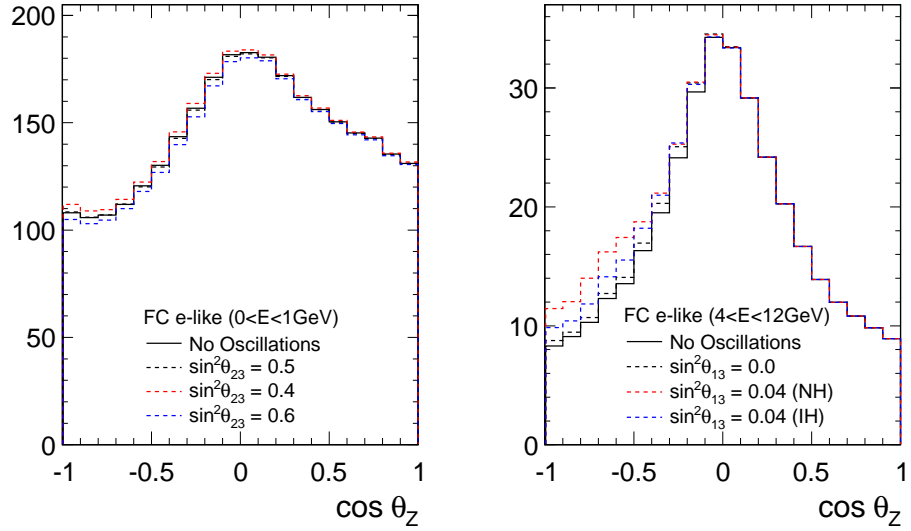
FIG. 66. Zenith angle distributions for a low energy (left) and high energy (right) liquid argon e-like data sample. Oscillation parameter values are given in the text.

small as far as atmospheric neutrino analyses are concerned, and for the conclusions here we are considering them to be a relatively small perturbation.

Configuration options that involve placing a liquid argon detector at shallow depths will require more study, but it appears at this time that the analysis and conclusions of [128] which studies cosmogenic backgrounds to proton decay are also directly for atmospheric neutrinos. The veto shield, as proposed, follows the conclusions of this study and should therefore provide sufficient information to work at the depth of 800 ft with a 17 kt analysis fiducial volume, which is the fiducial volume assumed in the studies mentioned previously, and is the fiducial volume available at 4850 ft.
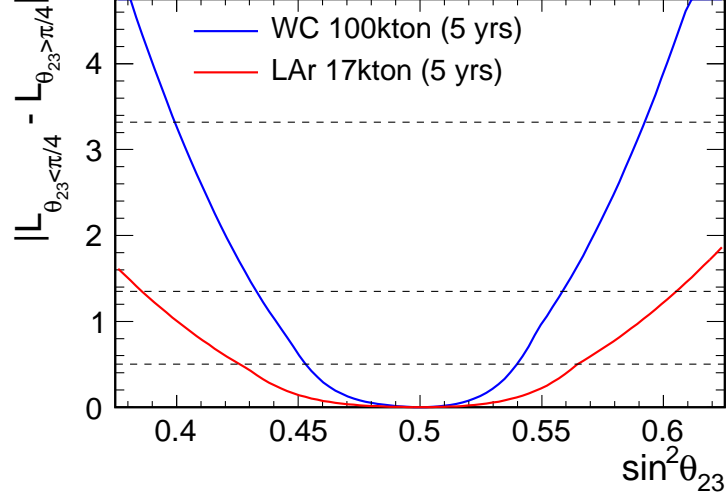
FIG. 67. Sensitivity to the octant of θ_{23} for five years of running with a 100 kt fiducial mass water Cerenkov detector (blue) or a 17 kt fiducial mass liquid argon detector (red).
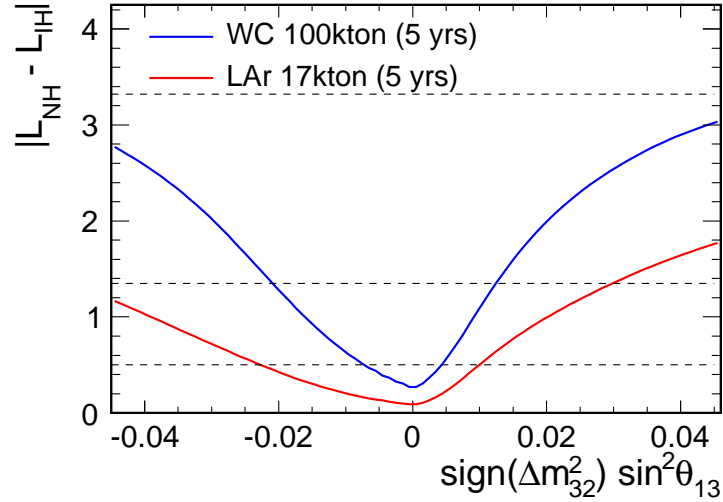
FIG. 68. Sensitivity to the determination of the mass hierarchy as a function of the true value of θ_{13} for five years of running with a 100 kt fiducial mass water Cerenkov detector (blue) or a 17 kt fiducial mass liquid argon detector (red).

VIII. ULTRA-HIGH ENERGY NEUTRINOS

The field of neutrino astronomy, using high-energy neutrinos as cosmic messengers to probe the internal mechanisms of the most energetic astrophysical objects, offers a new window on the universe. Where the traditional astronomical messengers of photons and charged particles are either absorbed by material or radiation in astrophysical environments or are deflected into random directions by magnetic fields, neutrinos, with no charge and a small interaction cross section, offer an unobstructed view inside the acceleration regions where the highest energy cosmic rays are created. The source of these highest energy cosmic rays still remains as one of the long-standing open questions in physics. Any astrophysical object capable of producing these highest energy protons will almost certainly be a source of high energy neutrinos, as some fraction of these protons will interact with matter or radiation fields in and near the source. Potential sources of high-energy neutrinos include active galactic nuclei, supernova remnants [135], gamma-ray bursts (GRBs) [136, 137]. Observation of neutrinos from these sources, in combination with photon observations at several wavelengths, will likely be needed to identify and understand the acceleration mechanisms at work in these sources.

Other potential sources of high-energy neutrinos include annihilation of weakly interacting massive particles (WIMPs), a potential dark matter candidate, after they are gravitationally captured by objects such as the sun or earth [138].

A. Motivation and Scientific Impact of Future Measurements

High energy neutrinos are observed by detecting the charge leptons arising from the charged-current neutrino interaction with a nucleon: $\nu_l + N \rightarrow X + l$. In the case of ν_μ interactions, the sensitive volume exceeds the detector physical volume, as long as the resulting μ passes through the detector volume. This yields substantially more detectable events at higher neutrino energies. To quantify this effect, the effective area of a detector to neutrinos is used as a measure of detector sensitivity. For a incoming neutrino flux Φ, the number of detected neutrino events is given by:

$$N_D = \int dt \, \int d\Omega \, \int dE \, \Phi_\nu(t, \Omega, E) \, A_{eff}(\Omega, E)$$

At neutrino energies > 100 GeV, the resulting muons have a strong angular correlation (~ 3 degrees or better) with the incoming neutrino direction.

This strong correlation between neutrino and muon directions as neutrino energy increases is shown in Figure 69. By exploiting this angular correlation, and potentially using time correlations with other astronomical observations of high energy phenomena (GRB alerts, for example), the impact of the irreducible background from atmospheric neutrino events can be reduced, enabling searches for cosmic neutrinos and neutrino astronomy.
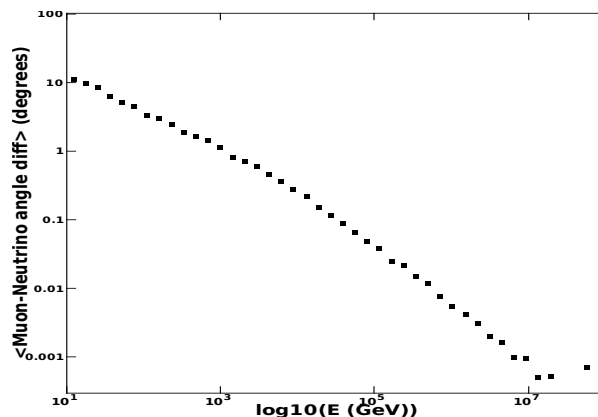
FIG. 69. Mean angular separation between incoming neutrino direction and outgoing muon direction for charged-current interactions as a function of neutrino energy. From toy Monte Carlo study, see section VIII B.

Previous generations of experiments have performed searches for cosmic neutrino signals, but to date, have only set limits. The first generation of these detectors, AMANDA [139], Baikal [140], and ANTARES [141], as well as the current generation of detectors (IceCube, including the DeepCore low energy extension [142]) have been specifically designed to search for cosmic neutrino fluxes and have set the strongest limits on cosmic neutrino fluxes from point sources [143], diffuse ultra-high-energy sources [144], coincident neutrino emission from GRBs [145]) and WIMPs [146]. Super-Kamiokande has also performed similar searches [147–149], also with no positive detection of a source. Within the last year, the IceCube detector has been augmented with the DeepCore extension (volume ~ 15 Mt), with several additional optical sensors added to the deepest, clearest portion of the instrumented volume to significantly increase the sensitivity of the detector to below 100 GeV. In the next 5-15 years, the continued operation of both the northern and southern hemisphere neutrino telescopes will either result in a set of sources to follow up with more detailed limits or stringent limits on neutrino emission from astrophysical sources about ~ 10 GeV.

B. Sensitivity of Reference Configurations

In order to evaluate the sensitivities of the proposed far detector technology options for the LBNE experiment to a astrophysical neutrino signal, a toy event simulation study was produced. This toy simulation was used considering that full detector simulations are still in early stages of readiness and there was limited manpower to perform these studies. These simulations made a set of assumptions that simplified the far detectors:

- The detector fiducial volumes were modeled as spheres with radii producing the same volumes as reference configurations. The detector cross-sectional areas were reproduced to within ∼20%.
- Detectors were assumed to be fully efficient at triggering and reconstructing any muon track within the modeled fiducial volumes for muon energies > 100 MeV.
- Variations in detector technology choices (depth, Gd loading, PMT coverage) are neglected in this study, but do not greatly impact detection of muons with E > 100 MeV.
- Backgrounds from misreconstructed atmospheric muons and atmospheric neutrinos have not been included.

These should be included in future studies aimed to produce more accurate sensitivities.

As part of this simulation, 1 GeV–100 PeV neutrinos were propagated through the earth and weighted based on interaction probability. Both charged-current and neutral-current interactions are included. Any resulting muons are propagated until they range out, with special focus on the region surrounding the detector volume. Events that produced a muon of sufficient energy within the modeled detectors were counted and used to calculate the detector neutrino effective areas as a function of energy. The effective areas obtained from this toy simulation are shown in Figure 70 for a 100 kt water cherenkov detector and the 17 kt liquid argon detectors. More details of these simulations are available in a UHE TG call presentation [150]

This toy simulation tool was also applied to an IceCube-like detector (detector radius of 500 m and muon detection threshold of 20 GeV). From this simulation, effective areas and events rates that agree with current sensitivities of the IceCube detector were obtained, verifying the approximations made and event rates obtained to an accuracy of roughly a factor of 2-3.
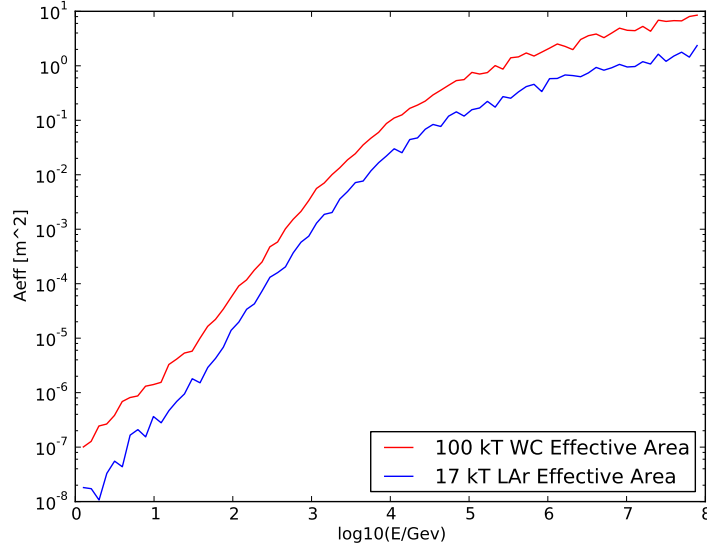
FIG. 70. 100 kt water cherenkov(WC) and 17 kt Liquid Argon (LAr) effective areas as a function of neutrino energy from the toy simulation. For comparison, the IceCube effective area at 1 TeV is ∼1 m^2.

To evaluate the sensitivity of these detector to predicted astrophysical neutrino fluxes, three test cases where selected:

1. A generic E^{-2} point source in the northern hemisphere with a flux roughly equal to the current ANTARES point source sensitivity ($\frac{dN}{dEe} = 5 \times 10^{-8}E^{-2}[GeV^{-1} \ cm^{-2}sec^{-1}]$) [151]
2. 150 gamma-ray bursts with a neutrino fluence from the Waxman-Bahcall fireball model [136]
3. 100 GeV mass WIMP annihilation at the Galactic Center (GC). This portion of the study is still a work in progress. Results to be updated soon. [152]

Predicted event rates are produced by convolving the neutrino effective area for each detector with the predicted neutrino flux. The predicted event rates *per year* are summarized in Table XIX and can be appropriately scaled to the number of detectors of each type under consideration. Even with these smaller detector volumes, it should be noted that the most probably neutrino energy detected is ∼10 TeV, as shown in Fig. 71, the "sweet spot" when convolving a falling neutrino spectrum with the rise in neutrino effective area.

	(1) Point source	(2)100 WB GRB	(3) GC WIMPs
100 kt WC	0.7	0.07	TBD
17 kt LAr	0.2	0.02	TBD
Toy IceCube	214	18	∼10s

TABLE XIX. Predicted number of events per year for 3 studied astrophysical sources. Event rates in 1, 2 or 3 of each detector technology can be obtained by multiplication of numbers by N_{detector} for each type.
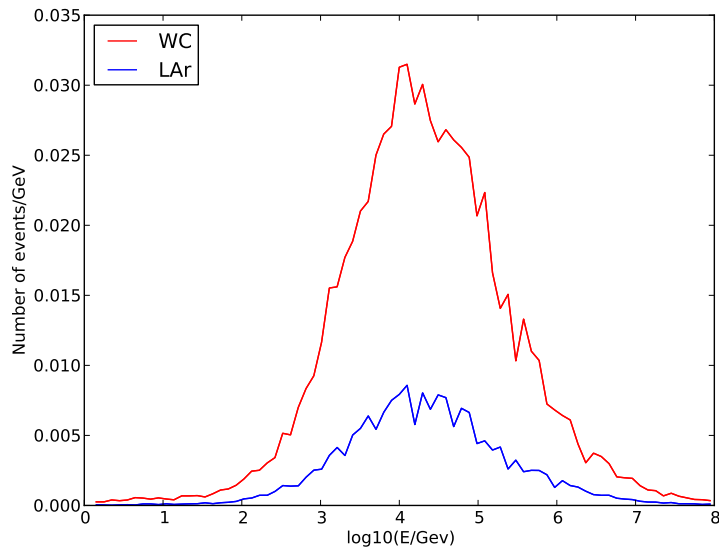
FIG. 71. Energy distribution for detected events from a hypothetical point source with an E^{-2} spectrum. For both WC and LAr, the mean energy predicted is ∼10 TeV.

C.   Next Steps

One item still needs to be completed as part of this study:

- Finish the calculation of expected neutrino rates from the galactic center for 100-GeV WIMPs. This WIMP mass is likely the best chance for an significant impact, given them threshold of the larger neutrino observatories, but rates are still expected to be small.

D.   Conclusions

While somewhat simple in nature, this preliminary study of astrophysical neutrino fluxes in the proposed LBNE far detector technology options indicates that neither 100-300 kt of water cherenkov detector or 17-51 kt of Liquid Argon are optimal detectors for these neutrino signals. Predicted event rates in the proposed detector geometries are not competitive with the operating generation of neutrino telescopes. There is a slight advantage for the water-cherenkov options in terms of predicted event rates, based on the larger detector cross-sectional area for muon detection, but this difference is small, and should not be over-emphasized.

This study should not prevent the investigation of astrophysical neutrinos signals in the operating detectors. Pursuing searches that search for signals at the edge of detector capabilities ensure that background sensitivities (in this case, to atmospheric neutrinos) are very well understood and provide an excellent learning opportunities for students.

IX. SOLAR NEUTRINOS

A. Motivation and Scientific Impact of Future Measurements

Even after the long standing mystery of missing solar neutrinos [153] was explained by data from the Super-Kamiokande and SNO [154] experiments as flavor transformation of solar neutrinos, there are still interesting open questions in solar neutrino physics. Some of these are astrophysical (like a measurement of the fraction of energy production via CNO cycle in the sun, or flux variations due to helio-seismological modes which reach the solar core, or long-term stability of the solar core temperature). But even particle physics questions remain. Can the MSW model explain the amount of flavor transformation as a function of energy, or are non-standard neutrino interactions required? Do solar neutrinos and reactor anti-neutrinos oscillate with the same parameters? Some of these questions will be answered by experimental data in the immediate future (like SNO+, KamLAND solar phase, further Borexino data, etc.), but high statistics measurements will be necessary to further constrain alternatives to the standard oscillation scenario. Either a large water Cherenkov detector, or a large liquid Argon detector, or a large liquid scintillation detector offers unique possibilities to study these questions.

B. Sensitivity of Reference Configurations

Using event selection and reconstruction efficiency similar to Super-Kamiokande, a 300 kt water Cherenkov detector at DUSEL would collect 470,000 recoil electrons (after selection efficiency) in ten years from ^{8}B solar neutrinos above 7 MeV. It could trace the MSW flavor transformation curve with high precision (the uncertainties of 0.5 MeV-wide energy bins range from 0.3% to 3%) and should be sensitive to the change in flavor transformation due to the earth's matter density which leads to the so-called day/night effect, the asymmetry $A_{\mathrm{DN}} = \frac{D-N}{0.5(D+N)}$ between the event rates during the day $(= D)$ and night $(= N)$. This asymmetry is expected to be only 1.5 to 2% [155]; it would be measured by a 300 kt water Cherenkov detector to 0.3% statistical uncertainty thereby constraining $\Delta m^2_{\mathrm{solar}}$, which is large when measured by solar neutrinos only. This uncertainty is unlikely to improve otherwise, since future low energy solar neutrino measurements cannot constrain it. It is also interesting since a deviation in this parameter between solar neutrinos and reactor anti-neutrinos cannot be reconciled by three-flavor mixing effects (like the mixing angle).

Obviously, sparser instrumentation of this 300 kt water Cherenkov detector immediately worsens its sensitivity to solar neutrinos. Not only will the energy threshold increase, but also the energy resolution and therefore background contamination worsens. Super-Kamiokande-II demonstrated solar neutrino measurements in a large water Cherenkov detector with ~ 3 photo-electrons per MeV with a threshold of 7 MeV. Radioactive background from radon decays fluctuated above this threshold and contaminated the $\sim 7,200$ solar neutrino events collected. The statistical uncertainty of the day/night asymmetry increased to 4.2% from the expected 2.4%. As a conservative estimate, we can expect the statistical accuracy of the day/night asymmetry measured by a 300 kt water Cherenkov detector to reach 0.6% after ten years, if it collects only 3 photo-electrons per MeV. Super-Kamiokande (if it runs continuously until then) will have reached $\sim 0.75\%$ at that time.

The solar neutrino physics potential of a 17 kt liquid Argon TPC largely depends on the energy threshold and depth. Since the spallation of the ^{40}Ar (a rather complex nucleus compared to ^{16}O) is likely to produce many long-lived spallation products, only a TPC at the deepest location has a reasonable chance of detecting solar neutrinos. Given a 10 MeV neutrino energy threshold (as reported by the ICARUS collaboration [156]), it could then measure the CC/NC ratio of ^{8}B solar neutrinos with high statistical accuracy and thereby test the MSW flavor transformation curve with high precision if the detector itself has low radioactivity levels.

The main advantage of a large, clean liquid scintillator detector is its ability to measure low energy solar neutrinos as well. Borexino has demonstrated an energy threshold of 3 MeV for ^{8}B solar neutrinos. Since DUSEL is deep underground. A large, clean liquid scintillator detector could precisely measure the pep flux (constraining the solar mixing angle to 1%), measure the CNO fluxes and test the MSW flavor transformation curve where it transitions from the vacuum oscillation expectation.

C. Conclusions

Even after several decades of solar ^{8}B neutrino experiments, the LBNE detector at DUSEL has the potential to make unique precision measurements. For the water Cherenkov option, the full potential is only reached with a high density photo-sensor instrumentation yielding at least ~ 6 photo-electrons per MeV. A large liquid argon TPC will only impact solar neutrino physics, if the threshold is kept low and the detector is build with state-of-the art

Configuration Number	WC Signal Size p.e. per MeV	WC Day/Night Asymmetry St. Acc. (10 years)
1	~ 3	0.6%
1a	~ 6	0.3%
1b	~ 6	0.3%
2	n/a[a]	n/a
2a	n/a	n/a
2b	n/a	n/a
3	~ 3	0.7%
3a	~ 6	0.4%
3b	$\sim 3\&6$	0.5%
4	~ 3	0.7%
4a	~ 6	0.4%
4b	$\sim 3\&6$	0.5%
5	~ 6	0.5%
6	~ 6	0.5%

[a] Sensitivity to charged-current to neutral-current ratio depends critically on the threshold and cleanliness of the liquid argon TPC.

TABLE XX. Summary of solar neutrino capabilities of the reference configurations. For liquid argon TPC at $300'$ and $800'$, spallation backgrounds are likely to overwhelm the solar signal.

radiopurity requirements (as demonstrated by the Sudbury Neutrino Observatory and the BOREXINO). A large clean liquid scintillator detector has the best solar neutrino physics potential: at this depth it could not only measure elastic scattering of electrons and solar ^{8}B neutrinos to very low energies (~ 3 MeV) but also probe CNO cycle and pep neutrinos.

X. GEONEUTRINOS AND REACTOR NEUTRINOS

Within the earth it is believed that radioactive decays of uranium and thorium are the most significant source of heat that causes mantle convection, the fundamental geological process that regulates the thermal evolution of the earth and shapes its surface. Until recently, estimates of the total uranium and thorium content of the earth were inferred from earth formation models. However, it has been known for a long time that the uranium and thorium decays produce electron anti-neutrinos, so-called geo-neutrinos, and the detection of these geo-neutrinos near the surface of the earth can directly inform us of the deep earth uranium and thorium content. The low flux of electron anti-neutrinos from reactors, so called reactor neutrinos, at DUSEL makes it ideal for demonstrating the ability of future large detectors designed for long range nuclear reactor monitoring.

A. Motivation and Scientific Impact of Future Measurements

The geo-neutrino flux observed near the surface of the earth has a contribution from uranium and thorium in the crust and mantle. For detectors located in continental crust approximately 80% of the signal comes from the crust, with the remainder coming from the mantle. Without the ability to determine the origin of the observed geo-neutrinos, it is not possible to determine the relative contribution from the crust and mantle with a single detector. However, with accurate knowledge of the uranium and thorium content in the crust surrounding DUSEL with approximately 200 km, it should be possible to determine the geo-neutrino contribution from the mantle although this requires higher precision due to the small fraction coming from the mantle.

KamLAND and BOREXINO have currently observed total geo-neutrinos fluxes with sensitivities limited by statistics to approximately 30%, this sensitivity will improve only slightly with more time. The SNO+ experiment, which is currently under construction, should be able to measure the total geo-neutrino flux to a sensitivity of approximately 20%. Because of the low reactor neutrino flux and the large size, a detector at DUSEL would be able to measure the geo-neutrino flux to approximately 5% (limited by systematic errors) in 1 year. This should also allow for a relatively accurate measurement of the mantle geo-neutrino contribution with detailed knowledge of the local uranium and thorium crustal geo-neutrino contribution.

There are two other large geo-neutrino detectors proposed. The LENA detector would be competitive with a large detector at DUSEL, while the Hanohano detector would be complementary, as it would directly probe the mantle, so combination with a detector on the crust would determine the crustal contribution.

Aside from measuring the total uranium and thorium flux, it is predicted that the ratio of the Th/U abundance ratio in the earth is about 4/1, and measuring deviations from this value could inform us on the processing of the crustal material. Because this is a ratio, accurate measurement of this requires a larger detector than KamLAND, BOREXINO, or SNO+.

Although the flux of reactor neutrinos at DUSEL is about 24 times smaller than that at KamLAND, with a detector more than 24 times as large it should be possible to observe more reactor neutrinos. The advantage of DUSEL is that the nuclear reactors are located further away, resulting in more neutrino oscillation "wiggles" in the energy spectrum. With sufficient energy resolution it might be possible to measure the neutrino mixing parameter Δm_{12}^2 to approximately 1%, an improvement upon the 3% accuracy achieved with KamLAND.

B. Sensitivity of Reference Configurations

In a water Cherenkov detector electron anti-neutrinos can be detected by neutron inverse-beta-decay

$$\bar{\nu}_e + p \rightarrow n + e^+ \tag{4}$$

The positrons energy is equal to the antineutrinos energy minus 1.8 MeV. The maximum energy for geo-neutrinos is 3.3 MeV, although the peak in the signal is at 2.3 MeV, this results in positrons with a peak energy of 0.5 MeV and a maximum of 1.5 MeV, making it impossible to detect with a water Cherenkov detector even with the addition of gadolinium and high photocathode coverage. The energy of reactor neutrinos extends up to approximately 9 MeV making it possible to detect them with a water Cherenkov detector, however all configurations would have energy resolution below $5\%/\sqrt{E[\text{MeV}]}$, which would wash out the oscillation spectrum, limiting the measurement to a total flux measurement.

In a liquid Ar detector electron anti-neutrinos can be detected by Ar inverse-beta-decay

$$\bar{\nu}_e + {}^{40}Ar \rightarrow {}^{40}Cl^* + e^+ \tag{5}$$

The threshold for this reaction is approximately 8.5 MeV, which means that it cannot be used to detect either geo-neutrinos or reactor neutrinos. There are also elastic scattering reactions; however, these are sensitive to neutrinos as well as antineutrinos, so in order to eliminate backgrounds from solar neutrinos we need to be able to reject these by pointing at a level better than one in a thousand. At these low energies this is probably not possible with a liquid Ar detector.

C. Conclusions

The science case for detecting geo-neutrinos is very strong, it is somewhat weaker for detecting reactor neutrinos. However, it is likely not possible that these can be detected with any of the LBNE reference detector configurations, although it may be possible with a large liquid scintillator detector.

XI. SHORT BASELINE PHYSICS

The design of the near detector complex is still evolving, but for the purposes of this fall 2010 report we have considered configurations with combinations of the most likely technologies based on previous studies [157]: a multi-ton liquid argon TPC (LAr) and two designs for Fine-Grained detectors with embedded targets of H_2O or D_2O. In this section we will try to evaluate the physics potential of all the proposed detectors, with particular emphasis on the combined performance of different technologies that could be accommodated together within the near detector complex.

One limitation of our studies is the lack of a complete GEANT simulation for any of the reference detector options. Therefore, we evaluate the sensitivity to different measurements based on calculations and parameterizations of the resolutions and detector response. Whenever possible, we try to extrapolate the detector performance from similar existing or past experiments. This is particularly relevant for the fine-grained tracker, for which we used results achieved by MINERνA for the scintillator option and by NOMAD for the straw tube option (HiResMν).
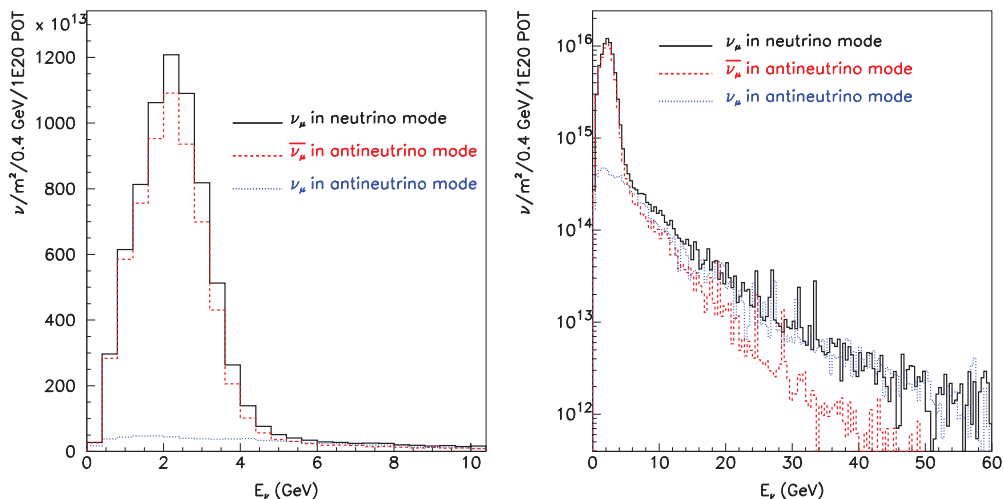
FIG. 72. Comparison of predicted neutrino and antineutrino mode fluxes at the LBNE near detector situated at 670 m on a linear (left) and log scale (right). Shown in black is the ν_μ flux in neutrino mode. Both the $\bar{\nu}_\mu$ (red) and ν_μ (blue) fluxes are plotted for antineutrino mode. All fluxes assume the 120 GeV NuMI-based design with a 250 kA horn current, and a 2 m radius 280 m long decay region. These distributions have not been cross section weighted [158].

For the beam, we take as a reference the "Low Energy (LE) beam" spectrum, with the near detector located 670 m from the target, a proton energy of 120 GeV, a horn current of 250 kA and a 2 m radius by 280 m long decay region. All the sensitivity studies are performed with the 2009 NuMI-based beam design. Fig. 72 shows the resulting spectra for both the neutrino and the anti-neutrino mode of the beam. It is worth noting that, as discussed in Section III B, different beam parameters resulting in different beam spectra are being considered for the LBL oscillation analysis. The differences with respect to our reference spectrum can be large, especially in the high energy tail, which is particularly relevant for the short baseline measurements. Table XXI lists the expected number of muon neutrino interactions at the LBNE 670-m near detector site per ton of detector and for equivalent beam exposures for both water and argon-based detectors. Neglecting detection efficiencies and acceptance, the total raw event yields are similar for water and argon. We evaluate the physics potential resulting from two different assumptions for the total exposure:

- Scenario A: A nominal long-baseline program that delivers 7.3×10^{20} protons-on-target (POT)/year for three years in neutrino mode and three years in anti-neutrino mode with a beam power of 700 kW.

- Scenario B: A high statistics program that delivers a total 10^{22} POT. With a 700 kW beam this program would require 14+14 years of running (a > 2 MW beam would be required to complete this scenario in a 3+3 year run).

The reference fiducial mass is assumed to be 7 t for the fine-grained tracker (both for the scintillator and for the straw tube options), 100 t for the LAr without a magnetic field and 25 t with a magnetic field.

For better clarity, we group the sensitivity studies in two categories:

1. Measurements to constrain systematic uncertainties in the Long-Baseline (LBL) neutrino oscillation analyses;

2. Precision measurements of neutrino interactions.

The design of the ND and the focus of our sensitivity studies are driven mainly by the first category since the primary goal of the LBNE project is to perform these measurements with the best possible sensitivity. However, the associated performance requirements for the ND complex have not yet been established. For example, the precision required on the absolute flux is still under investigation by the Long-Baseline and ND groups. For the purposes of the study reported here, we have investigated the capability of several candidate ND configurations and show that they meet or exceed the anticipated required precision based on preliminary estimates.

As will be discussed in the following sections, the two categories of measurements are highly complementary. In general, the measurements required for the oscillation studies involve the same physics processes as the precision measurements and the accuracy needed for the latter will certainly benefit the oscillation measurements and further study may show that a similar level is actually required. In some cases a combined analysis extracting simultaneously the underlying physics parameters is the only way to reduce systematic uncertainties. One primary example is the determination of the (anti)-neutrino fluxes in the presence of high Δm^2 oscillations. Similarly, a precise extraction of the (anti)-neutrino fluxes is a necessary condition for any precision measurement of cross sections or fundamental properties of (anti)-neutrino interactions.

A. Measurements to Support the Far Detector Studies

In order to allow the sensitivity of the FD to be exploited to its fullest, the Near Detector (ND) should establish the number of expected events in the FD in the absence of oscillations with a high precision. It will not be sufficient to merely compare the event rates at the two detectors because the neutrino energy distributions will be somewhat different at the two detectors. The differences in neutrino energy between the far and near detectors are readily calculable, but the effect of these differences on the observed event rates depends on neutrino interactions in the material of the FD. The rates observed at the FD depend on fluxes and cross sections, which must be known for both ν and $\bar{\nu}$ as a function of energy, for all the processes involved in the FD oscillation studies. In addition, a robust computerized simulation of the response of the FD is required. Hence high statistics information from the ND on the energy dependence of the yields of interactions of the various neutrino types must also be supplied. With its greater flux and sensitivity the ND can quantify any background processes that could interfere with the signal at the FD that is not adequately incorporated in the simulation of the FD response.

Production mode	H_2O	Ar	Ar/H_2O ratio
CC QE ($\nu_\mu n \to \mu^- p$)	18,977	23,152	1.22
NC elastic ($\nu_\mu N \to \nu_\mu N$)	7,094	7,165	1.01
CC resonant π^+ ($\nu_\mu N \to \mu^- N \pi^+$)	25,821	24,014	0.93
CC resonant π^0 ($\nu_\mu n \to \mu^-\, p\,\pi^0$)	6,308	7,696	1.22
NC resonant π^0 ($\nu_\mu N \to \nu_\mu\, N\, \pi^0$)	6,261	6,198	0.99
NC resonant π^+ ($\nu_\mu p \to \nu_\mu\, n\, \pi^+$)	2,694	2,182	0.81
NC resonant π^- ($\nu_\mu n \to \nu_\mu\, p\, \pi^-$)	2,325	2,930	1.26
CC DIS ($\nu_\mu N \to \mu^- X$, $W > 2$)	29,989	31,788	1.06
NC DIS ($\nu_\mu N \to \nu_\mu X$, $W > 2$)	10,183	10,285	1.01
CC coherent π^+ ($\nu_\mu A \to \mu^- A \pi^+$)	1,505	1,505	1.01
NC coherent π^0 ($\nu_\mu A \to \nu_\mu A \pi^0$)	790	790	1.01
NC resonant radiative decay ($N^* \to N\gamma$)	41		
Inverse Muon Decay ($\nu_\mu e \to \mu^- \nu_e$)	6	6	1.00
$\nu_\mu e^- \to \nu_\mu e^-$	11	11	1.00
Other	17,023	17,193	1.01
Total CC	94,948	100,645	1.06
Total NC+CC	129,028	134,189	1.04

TABLE XXI. Estimated ν_μ production rates for both water and argon targets per ton (water or argon) for 1×10^{20} POT at 670 m assuming neutrino cross sections predictions from Nuance [159] and a 120 GeV proton beam, 250 kA horn current, and a 2 m radius 280 m long decay region. Processes are defined at the initial neutrino interaction vertex and thus do not include final state effects. These estimates do not include detector efficiencies or acceptance [158, 160].

1. In Situ Measurement of Fluxes for the LBL Oscillation Studies

since the ND is close to the neutrino source it sees a neutrino energy spectrum slightly, but significantly, different from that at the FD. There are differences in the energy of the principal components of the ν_μ and $\bar\nu_\mu$ beams that must be accounted for quantitatively. The main task of the near detector complex is the measurement of the flux as a function of neutrino energy for each neutrino species ($\nu_\mu, \bar\nu_\mu, \nu_e, \bar\nu_e$). Ideally this flux measurement should be an absolute measurement using known cross sections to verify the fluxes calculated by the neutrino production models. This verification is essential in providing confidence in the knowledge of the flux.

As discussed in the following, we will have several independent methods to determine the (anti-)neutrino fluxes from the ND data at LBNE. The combination of the large statistics expected at LBNE with the finely segmented detectors at the near site allows comparable precisions from different techniques. This redundancy of measurements is a necessary condition for the validation of the flux extraction at the level of accuracy expected at LBNE.

The in situ determination of neutrino fluxes is not only a service measurement crucial for the oscillation studies in the FD, but it is closely related to the precision measurements of fundamental interactions discussed in Section XI B. Indeed, the possibility to make unexpected discoveries within the short baseline physics program critically depends upon the knowledge of the incoming (anti)neutrino flux. Historically, the uncertainty on the fluxes has always been one of the main limiting factors for all past neutrino scattering experiments. The high intensity of the LBNE beam coupled with the excellent granularity in the ND complex would allow a substantial reduction of the flux uncertainty. Furthermore, as discussed in the following, the extraction of the fluxes themselves relies upon the knowledge of specific physics processes, requiring an understanding of the theoretical and experimental issues related to their measurements.

Flavor	Technique	Relative abundance	Absolute normalization	Relative flux $\Phi(E_\nu)$	Detector requirements
ν_μ	$\nu e^- \to \nu e^-$	1.00	1-3%	$\sim 5\%$	e identification/resolution e^-/e^+ separation
ν_μ	$\nu_\mu e^- \to \mu^- \nu_e$	1.00	1-4%		μ^-/μ^+ separation μ energy scale
ν_μ	$\nu_\mu n \to \mu^- p$ $Q^2 \to 0$	1.00	$3-5\%$	$3-5\%$	D target p angular and momentum resolution
ν_μ	low-ν_0	1.00		2.0%	Magnetized detector separating μ^-/μ^+
ν_e	low-ν_0	0.01	1-3%	2.0%	e^-/e^+ separation (K_L^0)

TABLE XXII. Precisions achievable from in situ ν_μ and ν_e flux measurements in the fine-grained ND with different techniques. The reference beam configuration with a distance from the target of 670 m, a 120 GeV proton beam, 250 kA horn current, and a 2 m radius 280 m long decay region is assumed.

a. **Determination of the Absolute Flux Normalization**   The experimental determination of the absolute neutrino flux relies upon the measurement of well-known physics reactions in the ND. There are three main complementary options to be exploited at LBNE:

1. Neutral-Current elastic scattering off electrons: $\nu e^- \to \nu e^-$;
2. Inverse Muon Decay (IMD) interactions: $\nu_\mu e \to \mu^- \nu_e$;
3. Quasi-elastic (QE) Charged-Current interactions in the limit $Q^2 \to 0$: $\nu_\mu n \to \mu^- p$.

The total cross section for NC elastic scattering off electrons is given by [162]:

$$\sigma(\nu_l e \to \nu_l e) = \frac{G_\mu^2 m_e E_\nu}{2\pi}\left[1 - 4\sin^2\theta_W + \frac{16}{3}\sin^4\theta_W\right] \tag{6}$$

$$\sigma(\bar\nu_l e \to \bar\nu_l e) = \frac{G_\mu^2 m_e E_\nu}{2\pi}\left[\frac{1}{3} - \frac{4}{3}\sin^2\theta_W + \frac{16}{3}\sin^4\theta_W\right] \tag{7}$$

where θ_W is the weak mixing angle. For $\sin^2\theta_W \simeq 0.23$ the above cross sections are very small $\sim 10^{-42}(E_\nu/\text{GeV})\,cm^2$. The NC elastic scattering off electrons can be used to determine the absolute flux normalization since the cross sections only depend upon the the knowledge of $\sin^2\theta_W$.

The value of $\sin^2\theta_W$ at the average momentum transfer expected at LBNE $Q \sim 0.07\,\text{GeV}$ can be extrapolated down from the LEP/SLC measurements with a precision of $\sin 0.2\%$ within the Standard Model (SM). However, in order to take into account potential deviations from the SM predictions, in the flux extraction we must initially consider a theoretical uncertainty $\leq 1\%$, obtained from direct measurements of $\sin^2\theta_W$ at momentum scales comparable to the LBNE one.

As discussed in Section XI B 1 a, precision electroweak measurements with the ND data at LBNE can determine the value of $\sin^2 \theta_W$ to better than 0.3%. The theoretical uncertainty on the absolute flux normalization can therefore be improved substantially by a combined analysis with the electroweak measurements.
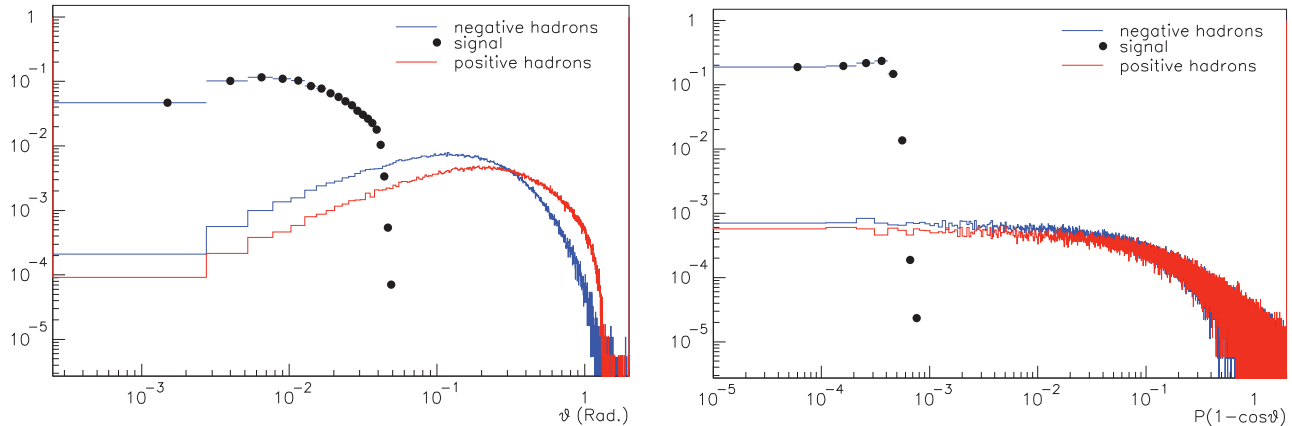

FIG. 73. Distributions of the angle of the electron with respect to the beam direction (left) and of the discriminating variable $P(1 - \cos\theta)$ (right) for NC elastic scattering off electrons and for the corresponding backgrounds in the ND.

The signature of the process $\nu_l(\bar{\nu}_l)e \to \nu_l(\bar{\nu}_l)e$ is a single electron in the final state, emitted almost collinearly with the beam direction ($\theta \sim$ mrad). The dominant backgrounds are given by NC π^0 production and single photon production, in which one photon fakes a single electron. A smaller background contribution is given by ν_e quasi-elastic scattering events in which the proton is not visible. This measurement requires a detector that can efficiently distinguish photons from electrons.

The low density magnetized tracker proposed for LBNE can identify electrons and positrons and reconstruct the corresponding track parameters, allowing a background rejection $\leq 10^{-6}$ with an overall efficiency for NC elastic scattering events of 64%. Figure 73 shows the distributions of kinematic variables for signal and background. It is thus possible to select a sample of NC elastic scattering events off electrons with small background in the LBNE ND. The main limitation of such a measurement is the statistics of the selected sample, which, for the reference beam configuration with 22×10^{20} pot and a fiducial mass of about 7 t, corresponds to about 1000 events with a background of six events, giving a 3% precision on the flux normalization. It must be noted that in a low density magnetized design the background originates from asymmetric γ conversions in which the positron is not reconstructed. This type of background is expected to be charge-symmetric and this fact gives a powerful tool to calibrate the π^0/γ background in situ.

We can now consider the performance of a LAr TPC, which is one of the options considered for the ND. It has good electron identification and energy resolution for electromagnetic showers ($3\%/\sqrt{E}$) and the rejection factor of π^0 background is at the level of $2 - 5 \times 10^{-3}$ with an electron reconstruction efficiency of $80 - 90\%$. A measurement of NC elastic scattering off electrons can therefore be competitive if we have a fiducial mass of the order 100 t. This would imply about 20,000 selected events with the reference beam configuration, giving a statistical precision on the flux normalization of 0.7%.

The measurement in LAr has substantially more background than the one performed in a low density magnetized detector and the analysis has to rely upon background subtraction as a function of the kinematic variable $E\theta^2$ (cf. CHARM II analysis). A combined analysis between the LAr massive detector and the low density magnetized tracker can achieve the optimal sensitivity. The low density magnetized detector provides a precise calibration of the background shape for the subtraction procedure, while the LAr massive detector gives the required statistics. The difference in target nuclei (carbon vs. argon) is not critical once the background shape is constrained as a function of $E\theta^2$, since the absolute background scale can be determined directly in LAr with the side bands. In addition, the NC π^0/γ production can be constrained by dedicated measurements in LAr and in the magnetized tracker. In summary, a combined analysis of the two detectors has the potential to extract the absolute flux normalization at LBNE to $\sim 1\%$ precision with the reference beam configuration.

The measurement of NC elastic scattering off electrons can only provide the integral of all neutrino flavors, which, for the neutrino mode, includes about 92% ν_μ, 7% $\bar{\nu}_\mu$ and 1% $\nu_e + \bar{\nu}_e$. In order to determine the individual ν_μ and $\bar{\nu}_\mu$ components we need to measure the ratio $\bar{\nu}_\mu/\nu_\mu$ from CC interactions to better than 10%. This requirement is relatively loose since with a magnetized detector we can measure $\bar{\nu}_\mu/\nu_\mu$ to a few percent. It must be noted that

the reactions $\nu_e e \to \nu_e e$ and $\bar{\nu}_e e \to \bar{\nu}_e e$ result from combined W and Z boson exchange. The corresponding cross section for $\nu_e(\bar{\nu}_e)$ is enhanced by a factor of about six (three) with respect to $\nu_\mu(\bar{\nu}_\mu)$. The relative ν_e contributions to the measured NC elastic scattering sample is therefore increased to about 6% of the total, requiring an additional measurement of the ratio ν_e/ν_μ from CC interactions to $10-15\%$.

The possibility to achieve the high statistics beam exposure (Scenario B) would have a substantial impact on the precision achievable with the NC elastic scattering off electrons since this channel is dominated by statistical uncertainties with the reference beam configuration. The resulting increase in the number of protons on target by a factor of four would allow the collection of about 80,000 events in the LAr detector, providing a statistical precision of $\sim 0.3\%$. At this level of precision the theoretical uncertainty on the knowledge of $\sin^2 \theta_W$ will start to play a role in the determination of the absolute flux normalization and a analysis will require a complementary precision electroweak measurement (Section XI B 1 a).

A second process that can be used to crosscheck the absolute flux normalization is the Inverse Muon Decay (IMD): $\nu_\mu e^- \to \mu^- \nu_e$. However, this reaction is characterized by a very high energy threshold $E_\nu > (m_\mu^2 - m_e^2)/2m_e \simeq 10.9$ GeV and therefore we expect only about 700 events in the fine-grained tracker with the reference beam configuration. With a fiducial mass of 100 tons we can collect about 10,000 IMD events in the LAr detector, which would provide an independent flux normalization with a statistical precision of $\sim 1\%$. The analysis has to rely upon the subtraction of the large background from ν_μ CC Quasi-Elastic events with a single reconstructed track in the final state and from the corresponding resonance and DIS events. The identification of the charge of the muon is a crucial requirement for this measurement. This task can be easily accomplished by the downstream magnetized tracker given that $E_\mu \geq 10.9$ GeV. The use of IMD provides a direct measurement of the ν_μ flux in the high energy tail of the spectrum. A relative determination of the flux as a function of E_ν is required to fully constrain the spectrum and to extract the corresponding total integral.

A third independent method to extract both the absolute flux normalization and the relative flux as a function of E_ν is through the Quasi-Elastic (QE) CC scattering $\nu_\mu n(p) \to \mu^- p(n)$. Neglecting terms in $(m_\mu/M_n)^2$, at $Q^2 = 0$ the QE cross section is independent of neutrino energy for $(2E_\nu M_n)^{1/2} > m_\mu$:

$$\frac{d\sigma}{dQ^2} \mid Q^2 = 0 \mid = \frac{G_\mu^2 \cos^2 \theta_c}{2\pi} \left[F_1^2(0) + G_A^2(0) \right] = 2.08 \times 10^{-38} \ cm^2 \, \text{GeV}^{-2} \tag{8}$$

which is determined by neutron β decay and has a theoretical uncertainty $< 1\%$. The flux can be extracted experimentally by measuring low Q^2 QE interactions $(0 - 0.05$ GeV$)$ and extrapolating the result to the limit of $Q^2 = 0$. This measurement requires a deuterium or hydrogen (for anti-neutrino) target to minimize the smearing due to Fermi motion and other nuclear effects. This requirement can only be achieved by using both H_2O and D_2O targets embedded into the fine-grained tracker and to extract the events produced in deuterium by statistical subtraction of the larger oxygen component. The experimental resolution on the muon and proton momentum and angle is crucial. A low density tracker with $\rho \sim 0.1$ g/cm^3 would increase the proton range by about one order of magnitude, thus increasing the proton reconstruction efficiency in the region of $Q^2 \leq 0.05$ GeV^2. The dominant uncertainties are related to the extrapolation to $Q^2 = 0$, to the theoretical cross section on deuterium, the experimental resolution, and to the statistical subtraction. Overall, it seems feasible to achieve a precision of $3 - 5\%$ on the fluxes with the current understanding of the theoretical cross sections.

b. **Determination of the Relative Flux as a Function of Energy** A precise determination of the relative neutrino flux as a function of energy can be achieved with the low-ν_0 method. The dynamics of neutrino-nucleon scattering implies that the number of events in a given energy bin with hadronic energy $E_{\text{had}} < \nu_0$ is proportional to the neutrino (antineutrino) flux in that energy bin up to corrections $\mathcal{O}(\nu_0/E_\nu)$ and $\mathcal{O}(\nu_0/E_\nu)^2$. The method follows from the general expression of the ν-nucleon differential cross section:

$$\mathcal{N}(\nu < \nu_0) = C\Phi(E_\nu)\nu_0 \left[\mathcal{A} + \left(\frac{\nu_0}{E_\nu} \right) \mathcal{B} + \left(\frac{\nu_0}{E_\nu} \right)^2 \mathcal{C} + \mathcal{O} \left(\frac{\nu_0}{E_\nu} \right)^3 \right] \tag{9}$$

where the coefficients $cal A = \mathcal{F}_2$, $\mathcal{B} = (\mathcal{F}_2 \pm \mathcal{F}_3)/2$, $\mathcal{C} = (\mathcal{F}_2 \mp \mathcal{F}_3)/6$ and $\mathcal{F}_i = \int_0^1 \int_0^{\nu_0} F_i(x) dx d\nu$ is the integral of structure function F_i. The number $\mathcal{N}(\nu < \nu_0)$ is proportional to the flux up to correction factors of the order $\mathcal{O}(\nu_0/E_\nu)$ or smaller, which are not significant for small values of ν_0 at energies $\geq \nu_0$. It should be pointed out that the coefficients $\mathcal{A}, \mathcal{B}, \mathcal{C}$ are determined for each energy bin and neutrino flavor within the ND data themselves. Since our primary interest is the relative flux determination, i.e. neutrino flux in an energy bin relative to another energy bin, variations in the coefficients do not affect the relative flux.

The prescription for the relative flux determination is simple: we count the number of ν-CC events below a certain small value of hadronic energy (ν_0). The observed number of events, up to the correction due to the finite ν_0 of the

order $\mathcal{O}(\nu_0/E_\nu)$, in each total visible energy bin is dominated by the corresponding lepton energy, is proportional to the relative flux. The smaller the factor ν_0/E_ν, the smaller is the correction. It is apparent from the above discussion that this method of relative flux determination is not very sensitive to nucleon structure, QCD corrections, and types of ν-interactions such as scaling or non-scaling. With the excellent granularity and resolution foreseen in the low density magnetized tracker it will be possible to use a value of $\nu_0 \sim 0.5$ GeV or lower, thus allowing flux predictions down to $E_\nu \sim 0.5$ GeV. For the scintillator option the value of a usable ν_0 is yet to be determined but it is expected to be higher than that for the low density tracker. Note that the non-prompt backgrounds will be larger with the higher density detectors, especially for the $\bar{\nu}_\mu$ component at low energy.

In this analysis, the key measurable quantities are the resolution for the low-ν events and the systematic precision of the muon-momentum. The $\nu_\mu(\bar{\nu}_\mu)$-CC flux provides a measure of the $\pi^+/K^+/\mu^+(\pi^-/K^-/\mu^-)$ content of the beam. We first obtain the relative $\nu_\mu(\bar{\nu}_\mu)$ flux at the ND. We then fit the $d^2\sigma/dx_F dP_T^2$ of the parent mesons to the ν_μ flux with a simple parametrization:

$$\frac{d^2\sigma}{dx_F dP_T^2} = f(x_F)g(P_T)h(x_F, P_T) \tag{10}$$

The ingredients to this empirical fit to the meson production cross section (EP) are the following:

- Trace parent mesons through a simulation of the beam elements;
- Decay the parent mesons;
- Predict ν_μ and $\bar{\nu}_\mu$ fluxes by folding experimental acceptance;
- Add external constraints on π/K from hadro-production experiments (MIPP);
- Compare predictions to the measured spectra at the ND and minimize the corresponding χ^2.

It must be noted that the simple smoothness requirement on the functional form in Eqn. (10) allows to extend the flux predictions down to $E_\nu \sim \nu_0$. In order to evaluate the sensitivity which can be achieved at LBNE with the low-ν_0 method we performed the flux analysis for the neutrino beam mode (positive focusing) using $\nu_\mu + \bar{\nu}_\mu$ CC mock-data from the low density magnetized detector and $\nu_0 < 1$ GeV. The systematic error analysis included the following effects:

- Variation of the functional form in Equation (10);
- Variation of both muon and hadron energy scales;
- Systematic shift of the ν_0 values by $\pm 20\%$;
- Variation of quasi-elastic, resonance and DIS cross sections by $\pm 20\%$;
- Effect of the beam-transport elements.

The beam-transport uncertainty will require additional studies after completing the design of the beam line since it depends on the precise beam and on the inert material that the hadrons encounter. Depending upon our knowledge of $p/\pi/K$ nuclear collisions, this uncertainty can become dominant for $\bar{\nu}_\mu$ production in the neutrino beam mode at low energy. Figure 74 shows the mock-data and the corresponding fitted flux with the ND positioned at 500 m from the target. Having constrained the $d^2\sigma/dx_F dP_T^2$ of the pions/kaons, we can predict the flux at the ND location. Overall we achieved a precision $\leq 2\%$ on the relative ν_μ flux with the low-ν_0 method in the energy region $1 \leq E_\nu \leq 30$ GeV in the fit with $\nu_0 < 1$ GeV. Similar uncertainties are expected for the $\bar{\nu}_\mu$ component (dominant one) in the anti-neutrino beam mode (negative focusing).

The low-ν_0 method was used to study the effect of different locations of the near detector on the flux predictions at the FD site. The low-ν_0 fit described above was repeated assuming a distance of the ND from the target of 1500 m, 1000 m, 750 m, and 500 m, respectively. It must be noted that the ratio between the spectra at the FD and ND sites is not flat even at L=1000 m. However, the spectral distortions increase substantially for $E_\nu < 5$ GeV as the distance from the target is reduced. The low-ν_0 method can correct for such spectral distortions since it directly extracts the parent $\pi^\pm/K^\pm/K_L^0$ content from the ND data and extrapolates the fluxes at the FD site by taking into account the beam transport elements and by decaying the mesons. Results show that the FD/ND ratio predicted by the low-ν_0 technique can reproduce the actual FD/ND ratio to better than 2%, regardless of the distance between the ND and the target. As a consequence the ND can be located closer to the target without increasing the systematic uncertainties for the LBL oscillation searches.

The relative flux as a function of energy could be also determined from NC elastic scattering off electrons, which is a two body process with the initial electron being at rest. The calculation of the incoming neutrino energy requires a resolution of few milliradians on the angle of the outgoing electron as well as a good energy resolution. The low density magnetized tracker can in principle fulfill such requirements. However, the limited statistics does not allow a

precision better than $\sim 5\%$ on the relative flux. The angular resolution of the LAr detector for electrons $\sim 8°$ does not allow a precise measurement of the spectrum due to multiple scattering and shower development.

A third independent method to determine the relative flux as a function of energy is using the quasi-elastic interactions on a deuterium target in the limit of $Q^2 \to 0$. The precision achievable with this technique is the same as the corresponding absolute flux measurement discussed in the previous Section.

ν_μ, Low-Nu0 Fit, ND at 500m
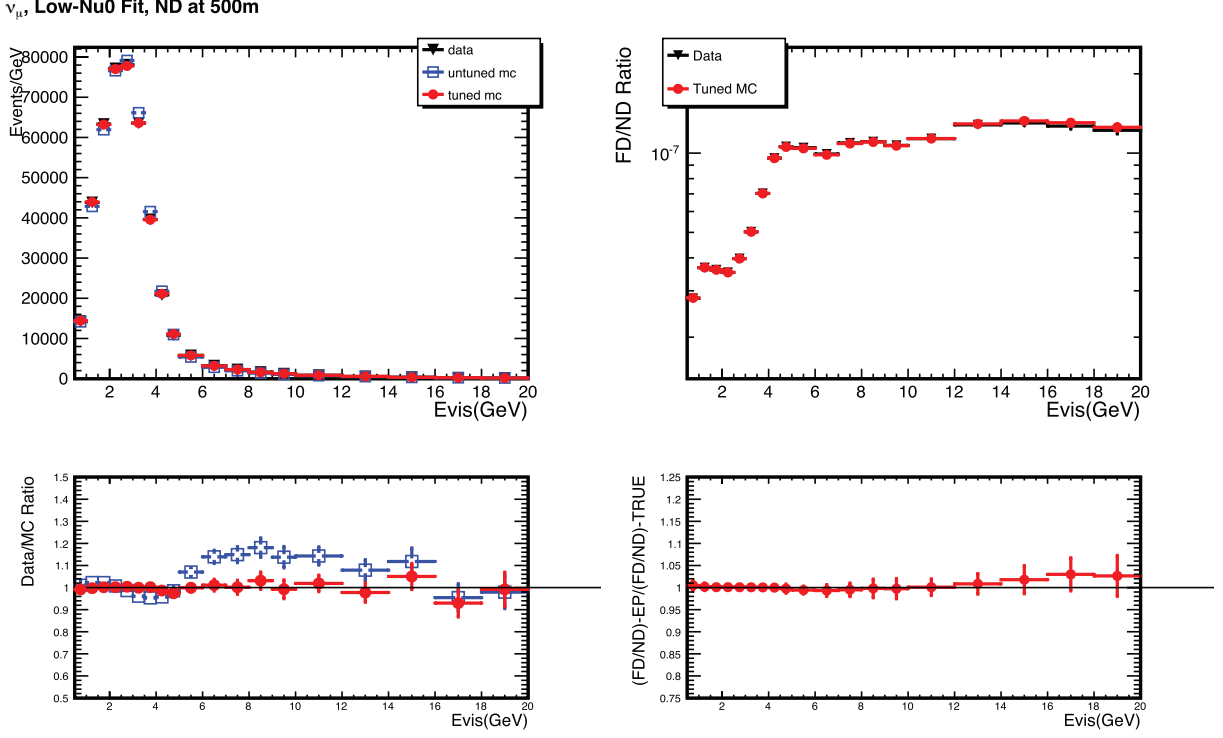
FIG. 74. Ratio FD/ND as determined in the ND with the low-ν_0 method for the ν_μ flux and a ND located at a distance of 500 m.

c. **Flavor Content of the Beam: $\nu_\mu, \bar{\nu}_\mu, \nu_e, \bar{\nu}_e$** As discussed in the previous Section, the low-ν_0 method allows the prediction of both the relative ν_μ and $\bar{\nu}_\mu$ at the FD location from the measure of the $\pi^+/K^+/\mu^+(\pi^-/K^-/\mu^-)$ content of the beam at ND. In addition, with a ND capable of identifying $\bar{\nu}_e$ CC interactions we can directly extract the elusive K_L^0 content of the beam. Therefore, an accurate measurement of $\nu_\mu, \bar{\nu}_\mu$ and $\bar{\nu}_e$ CC interactions provides an absolute prediction of the ν_e content of the beam, which is an irreducible background for the ν_e appearance search in the FD:

$$\nu_e \equiv \mu^+(\pi^+ \to \nu_\mu) \oplus K^+(\to \nu_\mu) \oplus K_L^0 \tag{11}$$

$$\bar{\nu}_e \equiv \mu^-(\pi^- \to \bar{\nu}_\mu) \oplus K^-(\to \bar{\nu}_\mu) \oplus K_L^0 \tag{12}$$

The μ component is well constrained from $\nu_\mu(\bar{\nu}_\mu)$ CC data at low energy, while the $K^\pm$ component is only partially constrained by the $\nu_\mu(\bar{\nu}_\mu)$ CC data at high energy and requires external hadro-production measurements of $K^\pm/\pi^\pm$ ratios at low energy from MIPP. Finally, the K_L^0 component can be constrained by the $\bar{\nu}_e$ CC data and by external dedicated measurements at MIPP. The relative contributions to the ν_e spectrum are 87% (54%) for the μ^+, 10% (33%) for the K^+ and 3% (15%) for the K_L^0 in the energy range $1(5) \le E_\nu \le 5(15)$ GeV. Based on the NOMAD experience, we expect to achieve a precision of $\le 0.1\%$ on the flux ratio ν_e/ν_μ. Taking into account the projected precision of the ν_μ flux discussed in the previous Section, this translates into an absolute prediction for the ν_e flux at the level of 2%. It should be pointed out that while the scintillator based ND option will be able to measure the $\nu_\mu, \bar{\nu}_\mu, \nu_e + \bar{\nu}_e$ flavor content of the beam it will not be able to distinguish between ν_e and $\bar{\nu}_e$. The non-prompt backgrounds in the $\nu_e + \bar{\nu}_e$ and in the $\bar{\nu}_\mu$ would also be larger.

Finally, the fine-grained ND can directly identify ν_e CC interactions from the LBNE beam. The relevance of this measurement is twofold: a) it provides an independent validation for the flux predictions obtained from the low-ν_0 method and b) it can further constrain the uncertainty on the knowledge of the absolute ν_e flux.

The flux ratio $\bar{\nu}_\mu/\nu_\mu$ as a function of energy can be determined with the low-ν_0 method with an accuracy of $\leq 2\%$ in the region $1.5 < E_\nu < 30\,\mathrm{GeV}$ and of $\sim 3\%$ in the region $0.5 < E_\nu < 1.5\,\mathrm{GeV}$. These numbers refer to the neutrino beam mode (positive focusing) and are obtained from a fit to mock-data from the low density magnetized detector to extract the parent π/K distributions. The beam-transport uncertainty can become dominant for $\bar{\nu}_\mu$ production (contamination) in the neutrino beam mode.

d. **Effects of High Δm^2 Oscillations on the Flux Extraction**   All the results described in the previous Sections were obtained under the assumption the events observed in the ND are originated by the same (anti)-neutrino flux produced by the decay of the parent mesons. The recent results from the MiniBooNE experiment might suggest the possibility of relatively high Δm^2 anti-neutrino oscillations consistent with the LSND signal. This effect, if confirmed, seem to indicate a different behavior between neutrinos and anti-neutrinos which would imply CP or CPT violation. The MINOS experiment also reported different oscillation parameters between ν_μ and $\bar{\nu}_\mu$ from the disappearance analysis.

The presence of high Δm^2 oscillations with characteristic oscillation length comparable with the ND baseline at the LBNE energies, would imply the spectra observed in the ND could be already distorted by neutrino oscillations. Two main effects are expected on the flux extraction from a MiniBooNE/LSND oscillation:

- The ν_e and $\bar{\nu}_e$ CC spectra cannot be directly used to extract the K_L^0 content in Equation (11) nor to predict event rates in the FD;
- A deficit is induced in the $\bar{\nu}_\mu$ CC spectrum from a significant disappearance rate.

Any in situ determination of the fluxes would then require the unfolding of the oscillation effect from the measured spectra. The measurement strategy in the ND should necessarily include a combined oscillation and flux analysis. Since the ND cannot be easily moved, different complementary measurements are needed. A MiniBooNE/LSND signal imposes stringent constraints on the ND design, as described in Section XI B 3 b.

Several follow-up experiments have been proposed to investigate the MiniBooNE/LSND effects: move MiniBooNE to a near detector location [163], OscSNS at the ORNL neutron spallation source [164] or a two-detector LAr experiment at the CERN PS [165]. All of them are expected to cover the region in the oscillation parameters consistent with MiniBooNE/LSND data, so that by the time LBNE will take data we might have a confirmation or disprove of the high Δm^2 oscillation hypothesis. However, the precision that will be ultimately achieved in the determination of the fluxes at LBNE is directly connected to the high Δm^2 oscillation parameters. If the oscillation is confirmed, we will need dedicated precision measurements in the ND at LBNE.

e. **External Constraints from Hadro-production Measurements**   One of the key points for an accurate determination of the fluxes is the possibility to exploit different complementary techniques, providing the redundancy necessary to reach precision of the order of few percent. In the previous Sections we have studied the measurements to be performed in situ. However, in order to fully exploit the power of the ND data some external measurements are required to constrain the yields of the parent mesons decaying into (anti)-neutrinos:

- K^+/π^+ as a function of $P(2 \leq P \leq 20\ \mathrm{GeV})$ and $P_T(\leq 0.4\ \mathrm{GeV})$ of K^+ and π^+;
- K^-/π^- as a function of $P(2 \leq P \leq 20\ \mathrm{GeV})$ and $P_T(\leq 0.4\ \mathrm{GeV})$ of K^- and π^-;
- K^0/K^+ ratio.

These can be performed with dedicated hadro-production experiments (e.g. MIPP at Fermilab). The accuracy in the external measurements must be comparable to the precision of the ND data and to the target precision for the flux extraction. The program must include separate measurements of the above quantities off different targets:

- The LBNE neutrino target;
- All the thin/thick Al, Cu, etc. targets that compose the horn and the beam elements;
- Air (N).

The external hadro-production measurements are crucial for the LBL ν_e appearance search since they allow a prediction of the $\nu_e(\bar{\nu}_e)$ flux independent from the ν_e and $\bar{\nu}_e$ CC events observed in the ND, as shown in Equation (11). It must be also noted that in the presence of high Δm^2 oscillations external hadro-production measurements are the only source of information which can be used to extract the K_L^0 contribution.

2. Background Measurements for the LBL Oscillation Studies

a. **Measurement of NC cross sections**   The most threatening background to the ν_e and $\bar{\nu}_e$ appearance measurements in LBNE is NC events in which the detritus of a π^0 decay mimics an electron. Similarly, in the ν_μ

and $\bar{\nu}_\mu$ disappearance study the largest background comes from the muonic-decay of a pion/kaon produced in a NC event. These backgrounds are particularly challenging in the energy region $0.5 \leq E_\nu \leq 3$ GeV where an additional complication arises from substantial matter induced neutrino oscillation. It follows that the largest background to the CC events in the far detector (FD) comes from non-prompt leptons, originating from the hadronic shower in NC and high-y_{Bj} CC interactions. As a first step to constrain the error on the non-prompt background to CC events in the FD, the fine-grained ND must measure the NC cross sections for different processes and the NC/CC ratio as function of the hadron-energy E_{had}.

b. **Measurement of π^0 and γ production in NC and CC** The near detector must determine the proportion of NC events as a function of neutrino energy, the yield of secondary π^0 in the NC interactions, and the energy and angular distributions of the π^0. Similarly, the ND must accurately identify single-photon yields in NC interactions and, in particular, the radiative decays of resonances where only a single energetic photon is evident. The prevalence of these decays are much affected by poorly characterized final state interactions and hence will require information from the ND. Recent theoretical work has pointed out that there are NC processes that produce single energetic photons at a level that could effect LBNE [166, 167]. Thus the ND must provide a detailed characterization of π^0 and γ in every class of event: multiplicity, energy, and transverse momentum dependence for a given E_{had} in NC and CC.

c. **Muonic decays of $\pi^\pm$ and $K^\pm$ from measurement of charged multiplicities** The dominant background to ν_μ and $\bar{\nu}_\mu$ CC events in the FD will come from the muonic decay of pions and kaons in NC and CC processes. Having determined the NC cross section relative to CC, the ND must determine the charged hadron multiplicity, energy and transverse momentum dependence, and provide an empirical determination of exclusive charged hadron production in ν-interaction.

d. **Calibration of the neutrino energy scale from reconstructed events** The neutrino energy scale directly affects the precision of the oscillation scale parameter. The ND measurements should provide an in situ calibration of the E_ν scale by measurement of the final state charged lepton and the energy in the hadronic debris.

e. **Measurement of exclusive and semi-exclusive processes and their nuclear dependence** The ND must provide differential cross section measurements for various exclusive, semi-exclusive, and inclusive ν_μ and $\bar{\nu}_\mu$ CC interactions. Among these, the most important to the FD measurement is the quasi-elastic (QE) interaction. The challenge for ND is to reduce and quantify the error due to nuclear effects, arising from initial and final state interactions, Fermi motion, Pauli-blocking, etc., in the QE and other CC interactions. To minimize the systematic error, ND should also determine exclusive and inclusive processes involving nucleon resonances. This measurement of background processes from exclusive and semi-exclusive reactions is part of the precision studies outlined in Section XI B 5 and Section XI B 7.

3. Measurement of Neutrino Induced Background to Proton Decay

In addition to backgrounds measurements for the long-baseline program, the ND complex can also provide an estimate of the ν induced background to the search for proton (nucleon) decay described in Section IV. Two generic proton decay modes are under study [168]: the π^0-mode, $e^+(\mu^+) + \pi^0$ and the kaon-mode, $\nu + K^+$, and $e^+(\mu^+) + K^0$.

The atmospheric neutrino spectrum is different from than that of the LBNE beam. However, an accurate determination of exclusive channels induced by the LBNE neutrino beam at $E_\nu \simeq 2$ GeV will provide empirical constraints for the atmospheric-neutrino background to proton decay at the FD, thus reducing the corresponding systematic uncertainty.

π^0 Decay Mode The K2K-ND has provided a definitive measurement of $e^+ + \pi^0$ [169]. The ND at LBNE will have an efficient π^0 and e^+ identification with purity exceeding 95% and the identification of μ^+-mode will be straightforward. In addition, and importantly, the ND aims to measure the exclusive first-generation mesons such as η, ρ^0, etc., besides π^0 accompanied by an e^+ or a μ^+.

Kaon Decay Mode Supersymmetric models favor the proton-to-kaon decay mode. The main focus of the ND measurements at LBNE is the exclusive K^0 production, i.e. $e^+/\mu^+ + K^0$. There is an existence proof of precise determination of K_S^0 in ν CC and NC interactions [170, 171]. The ND at LBNE will extend the K^0 measurement to lower energy. The $\nu + K^+$ is a challenge. However, it should be pointed out that if the K^0-mode is precisely measured then the K^+-channel can be accurately predicted.

B. Study of Neutrino Interactions

The unprecedented large neutrino fluxes available for the LBNE program will allow the collection of $\mathcal{O}(10^8)$ inclusive neutrino charged-current (CC) interactions, in the high statistics Scenario B with a goal of 10^{22} POT. The reduction of systematic uncertainties for the neutrino oscillation program requires a highly segmented near detector, thus providing excellent resolution in the reconstruction of neutrino events. The combination of this substantial flux with a finely segmented near detector offers a unique opportunity to produce a range of neutrino scattering physics measurements in addition to those needed by the long base line oscillation program. The combined statistics and precision expected in the ND will allow precise tests of fundamental interactions and better understanding of the structure of matter.

Since the potential of the neutrino probe is largely unexplored, the substantial step forward offered by the LBNE program also provides the opportunity for unexpected discoveries. Given the broad energy range of the beam, a diverse range of physics measurements is possible in the LBNE ND, complementing the physics programs using proton, electron or ion beams from colliders to the Jefferson Laboratory. This complementarity not only would boost the physics output of LBNE, but it can also attract new collaborators into the LBNE project from different physics communities.

In the following sections we list the main physics topics, grouping them into seven broad categories. To provide a flavor for the outstanding physics potential, we give a short description of the studies which can be performed at LBNE for few selected topics. A more detailed and complete discussion of the short baseline physics potential will appear in a separate physics working group paper.

1. Structure of the Weak Current

Main topics:

- Electroweak Physics
- Conservation of the Vector Current (CVC)
- PCAC and Low Q^2 Behavior of Cross Sections

a. **Electroweak Physics** Neutrinos are a natural probe for the investigation of electroweak physics. Interest in a precise determination of the weak mixing angle ($\sin^2\theta_W$) at LBNE energies via neutrino scattering is twofold: a) it provides a direct measurement of neutrino couplings to the Z boson and b) it probes a different scale of momentum transfer than LEP by virtue of not being on the Z pole. The weak mixing angle can be extracted experimentally from three main NC physics processes:

1. Deep Inelastic Scattering off quarks inside nucleons: $\nu N \to \nu X$;
2. Elastic Scattering off electrons: $\nu e^- \to \nu e^-$;
3. Elastic Scattering off protons: $\nu p \to \nu p$.

Figure 75 shows the corresponding Feynman diagrams for the three processes.
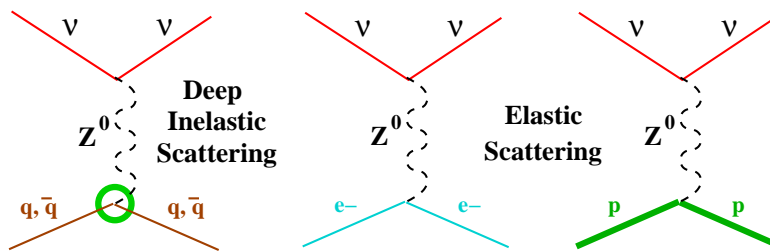
FIG. 75. Feynman diagrams for the three main Neutral-Current processes which can be used to extract $\sin^2\theta_W$ with the LBNE Near Detector complex.

The most precise measurement of $\sin^2\theta_W$ in neutrino deep inelastic scattering (DIS) comes from the NuTeV experiment which reported a value that is 3σ from the standard model [161]. The LBNE ND can perform a similar analysis in the DIS channel by measuring the ratio of NC and CC interactions induced by neutrinos:

$$\mathcal{R}^\nu \equiv \frac{\sigma_{\mathrm{NC}}^\nu}{\sigma_{\mathrm{CC}}^\nu} \simeq \rho^2 \left(\frac{1}{2} - \sin^2\theta_W + \frac{5}{9}\left(1+r\right)\sin^4\theta_W \right) \tag{13}$$

where ρ is the relative coupling strength of the neutral to charged-current interactions ($\rho = 1$ at tree level in the Standard Model) and r is the ratio of anti-neutrino to neutrino cross section ($r \sim 0.5$). The absolute sensitivity of $\mathcal{R}^\nu$ to $\sin^2 \theta_W$ is 0.7, which implies a measurement of $\mathcal{R}^\nu$ of 1% precision would provide $\sin^2 \theta_W$ with a precision of 1.4%. Contrary to the NuTeV experiment the anti-neutrino interactions cannot be used for this analysis at LBNE, due to the large number of ν_μ DIS interactions in the $\bar{\nu}_\mu$ beam, compared to the $\bar{\nu}_\mu$ DIS interactions. While removing some cancelation of systematics between ν and $\bar{\nu}$, this fact reduces the statistical uncertainty of the measurement.

The measurement of $\sin^2 \theta_W$ from DIS interactions can be only performed with the low density magnetized tracker since an accurate reconstruction of the NC event kinematics and of the ν_e CC interactions are crucial to keep the systematic uncertainties on the event selection under control. The analysis selects events in the ND after imposing a cut on the visible hadronic energy of $E_{\mathrm{had}} > 3$ GeV, as in the NOMAD $\sin^2 \theta_W$ analysis (the CHARM analysis had $E_{\mathrm{had}} > 4$ GeV). With the reference 700 kW beam we expect about 3.3×10^6 CC events and 1.1×10^6 NC events, giving a statistical precision of 0.11% on $\mathcal{R}^\nu$ and 0.15% on $\sin^2 \theta_W$ (Table XXIII).

The use of a low density magnetized tracker can substantially reduce systematic uncertainties with respect to a massive calorimeter. Table XXIII shows a comparison of the different uncertainties on the measured $\mathcal{R}^\nu$ between NuTeV and LBNE. The largest experimental systematic uncertainty in NuTeV is related to the subtraction of the ν_e CC contamination from the NC sample. Since the low density tracker at LBNE can efficiently reconstruct the electron tracks, the ν_e CC interactions can be identified on an event-by-event basis, reducing the corresponding uncertainty to a negligible level. Similarly, uncertainties related to the location of the interaction vertex, noise, counter efficiency etc. are removed by the higher resolution and by the different analysis selection. The experimental selection at LBNE will be dominated by two uncertainties: the knowledge of the $\bar{\nu}_\mu$ flux and the kinematic selection of NC interactions. The former is relevant due to the larger NC/CC ratio for anti-neutrinos. The total experimental systematic uncertainty on $\sin^2 \theta_W$ is expected to be about 0.14%.

| | $\delta R^\nu / R^\nu$ | |
Source of uncertainty	NuTeV	LBNE
Data statistics	0.00176	0.00110
Monte Carlo statistics	0.00015	
Total Statistics	0.00176	0.00110
$\nu_e, \bar{\nu}_e$ flux ($\sim 1.7\%$)	0.00064	0.00010
Energy measurement	0.00038	0.00040
Shower length model	0.00054	n.a.
Counter efficiency, noise	0.00036	n.a.
Interaction vertex	0.00056	n.a.
$\bar{\nu}_\mu$ flux	n.a.	0.00070
Kinematic selection	n.a.	0.00060
Experimental systematics	0.00112	0.00102
d,s→c, s-sea	0.00227	0.00130
Charm sea	0.00013	n.a.
$r = \sigma^{\bar{\nu}}/\sigma^\nu$	0.00018	n.a.
Radiative corrections	0.00013	0.00013
Non-isoscalar target	0.00010	N.A.
Higher twists	0.00031	0.00070
R_L (F_2, F_T, xF_3)	0.00115	0.00140
Nuclear correction		0.00020
Model systematics	0.00258	0.00206
TOTAL	0.00332	0.00255

TABLE XXIII. Comparison of uncertainties on the $\mathcal{R}^\nu$ measurement between NuTeV and LBNE with the reference beam. The corresponding relative uncertainties on $\sin^2 \theta_W$ must be multiplied by a factor of 1.4, giving for LBNE a projected overall precision of 0.36%.

The measurement of $\mathcal{R}^\nu$ will be dominated by model systematic uncertainties on the structure functions of the target nucleons. The estimate of these uncertainties for LBNE is based upon the extensive work performed for the NOMAD analysis and includes a NNLO QCD calculation of structure functions (NLO for charm production) [172–174], parton distribution functions (PDFs) extracted from dedicated low-Q global fits, high twist contributions [172], electroweak corrections [175] and nuclear corrections [176–178]. The charm quark production in CC, which has been the dominant source of uncertainty in all past determinations of $\sin^2 \theta_W$ from νN DIS, is reduced to about 2.5% of the total ν_μ CC DIS with $E_{\mathrm{had}} > 3$ GeV with the low energy beam spectrum at LBNE. This number translates into a systematic uncertainty of 0.13% on $\mathcal{R}^\nu$ (Table XXIII), assuming a knowledge of the charm production cross

section to 5%. It is worth noting the recent measurement of charm dimuon production by the NOMAD experiment allowed a reduction of the uncertainty on the strange sea distribution to $\sim 3\%$ and on the charm quark mass m_c to ~ 60 MeV [179]. The lower neutrino energies available at LBNE reduce the accessible Q^2 values with respect to NuTeV, increasing in turn the effect of non-perturbative contributions (High Twists) and R_L. The corresponding uncertainties are reduced by the recent studies of low-Q structure functions and by improved modeling with respect to the NuTeV analysis (NNLO vs. LO). The total model systematic uncertainty on $\sin^2\theta_W$ is expected to be about 0.29% with the reference beam configuration. The corresponding total uncertainty on the value of $\sin^2\theta_W$ extracted from νN DIS is 0.36% with the 700 kW beam.

Most of the model uncertainties will be constrained by in situ dedicated measurements using the large CC samples and employing improvements in theory that will have evolved over the course of the experiment. In the low density tracker we shall collect about 80,000 neutrino induced inclusive charm events with the 700 kW beam. The precise reconstruction of charged tracks will allow to measure exclusive decay modes of charmed hadrons (e.g. D^{*+}) and to measure charm fragmentation and production parameters. The average semileptonic branching ratio $B_\mu \sim 5\%$ with the low energy LBNE beam. The presence a 100-ton LAr TPC in front of the low density tracker will further increase the potential of the charm analysis, allowing the collection of about 50,000 charm dimuon events with the reference beam. This sample represent shall be compared with the largest existing sample of 15,400 dimuon events collected by the NOMAD experiment [179]. Finally, precision measurements of CC structure functions in both the fine-grained tracker and the LAr detector would further reduce the uncertainties on PDFs and on High Twist contributions.

The precision that can be achieved from νN DIS interactions is limited by both the event rates and by the energy spectrum of the reference 700 kW beam configuration. The high statistics beam exposure of Scenario B (10^{22} pot) combined with a dedicated run with the high energy beam option would increase the statistics by more than a factor of 20. This major step forward would not only reduce the statistical uncertainty to a negligible level, but would provide large control samples and precision auxiliary measurements to reduce the systematic uncertainties on structure functions. The two dominant systematic uncertainties, charm production in CC interactions and low Q^2 structure functions, are essentially defined by the available data at present. Overall, the use of a high energy beam within the Scenario B can potentially improve the precision achievable on $\sin^2\theta_W$ from νN DIS to about 0.2%. It is worth mentioning the high energy beam is also required for the determination of the fluxes in case high Δm^2 oscillations are present (see Section XI B 3 b).

A second independent measurement of $\sin^2\theta_W$ can be obtained from NC $\nu_\mu e$ elastic scattering. This channel has lower systematic uncertainties since it does not depend upon the knowledge of the structure of nuclei, but has limited statistics due to its very low cross section. The value of $\sin^2\theta_W$ can be extracted from the ratio of neutrino to anti-neutrino interactions [162]:

$$\mathcal{R}_{\nu e}(Q^2) \equiv \frac{\sigma(\bar\nu_\mu e \to \bar\nu_\mu e)}{\sigma(\nu_\mu e \to \nu_\mu e)}(Q^2) \simeq \frac{1 - 4\sin^2\theta_W + 16\sin^4\theta_W}{3 - 12\sin^2\theta_W + 16\sin^4\theta_W} \tag{14}$$

in which systematic uncertainties related to the selection and electron identification cancel out. The absolute sensitivity of this ratio to $\sin^2\theta_W$ is 1.79, which implies a measurement of $\mathcal{R}_{\nu e}$ of 1% precision would provide $\sin^2\theta_W$ with a precision of 0.65%.

The event selection was described in details on Section XI A 1 a since the NC elastic scattering off electrons is also used for the absolute flux normalization. This analysis can be performed only with the low density magnetized tracker and with a large LAr detector. In the former case the total statistics available is limited to about 1000 (600) $\nu(\bar\nu)$ events with the minimal exposure of Scenario A and 4500 (2800) $\nu(\bar\nu)$ events with the Scenario B. These numbers do not allow a competitive determination of $\sin^2\theta_W$ by using the magnetized tracker alone. However, if we consider a 100 t LAr detector in the ND complex, we expect to collect about 20,000 (12,000) $\nu(\bar\nu)$ events with Scenario A and 80,000 (50,000) $\nu(\bar\nu)$ events with Scenario B.

As discussed in Section XI A 1 a a combined analysis of both detectors can achieve the optimal sensitivity: the fine-grained tracker is used to reduce systematic uncertainties (measurement of backgrounds and calibration), while the LAr ND provides the statistics required for a competitive measurement. Overall, the use of the massive LAr detector can provide a statistical accuracy on $\sin^2\theta_W$ of about 0.3% with the high statistics Scenario B. However, the extraction of the weak mixing angle is dominated by the systematic uncertainty on the $\bar\nu_\mu/\nu_\mu$ flux ratio, which is entering Equation (14). We evaluated this uncertainty with the low-ν_0 method for the flux extraction (see Section XI A 1 c) and we obtained a systematic uncertainty of about 1% on the ratio of the $\bar\nu_\mu/\nu_\mu$ flux integrals. Therefore, the overall precision on $\sin^2\theta_W$ achievable from NC elastic scattering off electrons is limited to about 0.9% in Scenario A and 0.6% in Scenario B. An improvement of this result in Scenario B would require a better understanding of the low-ν (anti)-neutrino cross sections, of the beam transport elements and of the nuclear cross sections.

Together, the DIS and the NC elastic scattering channels involve substantially different scales of momentum transfer, providing a tool to test the running of $\sin^2\theta_W$ in a single experiment. To this end, the study of NC elastic scattering off protons can provide additional information since it occurs at a momentum scale which is intermediate between
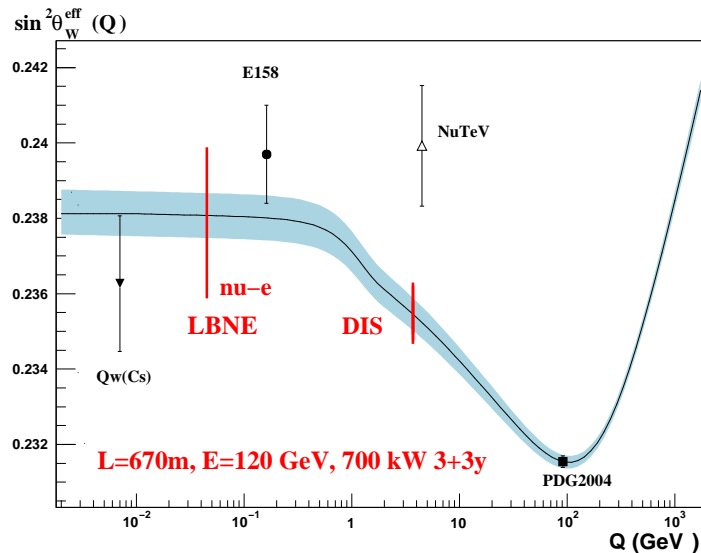
FIG. 76. Expected sensitivity to the measurement of $\sin^2\theta_W$ from the LBNE ND with the reference 700 kW beam. The curve shows the Standard Model prediction as a function of the momentum scale [180]. Previous measurements from Atomic Parity Violation [181, 182], Moeller scattering (E158 [183]), ν DIS (NuTeV [161]) and the combined Z pole measurements (LEP/SLC) [182] are also shown for comparisons. The use of a high energy beam with the maximal exposure of 10^{22} pot can reduce the LBNE uncertainties by almost a factor of two.

the two other processes. Figure 76 summarizes the target sensitivity from the LBNE ND, compared with existing measurements as a function of the momentum scale.

2. Strange Content of the Nucleon

Main topics:

- NC Elastic Scattering and Measurement of Δs
- Strange Form Factors
- Charm Production and (anti)strange Parton Distribution Function
- Strange Particle Production in NC and CC

The role of the strange quark in the proton remains a central investigation in hadronic physics. The interesting question is whether the strange quarks contribute substantially to the vector and axial-vector currents of the nucleon. A large observed value of the strange quark contribution to the nucleon spin (axial current), Δs, would require further theoretical speculations with respect to present assumptions. The spin structure of the nucleon also affects the couplings of axions and supersymmetric particles to dark matter.

The strange *vector* elastic form factors of the nucleon have been measured to high precision in parity-violating electron scattering (PVES) at Jefferson Lab, Mainz and elsewhere. A recent global analysis [184] of PVES data finds a strange magnetic moment $\mu_s = 0.37 \pm 0.79$ (in units of the nucleon magneton), so that the strange quark contribution to proton magnetic moment is less than 10%. For the strange electric charge radius parameter ρ_s, defined in terms of the Sachs electric form factor at low Q^2 as $G_E^s = \rho_s Q^2 + \rho'_s Q^4 + \mathcal{O}(Q^6)$, one finds a very small value, $\rho_s - 0.03 \pm 0.63$ GeV^{-2}, consistent with zero.

Both of these results are consistent with theoretical expectations based on lattice QCD and phenomenology [185]. In contrast, the strange *axial vector* form factors are not nearly as well determined. A similar global study of PVES data [184] finds $\widetilde{G}_A^N(Q^2) = \widetilde{g}_A^N \left(1 + Q^2/M_A^2\right)^2$, with the effective proton and neutron axial charges $\widetilde{g}_A^p = -0.80 \pm 1.68$ and $\widetilde{g}_A^n = 1.65 \pm 2.62$.

The strange axial form factor at $Q^2 = 0$ is related to the *spin* carried by strange quarks, Δs. Currently the world data on the spin-dependent g_1 structure function constrain Δs to be ≈ -0.055 at a scale $Q^2 = 1$ GeV^2, with a significant fraction of this coming from the region $x < 0.001$. In addition, the HERMES collaboration [186] extracted

the strange quark spin from semi-inclusive DIS data over the range $0.02 \leq x \leq 0.6$, yielding a *negative* central value, $\Delta s = 0.037 \pm 0.019 \pm 0.027$, although still consistent with the above global average.

A	B	C
$\frac{1}{4}\left[G_1^2\left(1+\tau\right) - \left(F_1^2 - \tau F_2^2\right)\left(1-\tau\right) + 4\tau F_1 F_2\right]$	$-\frac{1}{4}G_1\left(F_1 + F_2\right)$	$\frac{1}{16}\frac{M_p^2}{Q^2}\left(G_1^2 + F_1^2 + \tau F_2^2\right)$

TABLE XXIV. Coefficients entering Eqn. 15 for NC elastic scattering and CC QE interactions, with $\tau = Q^2/4M_p$.

An independent extraction of Δs, which does not rely on the difficult measurements of the g_1 structure function at very small x values, can be obtained from (anti-)neutrino NC elastic scattering off proton (see Fig. 75). This process provides indeed the most direct measurement of Δs. The differential cross section for NC elastic and CC QE scattering of (anti-)neutrinos from protons can be written as:

$$\frac{d\sigma}{dQ^2} = \frac{G_\mu^2}{2\pi}\frac{Q^2}{E_\nu^2}\left(A \pm BW + CW^2\right); \quad W = 4E_\nu/M_p - Q^2/M_p^2 \tag{15}$$

where the positive (negative) sign is for (anti-)neutrino scattering and the coefficients A, B, and C contain the vector and axial form factors as listed in Table XXIV.

The axial-vector form factor for NC scattering can be written as the sum of the known axial form factor G_A plus a strange form factor G_A^s:

$$G_1 = \left[-\frac{G_A}{2} + \frac{G_A^s}{2}\right] \tag{16}$$

while the NC vector form factors can be written as:

$$F_{1,2} = \left[\left(\frac{1}{2} - \sin^2\theta_W\right)\left(F_{1,2}^p - F_{1,2}^n\right) - \sin^2\theta_W\left(F_{1,2}^p + F_{1,2}^n\right) - \frac{1}{2}F_{1,2}^s\right] \tag{17}$$

where $F_1^{p(n)}$ is the Dirac form factor of the proton (neutron), $F_2^{p(n)}$ is the corresponding Pauli form factor, and $F_{1,2}^s$ are the strange vector form factors. These latter are expected to be small from the PVES measurements summarized above. In the limit $Q^2 \to 0$, the differential cross section is proportional to the square of the axial-vector form factor $d\sigma/dQ^2 \propto G_1^2$ and $G_A^s \to \Delta s$. The value of Δs can therefore be extracted experimentally by extrapolating the NC differential cross section to $Q^2 = 0$.

Previous neutrino scattering experiments have been limited by the statistics and by the systematic uncertainties on background subtraction. The only information available comes from the analysis of 951 NC νp and 776 NC $\bar{\nu}p$ collected by the experiment BNL E734 [187–189]. The LBNE neutrino beam will be sufficiently intense that a measurement of NC elastic scattering on proton in the fine-grained water ND can provide a definitive statement on the contribution of the strange sea to either the axial or vector form factor.

Systematic uncertainties can be reduced by measuring the NC/CC ratios for both neutrinos and anti-neutrinos:

$$\mathcal{R}_{\nu p}(Q^2) \equiv \frac{\sigma(\nu_\mu p \to \nu_\mu p)}{\sigma(\nu_\mu n \to \mu^- p)}(Q^2); \quad \mathcal{R}_{\bar{\nu}p}(Q^2) \equiv \frac{\sigma(\bar{\nu}_\mu p \to \bar{\nu}_\mu p)}{\sigma(\bar{\nu}_\mu p \to \mu^+ n)}(Q^2) \tag{18}$$

as a function of Q^2. Figure 77 shows the absolute sensitivity of both ratios to Δs for different values of Q^2. The sensitivity for $Q^2 \sim 0.25$ GeV^2 is about 1.2 for neutrinos and 1.9 for anti-neutrinos, which implies that a measurement of $\mathcal{R}_{\nu p}$ and $\mathcal{R}_{\bar{\nu}p}$ of 1% precision would enable the extraction of Δs with an uncertainty of 0.8% and 0.5%, respectively.

The design of the fine-grained water ND involves a combination of different nuclear targets. Therefore, most of the neutrino scattering is from nucleons embedded in a nucleus, requiring nuclear effects to be taken into account. Fortunately, in the ratio of NC/CC yields, the nuclear corrections are expected to largely cancel out. The Δs analysis requires a good proton reconstruction efficiency as well as high resolution on both the proton angle and energy. To this end, the low density magnetized tracker at LBNE can increase the range of the protons inside the ND, allowing the reconstruction of proton tracks down to $Q^2 \sim 0.07$ GeV^2. This fact will reduce the uncertainties in the extrapolation of the form factors to the limit $Q^2 \to 0$.

Table XXV summarizes the expected proton ranges for both the scintillator and the low density ($\rho \sim 0.1$ g/cm^3) ND options. With the reference 700 kW beam we expect about $2.5(1.5) \times 10^5$ $\nu p(\bar{\nu}p)$ events after the selection cuts in the low density tracker, yielding a statistical precision of the order of 0.2%.

We follow the analysis performed by the FINeSSE collaboration [190] and in the SciBooNE experiment for the determination of Δs. In particular, based upon the latter, with the scintillator tracker we expect a purity of about
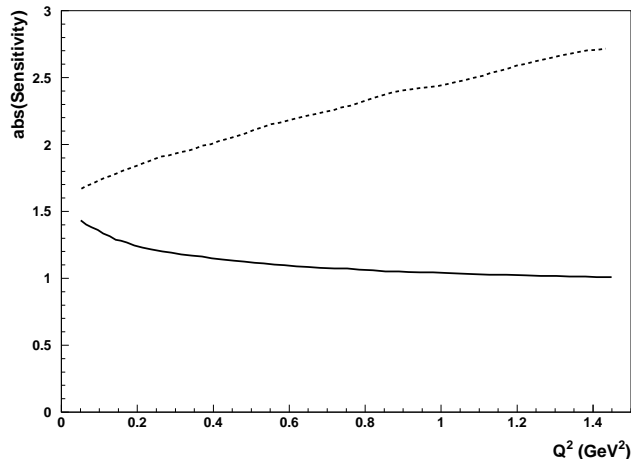
FIG. 77. Absolute sensitivity of the ratios $\mathcal{R}_{\nu p}$ (solid) and $\mathcal{R}_{\bar{\nu} p}$ (dashed) to the strange contribution to the spin of the nucleon, Δs, as a function of Q^2.

T_p	Q^2	Range Sci	Range STT	P_p
MeV	GeV$^2/c^2$	cm	cm	GeV/c
20	0.038	0.42	4.2	0.195
40	0.075	1.45	14.5	0.277
60	0.113	3.03	30.3	0.341
80	0.150	5.08	50.8	0.395
100	0.188	7.57	75.7	0.445

TABLE XXV. Expected proton range for the scintillator and low density ($\rho \sim 0.1 \ g/cm^3$) tracker options. The first column gives the proton kinetic energy and the last column the proton momentum. The Q^2 value producing T_p is calculated assuming the struck nucleon was initially at rest.

50%, with background contributions of 20% from neutrons produced outside of the detector, 10% νn events and 10% NC pion backgrounds. The dominant systematic uncertainty will be related to the background subtraction. The low energy beam spectrum at LBNE provides the best sensitivity for this measurement since the external background from neutron-induced proton recoils will be reduced by the strongly suppressed high energy tail. The low density magnetized tracker is expected to increase the purity by reducing the neutron background and the NC pion background. Overall, it seems possible to achieve a precision on Δs of about $0.02 - 0.03$ in this case. The maximal exposure available with Scenario B will further improve the sensitivity due to higher statistics and better constraints on the background subtraction procedure from data control samples.

3. Search for New Physics

The Standard Model (SM) of elementary particles is in conflict with several experimental observations: non-zero neutrino masses and oscillations, the excess of matter over antimatter in the Universe, and the presence of non-baryonic dark matter. In addition, a number of fine-tuning problems (such as the gauge hierarchy problem, and cosmological constant problem) may indicate the existence of new physics between the electroweak and the Planck scales.

The energy scale of new physics is not known at present. If it exists at energies above the Fermi scale (examples include supersymmetry, large or warped extra dimensions, models with dynamical electroweak symmetry breaking), the search for new particles can be carried out in direct experiments, such as ATLAS or CMS at LHC. In addition,

new hypothetical heavy particles inevitably appear as virtual states, leading to different rare processes, absent in the SM. These effects can be found at experiments such as LHCb, charm and beauty factories and are competitive with the direct searches. If the new physics is associated with existence of new relatively light particles (an example is given by the νMSM, see below) then the search for rare processes is superior to high energy experiments. Moreover, it provides a unique possibility for discovery of new physics, not accessible by any of the LHC experiments. We will argue here that the LBNE near detector can be used for these searches.

Main topics:

- Search for νMSM Neutral Leptons
- High Δm^2 Neutrino Oscillations
- Radiative Decay of Sterile Neutrinos
- MiniBooNE Low Energy Anomaly
- Decay of Heavy Weakly Interacting Particles
- $\nu_\mu \to \nu_e$ Transitions

a. **Search for νMSM Neutral Leptons** The most economic way to handle in a unified way the problems of neutrino masses, dark matter and baryon asymmetry of the Universe may be to add to the SM three Majorana singlet fermions with masses roughly of the order of masses of known quarks and leptons. The appealing feature of this theory (called the νMSM for "Neutrino Minimal SM") is the fact that there every left-handed fermion has a right-handed counter-part, leading thus an equal way of treating of quarks and leptons. The lightest of the three new leptons is expected to have a mass from 1 keV to 50 keV and play the role of the dark matter particle. Two other neutral fermions are responsible for giving masses to ordinary neutrinos via the see-saw mechanism at the *electroweak scale* and to creation of the baryon asymmetry of the Universe (for a review see [191]). The masses of these particles and their coupling to ordinary leptons are constrained by particle physics experiments and cosmology. They should be almost degenerate, forming thus nearly Dirac fermion (this is coming from the requirement of successful baryogenesis). Different considerations indicate that their mass should be in $\mathcal{O}(1)$ GeV region [192].

The νMSM is described by the most general renormalizable Lagrangian containing all the particles of the SM and three singlet fermions. For the purpose of the present discussion we take away from it the lightest singlet fermion N_1 (the "dark matter sterile neutrino"), which is coupled extremely weakly to the ordinary leptons. In addition, we take N_2 and N_3 degenerate in mass, $M_2 = M_3 = M$. Then the convenient parametrization of the interaction of $N's$ with the leptons of SM is:

$$L_{\text{singlet}} = \left(\frac{\kappa M m_{atm}}{v^2} \right)^{\frac{1}{2}} \left[\frac{1}{\sqrt{\epsilon e^{i\eta}}} \bar{L}_2 N_2 + \sqrt{\epsilon e^{i\eta}} \bar{L}_3 N_3 \right] \tilde{H} - M \bar{N_2}^c N_3 + \text{h.c.}, \tag{19}$$

where L_2 and L_3 are the combinations of L_e, L_μ and L_τ

$$L_2 = \sum_\alpha x_\alpha L_\alpha , \qquad L_3 = \sum_\alpha y_\alpha L_\alpha . \tag{20}$$

with $\sum_\alpha |x_\alpha|^2 = \sum_\alpha |y_\alpha|^2 = 1$.

In eq.(19) $v = 246$ GeV is the vacuum expectation value of the Higgs field H, $\tilde{H}_i = \epsilon_{if} H_j^*$, $m_{atm} \simeq 0.05$ eV is the atmospheric neutrino mass difference, $\kappa = 1$ (2) for normal (inverted) hierarchy of neutrino masses. The x_α and y_α can be expressed through the parameters of the active neutrino mixing matrix (explicit relations can be found in [192]). The parameter ϵ (by definition, $\epsilon < 1$) and the CP-breaking phase η cannot be fixed from consideration of neutrino masses and mixings.

If the mass of N is fixed, smaller ϵ yields stronger interactions of singlet fermions to the SM leptons. This leads to equilibration of these particles in the early Universe above the electroweak temperatures, and, therefore, to erasing of the baryon asymmetry. In other words, the mixing angle U^2 between neutral leptons and active neutrinos must be small, explaining why these new particles has not been seen previously. For small ϵ,

$$U^2 = \frac{\kappa m_{atm}}{4 M \epsilon} . \tag{21}$$

The region, where baryogenesis is possible in $U^2 - M$ plane is shown in Fig. 78. Also shown are the exclusion regions coming from different experiments such as BEBC [194], CHARM [195], and NuTeV [196] and CERN PS191 experiment [197, 198] (see also discussion of different experiments in [199]). For the case of normal hierarchy, only CERN PS191 have significantly entered into the cosmologically interesting part of the parameter space of the νMSM, situated below the mass of the kaon. If the hierarchy is inverted, there are some constraints even for higher N masses.
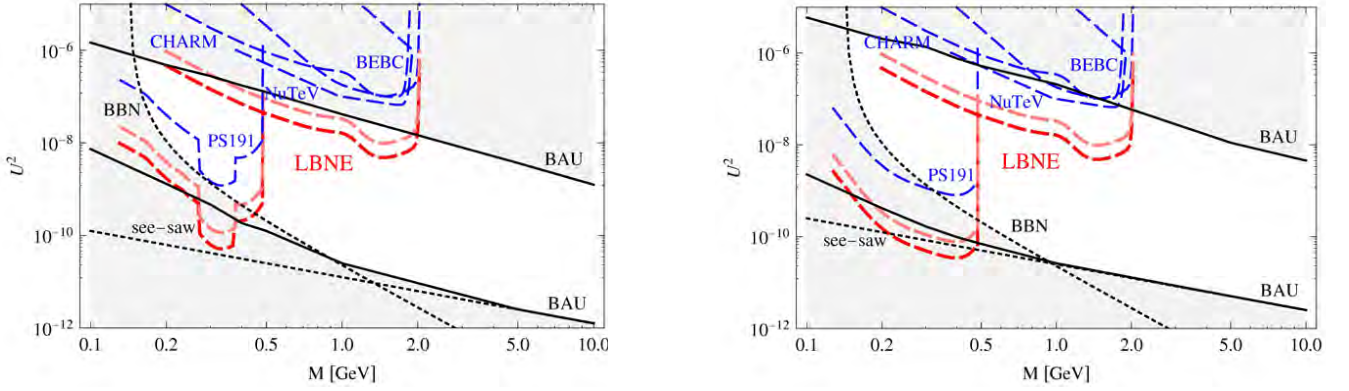
FIG. 78. Constraints on U^2 coming from the baryon asymmetry of the Universe (solid lines), from the see-saw formula (dotted line) and from the big bang nucleosynthesis (dotted line). The regions corresponding to different experimental searches are outlined by blue dashed lines. Left panel: normal hierarchy; right panel: inverted hierarchy (adopted from Ref. [193]). Pink and red curves indicate the expected sensitivity of the LBNE near detector with the Scenario B exposure of 10^{22} pot for detector lengths of 7 m and 30 m, respectively (see text for details).

The lower constraint on U^2, coming from baryon asymmetry of the Universe, is somewhat stronger than the "see-saw" constraint.

The most efficient mechanism of sterile neutrino production is through weak decays of heavy mesons and baryons, as can be seen from the left panel of Fig. 79, showing some examples of relevant two- and three-body decays. Heavy
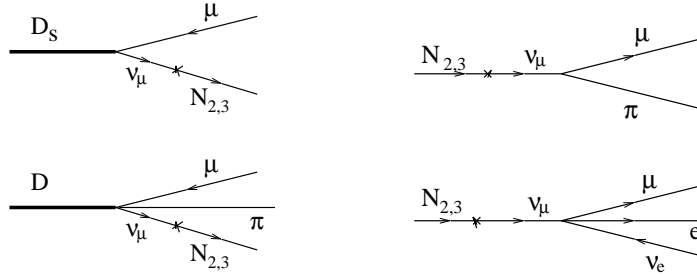

FIG. 79. Left panel: Feynman diagrams of meson decays producing heavy sterile neutrinos. Right panel: Feynman diagrams of sterile neutrino decays.

mesons can be produced by energetic protons scattering off the target material.

In case of the LBNE experiment the relevant heavy mesons are charmed ones. With a typical lifetime (in the rest frame) of about 10^{-10} s these mesons mostly decay before further interaction, yielding the sterile neutrino flux. Since these sterile neutrinos are very weakly interacting (see Fig. 78) they can cover quite a large distance before decay, significantly exceeding the distance of 670 m from the target to the near LBNE near detector. Neutrino decays into SM particles due to mixing with active neutrinos can be searched for in the ND, provided a sufficiently long instrumented decay region is available. Two examples of the interesting decay modes are presented on the right panel of Fig. 79. More examples can be found in Ref. [200].

We can obtain an estimate of sterile neutrino events to be observed in the LBNE near detector, N_{signal}^{LBNE}, by comparing the relevant parameters of the LBNE and CHARM experiments, which are summarized in Table XXVI.

	PoT	detector length	distance to target	beam energy	detector area	charm production
LBNE	1.0×10^{22}	7 m	670 m	120 GeV	4×4 m^2	1.0×10^{-4}
CHARM	2.5×10^{18}	34 m	480 m	400 GeV	3×3 m^2	4.5×10^{-4}

TABLE XXVI. Characteristics of LBNE and CHARM experiments.

The number of events linearly grows with the number of proton on target, the number of produced charmed mesons,

the detector length (decay region) and the detector area. In particular, this latter condition is valid if the angular spread of the neutrino flux, which is of the order of $N_m M_D / E_{beam}$, is larger than the angle at which the ND is seen from the target. Here N_m is the multiplicity of the produced hadrons, and the above condition is valid for both LBNE and CHARM. The number of events also decreases linearly when the energy increase, since it increases the lifetime, reducing the decay probability within the detector.

Finally, the number of mesons decreases quadratically with the distance between the target and the detector. These considerations imply a search for νMSM sterile neutrinos can be only competitive with the Scenario B exposure of 10^{22} pot and with a proton energy of 120 GeV.

The analysis can be performed with all detector options, although a low density long decay region reduces backgrounds and allows the detection of both leptonic and hadronic decay modes. Assuming the length of the magnetized tracker (7 m) as decay region, we can then estimate the ratio between the signal event to be observed in the LBNE ND and the ones observed by the CHARM experiment to be about 50.

The CHARM experiment found no sterile neutrino events with zero background and very high (about 65%) efficiency. Since both production and decay rates are proportional to the neutrino mixing angles squared, LBNE will be able to achieve an improvement by about a factor of seven in the neutrino mixing angle squared U^2 with respect to the CHARM experiment. Somewhat smaller numbers can be obtained for kaons by comparing the LBNE and PS191 experiments. The expected sensitivity is indicated with red dashed curves in Fig. 78.

The presence of a long LAr detector in front of the fine-grained tracker can enhance the sensitivity to sterile neutrinos by providing an additional, fully instrumented, decay region. In addition, a combined analysis of a massive LAr detector with the fine-grained magnetized tracker would allow the search for new weakly interacting particles produced in NC neutrino interactions within LAr and decaying inside the fiducial volume of the fine-grained tracker.

A better sensitivity to νMSM can be achieved by instrumenting the upstream region of the ND hall (e.g. with the LAr detector and some minimal tracking device upstream). The fiducial volume of the new detector has to be empty (material-free) or fully sensitive in order to suppress background events. The geometry of the ND hall would allow a maximal decay length of about 30 m. The sensitivity of this configuration can be estimated by rescaling the expected limits on mixing U^2. The expected number of signal events with a total decay length of ~ 30 m exceeds by about 200 times the number of events in CHARM, which implies an improvement by a factor of 15 in sensitivity to U^2 with respect to the CHARM experiment.

It must be noted that if the magnetic moment of the sterile neutrinos is sizeable, the dominant decay channel would be a radiative electromagnetic decay into $\gamma\nu$, which has also been proposed as a possible explanation for the observed MiniBooNE low energy excess [201]. This fact, in turn, requires a detector capable of identifying and reconstructing single photon events.

b. **High Δm^2 Neutrino Oscillations** The evidence for neutrino oscillations obtained from atmospheric, long-baseline accelerator, solar, and long-baseline reactor data from different experiments consistently indicates two different scales with $\Delta_{32} m^2 \sim 2.4 \times 10^{-3} eV^2$ defining the atmospheric oscillations and $\Delta_{21} m^2 \sim 7.9^{-5} eV^2$ defining the solar oscillations. The only way to accommodate oscillations with relatively high Δm^2 at the eV^2 scale is therefore to add one or more sterile neutrinos to the conventional three light neutrinos.

The MiniBooNE experiment reported their anti-neutrino data might be consistent with the LSND $\bar{\nu}_\mu \to \bar{\nu}_e$ oscillation with $\Delta m^2 \sim eV^2$. Contrary to the anti-neutrino data, the MiniBooNE neutrino data seem to exclude high Δm^2 oscillations, possibly indicating a a different behavior between neutrinos and anti-neutrinos. This difference, which would require CP or CPT violation, could also be consistent with the MINOS disappearance analysis.

Models with five (3+2) or six (3+3) neutrinos can potentially explain the MiniBooNE results [202]. In addition to the cluster of the three neutrino mass states accounting for "solar" and "atmospheric" mass splitting two (or three) states at the eV scale are added, with a small admixture of ν_e and ν_μ to account for the LSND signal. One distinct prediction from such models is a significant probability for $\bar{\nu}_\mu$ disappearance into sterile neutrinos, of the order of 10%, in addition to the small probability for $\bar{\nu}_e$ appearance.

The Near Detector at LBNE is located at a baseline of 670 m and with the reference "Low Energy (LE)" beam spectrum so it can reach the same value $L/E_\nu \sim 1$ of MiniBooNE and LSND. The large fluxes and the availability of fine-grained detectors make the LBNE program well suited to search for oscillations at the eV^2 scale. Due to the potential differences between neutrinos and anti-neutrinos four possibilities have to be considered in the analysis: ν_μ disappearance, $\bar{\nu}_\mu$ disappearance, ν_e appearance and $\bar{\nu}_e$ appearance. As discussed in Section XI A 1 d, the search for high Δm^2 oscillations has to be performed simultaneously with the in situ determination of the fluxes.

To this end, we need to obtain an independent prediction of the ν_e and $\bar{\nu}_e$ fluxes starting from the measured ν_μ and $\bar{\nu}_\mu$ CC distributions since the ν_e and $\bar{\nu}_e$ CC distributions could be distorted by the appearance signal. The low-ν_0 method can provide such predictions if external measurements for the K_L^0 component are available from hadro-production experiments (Section XI A 1 c).

We will the follow an iterative procedure:

- Extract the fluxes from ν_μ and $\bar{\nu}_\mu$ CC distributions assuming no oscillations are present;

- Comparison with data and determination of oscillation parameters (in any);
- New flux extraction after subtraction of the oscillation effect;
- Iterate until convergence.

The analysis has to be performed separately for neutrinos and anti-neutrinos due to potential CP or CPT violation according to MiniBooNE/LSND data.

We measure the ratio of electron to muon CC events:

$$\mathcal{R}_{e\mu}(L/E) \equiv \frac{\# \ of \ \nu_e N \to e^- X}{\# \ of \ \nu_\mu N \to \mu^- X}(L/E); \qquad \bar{\mathcal{R}}_{e\mu}(L/E) \equiv \frac{\# \ of \ \bar{\nu}_e N \to e^+ X}{\# \ of \ \bar{\nu}_\mu N \to \mu^+ X}(L/E) \tag{22}$$

which is then compared with the predictions obtained from the low-ν_0 method. Deviations of $\mathcal{R}_{e\mu}$ or $\bar{\mathcal{R}}_{e\mu}$ from the expectations as a function of L/E would provide evidence for oscillations. It must be noted that this procedure only provides a relative measurement of $\nu_e(\bar{\nu}_e)$ vs. $\nu_\mu(\bar{\nu}_\mu)$. Actually, since the fluxes are extracted from the observed ν_μ and $\bar{\nu}_\mu$ CC distributions an analysis of the $\mathcal{R}_{e\mu}(\bar{\mathcal{R}}_{e\mu})$ ratio cannot distinguish between $\nu_\mu(\bar{\nu}_\mu)$ disappearance and $\nu_e(\bar{\nu}_e)$ appearance.

The process of NC elastic scattering off protons (Section XI B 2) can provide the complementary measurement needed to disentangle the two hypotheses of $\nu_\mu(\bar{\nu}_\mu)$ disappearance into sterile neutrinos and $\nu_e(\bar{\nu}_e)$ appearance. In order to cancel systematic uncertainties, we will measure the NC/CC ratio with respect to quasi-elastic scattering:

$$\mathcal{R}_{NC}(L/E) \equiv \frac{\# \ of \ \nu p \to \nu p}{\# \ of \ \nu_\mu n \to \mu^- p}(L/E); \qquad \bar{\mathcal{R}}_{NC}(L/E) \equiv \frac{\# \ of \ \bar{\nu} p \to \bar{\nu} p}{\# \ of \ \bar{\nu}_\mu p \to \mu^+ n}(L/E) \tag{23}$$

We can reconstruct the neutrino energy from the proton angle and momentum under the assumption of neglecting the nuclear smearing (the same for the neutrino CC sample). In the oscillation analysis we are only interested in relative distortions of the ratio $\mathcal{R}_{NC}(\bar{\mathcal{R}}_{NC})$ as a function of L/E and not in the absolute values of the ratios. For $Q^2 > 0.2$ GeV^2 the relative shape of the total cross sections is not very sensitive to the details of the form factors. To improve the energy resolution we can use events originating from the deuterium inside the D$_2$O target embedded into the fine-grained tracker.

An improved oscillation analysis is based on a simultaneous fit to both $\mathcal{R}_{e\mu}(\bar{\mathcal{R}}_{e\mu})$ and $\mathcal{R}_{NC}(\bar{\mathcal{R}}_{NC})$. The first ratio provides a measurement of the oscillation parameters while the latter constrains the $\nu_e(\bar{\nu}_e)$ appearance vs. the $\nu_\mu(\bar{\nu}_\mu)$ disappearance. This analysis results in two main requirements for the ND:

- e^+/e^- separation to provide an unambiguous check of the different behavior between neutrinos and anti-neutrinos suggested by MiniBooNE;
- Accurate reconstruction of proton momentum and angle.

In order to validate the unfolding of the high Δm^2 oscillations from the in situ extraction of the (anti-)neutrino flux, we would also need to change the beam conditions, since the ND cannot be easily moved. To this end, it will be important to have the possibility of a short run with a high energy beam and to change/switch off the beam focusing system.

4. Isospin Relations

Main topics:

- Adler Sum Rule
- Tests of Isospin (Charge) Symmetry in Nucleons and Nuclei

The Adler sum rule relates the integrated difference of the anti-neutrino and neutrino F_2 to the isospin of the target:

$$\mathcal{S}_A(Q^2) = \int_0^1 dx \ \left[F_2^{\bar{\nu}}(x, Q^2) - F_2^{\nu}(x, Q^2)\right]/(2x) = 2 \, I_z, \tag{24}$$

where the integration is performed over the entire kinematical range of the Bjorken variable x and I_z is the projection of the target isospin vector on the quantization axis (z axis). For the proton $\mathcal{S}_A^p = 1$ and for the neutron $\mathcal{S}_A^n = -1$.

In the quark parton model the Adler sum is the difference between the number of valence u and d quarks of the target. The Adler sum rule survives the strong interaction effects because of CVC and provides an exact relation to test the local current commutator algebra of the weak hadronic current. We note in the derivation of the Adler

sum rule the effects of non-conservation of the axial current as well as heavy quark production are neglected (see, e.g. [203]).

Experimental tests of the Adler sum rule require the use of a hydrogen target to avoid nuclear corrections to the bound nucleons inside nuclei. The structure functions $F_2^{\bar{\nu}}$ and F_2^{ν} have to be determined from the corresponding differential cross sections and must be extrapolated to small x values in order to evaluate the integral (24). The only test available is limited by the modest statistics and was performed in bubble chambers by the BEBC collaboration using about 9,000 $\bar{\nu}$ and 5,000 ν events collected on hydrogen [204].

The LBNE program can provide the first precision test of the Adler sum rule. To this end, the use of the high energy beam configuration would significantly increase the sensitivity allowing to reach higher Q^2 values. Since the use of a liquid H_2 bubble chamber is excluded in the ND hall, the (anti)-neutrino interactions off a hydrogen target can only be extracted with a subtraction method from the composite materials of the ND targets. The position resolution in the location of the primary vertex is crucial with this technique to reduce systematic uncertainties. For this reason a precision test of the Adler sum rule can be only performed with the low density magnetized ND.

Two different targets are used resulting in a fiducial hydrogen mass of about 1 ton: the polypropylene $(C_3H_6)_n$ foils placed in front of the tracking modules and pure carbon foils. The statistical subtraction increases the statistical uncertainty by a factor of four. With the LBNE fluxes of the minimal exposure (Scenario A) we would collect about $1.4(1.0) \times 10^6$ inclusive $\nu(\bar{\nu})$ CC events on the hydrogen target. The number of events will increase to $6.4(4.5) \times 10^6$ for $\nu(\bar{\nu})$ CC with the Scenario B exposure of 10^{22} pot. This level of precision will offer the possibility to make new discoveries in the quark and hadron structure of the proton.

5. Exclusive and Semi-exclusive Processes in NC and CC

Main topics:

- Quasi-elastic Interactions
- Resonance Production
- Coherent Meson Production
- Diffractive Production
- Deep Inelastic Scattering

At the time of LBNE running it is expected that our knowledge of the (anti)-neutrino cross sections will be much improved over present levels. The MINERνA experiment is now running and is expected to collect a total number of inclusive CC interactions of 9×10^6 on a CH target, and 2.7×10^6 on both Fe and Pb targets. These raw (excluding efficiencies) rates are assuming a 3-ton fiducial mass, a LE beam run with an accumulated POT of 4.0×10^{20} and 12.0×10^{20} with the ME NuMI beam configurations in neutrino running mode. The statistical errors on most of the relevant processes will be of the order of 1%.

The goal of the MINERνA experiment is a 7% precision on the relative flux shape and 10% for the absolute normalization. Therefore, the uncertainties on the cross section measurements will be dominated by the systematic uncertainties associated with the flux determination. This level of precision on the flux is expected to be achieved using a series of special proton on target runs to probe different pion production kinematic regions and the neutrino data from these runs will be used to generate the hadron production off the target. The flux shape will be determined using the quasi-elastic sample and the absolute normalization using the high energy tail fixed to the CCFR/CHARM cross section measurements.

The analysis of data from the NOMAD experiment will provide complementary measurements of neutrino cross sections at energies which are much higher than the ones in MINERνA. The uncertainties on the neutrino fluxes were constrained to $2.5 - 8\%$ in NOMAD by detailed simulations of the beam transport, by external hadron-production measurements (SPY) and by the low-ν_0 technique. The reduced flux uncertainties coupled with the good detector resolution allowed a measurement of the NC coherent π^0 cross section to about 14% and a measurement of the neutrino QE cross section to about 6%. The main limitation of the NOMAD cross section measurements is the limited statistics collected, especially at low neutrino energies.

Due to the large statistics expected in the ND and the increased precision in the determination of the (anti)-neutrino fluxes described in Section XI A 1, LBNE will overcome the two main limitations of existing and past experiments. Even with the minimal exposure given by Scenario A, it would be possible to measure exclusive cross sections to a precision comparable to the one of the flux predictions, which will be in the range $1 - 3\%$.

Main topics:

- Measurement of Form Factors and Structure Functions
- QCD Analysis of Parton Distribution Functions
- d/u Parton Distribution Functions at Large x
- GLS Sum Rule and α_s
- Non-perturbative Contributions and High Twists
- Quark-hadron Duality
- Generalized Parton Distributions

A QCD analysis of the ND data in the framework of global fits to extract parton distribution functions is a crucial step to constrain systematic uncertainties on the electroweak measurements (Section XI B 1 a). In addition, precision measurements of (anti)-neutrino structure functions and differential cross sections would directly affect the LBL oscillation searches, providing an estimate of all background processes which are dependent upon the angular distribution of the outgoing particles in the FD.

For quantitative studies of inclusive deep-inelastic lepton-nucleon scattering, it is vital to have precise F_3 structure functions, which can only be measured with neutrino and antineutrino beams, as input into global PDF fits. Because it depends on weak axial quark charges, the F_3 structure function is unique in its ability to differentiate between the quark and antiquark content of the nucleon. On a proton target, for instance, the neutrino and antineutrino F_3 structure functions (at leading order in α_s) are given by

$$xF_3^{\nu p}(x) = 2x \left(d(x) - \bar{u}(x) + \bar{s}(x) + \cdots \right), \tag{25}$$

$$xF_3^{\bar{\nu} p}(x) = 2x \left(u(x) - \bar{d}(x) - \bar{s}(x) + \cdots \right). \tag{26}$$

In contrast, electromagnetic probes are sensitive only to a sum of quark and antiquark PDFs. Unfortunately, the neutrino scattering cross sections have considerably larger uncertainties than the electromagnetic inclusive cross sections at present. The high statistics of Scenario B offer the promise to reduce the gap between the uncertainties on the weak and electromagnetic structure functions, and would have a major impact on global PDF analyses.

Recent experiments at JLab have collected high-precision data on the individual F_1 and F_2 (or F_T and F_L) structure functions at large x from Rosenbluth-separated cross sections. This avoids the need for model-dependent assumptions about the ratio $R = \sigma_L/\sigma_T$ of the longitudinal to transverse cross sections in the extraction of the structure functions from the measured cross sections. Similar quality data on the individual F_T and F_L structure functions from neutrino scattering would be available from the ND at LBNE, to maximally complement and facilitate the flavor decomposition of these functions.

In addition to data in the DIS region, there is considerable interest in obtaining data at low Q^2 (down to $Q^2 \sim 1$ GeV^2) and low W ($W < 2$ GeV), to complement those from JLab. Unpolarized structure functions can be expressed in terms of powers of $1/Q^2$ (power corrections):

$$F_{2,T,3}(x, Q^2) = F_{2,T,3}^{\tau=2}(x, Q^2) + \frac{H_{2,T,3}^{\tau=4}(x)}{Q^2} + \frac{H_{2,T,3}^{\tau=6}(x)}{Q^4} + \ldots \tag{27}$$

where the first term ($\tau = 2$), expressed in terms of PDFs, represents the Leading Twist (LT) describing the scattering off a free quark and is responsible for the scaling of SF via perturbative QCD $\alpha_s(Q^2)$ corrections. The Higher Twist (HT) terms ($\tau = 4, 6$) reflect instead the strength of multi-parton correlations (qq and qg). The ND data at LBNE would allow a good separation of target mass and higher twist corrections, both of which are $1/Q^2$ suppressed at high Q^2, from leading twist contributions [172, 205].

Global PDF fits show that at large values of x ($x > 0.5 - 0.6$) the d quark distribution (or the d/u ratio) is very poorly determined. The main reason for this is the absence of free neutron targets. Because of the larger electric charge on the u quark than on the d, the electromagnetic proton F_2 structure function data provide strong constraints on the u quark distribution, but are relatively insensitive to the d quark distribution.

To constrain the d quark distribution a precise knowledge of the corresponding neutron F_2^n structure functions is required, which in practice is extracted from inclusive deuterium F_2 data. At large values of x the nuclear corrections in deuterium become large and, more importantly, strongly model dependent, leading to large uncertainties on the resulting d quark distribution.

Several planned experiments at JLab with the energy upgraded 12 GeV beam will measure the d/u ratio up to $x \sim 0.85$ using several different method to minimize the nuclear corrections. One method will use semi-inclusive

DIS from deuterium with a low-momentum ($|\mathbf{p}| < 100$ MeV) spectator proton detected in the backward center-of-mass hemisphere, to ensure scattering on an almost free neutron (so-called "BONUS" experiment [206]). Preliminary results have confirmed the feasibility of this method at the current 6 GeV energies, and a proposal for the extension at 12 GeV has been approved.

Perhaps the cleanest and most direct method to determine the d/u ratio at large x is from neutrino and antineutrino DIS on hydrogen. Existing neutrino data on hydrogen have relatively large errors and do not extend beyond $x \sim 0.5$ [207]. A new measurement of neutrino and antineutrino DIS from *hydrogen* at LBNE with significantly improved uncertainties would therefore make an important discovery about the d/u behavior as $x \to 1$. This measurement is possible with the Scenario B exposure and a statistical subtraction of the hydrogen target from the composite materials of the fine-grained ND(Section XI B 4). To be competitive with the proposed JLab 12 GeV experiments, the kinematical reach would need to be up to $x \sim 0.85$ and with as large a Q^2 range as possible to control for higher twist and other sub-leading effects in $1/Q^2$.

7. Nuclear Effects

Main topics:

- Nuclear Modifications of Form Factors
- Nuclear Modifications of Structure Functions
- Mechanisms for Nuclear Effects in Coherent and Incoherent Regimes
- A Dependence of Exclusive and Semi-exclusive Processes
- Effect of Final State Interactions
- Effect of Short Range Correlations
- Two Body Currents

The study of nuclear effects in (anti)-neutrino interactions off nuclei is directly relevant for the LBL oscillation search. The use of water or argon in the FD requires a measurement of nuclear cross sections on the same targets in the ND. In addition to the different p/n ratio in water and argon, nuclear modifications of cross sections can differ from 5% to 15% between oxygen and argon, while final state interactions are expected to be about a factor of two larger in argon [160].

Furthermore, nuclear modifications can introduce a substantial smearing of the kinematic variables reconstructed from the observed final state particles. Detailed measurements of the A dependence of different processes are then required in order to understand the absolute energy scale of neutrino events and to reduce the corresponding systematic uncertainties on the oscillation parameters.

In addition to understanding the structure of the free nucleon, an important question in nuclear physics is how that structure is modified when the nucleon is inside a nuclear medium. Studies of ratios of structure functions of nuclei to those of free nucleons (or in practice the deuteron) reveal nontrivial deviations from unity as a function of x and Q^2. These have been explored thoroughly in charged lepton scattering experiments, but little empirical information exists from neutrino scattering.

Another reason to investigate the medium modifications of neutrino structure functions is that most neutrino scattering experiments are performed on nuclear targets, from which information on the free nucleon is inferred by performing a correction for the nuclear effects. In practice this often means applying the same nuclear correction as for the electromagnetic structure functions, which introduces an inherent model dependence in the result.

In particular, significant differences between photon-induced and weak boson-induced nuclear structure functions are predicted, especially at low Q^2 and low x, which have not been tested. A striking example is offered by the ratio R of the longitudinal to transverse structure functions [177]. While the electromagnetic ratio tends to zero in the photoproduction limit, $Q^2 \to 0$, by current conservation, the ratio for neutrino structure functions is predicted to be *finite* in this limit. Thus significant discovery potential exists in the study of neutrino scattering from nuclei.

Finally, the extraction of (anti)-neutrino interactions on deuterium from the statistical subtraction of H_2O from D_2O, which is required to measure the fluxes (Section XI A 1 a), would allow the first direct measurement of nuclear effects in deuterium at LBNE. This measurement can be achieved since the structure function of free isoscalar nucleon is given by the average of neutrino and anti-neutrino structure functions on hydrogen ($F_2^{\nu n} = F_2^{\bar{\nu} p}$). A precise determination of nuclear modifications of structure functions in deuterium would play a crucial role in reducing systematic uncertainties from global PDF fits.

C.   Requirements for the Near Detector Complex

1.   Requirements for the LBL Oscillation Analysis

The detector requirements to support the LBL oscillation analysis are driven by the determination of the fluxes. Three main measurements are needed to obtain accurate predictions of the $\nu_\mu, \bar{\nu}_\mu, \nu_e, \bar{\nu}_e$ content of the beam: a) NC elastic scattering off electrons; b) low-ν_0 technique; and c) QE CC scattering off deuterium in the limit $Q^2 = 0$. The most important background measurement for the $\nu_e(\bar{\nu}_e)$ appearance search is the determination of the π^0/γ content in NC and high-y_{Bj} CC interactions. Similarly, the $\nu_\mu(\bar{\nu}_\mu)$ disappearance search requires a precise measurement of the yields of $\pi^\pm$ and $K^\pm$ and of their $\mu^\pm$ decays of as a function of energy and angle. In addition, QE, single π and DIS processes and their nuclear dependence must be measured in CC interactions. The above measurements define the key requirements for the ND complex:

- μ^-/μ^+ separation for the measurement of the ν_μ and $\bar{\nu}_\mu$ beam content, the low-ν_0 technique and the $\mu^\pm$ decays of $\pi^\pm/K^\pm$;

- e^-/e^+ separation for the measurement of the ν_e and $\bar{\nu}_e$ beam content, NC elastic scattering off electrons, and to unfold the fluxes in the presence of high Δm^2 oscillations;

- D_2O target embedded in the fine-grained tracker for the ν_μ flux extraction;

- Possibility to accommodate different nuclear targets to constrain nuclear effects on the predicted event rates and to study the calibration of the neutrino energy scale;

This list implies that at least part of the near detector complex must be magnetized. The e^-/e^+ separation and the measurement of $\mu^\pm$ decays of $\pi^\pm/K^\pm$ are possible only in a magnetized LAr detector or in the low density magnetized tracker.

The reference exposure of a 3+3 year run with the 700 kW beam seems adequate to achieve a precision of $\sim 1-3\%$ on fluxes and backgrounds, if these detector requirements are satisfied. The reference exposure will also provide the relevant information for the LBL oscillation analysis well before the completion of the nominal LBL data taking (5+5 years). An additional requirement would be the possibility to change the beam focusing system and to run with a higher energy beam spectrum. These options would be crucial to unfolding the fluxes if high Δm^2 oscillations are present.

2.   Additional Requirements for the Study of Neutrino Interactions

By satisfying the requirements described in the previous Section, there are no significant additional detector requirements for the ND complex in order to perform precision studies of fundamental interactions along with satisfying the requirements of LB oscillation studies. The only upgrade of the ND complex that might be considered is a modest instrumentation of the upstream end of the ND hall to increase the decay length for the search for neutral leptons to ~ 30 m. Indeed, in most cases the physics processes studied are the same as those used to constrain fluxes and backgrounds for LB measurements.

From the point of view of the beam design, our sensitivity studies show that the Scenario B high statistics exposure would be a crucial step to achieve a breakthrough in the precision tests of fundamental interactions and of the structure of matter. For most measurements we considered, the Scenario A reference exposure with the 700 kW beam provides only limited improvements over existing or future programs, whereas, Scenario B has the potential to bring the LBNE program to a level of precision similar to e^+e^- colliders. To this end, it is also worth noting a run with the high energy beam option would substantially enhance the physics potential of LBNE.

3.   Conclusions

The short baseline measurements are an integral part of the LBL program since the LBL oscillation analysis requires precise predictions of fluxes and backgrounds. The precision and resolution achieved by a fine-grained ND complex can therefore directly affect the design of the FD, especially for the detector options characterized by larger background levels and lower resolution (e.g. water Cherenkov).

The choice between water Cherenkov and LAr for the technology of the FD has, in turn, some implications in the design of the ND complex. Since sizeable nuclear modifications are expected on cross sections, the minimal

requirement is that the nuclear targets selected for the FD shall also be present in the ND. This condition can be achieved either by using a combination of different detectors at the near site, or by using different dedicated nuclear targets within the same detector technology.

A hybrid FD with water Cherenkov and LAr technologies clearly implies the need for an ND complex with both a LAr TPC and a fine-grained tracker with a water target embedded. Our sensitivity studies showed that, with a magnetized tracker capable of e^+/e^- separation, such a combination in the ND has an advantage also in terms of physics potential over a single detector, regardless of the specific choice of the FD technology. A combined analysis can provide the absolute normalization of the fluxes to $\sim 1\%$ from NC elastic scattering off electrons in LAr and the relative fluxes as a function of energy to $\leq 2\%$ from the low-ν_0 method in the magnetized tracker. *We conclude that the inclusion of an LAr TPC with a magnetized tracker in the ND complex is preferred regardless of the FD configuration.* The LAr TPC in the ND does not need necessarily to be magnetized when coupled with the tracker since this latter will also serve as a spectrometer for the LAr detector. The crucial parameter for the LAr TPC in light of a combined performance is a fiducial mass of the order of 100 tons.

With at least one water Cherenkov detector in the far site the most effective solution would be to have a large LAr TPC without magnetic field with a magnetized tracker. If LAr alone is the choice of the technology for the FD, the possibility of a single magnetized LAr detector might be considered, even if this solution would still have a reduced physics potential with respect to a two-detector complex with a LAr TPC and a magnetized tracker. The magnetic field should be sufficiently high to allow e^+/e^- separation and the LAr active volume should provide a good containment of the neutrino events. Detailed simulations of (anti)-neutrino interactions in the LAr and a complete flux analysis are required in order to evaluate the figure of merit of a single LAr magnetized detector.

We note that an important issue to be addressed by the LAr detector design is the capability to handle the high event rates expected at LBNE given the typical drift time of about 600 μs for a 1 m drift length, this issue would be more prominent if the beam power were increased above the nominal 700 kW.

Table XXVII summarizes the scorecard for the different ND configurations. In addition to the individual detector options, we list the two best configurations from the point of view of a combined analysis including a LAr detector and a fine-grained tracker. While a magnetized LAr is not needed with the low density magnetized tracker, it would be required to extend the physics potential of the scintillator tracker. The main limitation of the magnetized LAr detector currently considered is the relatively small fiducial volume ($\sim$20 tons), which would not allow a complete containment of the events so reducing the usable statistics.

Measurement	STT	Sci+μDet	LAr	LArB	LArB+Sci+μDet	LAr+STT
In Situ Flux Measurements for LBL:						
$\nu e^- \to \nu e^-$	Yes	No	Yes	No	No	Yes
$\nu_\mu e^- \to \mu^- \nu_e$	Yes	Yes	No	Yes	Yes	Yes
$\nu_\mu n \to \mu^- p$ at $Q^2 = 0$	Yes	Yes	No	No	Yes	Yes
Low-ν_0 method	Yes	Yes	No	Yes	Yes	Yes
ν_e and $\bar{\nu}_e$ CC	Yes	No	No	Yes	Yes	Yes
Background Measurements for LBL:						
NC cross sections	Yes	Yes	No	Yes	Yes	Yes
π^0/γ in NC and CC	Yes	Yes	Yes	Yes	Yes	Yes
μ decays of $\pi^\pm, K^\pm$	Yes	No	No	Yes	Yes	Yes
(Semi)-Exclusive processes	Yes	Yes	Yes	Yes	Yes	Yes
Precision Measurements of Neutrino Interactions:						
$\sin^2 \theta_W$ ν N DIS	Yes	No	No	No	No	Yes
$\sin^2 \theta_W$ νe	Yes	No	Yes	No	No	Yes
Δs	Yes	Yes	Yes	Yes	Yes	Yes
νMSM neutral leptons	Yes	Yes	Yes	Yes	Yes	Yes
High Δm^2 oscillations	Yes	No	No	Yes	Yes	Yes
Adler sum rule	Yes	No	No	No	No	Yes
$D/(p+n)$	Yes	No	No	No	No	Yes
Nucleon structure	Yes	Yes	Yes	Yes	Yes	Yes
Nuclear effects	Yes	Yes	Yes	Yes	Yes	Yes

TABLE XXVII. Summary of measurements that can be performed by different ND reference configurations.

XII. SUMMARY

In this report we have summarized the interim findings of a 2010 study by the LBNE Science Collaboration Physics Working Group. It provides a snapshot of the projected science capability of various potential LBNE far and near detector configurations based on a particular set of assumptions, particularly with respect to the far detector performance parameters. Table XXVIII summarizes some of the assumptions that may significantly affect the conclusions if they are incorrect. Work to mitigate the uncertainties in the detector and physics models continues and will be reported in future documents.

A. The muon veto for the 800-foot LAr option is >80% effective in conserving fiducial volume in liquid argon.

B. Gadolinium-loaded water reduces SRN background by a factor of five.

C. For LAr, background during a supernova burst is not significant for any depth, and that an appropriate triggering scheme will be implemented for high signal efficiency during a burst.

D. SK-1(2) detector performance parameters are used for the LBNE WC 30%(15%) pmt coverage studies.

E. For LAr, 80% efficiency and <1% background are used for Long-Baseline studies.

F. In evaluating impact for proton decay studies, 10 years LBNE running is compared to continued running of SK.

G. For WC, current Super-K background rates are assumed for proton decay.

H. *K select* trigger for proton decay mitigates the need for photon trigger in the 300-foot LAr option.

TABLE XXVIII. Summary of some critical performance assumptions on which the section conclusions are based (in no special order). The full set of assumptions is detailed in the relevant sections.

ACKNOWLEDGMENTS

Appendix A: Long-Baseline Oscillation Sensitivity Assumptions

This section details the assumptions used in the long-baseline oscillation sensitivity projections for LBNE. All calculations (with the exception of those that did not include detector response) were performed using the GLoBES [7] software package. The same neutrino fluxes (Fig. 80) and cross sections (Fig. 81) are used in GLoBES for both WC and LAr detectors. Inputs that differ between the two sets of detectors include assumptions about the detector performance (i.e. energy resolutions and detection efficiencies), specific signal processes, and backgrounds. These differences are outlined in the following sections. A summary of preliminary liquid argon TPC performance parameters for use with GLoBES can be found in a presentation by Bonnie Fleming to the Long-Baseline group [209]. All estimates assume a 700 kW LBNE beam, which implies a beam delivery of 7.3×10^{20} POT/year.
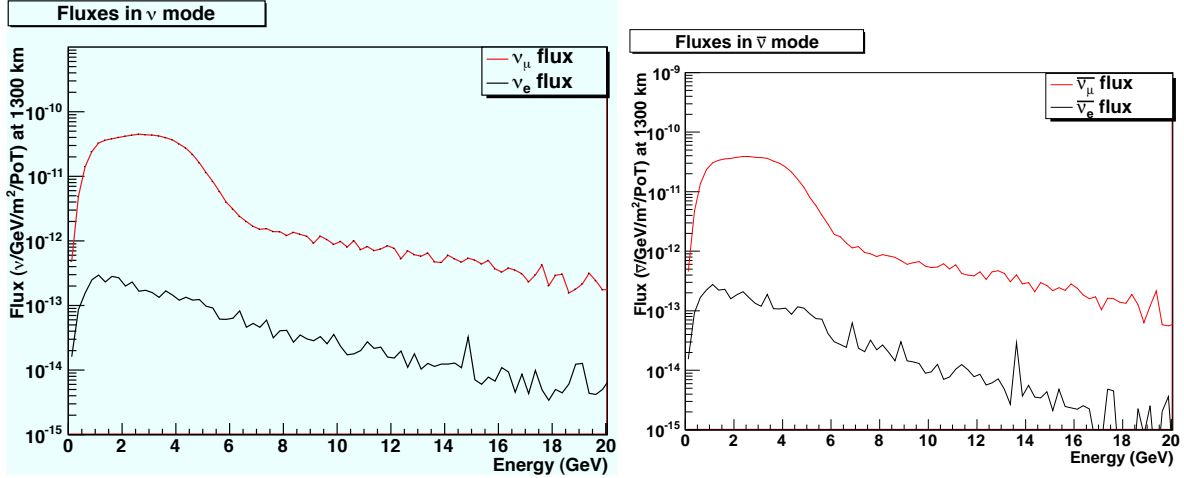

FIG. 80. The "August 2010" ν (left) and $\bar{\nu}$ (right) mode fluxes (`dusel120e250(n)i002dr280dz-tgtz30-1300km-0kmoa-flux.txt`). This is a 120 GeV optimized beam tune using two parabolic NuMI horns with the target pulled out 30 cm and assuming a 250 kA horn current and 280 m long, 2 m radius decay region (red curve in Fig. 2). This same set of fluxes is consistently used for all ν_e appearance and ν_μ disappearance studies in this document.

1. Inputs for ν_e Appearance

For the estimate of θ_{13}, δ_{CP}, and mass hierarchy sensitivities, GLoBES requires information on ν_e efficiencies, backgrounds, and energy resolutions for both WC and LAr detectors. These inputs are summarized in Table XXIX and detailed below.

Input	Water Cerenkov	Liquid Argon TPC
signal channel	ν_e QE	ν_e CC
signal efficiencies	Fig. 82	80%
signal E_ν resolution, $\sigma(E)/E$	Fig. 85	$0.15/E$
signal normalization error	1%	1%
background channels	ν_μ CC, ν_μ NC, intrinsic ν_e	ν_μ CC, ν_μ NC, intrinsic ν_e
background efficiencies	Fig. 82	1%, 1%, 80%
background E_ν resolution, $\sigma(E)/E$	Figs. 87, 86	$0.15/E$, Fig. 86, $0.15/E$
background normalization error	5%	5%

TABLE XXIX. Summary of GLoBES inputs for both detector technologies for the LBNE ν_e appearance sensitivity estimates. While not listed above, the ν contribution for each channel is explicitly included in GLoBES in the case of $\bar{\nu}$ running.

It should be noted that the treatment of systematic errors is admittedly not very sophisticated at present. In all long-baseline oscillation studies up to now, the total background normalization is allowed to vary by 5% as a source of systematic error. Background contributions are assumed to have a perfectly known shape and are not allowed to vary independently. Also, separate uncertainties on neutrino vs. antineutrino interactions have not yet been assessed. A more rigorous and complete systematic error handling in GLoBES is currently being developed for LBNE.
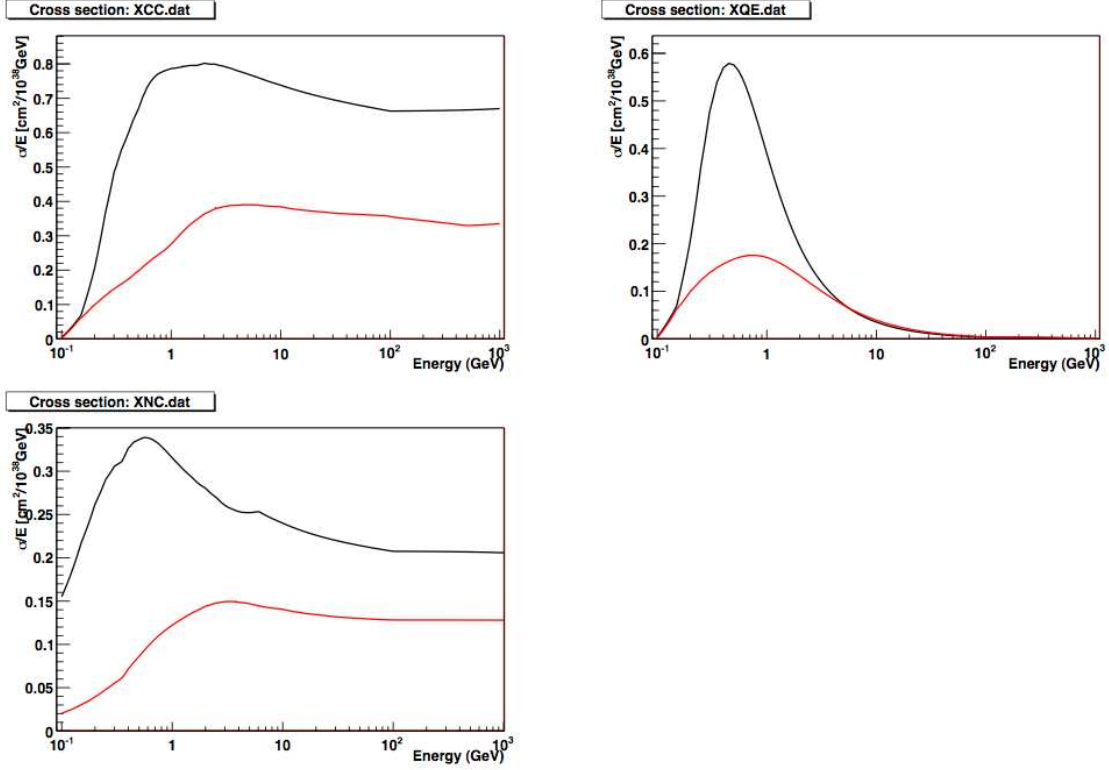
FIG. 81. The QE, total CC, and total NC ν_μ (black) and $\bar{\nu}_\mu$ (red) cross sections used in the long-baseline calculations. The same cross sections are currently used for both WC and LAr. These files were provided with GLoBES and have not been additionally modified [208]. Using the same input GLoBES cross sections for WC and LAr is not a bad assumption for now given that all of the signal samples in LAr are selected to be inclusive CC channels where the cross sections for Ar and H_2O are similar [160]. However, if a QE signal channel is used for LAr in the future, the $\sim 20\%$ neutron excess in argon would have to be accounted for in GLoBES. Also, π^0 absorption rates are about a factor of two larger in Ar than in H_2O [160]. This potentially leads to a factor of two fewer π^0's that can decay and lead to ν_e-like backgrounds in LAr. This difference can be accounted for in the π^0 efficiency factors for LAr rather than in the cross sections.

Fig. 83 shows the net signal and background efficiencies plotted as a function of neutrino energy for each detector type. Fig. 84 further breaks down the background efficiencies by source.

There are several things to note. In the case of WC, the efficiencies are based on modified Super-K simulations set to retain 40% of all ν_e signal events and assume 40% PMT coverage [210]. The energy resolutions for each process were obtained from Nuance simulations [159] and checked against Super-K Monte Carlo [211]. In the case of LAr, the background efficiency factors imply that 1% of ν_μ CC events, 1% of NC events, and 80% of intrinsic ν_e's pose backgrounds to the ν_e appearance search and not that 1% of the total sample is ν_μ CC, 1% is NC, etc. Also, in GLoBES, the background sources are varied by a $\pm 5\%$ uncertainty in a process and energy independent way (i.e., the overall normalizations of the ν_μ CC, NC, and ν_e backgrounds are varied together). This is true for both WC and LAr and will be upgraded to more realistic spectral uncertainties in the near future. Overall, the inputs were chosen to conservatively reflect the performance that we think we can realistically achieve with each detector technology and are subject to further change.
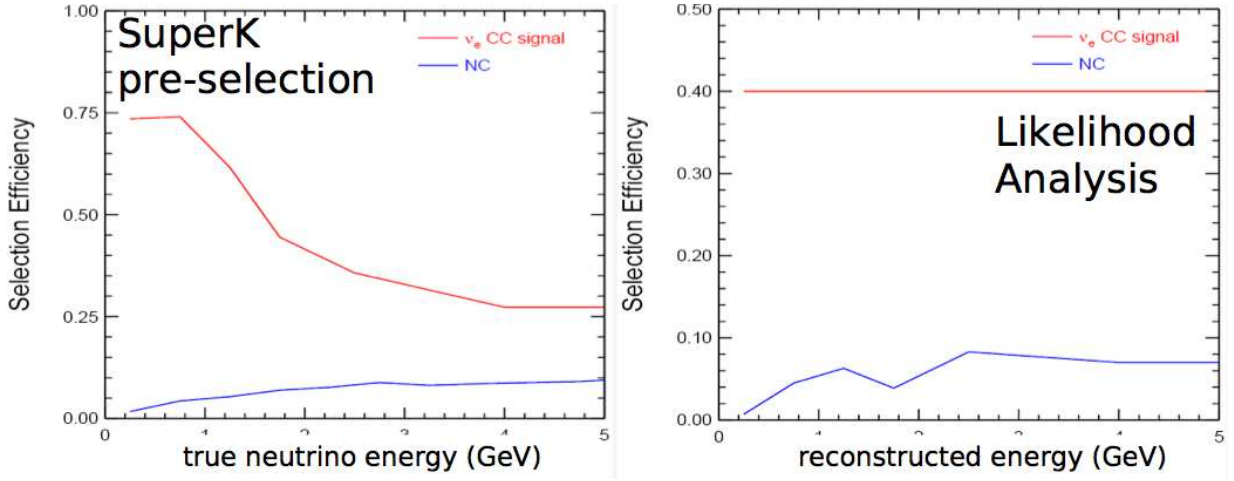
FIG. 82. Efficiencies for both ν_e (red) and NC background (blue) events assumed for a WC detector in GLoBES. The efficiencies are based on improvements to the Super-K reconstruction using a specialized fitter (POLfit) and are based on 40% photocathode coverage [210]. The efficiencies associated with the pre-cuts (left) are a function of true neutrino energy and reflect the Super-K requirement of a single-ring, electron-like event with no decay electron in the fiducial volume. The efficiencies resulting from the likelihood analysis (right) are functions of reconstructed neutrino energy and were set to retain 40% of ν_e signal events (which in turn specifies the level of NC background). The product of these two efficiencies yields the total efficiency. Combined, this results in an overall 16% (28%) ν_e efficiency at 2 GeV (0.8 GeV) for WC (see also Fig. 83).
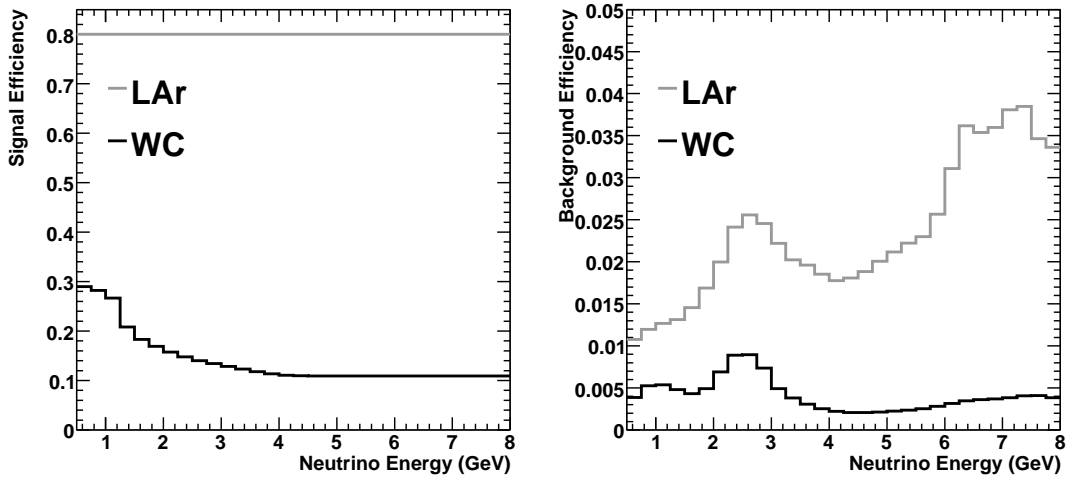

FIG. 83. Assumed ν_e signal (left) and total background (right) efficiencies plotted as a function of neutrino energy for WC (black) and LAr (gray). This reflects the fraction of signal and background events that enter the ν_e appearance sample. The individual factors that make up the total signal ν_e efficiency in the case of WC is provided in Fig. 82. Note: while not shown, the efficiency for $\bar{\nu}_e$'s is slightly higher than that for ν_e's in WC to account for the fact that the QE fraction is larger for antineutrinos as one moves up in energy. The efficiency for the total background is the weighted average of the individual efficiencies, i.e. the efficiency has been weighted by the amount of background in each energy bin. This is why the total background efficiencies are not constant in energy. A breakdown of the efficiencies for each of the individual background sources is provided in Fig. 84.
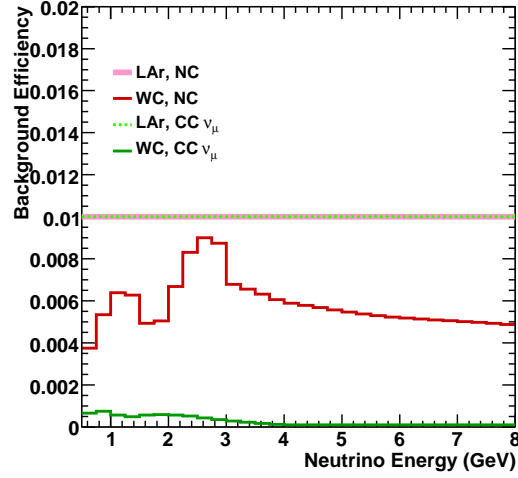
FIG. 84. Assumed efficiencies plotted as a function of neutrino energy for each background source in WC and LAr. This reflects the fraction of the background that enters the ν_e sample. A 1% energy-independent efficiency is assumed for each of the NC and ν_μ CC backgrounds in LAr (pink and dashed green lines). The efficiencies for NC and ν_μ CC are energy-dependent in the case of WC (red and solid green lines). Not shown are the intrinsic ν_e backgrounds which are assumed to have the same efficiency as ν_e signal events (left panel in Fig. 83).
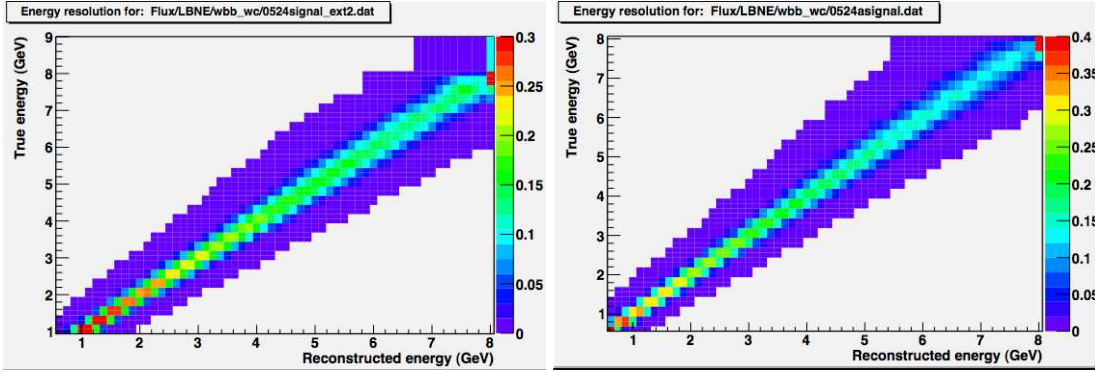

FIG. 85. Energy resolutions for ν_e (left) and $\bar{\nu}_e$ (right) events for water Cerenkov (`0524signal-ext2.dat` and `0525asignal-ext2.dat`). This smearing is used to simulate the energy resolution of the detector for both ν_e signal and intrinsic ν_e backgrounds.
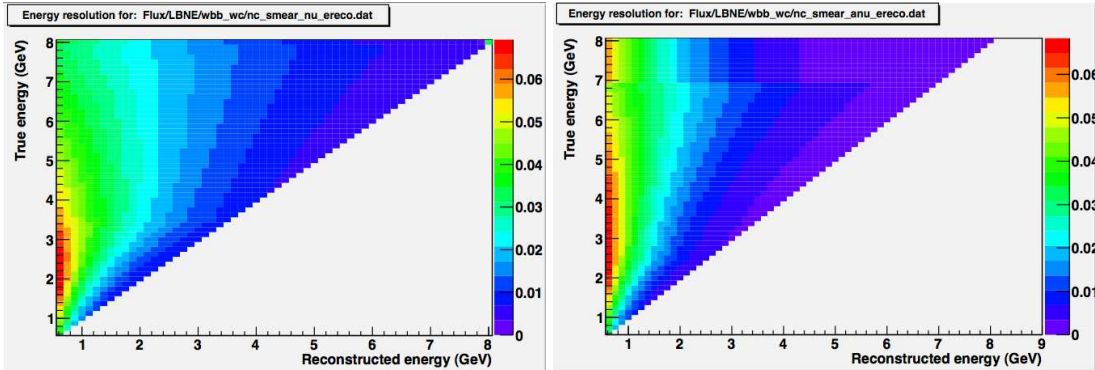

FIG. 86. Energy resolutions for NC backgrounds in neutrino (left) and antineutrino (right) modes for water Cerenkov (`nc-smear-nu-ereco.dat` and `nc-smear-anu-reco.dat`). This smearing is used to simulate the energy resolution of the detector for ν_μ NC events.
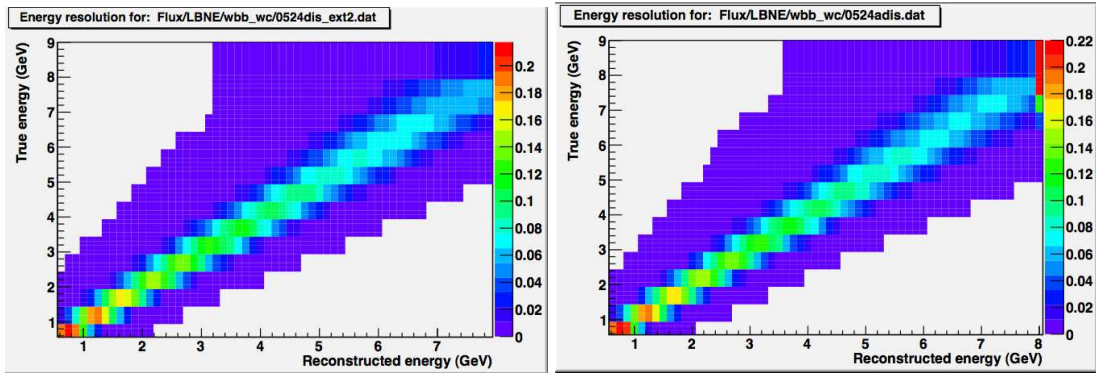
FIG. 87. Energy resolutions for ν_μ mis-ID backgrounds in neutrino (left) and antineutrino (right) modes for water Cerenkov (`0524dis-ext2.dat` and `0524adis.dat`). This smearing is used to simulate the energy resolution of the detector for ν_μ CC events.

2.   Inputs for ν_μ Disappearance

To estimate how accurately LBNE can measure $\sin^2 2\theta_{23}$ and Δm_{32}^2, GLoBES requires information on ν_μ efficiencies, backgrounds, and energy resolutions for both WC and LAr detectors. These inputs are summarized in Table XXX and detailed below.

Input	Water Cerenkov	Liquid Argon TPC
signal channel	ν_μ QE	ν_μ CC
signal efficiencies	97%	85%
signal E_ν resolution, $\sigma(E)/E$	Fig. 87	$0.20/\sqrt{E}$
signal normalization error	5%	5%
signal E_ν scale error	3%	2%
background channels	ν_μ CC π^+	ν_μ NC
background efficiencies	97%$^{(*)}$	0.5%
background E_ν resolution, $\sigma(E)/E$	Fig. 89	$0.20/\sqrt{E}$
background normalization error	10%	10%
background E_ν scale error	3%	2%

TABLE XXX. Summary of GLoBES inputs for both detector technologies for the LBNE ν_μ disappearance sensitivity estimates. While not listed above, the neutrino contribution for each channel is explicitly included in GLoBES in the case of antineutrino running. (*) The CC π^+ event rate is calculated from the QE cross section rescaled by a factor of 0.21. This value of 0.21 appears as an additional efficiency factor for this process in the GLoBES input file. Even though the QE cross section is used, the energy smearing takes into account the fact that this background is largely due to CC π^+ events (Fig. 89). This was done for convenience.

Fig. 88 shows the net signal and background efficiencies plotted as a function of neutrino energy for each detector type. In both cases, efficiencies that are flat in energy are used.
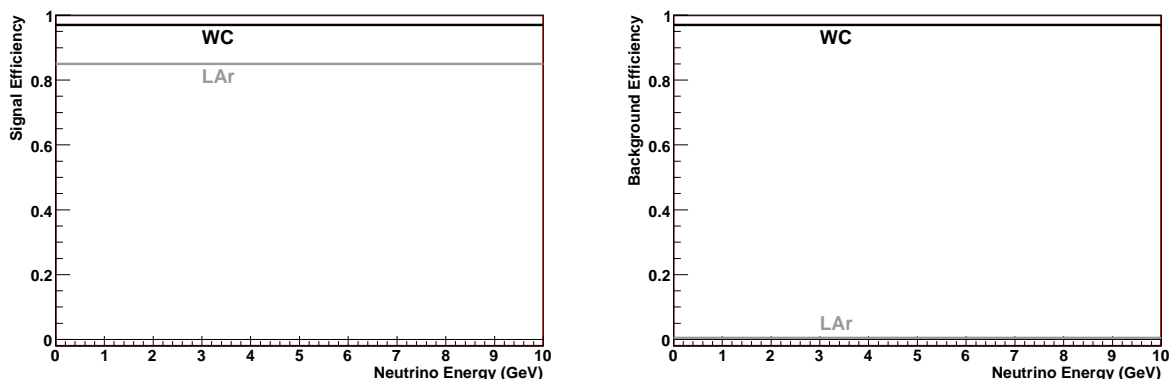

FIG. 88. Assumed ν_μ signal (left) and background (right) efficiencies plotted as a function of neutrino energy for WC (black) and LAr (gray). This reflects the fraction of signal and background events that enter the ν_μ disappearance sample. For WC, a 97% efficiency is assumed for both ν_μ QE signal and non-QE backgrounds. For LAr, a signal efficiency of 85% and a NC background efficiency of 0.5% is assumed.

There are several things to note. The WC and LAr disappearance fits differ in that a ν_μ QE sample is selected as the signal in one case (WC) and a ν_μ CC sample in the other (LAr). This does not mean than a QE sample could not be used in LAr or a CC sample in WC. This was simply the first choice for these initial LBNE sensitivity estimates. Optimization of the signal choice will be the subject of further study. Also, as has been pointed out, a 97% ν_μ QE efficiency in WC is probably too optimistic. This estimate will be better quantified and revised in future sensitivity estimates. In addition, there are several input values that have recently changed. Explicit energy scale uncertainties have been added for both WC and LAr and assigned conservative $2-3\%$ uncertainties based on the projected performance of similar detectors. Also, the neutrino energy resolutions for LAr have been increased to 20% to reflect the ability of a LAr detector to reconstruct E_ν from the energies of the outgoing muon and hadronic shower. Specifically, the value of $20\%/\sqrt{E}$ is based on an estimate of the neutrino energy resolution in ICARUS for events with $E_\nu < 1.25$ GeV [209, 212] and will be re-evaluated for LBNE energies using Monte Carlo. In addition,

the uncertainty on the normalization of signal events for both WC and LAr has been increased to 5%. Uncertainties on the normalization of the non-QE and non-CC backgrounds are conservatively set at 10%.
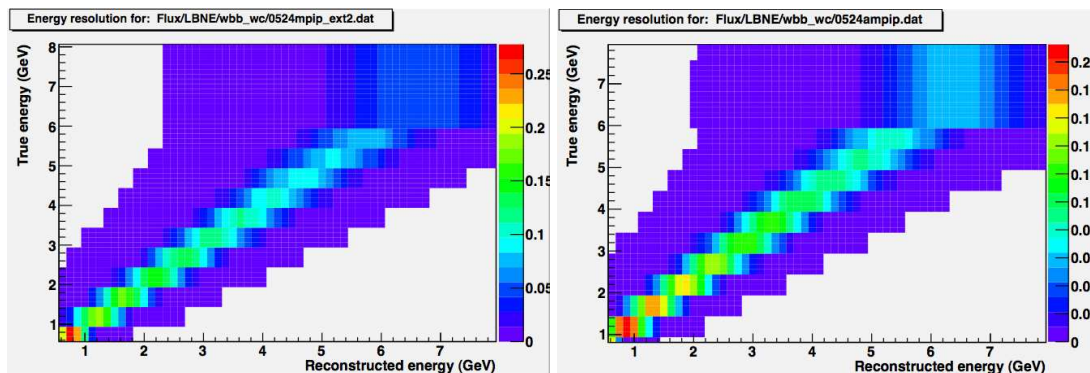

FIG. 89. Energy resolutions for ν_μ CC π^+ backgrounds in neutrino (left) and antineutrino (right) modes for water Cerenkov (`0524mpip-ext2.dat` and `0524ampip.dat`). These events will preferentially mis-reconstruct at lower energies when using a QE assumption, however the current smearing doesn't accurately reproduce this effect. This is under investigation.

For the measurement of the atmospheric parameters ($\sin^2 2\theta_{23}$ and Δm_{32}^2), assumptions must be made for θ_{13}, δ_{CP}, and the solar parameters. The values that were used are provided in Table XXXI.

parameter	value	uncertainty
θ_{12}	0.601	$\pm 10\%$
θ_{13}	0	$\pm 0\%$
δ_{CP}	0	$\pm 0\%$
Δm_{21}^2	7.59×10^{-5}	$\pm 4\%$
Δm_{31}^2	2.41×10^{-3}	$\pm 5\%$

TABLE XXXI. Oscillation parameters and uncertainties used in the LBNE ν_μ disappearance sensitivity estimates.

3. Inputs for Resolving θ_{23} Octant Degeneracy

The projections for LBNE's ability to resolve the θ_{23} octant degeneracy were generated by Joachim Kopp assuming the "August 2010" beam (`dusel120e250(n)i002dr280dz-tgtz30-1300km-0kmoa-flux`, red curve in Fig. 2). The same GLoBES inputs are used as the aforementioned ν_e appearance and ν_μ disappearance studies with a few exceptions. The energy scale uncertainties (as listed in Table XXX) are not yet included. Also, the energy resolutions from Table XXIX are used for LAr in the disappearance case rather than those from Table XXX.

4. Inputs for Non-Standard Interactions (NSI)

The projection for LBNE's sensitivity to new physics is based on work done by Joachim Kopp and Patrick Huber (see also [213] for an earlier version of this work). All of the GLoBES inputs are the same as in the LBNE ν_e appearance studies. The only input that differs is the neutrino flux. Kopp's NSI plots and estimates were made assuming the 2008/2009 LBNE beam design (`lbne120e300(n)i002dr250dz-1300m-0kmoa-flux.txt`, black curve in Fig. 2). The NSI projections for LBNE will likely be improved with the newer "August 2010" beam (`dusel120e250(n)i002dr280dz-tgtz30-1300km-0kmoa-flux`, red curve in Fig. 2) as a result of the higher flux in the 2-6 GeV region.

Appendix B: Supernova Burst Physics Sensitivity Assumptions

1. Assumptions for Event Rates in Water

We used WCsim [56] to evaluate the detection response in water for the 15% and 30% PMT coverage configurations. At the moment, we do not yet have a perfect match between WCsim output in Super-Kamiokande mode and published SK detector parameters in the few to few tens of MeV range [214, 215]– the agreement is at about the 10% level. The resolution used as a function of electron energy is shown in Fig. 90 (left); it was scaled by a factor of 0.66 in order that WCsim SK-mode output match the resolution in Ref. [214] (in addition to minor simulation mismatch, we do not have all SK software tools for energy response reconstruction at our disposal for WCsim output, which likely accounts for some of the discrepancy).

Trigger efficiency is shown in Fig. 90 (right) for the different configurations; this assumes a trigger requirement of 33 hits in 300 ns for the 15% PMT coverage configuration and 39 hits in 300 ns for the 30% configuration. (Note that we are assuming supernova neutrino events in water are self-triggered; one can imagine a configuration in which all digitized PMT hits are saved in the event of a high rate, which could improve efficiency.) These efficiencies are slightly worse than SK I [214] and SK II [215] efficiencies.
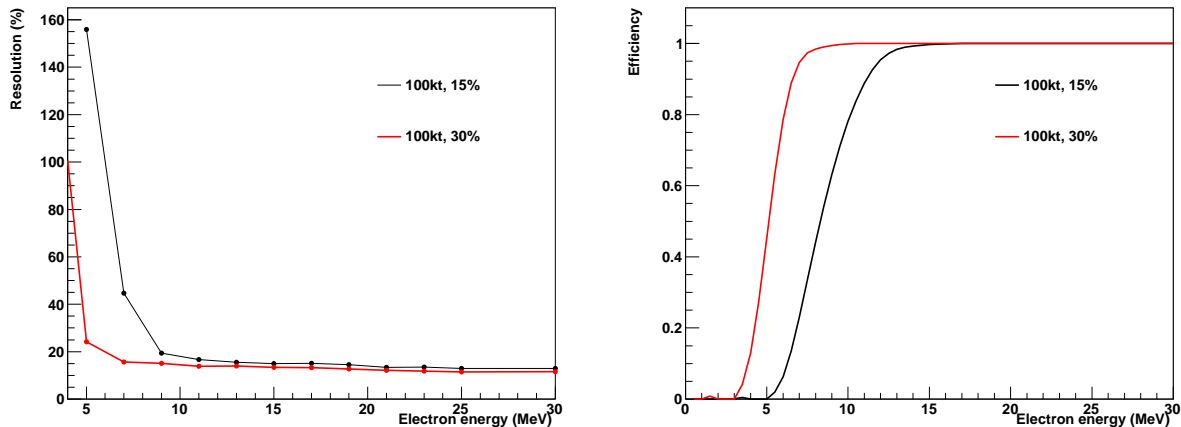

FIG. 90. Energy resolution (left) and trigger efficiency (right) as a function of electron energy, for 30% and 15% PMT coverages.

2. Assumptions for Event Rates in Argon

For event rate estimates in liquid argon, we assume a detection threshold of 5 MeV. We assume also that suitable triggering will be provided from photons, charge collection or from some external trigger. The energy resolution used is from Ref. [216], $\frac{\sigma}{E} = \frac{11\%}{\sqrt{E}} + 2\%$.

A summary of preliminary liquid argon TPC performance parameters can be found in a presentation by Bonnie Fleming to the Long-Baseline group [209].

[1] http://lbne.fnal.gov/
[2] A. Bernstein *et al.*, "Report on the Depth Requirements for a Massive Detector at Homestake," arXiv:0907.4183v2 [hep-ex]
[3] V. Barger *et al.*, "Report of the US long baseline neutrino experiment study", Fermilab-0801-AD-E, BNL-77973-2007-IR, arXiv:0705.4396v1 [hep-ph] (2007); http://nwg.phy.bnl.gov/~diwan/nwg/fnal-bnl/
[4] J. Hylen *et al.*, "Conceptual design for the technical components of the neutrino beam for the main injector (NuMI)", FERMILAB-TM-2018 (1997).
[5] D. G. Michael *et al.*, "Observation of muon neutrino disappearance with the MINOS detectors in the NuMI neutrino beam", hep-ex 0607088, FERMILAB-PUB-06-243, BNL-76806-2006-J A.
[6] R. Brun *et al.*, CERN-DD-78-2-REV.
[7] http://www.mpi-hd.mpg.de/lin/globes/; arXiv:0407333 [hep-ph] (2004) and arXiv:0701187 [hep-ph] (2007).
[8] D. Mohapatra, LBNE docdb #2683.
[9] EURONU WP6 2009 yearly report, J. Bernabeu *et al.*, arXiv:1005.3146 [hep-ph].
[10] "XXIV International Conference on Neutrino Physics and Astrophysics," Athens, Greece, (June, 2010), http://www.neutrino2010.gr/.
[11] K. Nakamura *et al.* (Particle Data Group), J. Phys. **G37**, 075021 (2010).
[12] P. Vahle, presentation at the XXIV International Conference on Neutrino Physics and Astrophysics (Neutrino 2010) in Athens, Greece; slides available at http://www.neutrino2010.gr/.
[13] T. Kobayashi, Neutrino 2010 presentation on the status of T2K.
[14] M.H. Ahn et al. (K2K Collaboration), Phys. Rev. **D74**, 072003 (2006), arXiv:0606032 [hep-ex].
[15] A. A. Aguilar-Arevalo et al. (MiniBooNE Collaboration), Phys. Rev. Lett. **103**, 061802 (2009).
[16] NOvA technical design report, http://www-nova.fnal.gov/nova_cd2_review/tdr_oct_23/tdr.htm
[17] B. Rebel, private communication.
[18] S. Davidson, C. Pena-Garay, N. Rius, and A. Santamaria, hep-ph/0302093.
[19] M.C. Gonzalez-Garcia, and M. Maltoni, Phys. Rept. **460**, 1 (2008), arXiv:0704.1800 [hep-ph].
[20] C. Biggio, M. Blennow, and E. Fernandez-Martinez, arXiv:0907.0097 [hep-ph].
[21] S. Antusch, J.P. Baumann, and E. Fernandez-Martinez, arXiv:0807.1003 [hep-ph].
[22] M.B. Gavela, D. Hernandez, T. Ota, and W. Winter, arXiv:0809.3451 [hep-ph].
[23] W.A. Mann, D. Cherdack, W. Musial, and T. Kafka, arXiv:1006.5720 [hep-ph].
[24] E. Akhmedov and T. Schwetz, arXiv:1007.4171 [hep-ph].
[25] J. Kopp, P. Machado, and S. Parke, to be published soon, the talk by PANM is available from http://www.int.washington.edu/talks/WorkShops/int_10_2b/People/Machado_P/Machado.pdf.
[26] A.A. Aguilar-Arevalo *et al.*, arXiv:1007.1150 [hep-ex].
[27] A. Friedland, Alexander and C. Lunardini Phys. Rev. **D72**, 053009 (2005), arXiv:0506143 [hep-ph].
[28] P. Astier *et al.*, Nucl. Phys. **B611**,
[29] Phys.Rev. **D81**, 093001 (2010).
[30] J. C. Pati and A. Salam, Phys. Rev. Lett. **31**, 661 (1973).
[31] H. Georgi and S. L. Glashow, Phys. Rev. Lett. **32**, 438 (1974).
[32] S. Dimopoulos, S. Raby and F. Wilczek, Phys. Lett. B **112**, 133 (1982).
[33] P. Langacker, Phys. Rept. **72**, 185 (1981).
[34] W. de Boer, Prog. Part. Nucl. Phys. **33**, 201 (1994) [arXiv:9402266 [hep-ph]].
[35] P. Nath and P. Fileviez Perez, Phys. Rept. **441**, 191 (2007) [arXiv:0601023 [hep-ph]].
[36] S. Raby *et al.*, arXiv:0810.4551 [hep-ph].
[37] G. Senjanovic, AIP Conf. Proc. **1200**, 131 (2010) [arXiv:0912.5375 [hep-ph]].
[38] T. Li, D. V. Nanopoulos and J. W. Walker, arXiv:1003.2570 [hep-ph].
[39] A. Bueno *et al.*, JHEP **0704**, 041 (2007) [arXiv:0701101 [hep-ph]].
[40] R. M. Barnett *et al.* [Particle Data Group], Phys. Rev. D **54**, 1 (1996).
[41] H. Nishino *et al.* [Super-Kamiokande Collaboration], Phys. Rev. Lett. **102**, 141801 (2009) [arXiv:0903.0676 [hep-ex]].
[42] http://www-sk.icrr.u-tokyo.ac.jp/whatsnew/new-20091125-e.html
[43] Y. Hayato *et al.* [Super-Kamiokande Collaboration], Phys. Rev. Lett. **83**, 1529 (1999) [arXiv:9904020 [hep-ex]].
[44] K. Kobayashi *et al.* [Super-Kamiokande Collaboration], Phys. Rev. D **72**, 052007 (2005) [arXiv:0502026 [hep-ex]].
[45] K. Scholberg, arXiv:0701081 [astro-ph].
[46] A. Dighe, arXiv:0809.2977 [hep-ph].
[47] R. M. Bionta *et al.*, Phys. Rev. Lett. **58**, 1494 (1987).
[48] K. Hirata *et al.* [KAMIOKANDE-II Collaboration], Phys. Rev. Lett. **58**, 1490 (1987).
[49] A. Mirizzi, G. G. Raffelt and P. D. Serpico, JCAP **0605**, 012 (2006) [arXiv:0604300 [astro-ph]].
[50] S. Choubey, B. Dasgupta, A. Dighe and A. Mirizzi, arXiv:1008.0308 [hep-ph].
[51] G. G. Raffelt, arXiv:9707268 [astro-ph].
[52] S. Hannestad and G. Raffelt, Phys. Rev. Lett. **87**, 051301 (2001) [arXiv:0103201 [hep-ph]].
[53] P. Antonioli *et al.*, New J. Phys. **6**, 114 (2004) [arXiv:0406214 [astro-ph]].
[54] K. Scholberg, Astron. Nachr. **329**, 337 (2008) [arXiv:0803.0531 [astro-ph]].
[55] K. Scholberg, J. Phys. Conf. Ser. **203**, 012079 (2010).

[56] https://wiki.bnl.gov/dusel/index.php/Simulation/Software
[57] http://www.phy.duke.edu/~schol/snowglobes/
[58] T. Totani, K. Sato, H. E. Dalhed and J. R. Wilson, Astrophys. J. **496**, 216 (1998) [arXiv:9710203 [astro-ph]].
[59] J. Gava, J. Kneller, C. Volpe and G. C. McLaughlin, Phys. Rev. Lett. **103**, 071101 (2009) [arXiv:0902.0317 [hep-ph]].
[60] H. Duan and A. Friedland, arXiv:1006.2359 [hep-ph].
[61] M. T. Keil, G. G. Raffelt and H. T. Janka, Astrophys. J. **590**, 971 (2003) [arXiv:0208035 [astro-ph]].
[62] E. Kolbe, K. Langanke and P. Vogel, Phys. Rev. D **66**, 013007 (2002).
[63] K. Langanke, P. Vogel and E. Kolbe, Phys. Rev. Lett. **76**, 2629 (1996) [arXiv:9511032 [nucl-th]].
[64] J. F. Beacom and P. Vogel, Phys. Rev. D **60**, 033007 (1999) [arXiv:9811350 [astro-ph]].
[65] R. Tomas, D. Semikoz, G. G. Raffelt, M. Kachelriess and A. S. Dighe, Phys. Rev. D **68**, 093013 (2003) [arXiv:0307050 [hep-ph]].
[66] M. Ikeda, http://www-sk.icrr.u-tokyo.ac.jp/sk/pub/m_ikeda_mron.pdf
[67] M. Ikeda *et al.* [Super-Kamiokande Collaboration], Astrophys. J. **669**, 519 (2007) [arXiv:0706.2283 [astro-ph]].
[68] I. Gil Botella and A. Rubbia, JCAP **0408**, 001 (2004) [arXiv:0404151 [hep-ph]].
[69] E. Kolbe, K. Langanke, G. Martinez-Pinedo and P. Vogel, J. Phys. G **29**, 2569 (2003) [arXiv:0311022 [nucl-th]].
[70] T. Totani, K. Sato and Y. Yoshii, Astrophys. J. **460**, 303 (1996) [arXiv:9509130 [astro-ph]].
[71] K. Sato, T. Totani and Y. Yoshii, *Prepared for 4th SFB-375 Ringberg Workshop on Neutrino Astrophysics, Ringberg Castle, Tegernsee, Germany, 20-24 Oct 1997*
[72] D. H. Hartmann and S. E. Woosley, Astropart. Phys. **7**, 137 (1997).
[73] R. A. Malaney, Astropart. Phys. **7**, 125 (1997) [arXiv:9612012 [astro-ph]].
[74] M. Kaplinghat, G. Steigman and T. P. Walker, Phys. Rev. D **62**, 043001 (2000) [arXiv:9912391 [astro-ph]].
[75] S. Ando, J. F. Beacom and H. Yuksel, Phys. Rev. Lett. **95**, 171101 (2005) [arXiv:0503321 [astro-ph]].
[76] C. Lunardini, Phys. Rev. D **75**, 073022 (2007) [arXiv:0612701 [astro-ph]].
[77] M. Fukugita and M. Kawasaki, Mon. Not. Roy. Astron. Soc. **340**, L7 (2003) [arXiv:0204376 [astro-ph]].
[78] A. Lien, B. D. Fields and J. F. Beacom, Phys. Rev. D **81**, 083001 (2010) [arXiv:1001.3678 [astro-ph.CO]].
[79] J. F. Beacom, arXiv:1004.3311 [astro-ph.HE].
[80] C. Lunardini, arXiv:1007.3252 [astro-ph.CO].
[81] M. Malek *et al.* [Super-Kamiokande Collaboration], Phys. Rev. Lett. **90**, 061101 (2003) [arXiv:0209028 [hep-ex]].
[82] L. E. Strigari, M. Kaplinghat, G. Steigman and T. P. Walker, JCAP **0403**, 007 (2004) [arXiv:0312346 [astro-ph]].
[83] J. F. Beacom and M. R. Vagins, Phys. Rev. Lett. **93**, 171101 (2004) [arXiv:0309300 [hep-ph]].
[84] H. Watanabe *et al.* [Super-Kamiokande Collaboration], arXiv:0811.0735 [hep-ex].
[85] A. Kibayashi and S. K. Collaboration, arXiv:0909.5528 [astro-ph.IM].
[86] Y. Koshio, Ph.D thesis, University of Tokyo (1998)
[87] http://www.phys.hawaii.edu/~jgl/post/A~White~Paper~for~Large~Liquid~Scintillation~Detectors~at~DUSEL.pdf
[88] P. Vogel and J. F. Beacom, Phys. Rev. D **60**, 053003 (1999) [arXiv:9903554 [hep-ph]].
[89] A. Strumia and F. Vissani, Phys. Lett. B **564**, 42 (2003) [arXiv:0302055 [astro-ph]].
[90] W. E. Ormand, P. M. Pizzochero, P. F. Bortignon and R. A. Broglia, Phys. Lett. B **345**, 343 (1995) [arXiv:9405007 [nucl-th]].
[91] M. Sajjad Athar and S. K. Singh, Phys. Lett. B **591**, 69 (2004).
[92] A. G. Cocco, A. Ereditato, G. Fiorillo, G. Mangano and V. Pettorino, JCAP **0412**, 002 (2004) [arXiv:0408031 [hep-ph]].
[93] http://nucleardata.nuclear.lu.se/nucleardata/toi/nuclide.asp?iZA=30011
[94] A. Rubbia, J. Phys. Conf. Ser. **171**, 012020 (2009) [arXiv:0908.1286 [hep-ph]].
[95] O.L.G. Peres *et al.*, Phys. Rev. **D79**, 113002 (2009).
[96] J. Bernabeu *et al.*, Nucl. Phys. **B669**, 255 (2003).
[97] M.C. Gonzalez-Garcia *et al.*, Phys. Rev. **D70**, 093005 (2004).
[98] O.L.G. Peres *et al.*, Phys. Lett. **B456**, 204 (1999).
[99] Akhmedov *et al.*, JHEP 0806 072 (2008).
[100] S.T. Petcov *et al.*, Nucl. Phys. **B**, 740 (2006).
[101] S. Palomares-Ruiz *et al.*, Nucl. Phys. **B712**, 392 (2005).
[102] Y. Ashie *et al.*, Phys. Rev. Lett **93**, 101801 (2004).
[103] Y. Ashie *et al.*, Phys.Rev. **D71**, 112005 (2005).
[104] K. Abe *et al.*, Phys. Rev. Lett. **97**, 171801 (2006).
[105] R. Wendell *et al.*, arXiv:1002.3471 [hep-ex] (2010).
[106] J. Hosaka *et al.*, Phys. Rev. **D74**, 032002 (2006).
[107] K. Abe *et al.*, Phys. Rev. **D77**, 052001 (2008).
[108] W. Wang, Ph. D Thesis (2007).
[109] G. Mitsuka Ph. D Thesis (2009).
[110] P. Adamson *et al.*, Phys. Rev. **D75**, 092003 (2007).
[111] D. Indumathi *et al.*, Phys. Rev. **D71**, 013001 (2005).
[112] S. Coleman and S. Glashow, Phys. Lett. **B405**, 249 (1997).
[113] F. Klinkhamer and G. Volovik, Intl. Jour. of Mod. Phys. **A20**, 2795 (2005).
[114] D. Colladay and V. Kostelecky, Phys. Rev. **D**, 116002 (1998).
[115] Y. Grossman *et al.*, Phys. Rev. **D72**, 125001 (2005).

[116] M. C. Gonzalez-Garcia *et al.*, Nucl. Phys. **B573**, 3 (2000).
[117] D. Kaplan *et al.*, Phys. Rev. Lett. **93**, 091801 (2004).
[118] J. Conrad *et al.*, arXiv:1008.2984 [hep-ph] (2010).
[119] P. Huber *et al.*, arXiv:0501037 [hep-ph] (2005).
[120] A. Rubbia, NNN99 Proceedings, arXiv:0001052 [hep-ex] (2001).
[121] M. Fechner *et al.*, Phys. Rev. **D79**, 112010 (2009).
[122] S. Petcov and T. Schwetz, arXiv:0511277 [hep-ph] (2005).
[123] C. Andreopoulos *et al.*, Nucl. Instrum. Meth. **A614**, 87 (2010).
[124] G. Barr *et al.*, Phys. Rev. **D70**, 023006 (2004).
[125] G. Battistoni *et al.*, Astropart. Phys. **19**, 269 (2003).
[126] T. Kajita, Talk at NOON2004 (Tokyo), 2004.
[127] M. Ishitsuka, Ph. D Thesis (2004).
[128] A. Bueno *et al.*, arXiv:0701101 [hep-ph] (2007).
[129] R. Gandhi *et al.*, Phys. Rev. D78:073001 (2008).
[130] F. Dufour, Ph. D Thesis (2009).
[131] V. Barger *et al.*, Phys. Rev. **D22**, 2718 (1980).
[132] M. Messier, private communication (2010).
[133] M. Sanchez *et al.*, Phys. Rev. **D68**, 113004 (2003).
[134] C. Ishihara, Ph. D Thesis (2010).
[135] J.G. Learned and K. Mannheim, Ann. Rev. Nucl. Part. Sci. **50** 679 (2000).
[136] Bahcall, J., Waxmann, E., 2001, Physical Review D, **64** 023002 (2001).
[137] Gueta, *et al.*, Astropart.Phys. **20** 429-455 (2004).
[138] M. Drees and M. M. Nojiri, Phys. Rev. D **47**, 376 (1993).
[139] DeYoung, T., *et al.*et al. (IceCube Collaboration), 2008. J. of Phys. Conf. Ser. **136** 022046 (2008).
[140] V. Aynutdinov,*et al.* (BAIKAL Collaboration), Astropart.Phys.25:140-150,2006.
[141] The Antares Collaboration Internal Report CPPM-P-1999-02 (1999), arXiv:9907432v1 [astro-ph].
[142] IceCube collaboration, in preparation.
[143] R. Abbasi, *et al.*, Astrophys.J **701** L47-L51 (2009).
[144] M. Ackermann, *et al.*, Astrophys.J **675** 1014 (2008).
[145] R. Abbasi, *et al.*, Astrophys.J. **710** 346-359 (2010).
[146] R. Abbasi, *et al.*, Phys. Rev. Lett. **102** 201302 (2009), [arXiv:0910.4480].
[147] S. Desai, *et al.*, Phys.Rev.D **70** 083523 (2004).
[148] E. Thrane, *et al.*, Astrophys.J **704** 503-512 (2009).
[149] M.E.C Swanson, *et al.*, Astrophys.J **652** 206-215 (2006).
[150] Private collaboration document DUSEL/LBNE R&D Document 994,
      `http://nwg.phy.bnl.gov/DDRD/cgi-bin/private/ShowDocument?docid=994`.
[151] E. Presani, *et al.*, Nuclear Physics B Proceedings Supplements **188** 270-272 (2009).
[152] H. Yuksel, S. Horiuchi, J. Beacom, S. Ando, Phys.Rev.D **76** 123506 (2007).
[153] B. T. Cleveland et al. **Astrophys. J. 496: 505** (1998).
[154] S. Fukuda et al., Phys. Rev. Lett. **86**, 5651 (2001); Q. R. Ahmad et al., Phys. Rev. Lett. **87), 071301**(2001).
[155] Phys.Rev. **D69**, 011104 (2004).
[156] A. Guglielmi, talk at XXIV Neutrino Conference (Neutrino 2010), Athens, Greece (June 2010).
[157] Internal collaboration document DUSEL/LBNE R&D Document 643-v2, "Reference Near Detector Parameters," `http://nwg.phy.bnl.gov/DDRD/html/0006/000643/002/Near%20Detector%20Reference%20Parameters.docx`
[158] G.P. Zeller, "Expected Event Rates in the LBNE Near Detectors", docdb #783, `http://nwg.phy.bnl.gov/DDRD/html/0007/000783/001/event-rates.pdf`, flux files in `http://www.phy.bnl.gov/~bishai/nwg/work/gnumi/prod/`
[159] D. Casper, Nucl. Phys. Proc. Suppl. **112**, 161 (2002), hep-ph/0208030.
[160] R. Petti and G.P. Zeller, "Nuclear Effects in Water vs. Argon", docdb #740.
[161] G.P. Zeller et al., Phys. Rev. Lett. **88**, 091802 (2002); erratum-ibid. **90**, 239902 (2003)
[162] W.J. Marciano and Z. Parsa, J. Phys. G **29** (2003) 2629-2645.
[163] I. Stancu et al., arXiv:0910.2698 [hep-ex].
[164] The OscSNS Neutrino Experiment `http://physics.calumet.purdue.edu/~oscsns/`.
[165] B. Baibussinov et al., arXiv:0909.0355 [hep-ex].
[166] J.A. Harvey, C.T. Hill and R.J. Hill, Phys. Rev. Lett. **99** (2007) 261601; Phys. Rev. D **77** (2008) 085017.
[167] J. Jenkins and T. Goldman, Phys. Rev. D **80** (2009) 053005.
[168] M.Shiozawa, Talk at NNN09;
      `http://nnn09.colostate.edu/Talks/Session02/091007-Shiozawa-Nucleon-decay-searches-dist.pdf`.
[169] S.Mine *et al*. (K2K Collaboration), Phys. Rev. D 77, 032003 (2008); H. Nishino *et al*. (Super-Kamiokande Collaboration), Phys. Rev. Lett. 102, 141801 (2009).
[170] P. Astier et al. [NOMAD collaboration], Nucl. Phys. B621/1-2 (2001) 3-34, arXiv:0111057 [hep-ex].
[171] D. Naumov et al. [NOMAD collaboration], Nucl.Phys.B 700 (2004) 51-68, arXiv:0409037 [hep-ex].
[172] S. Alekhin, S. A. Kulagin, and R. Petti, AIP Conf. Proc. **967**, 215 (2007), [arXiv:0710.0124].
[173] S. Alekhin, S. Kulagin, and R. Petti, (2008), arXiv:0810.4893 [hep-ph].
[174] S. Alekhin, S. Kulagin and R. Petti, Phys. Lett. B **675**, 433 (2009).

[175] A. B. Arbuzov, D. Y. Bardin and L. V. Kalinovskaya, JHEP **78**, 506 (2005); arXiv:0407203 [hep-ph].

[176] S. A. Kulagin and R. Petti, Nucl. Phys. **A765**, 126 (2006).

[177] S. A. Kulagin and R. Petti, Phys. Rev. **D76**, 094023 (2007).

[178] S. A. Kulagin and R. Petti, arXiv:1004.3062 [hep-ph].

[179] R. Petti and O. Samoylov, Proceedings of DIS10 - Firenze, Italy, 19-23 April 2010.

[180] A. Czarnecki and W.J. Marciano, Int. J. Mod. Phy. A15 (2000) 2365

[181] S.C. Bennet and C.E. Wieman, Phys. Rev. Lett. 82 (1999) 2484

[182] Particle Data Group, W.-M. Yao et al., Journal of Physics, G 33 (2006) 1

[183] P.L. Anthony et al [E158 collaboration], Phys.Rev.Lett. 95 (2005) 081601, hep-ex/0504049

[184] R. D. Young, J. Roche, R. D. Carlini and A. W. Thomas, Phys. Rev. Lett. **97**, 102002 (2006).

[185] D. B. Leinweber *et al.*, Phys. Rev. Lett. **94**, 212001 (2005).

[186] A. Airapetian *et al.*, Phys. Lett. B **666**, 446 (2008).

[187] L.A. Ahrens et al., Phys. Rev. D **35**, 785 (1987)

[188] G. Garvey et al., Phys. Rev. C **48**, 761 (1993)

[189] W.M. Alberico et al., Nucl. Phys. A **651**, 277 (1999)

[190] L. Bugel et al., arXiv:0402007 [hep-ex].

[191] A. Boyarsky, O. Ruchayskiy and M. Shaposhnikov, Ann. Rev. Nucl. Part. Sci. **59** (2009) 191 [arXiv:0901.0011 [hep-ph]]

[192] M. Shaposhnikov, JHEP **0808** (2008) 008 [arXiv:0804.4542 [hep-ph]].

[193] L. Canetti and M. Shaposhnikov, arXiv:1006.0133 [hep-ph].

[194] A. M. Cooper-Sarkar *et al.* [WA66 Collaboration], Phys. Lett. B **160** (1985) 207.

[195] F. Bergsma *et al.* [CHARM Collaboration], Phys. Lett. B **166** (1986) 473.

[196] A. Vaitaitis *et al.* [NuTeV Collaboration], Phys. Rev. Lett. **83** (1999) 4943 [arXiv:9908011 [hep-ex]].

[197] G. Bernardi *et al.*, Phys. Lett. B **166** (1986) 479.

[198] G. Bernardi *et al.*, Phys. Lett. B **203** (1988) 332.

[199] A. Atre, T. Han, S. Pascoli and B. Zhang, JHEP **0905** (2009) 030 [arXiv:0901.3589 [hep-ph]].

[200] D. Gorbunov and M. Shaposhnikov, JHEP **0710** (2007) 015 [arXiv:0705.1729 [hep-ph]].

[201] M. Soderberg, arXiv:0910.3433 [physics.ins-det]

[202] M. Maltoni and T. Schwetz, arXiv:0705.0107 [hep-ph]

[203] B. L. Ioffe, V. A. Khoze and L. N. Lipatov, "Hard Processes. Vol. 1: Phenomenology, Quark Parton Model," *Amsterdam, Netherlands: North-holland (1984) 340p*

[204] D. Allasia et al., Z. Physik C **28** (1985) 321-333.

[205] A. Accardi, M. E. Christy, C. E. Keppel, P. Monaghan, W. Melnitchouk, J. G. Morfin and J. F. Owens, Phys. Rev. D **81**, 034016 (2010).

[206] Jefferson Lab experimental proposal PR12-06-13, S. Bültmann, M. E. Christy, H. Fenker, K. A. Griffioen, C. E. Keppel, S. E. Kuhn, W. Melnitchouk and V. Tsvaskis, spokespersons,
`http://www.jlab.org/exp$_$prog/proposals/06/PR12-06-113.pdf`.

[207] A. Bodek and A. Simon, Z. Phys. C **29**, 231 (1985); G. T. Jones *et al.*, Z. Phys. C **44**, 379 (1989).

[208] M. Messier, UMI-99-23965; E.A. Paschos and J.Y. Yu, Phys. Rev. **D65**, 033002 (2002).

[209] Internal collaboration presentation LBNE R&D document docdb #972, "Efficiencies for LAr20 for GLoBES," B. Fleming, Long-Baseline TG meeting (7/26/2010).

[210] C. Yanagisawa, C.K. Jung, and P.T. Lee, `http://ale.physics.sunysb.edu/uno/publications/numunuePREBWv3.pdf`

[211] M. Diwan, private communication.

[212] B. Fleming, private communication and discussion at INT, August 2010.

[213] J. Kopp, LBNE internal document docdb #770.

[214] J. Hosaka *et al.* [Super-Kamiokande Collaboration], Phys. Rev. D **73**, 112001 (2006) [arXiv:0508053 [hep-ex]].

[215] J. P. Cravens *et al.* [Super-Kamiokande Collaboration], Phys. Rev. D **78**, 032002 (2008) [arXiv:0803.4312 [hep-ex]].

[216] S. Amoruso *et al.* [ICARUS Collaboration], Eur. Phys. J. C **33**, 233 (2004) [arXiv:0311040 [hep-ex]].

[217] `http://arxiv.org/`

[218] Institute for Nuclear Theory, University of Washington, summer program INT-10-2b, "Long-Baseline Neutrino Physics and Astrophysics," July 26 - August 27, 2010. `http://www.int.washington.edu/PROGRAMS/10-2b/`

[219] Publication INT-PUB-11-002, Institute for Nuclear Theory, University of Washington.